University of California

Los Angeles

Strangeness Production and Strange V0 & Charged Hadron Correlation in Heavy-Ion Collisions

A dissertation submitted in partial satisfaction

of the requirements for the degree

Doctor of Philosophy in Physics

by

Feng Zhao

2014

Abstract of the Dissertation

Strangeness Production and Strange V0 & Charged Hadron Correlation in Heavy-Ion Collisions

by

Feng Zhao

Doctor of Philosophy in Physics

University of California, Los Angeles, 2014

Professor Huan Z. Huang, Chair

In relativistic heavy-ion collisions, experimental evidence indicates that a new form of matter with de-confined quarks and gluons named the Quark-Gluon Plasma(QGP) has been created. The Relativistic Heavy Ion Collider (RHIC) provides a unique opportunity to study the QGP matter.

Strange hadron production is believed to be sensitive to parton dynamics in heavy-ion collisions. In particular, the strange quark production rate and its subsequent evolution in the dense partonic medium depend on the beam energy and the net baryon density. The productions of K^0_S, Λ, Ξ, Ω at mid-rapidity from Au+Au collisions at the beam energies of 7.7, 11.5, 19.6, 27, and 39 GeV from the RHIC Beam Energy Scan Program are measured. We investigate the strangeness enhancement and ratios of anti-baryon to baryon yields as a function of beam energy at RHIC. Nuclear modification factors and ratios of baryon to meson yields are also studied. Implications on collision dynamics due to the increase in the baryon chemical potential at low beam energy and constraints on chemical freeze-out parameters will also be discussed in this thesis.

Parity-odd domains are theorized to form inside the QGP and to cause electric

charge separation with respect to the reaction plane in the relativistic heavy-ion collisions via the Chiral Magnetic Effect (CME). Such charge separation has been studied at RHIC and LHC via the difference in two particle correlation between the opposite charge and same charge hadrons. The $\Lambda(\bar{\Lambda})$ and K^0_S particles are charge-neutral, and are supposed to bear no charge separation effects due to CME. We study the correlation between the neutral particle and charged hadron to investigate background for charged hadron correlation. In addition, the large angular momentum in heavy-ion collisions is predicted to lead to the Chiral Vortical Effect (CVE) which induces a baryon number separation, in analogy with the electric charge separation caused by CME. We carried out a study of $\Lambda - p$ correlations to search for the CVE. We present measurements of correlations for $\Lambda - h^{\pm}$, $K^0_S - h^{\pm}$, $K^0_S - p$, and $\Lambda - p$ in Au+Au collisions at 39 GeV and 200 GeV, to study the electric charge and baryon number separations across the reaction plane.

The dissertation of Feng Zhao is approved.

David Saltzberg

Yu Huang

Huan Z. Huang, Committee Chair

University of California, Los Angeles

2014

To my parents, grandparents and girlfriend,
who are always there for me.

Table of Contents

List of Figures

List of Tables

Acknowledgments

I give my most sincere gratitude to my advisor, Prof. Huan Z. Huang, for his guidance and encouragement. I would like to thank Prof. Graciela Gelmini, Prof. David Saltzberg, and Prof. Yu Huang for serving in the committee. I truly appreciate Dr. Gang Wang and Dr. Xianglei Zhu for a lot of useful discussion. Finally, I would like to thank the STAR Collaboration and all the members in UCLA Heavy Ion Group for advise on my data analysis and writing thesis.

Vita

July, 2008	Bachelor of Science, University of Science and Technology of China
March, 2010	Master of Science in Physics, University of California, Los Angeles
September, 2013	Master of Science in Statistics, University of California, Los Angeles
2008-2014	Research Assistant, Experimental QCD and neutrino physics group University of California, Los Angeles
2013-2014	Dissertation Year Fellowship, University of California, Los Angeles

CHAPTER 1

Introduction to Relativistic Heavy-Ion Collisions

The idea to create the Quark Gluon Plasma (QGP) in heavy-ion collisions was proposed in 1970s [1]. Since then, experimental efforts have been made to search for and study the QGP with the heavy-ion collisions.

The pioneering work began on the Bevalac accelerator at Lawrence Berkeley National Laboratory (LBNL) in the late 1970s and early 1980s. Since then, several fixed target experiment facilities have been used for heavy-ion collision physics, including the Heavy Ion Synchrotron at Helmholtzzentrum für Schwerionforschung (GSI), Alternating Gradient Synchrotron (AGS) at Brookhaven National Laboratory (BNL), and Super Proton Synchrotron (SPS) at European Organization for Nuclear Research (CERN). Those facilities have a center-of-mass energy ranging from below GeV to tens of GeV. Nowadays, heavy-ion colliders are built in US and Europe: the Relativistic Heavy Ion Collider (RHIC) at BNL runs with the beam energy from several GeV to 200 GeV, and the Large Hadron Collider at CERN reaches the energy of 2.76 TeV.

1.1 Initial Stages of the Collisions

The initial state of heavy-ion collisions can be characterized with beam energy, heavy ion species, and the impact parameter. The impact parameter, b, is the distance between the centers of the two nuclei. In relativistic heavy-ion collisions, the colliding nuclei are Lorenz-contracted into dishes in the center-of-mass frame.

Two colliding nuclei have an overlapping region in the collision. The nucleons within the overlap region are called participant nucleons, while the nucleons outside of the region are called spectator nucleons. In the collision of two identical nuclei with $b = 0$, almost all the nucleons participate in the collision, the collision is called a central collision. When b is a little less than twice of the radius of the nuclei, only a few nucleons participate in the collision, most of the nucleons are spectator nucleons, and the collision is called a peripheral collision. In the experiment, the impact parameter is not observable. However, the multiplicity of produced particles is related to the impact parameter. The centrality is the percentile of the multiplicity distribution, which reflects the impact parameter in the heavy-ion collisions. For example, 0-5% centrality contains the most central collisions, and corresponds to an impact parameter less than 3.5 fm.

In the central and semi-central collisions, a fireball is created from the participant nucleons. The energy density is so high that the fire ball reaches a (locally) thermalized equilibrium phase with partonic degrees of freedom and high temperature. This hot and dense material created is the QGP. The QGP medium expands rapidly, and the temperature decreases. A schematic view of the time evolution of QGP is shown in Figure 1.1. When the temperature is below the critical temperature, the medium becomes a mixed phase of partonic and hadronic matter. When the temperature decreases to T_{ch}, the chemical freeze-out takes place and the hadron species are fixed. When the temperature decreases to T_{ki} (or T_{fo} in Figure 1.1), the kinematic freeze-out takes place, and the hadrons stop interacting elastically with each other.

1.2 Quark Gluon Plasma

The quark gluon plasma is **a (local) thermally equilibrated state of matter in which quarks and gluons are deconfined from hadrons, so that color**

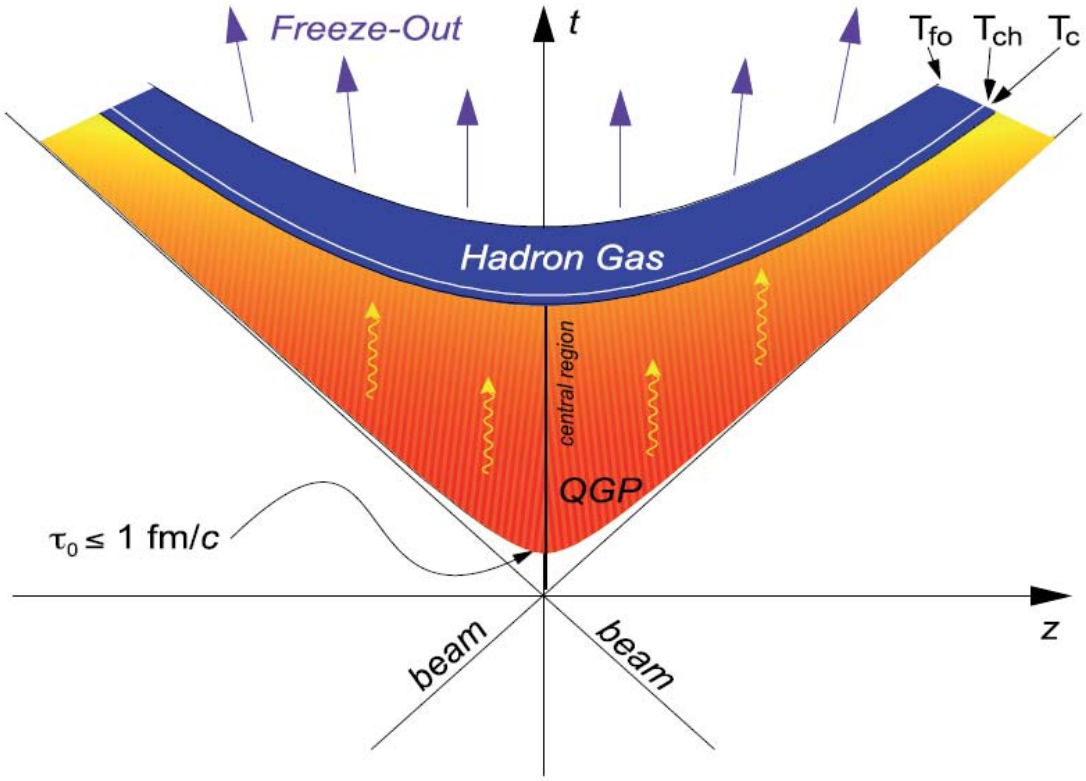

Figure 1.1: A schematic view of the evolution of a high energy heavy-ion collision. The figure is from [2].

degrees of freedom become manifest over nuclear, rather than merely nucleonic, volumes [3]. The QGP is expected to exist at very high temperature (such as the early stage of the Universe within one micro-second after the Big Bang), and/or very high baryon density (such as the neutron stars) environments. It could be produced in high-energy heavy-ion collisions.

For an ideal gas, the ratio of strongly interacting matter's pressure (p) to the temperature (T) to the fourth power (p/T^4) is proportional to the number of degrees of freedom [3][4]. The p/T^4 as a function of T is shown in Figure 1.2. It is shown that there is a sharp rise in the effective number of degrees of freedom at T of about 160 MeV. If the temperature reaches critical temperature (T_c), a deconfined state of quarks and gluons or the QGP will be created. It should be noted that although the quarks and gluons are deconfined above T_c, they are not completely free from interactions with each other, since the Stefan-Boltzmann limit of p/T^4 for an ideal gas is far above the curves, which is shown in Figure 1.2.

1.3 Experimental Probes of the QGP

The QGP is believed to be created in the central and near-central heavy-ion collisions, however, it cannot be detected directly. In experiments, we can only detect the final state particles and use them as probes to study the properties of the medium created in the collisions. In this section, we review some experimental observables, and discuss the properties of the medium created in the collisions.

1.3.1 Hadron Yields and Spectra

Particle yields and momentum spectra reflect the properties of the bulk of the matter produced in heavy-ion collisions. After the chemical freeze-out, particles only interact elastically, and the particle species will not change. The information of the system at chemical freeze-out stage can be obtained from the integrated

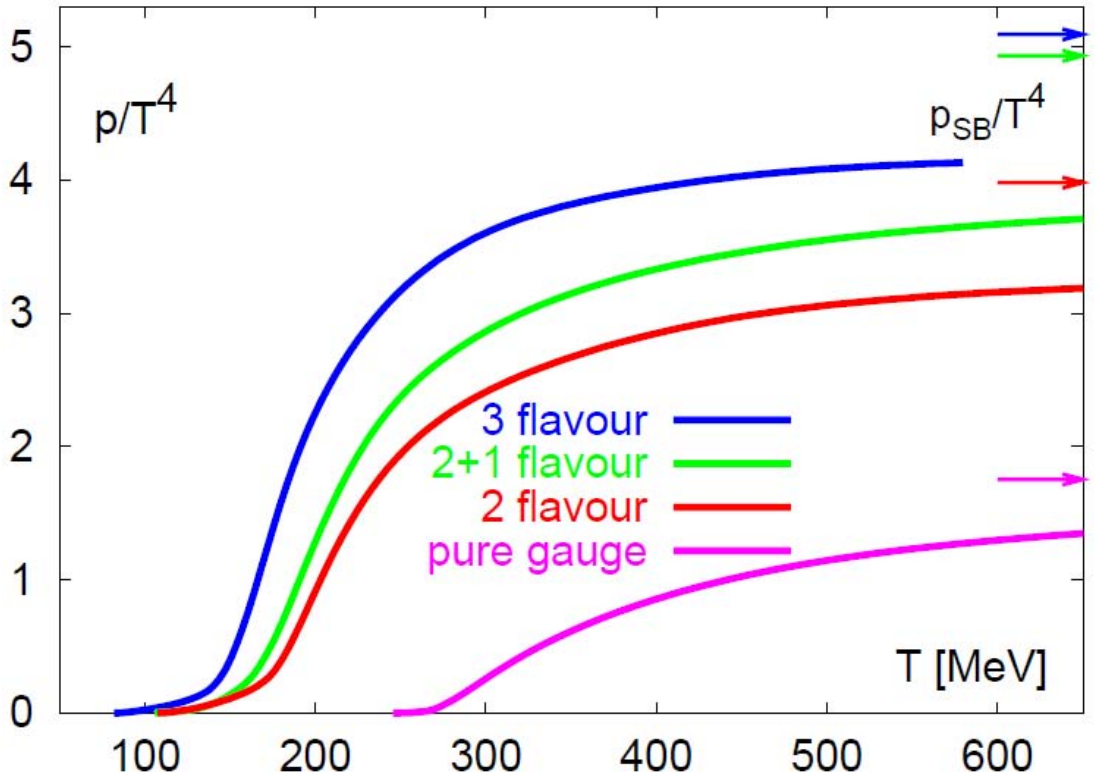

Figure 1.2: The pressure in QCD with different number of degrees of freedom as a function of temperature. The figure is from [4].

yields of different particles within the framework of statistical thermal models. After the kinetic freeze-out, the particles stop interacting, and the spectra will not change. Therefore, the spectra reflect the properties of the medium at kinetic freeze-out stage.

The integrated particle yield ratios for central Au+Au collisions at 200 GeV can be fitted successfully by a statistical thermal model, which is shown in Figure 1.3. Many statistical thermal models assume that the system is in thermal and chemical equilibrium at the stage, and the fitting parameters provide the information of temperature and baryon chemical potential at the chemical freeze-out. The excellent fitting to the particle ratios, including multi-strange hadrons, indicates that the light flavors u, d, s quarks may reach chemical equilibrium at central and near-central collisions. If the thermalization is indeed achieved by the medium prior to chemical freeze-out, the fitting temperature T_{ch} provides a lower limit on the thermalization temperature [3].

The characteristics of the system at the kinetic freeze-out stage can be obtained by analyzing the p_T spectra of different hadron species with the hydrodynamics-motivated fits [6]. The fitting model includes two extra parameters, which characterize the random (kinetic freeze-out temperature T_{fo}) and collective (radial flow velocity $\langle\beta_T\rangle$) motions. Figure 1.4 shows the fitting parameters for different centrality bins. From most peripheral to most central collisions, the bulk of the system, dominated by the yields of π, K, p, becomes cooler at kinetic freeze-out, and develops stronger collective flow [3].

The p_T and centrality dependence of hadron spectra shows a difference between mesons and baryons. The nuclear modification factors R_{CP} of various hadron species are shown in Figure 1.5. The R_{CP} is calculated as the ratio of particle yields from central collisions to yields from peripheral collisions scaled by the number of binary collisions (N_{bin}). In the low p_T range, the R_{CP} depends on the mass of the hadron, which is due to the radial flow. In the interme-

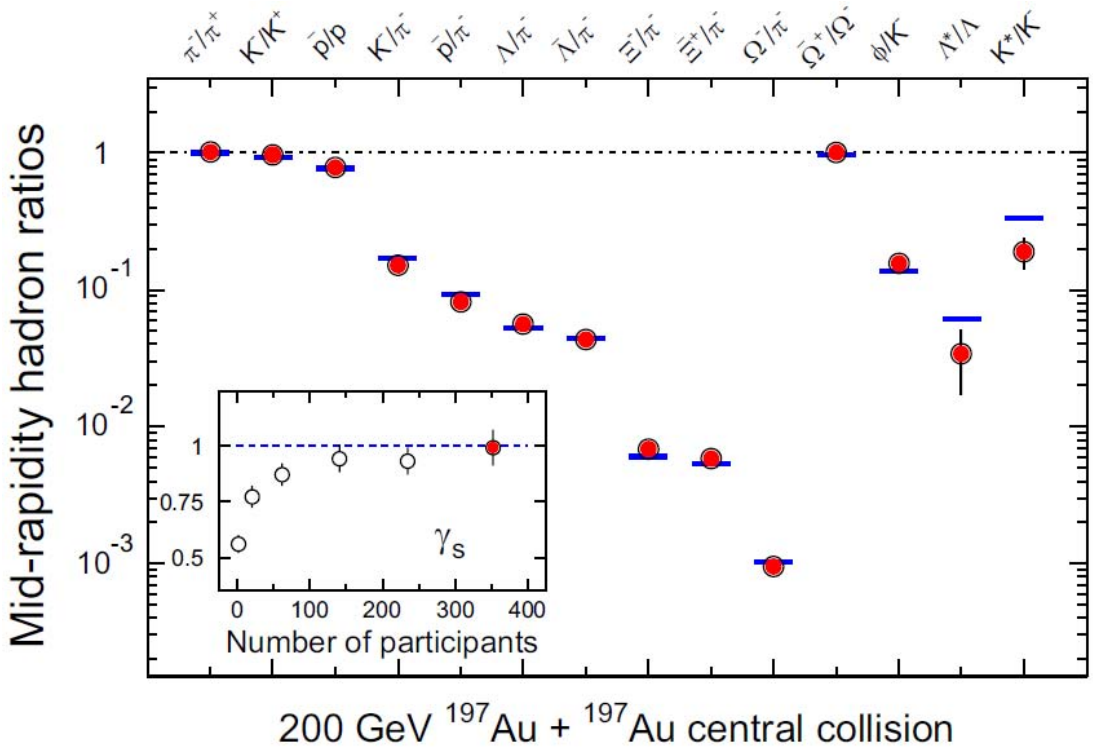

Figure 1.3: The ratios of p_T-integrated mid-rapidity yields for different hadron species measured in STAR for central Au+Au collisions at $\sqrt{s_{NN}}$ = 200 GeV. The horizontal bars are the statistical thermal model fits to the measured ratios. The γ_S is the strangeness phase space suppression factor modifying the yield of strangeness which does not reach its full equilibration [5]. The figure is from [3].

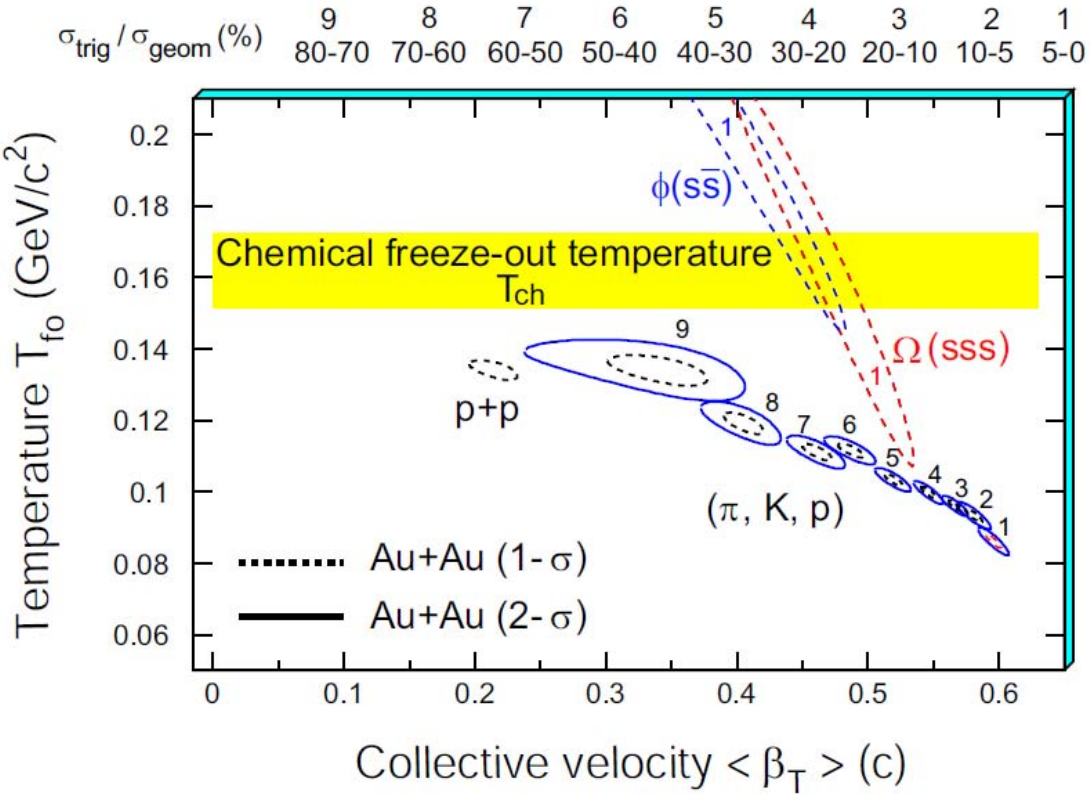

Figure 1.4: The χ^2 contours, extracted from thermal and radial flow fits. Dashed and solid lines are the 1-σ and 2-σ contours respectively. The figure is from [3].

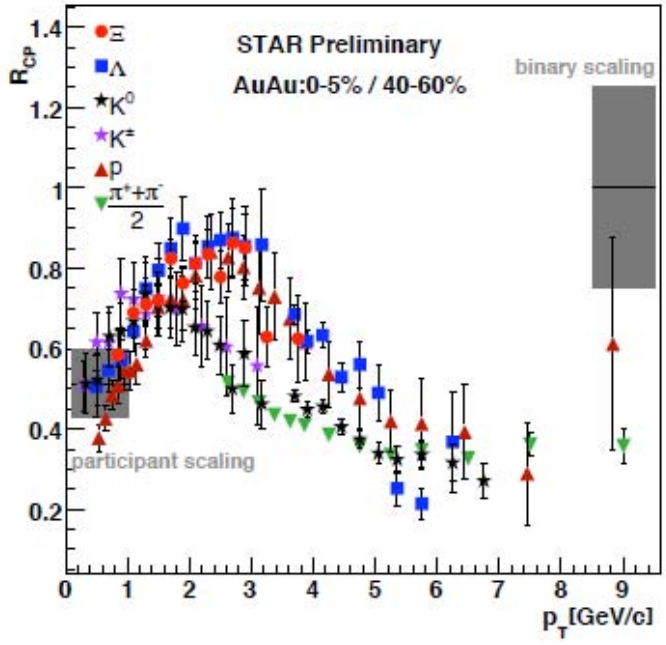

Figure 1.5: The plot shows the R_{CP} of $\pi^{\pm}$, $K^{\pm}$, K^0_S, p, Λ, and Ξ. The baryons and mesons at intermediate p_T follow different trends. The figure is from [7].

diate p_T range, the R_{CP} values of baryons and mesons follow different trends. The phenomena may be explained by the partonic energy loss in the medium and recombination/coalescence model, which is a consequence of the formation of strongly coupled quark-gluon plasma. At high p_T range, hadron yields are greatly suppressed in central Au+Au collisions. Figure 1.6 shows the R_{AA} and R_{dAu} of inclusive charged hadrons measured by STAR. The R_{AB} is calculated as the ratio of particle yields from A+B (either Au+Au or d+Au) collisions to yields from p+p collisions scaled by N_{bin}. Conventional nuclear effects, such as shadowing of parton distribution functions and initial state multiple scattering cannot account for the suppression. In addition, the suppression is not observed in d+Au collisions, which indicates the suppression is not from nuclear effects in the initial state (such as gluon saturation), but from the final state interaction of scattered partons or their fragmentation products in the dense medium generated in Au+Au collisions [3].

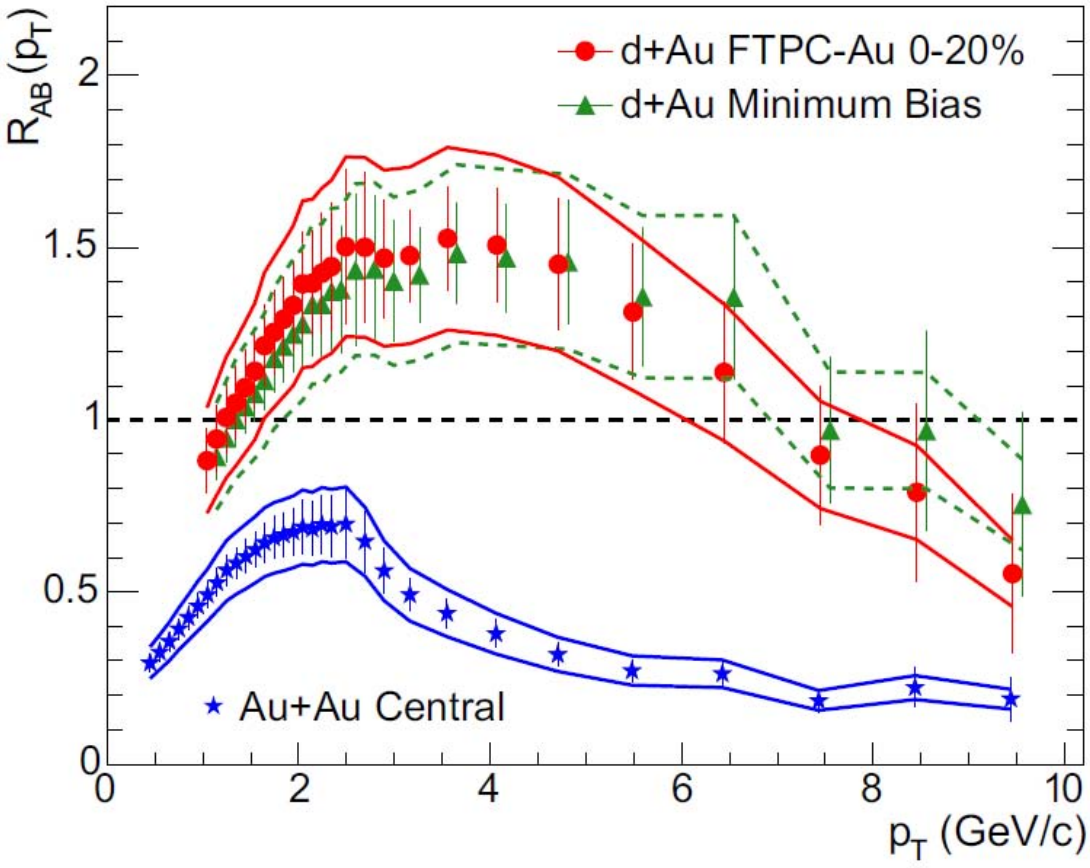

Figure 1.6: Binary-scaled ratio R_{AB} of charged hadron inclusive yields from 200 GeV Au+Au and d+Au relative to that from p+p collisions measured by STAR. The figure is from [3].

The observed hadron spectra at RHIC reveal three transverse momentum regions with distinct behavior: a soft physics region ($p_T < 2$ GeV/c) containing the vast majority of produced hadrons, representing most of the remnants of the bulk collision matter; a hard-scattering region ($p_T > 6$ GeV/c), providing partonic probes of the early collision matter; and an intermediate p_T region ($2 < p_T < 6$ GeV/c) where hard processes coexist with softer ones [3].

1.3.2 Elliptic Flow

In non-central heavy-ion collisions, the overlapping area of the two nuclei is an ellipsoid shape with a finite eccentricity. With a constant pressure at the boundary of the fireball, the pressure gradient along the minor axis is higher than that along the major axis, which will boost the collective motion of particles along the minor axis, and will lead to an azimuthal anisotropy in momentum space. At the same time, the original eccentricity of the fireball is diminishing, due to the faster expansion along the minor axis. The final azimuthal anisotropy is very sensitive to the early time evolution of the fireball and provides a valuable tool to probe the properties of the fireball. The azimuthal distribution of the produced particles can be expanded with a Fourier series:

$$\frac{dN}{d\phi} = 1 + 2v_1 \cos((\phi - \Psi)) + 2v_2 \cos(2(\phi - \Psi)) + \ldots, \tag{1.3.1}$$

where ϕ is the azimuthal angle of the emitted particle and Ψ is the reaction plane angle. The second Fourier coefficient, v_2, is called elliptic flow, which is the most significant term represents the azimuthal anisotropy of hadrons in momentum space [8]. The elliptic flow is defined as $v_2 = \langle \cos(2(\phi - \Psi)) \rangle$.

The elliptic flow has been measured for various hadrons at RHIC. Figure 1.7 shows the measurements from STAR experiment [9][10] and PHENIX experiment [11]. At low p_T range, elliptic flow varies for particles of different masses,

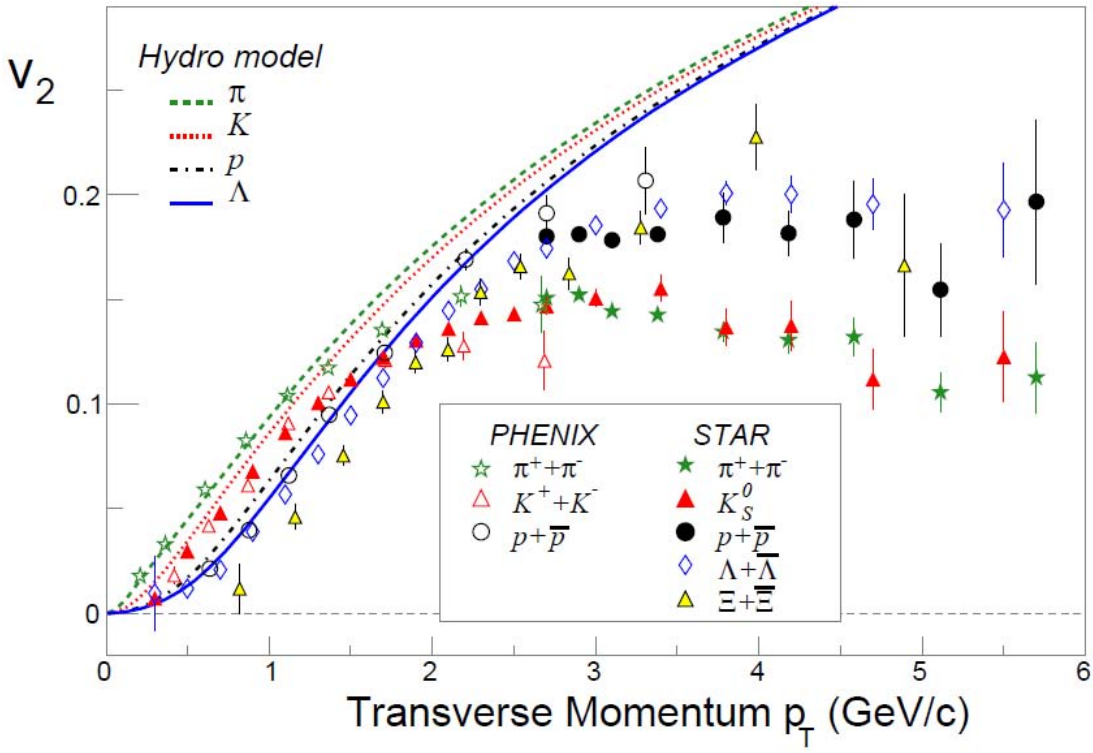

Figure 1.7: The elliptic flow of various hadrons as a function of p_T from STAR and PHENIX, compared with hydrodynamics calculation. The figure is from [12].

which is consistent with expectations from hydrodynamic calculations. A common collectivity pushes particles at a common velocity, and heavier hadrons are pushed to higher p_T. Therefore, heavier hadrons at higher p_T have the same elliptic flow as lighter hadrons at lower p_T.

At intermediate p_T, experimental elliptic flow values reach a saturation, as shown in Figure 1.8, and a particle type (meson vs. baryon) dependence is observed for identified hadrons. A Constituent Quark Number Scaling of v_2 was discovered experimentally. If both v_2 and p_T of various hadron species are divided by the number of constituent quarks (n_q) in the hadrons, i.e. $n_q = 2$ for mesons and 3 for baryons, then the scaled elliptic flows converge together, which is shown in Figure 1.8. This phenomenon can be understood as the elliptic flow of hadrons at intermediate p_T comes from the combination of constituent quarks with an universal distribution. The finding is one of the most direct pieces of evidence for partonic degrees of freedom in the medium created in the heavy-ion collisions. It also indicates that the hadrons at intermediate p_T range are produced via quark recombination/coalescence [13][14].

Elliptic flow v_2 measurements have been compared with hydrodynamic calculations to extract properties of QGP created at RHIC. Figure 1.9 shows the integrated v_2 as a function of number of participant (N_{part}) and differential v_2 as a function of p_T measured by PHOBOS and STAR, in comparison with viscous hydrodynamics with various viscosity-to-entropy (η/s) ratios. Both integrated v_2 as a function of N_{part} and differential v_2 as a function of p_T require very small values of η/s to match data and calculation. The best fit η/s value is between 0.03 and 0.08, below the conjectured KSS bound of $\frac{1}{4\pi}$ [15]. The QGP created at RHIC has almost a "perfect" fluidity, indicating the QGP is a strongly interacting QGP (sQGP).

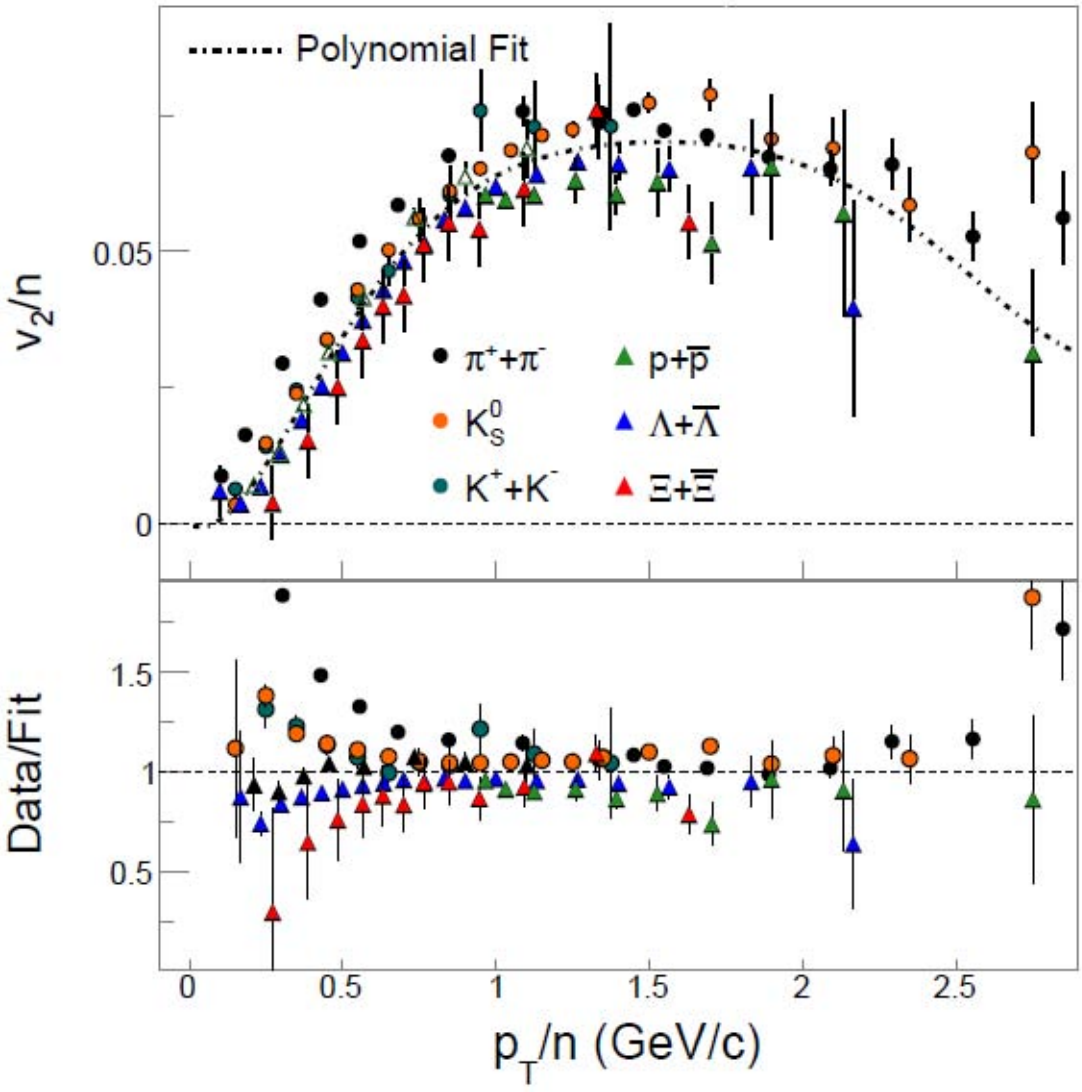

Figure 1.8: The number-of-quark-scaled elliptic flow of various hadrons as a function of number-of-quark-scaled p_T measured at RHIC. The figure is from [12].

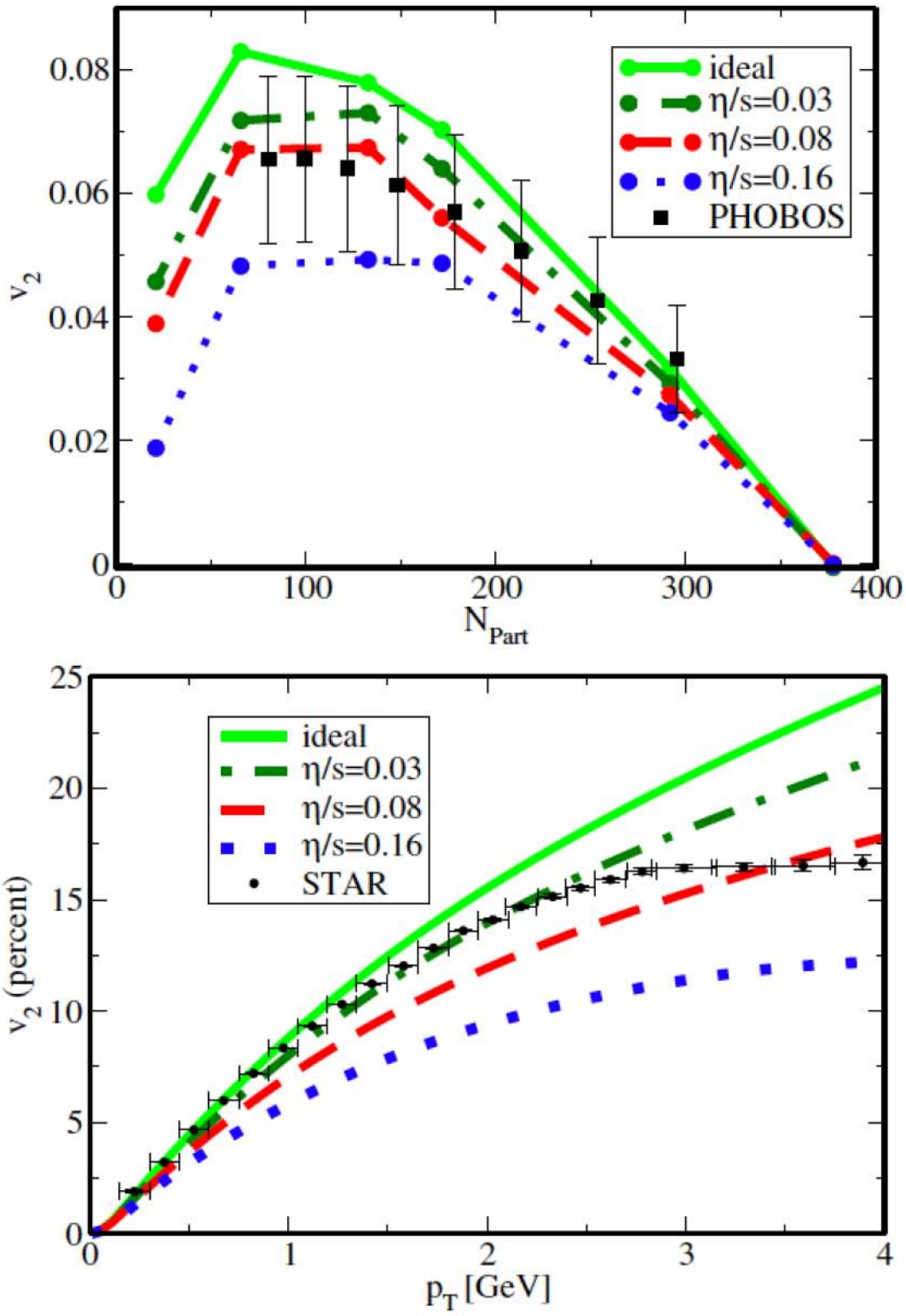

Figure 1.9: The elliptic flow as a function of N_{part} and p_T measured by PHOBOS [16] and STAR [17]. The figure is from [18].

1.3.3 Heavy Flavor

Heavy flavor quarks, including charm and bottom, are produced in the early stage of collisions mostly through the gluon fusion mechanism at RHIC. Therefore, the heavy flavor quarks can probe the complete space-time evolution of the collision process. When the heavy quarks traverse the medium, they also interact with the medium. Theoretical calculations predicted that the suppression for heavy quarks should not be as strong as light quarks due to the dead-cone effect [19]. The R_{AA} and elliptic flow of open heavy flavor and heavy flavor decay electrons have been measured in the STAR and PHENIX experiments. Figure 1.10 shows the R_{AA} of D^0 measured by STAR experiment. Figure 1.11 shows the R_{AA} and elliptic flow of heavy flavor decay electrons measured by PHENIX experiment. It is observed that the suppression of open heavy flavor and heavy flavor decay electrons is similar to the suppression of light quarks, which suggests a strong heavy flavor interactions to the QGP medium.

1.4 Dissertation Outline

This dissertation is organized into six chapters. The first chapter gives an introduction to the physics of heavy-ion collisions and reviews some valuable experimental results from RHIC. Chapter 2 describes the Relativistic Heavy Ion Collider at Brookhaven National Laboratory and the Solenoidal Tracker at RHIC (STAR) detector system. Chapter 3 presents the reconstruction technique of weakly decayed strange particles in the STAR experiment, those particles are reconstructed in the analysis of strangeness production and strange V0 and charged hadron correlation. Chapter 4 discusses the analysis of strangeness production in the RHIC Beam Energy Scan Program, and Chapter 5 shows the analysis of strange V0 and charged hadron correlation. The projects discussed in Chapter 4 and 5 are two parallel physics projects I did in my Ph.D career. In both Chapter 4 and 5, I give

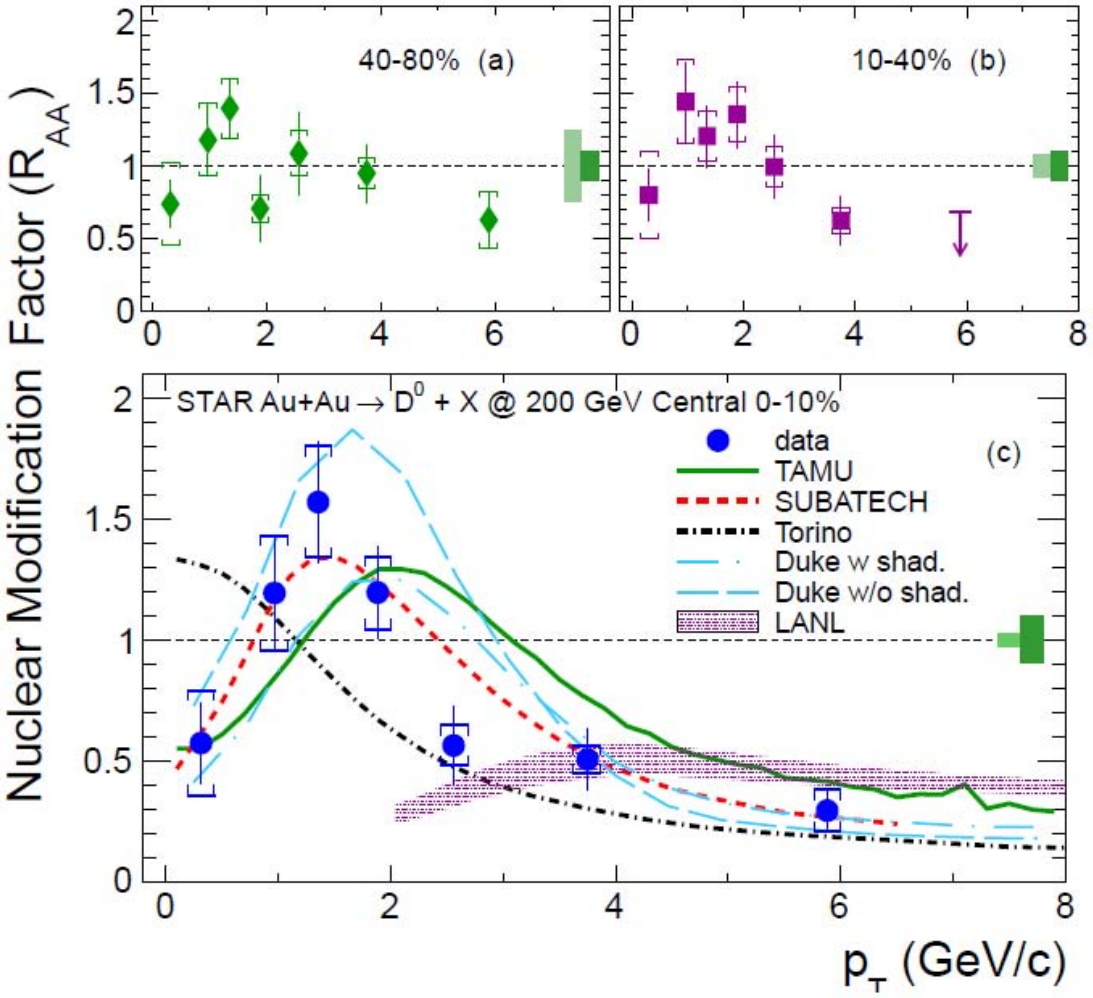

Figure 1.10: D^0 R_{AA} for peripheral 40-80%, semi-central 10-40% and most central 0-10% collisions compared with model calculations. The figure is from [20].

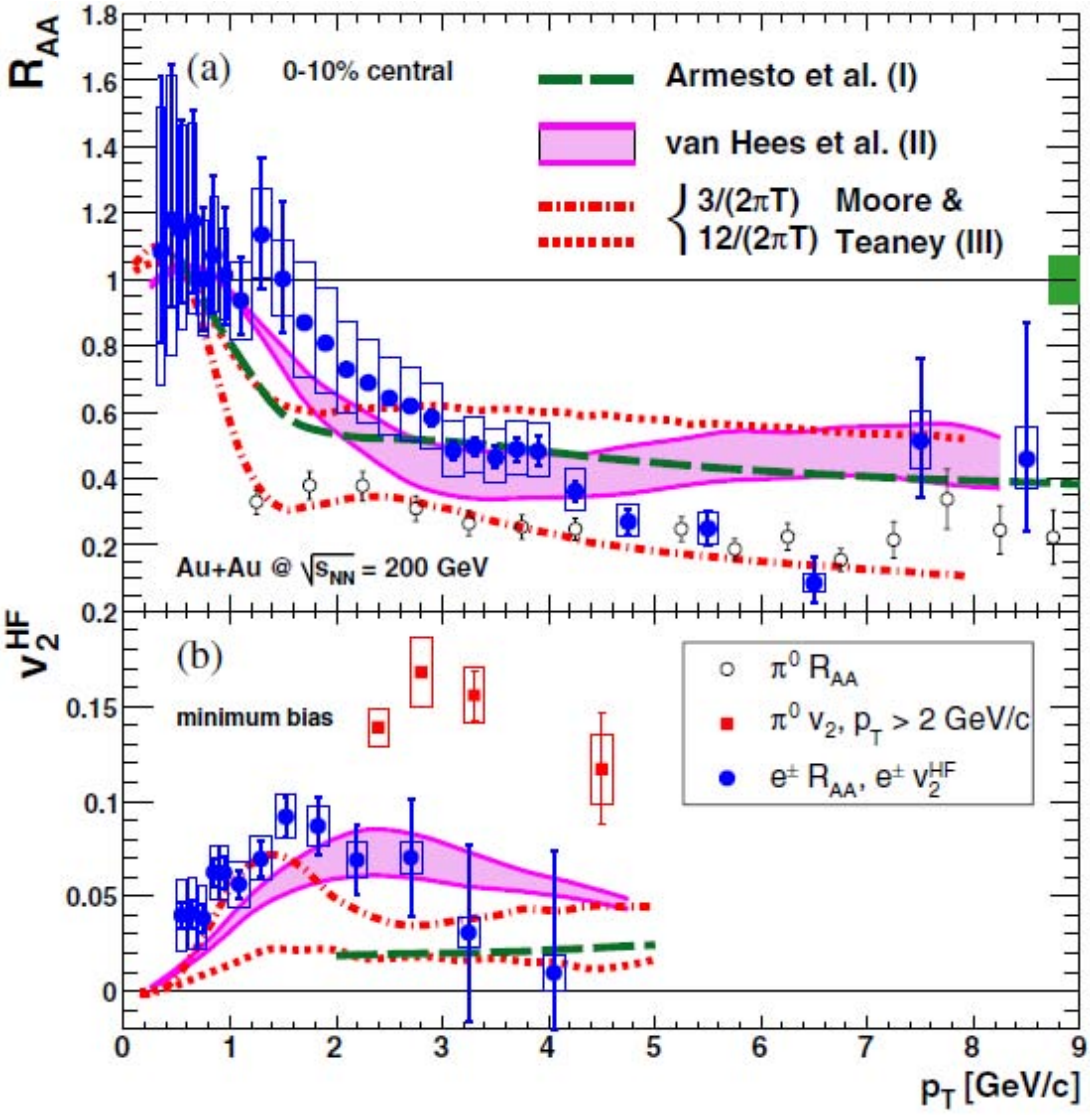

Figure 1.11: The R_{AA} and elliptic flow of heavy flavor decay electrons measured by PHENIX experiment. The figure is from [21].

the introduction and motivation to each project, and present the analysis process and results. Chapter 6 is a summary of the two projects and also gives an outlook related to the physics covered in this thesis.

CHAPTER 2

RHIC & STAR

2.1 Relativistic Heavy Ion Collider

The Relativistic Heavy Ion Collider (RHIC) is located at Brookhaven National Laboratory (BNL) in Upton, New York, which is the first collider machine in the world with the capability of colliding heavy ions. RHIC has the ability to accelerate various ion species to relativistic speed. Different combinations of nucleus have been explored, such as p+p, d+Au, Cu+Cu, Cu+Au, and Au+Au collisions. For Au+Au collisions, the beam energy can vary from 7.7 GeV to 200 GeV in center-of-mass energy of nucleon-nucleon pair. RHIC is also able to collide polarized protons, which is unique in the world.

The RHIC complex is composed of several subsystems, including the Tandem Van De Graaff accelerator, Booster Synchrotron, Alternating Gradient Synchrotron (AGS), the Relativistic Heavy Ion Collider (RHIC) and some other systems. A schematic drawing of the RHIC complex is shown in Figure 2.1.

The heavy ions begin the journey in the Tandem Van De Graaff accelerator. The heavy ions, taking a negative charge (q = -1), are extracted from a pulsed sputter ion source. Then they are carried to the Tandem Van De Graaff accelerator,which strips partial electrons and uses an electric potential to accelerate charged ions. For example, 33 electrons of a gold ion (Au^-) are stripped, and the gold ion is accelerated to 1 MeV per nucleon in the Tandem Van De Graaff accelerator. There are two Tandem Van De Graaff accelerators, allowing two different

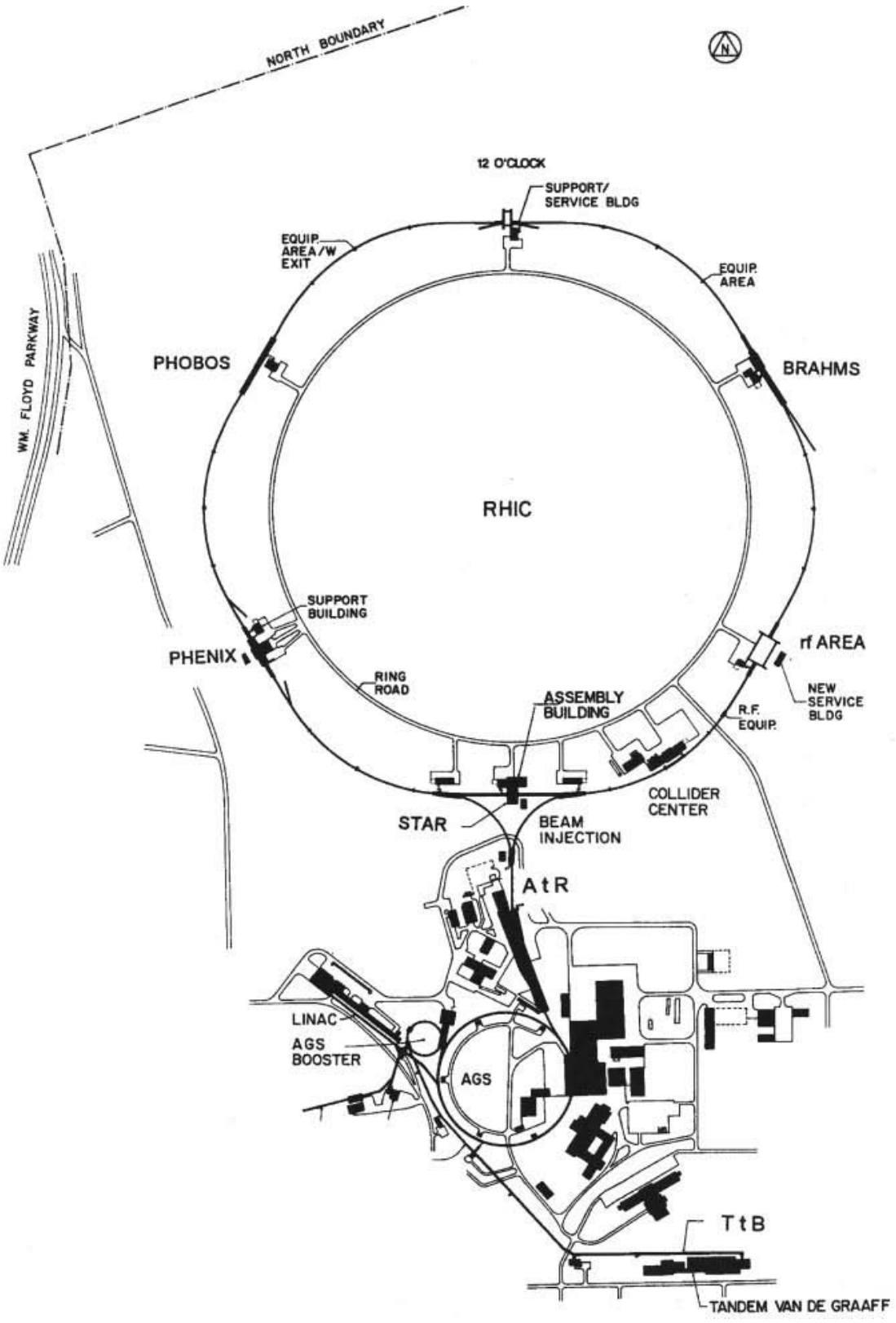

Figure 2.1: Overall layout of the RHIC complex. Figure is taken from [22].

ion species to be accelerated simultaneously to make the collision between two nucleus species, such as Cu+Au collisions. Since year 2012, a new beam injector, the Electron Beam Ion Source (EBIS), along with two small linear accelerators, have been constructed to take the place of Tandem Van De Graaff accelerators. They can be more easily operated and maintained, and have the ability to accelerate more ion species, such as Uranium. After the ions exiting the Tandem, they are carried to the Booster synchrotron, which is a powerful circular accelerator with a size of about one quarter of the AGS. The ion beam is bunched and accelerated to 95 MeV per nucleon, traveling with a speed of 37% of the light speed, and is stripped of more electrons. For gold ions, the charge is +77, when they exit from the Booster. The next step of acceleration is in the AGS. AGS is well known for the three Nobel Prizes from researches done at the facility over the years, which are the discoveries of J/ψ particle, CP violation in kaon decay, and the muon neutrino. In AGS, the ion beam is accelerated to 8.86 GeV per nucleon with a speed of 99.7% of the speed of light. In the beam line from AGS to RHIC, the last two electrons of gold ions are stripped. At the end of this beam line, ion bunches are directed either left to the clockwise RHIC ring or right to the counterclockwise ring. In the RHIC rings, the heavy ions are accelerated to the desired energy, typically 100 GeV per nucleon.

The 2.4-mile-circumference ring has six intersection points, where the two rings of accelerating magnets cross, allowing the beams to collide. Two large experiments STAR and PHENIX are located at 6 o'clock and 8 o'clock of the RHIC respectively.

2.2 Solenoidal Tracker at RHIC (STAR)

STAR is one of the two large detector systems at RHIC. The STAR system is designed for measurements of hadron production at mid-rapidity with full azimuthal

angle coverage. It has the capability of tracking thousands of charged particles produced in each heavy-ion collision [23].

2.2.1 Overview

The STAR detector system consists of several sub-detectors, each specializing in detecting certain types of particles or characterizing their motion. Figure 2.2 is a layout of the system. A schematic side view of the STAR detector system for RHIC 2011 run is displayed in Figure 2.3.

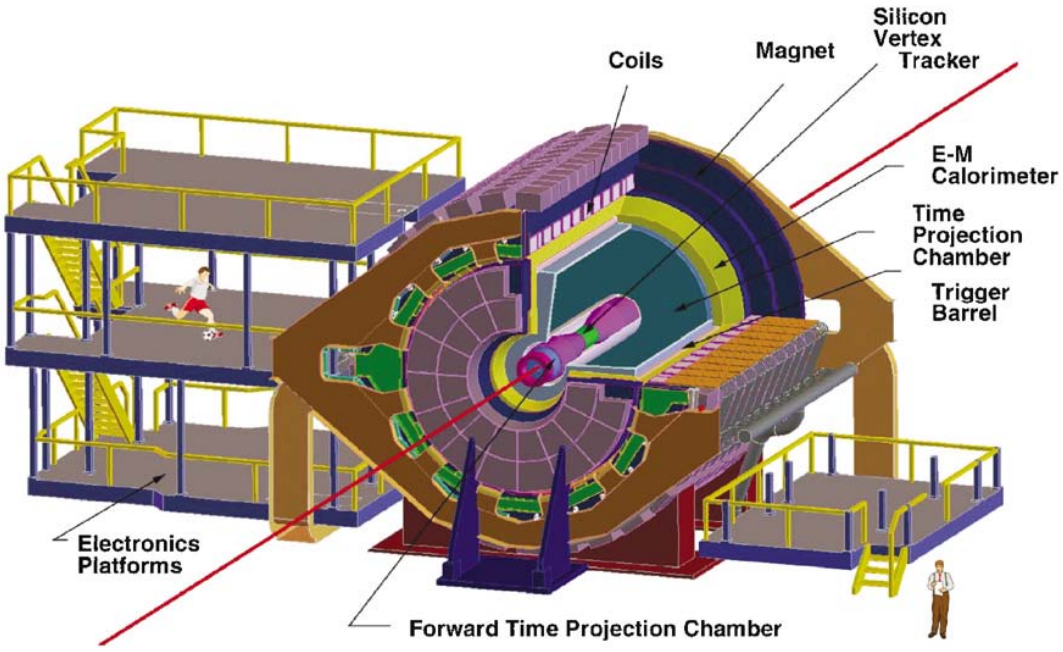

Figure 2.2: A layout of STAR detector system.

The Time Projection Chamber (TPC) is the heart of the STAR system [24], which is for charged particle tracking and identification. The TPC is four-meter long and covers a radial distance from 50 to 200 cm from the beam axis with a pseudo-rapidity range $|\eta| \leq 1.8$ and complete azimuthal angle ($\Delta\phi = 2\pi$). The details of the TPC will be discussed in Section 2.2.2. The Time-of-Flight Detector (TOF) [25] completed in 2010, is outside the TPC, covering $|\eta| \leq 1.0$ and $\Delta\phi = 2\pi$, which extends the particle identification ability to $p_T \approx 3$ GeV/c [25][26]. The

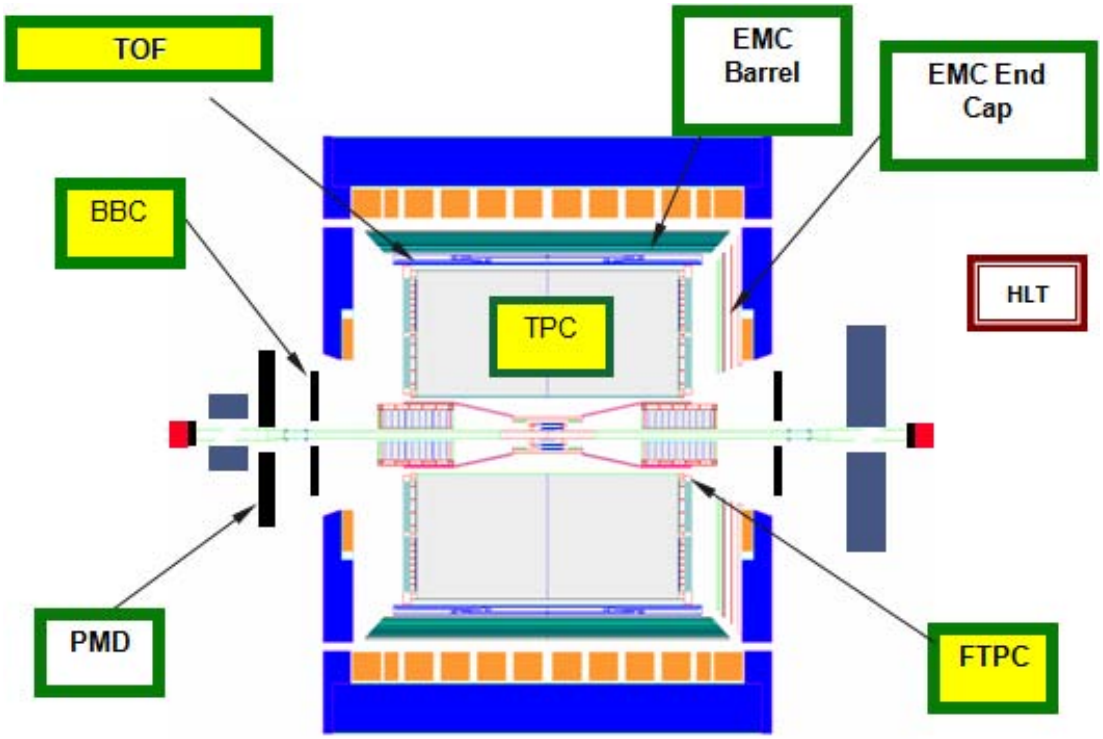

Figure 2.3: A side view of STAR detector system in 2011.

details of the TOF will be discussed in Section 2.2.3. The STAR calorimeter system is outside of TOF, which consists of the Barrel ElectroMagnetic Calorimeter (BEMC) and the Barrel Shower Maximum Detector (BSMD), measuring high p_T photons, electrons, and electromagnetically decaying hadrons [27]. There is also an End-cap ElectroMagnetic Calorimeter (EEMC) at one side of the STAR system, covering $1.086 \leq \eta \leq 2.00$, $\Delta\phi = 2\pi$ [28]. The STAR magnet coils and Iron York is outside the BEMC, which is capable of providing a magnetic filed along the beam line with ± 0.25 T and ± 0.5 T [29].

There are some other sub-detectors in the STAR system for beam monitoring and triggering, including the Beam-Beam Counters (BBC), the Zero Degree Calorimeter Detectors (ZDC), the Vertex Position Detectors (VPD). The BBC is a pair of scintillator detectors located at 3.5 meters away from the center of STAR system on either side for event rate monitoring in p+p collisions. A pair of ZDC

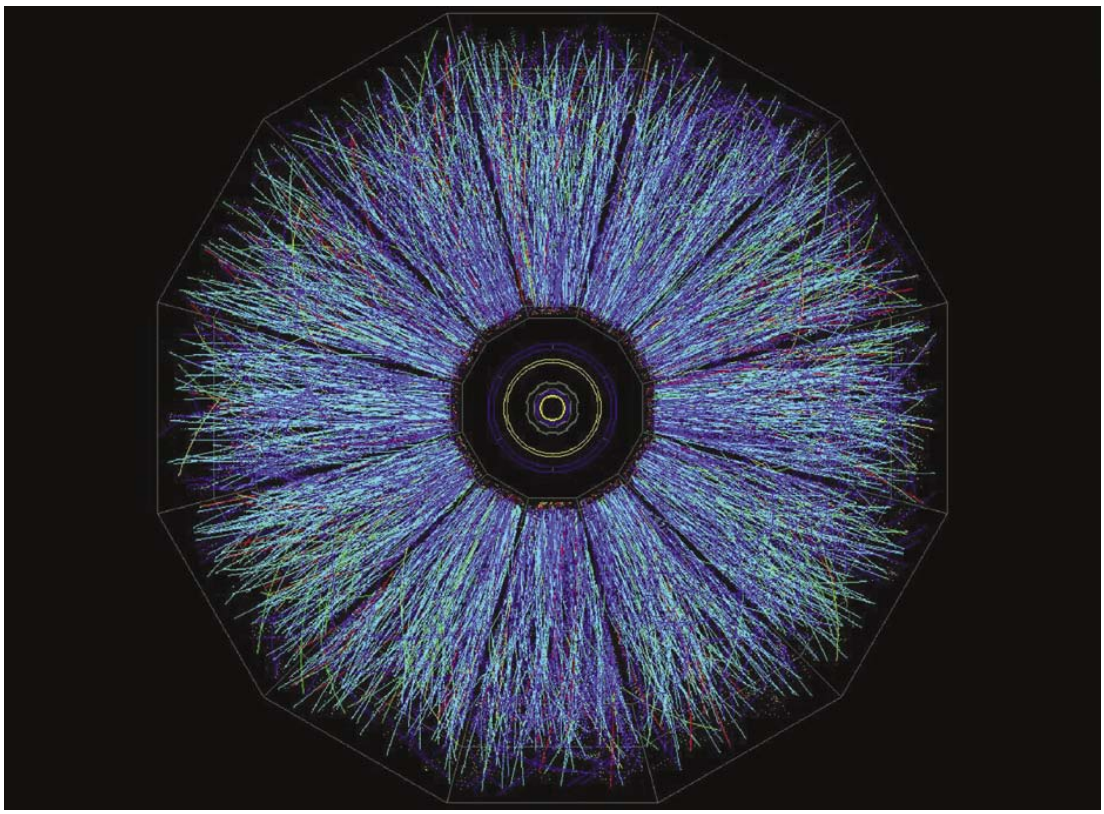

Figure 2.4: An event of Au+Au collision at RHIC recorded by STAR. End view of the TPC.

detectors are located 18 meters down the beam pipe on either side of the center of STAR, detecting spectator neutrons for triggering and offline analysis [30]. A pair of VPDs are part of TOF system, located at 5.6 m away from the center of STAR on both sides, providing the start time of collision, which is used for flight time measurements for particles [25]. These three detectors are fast detectors, and can serve as trigger detectors.

The STAR detector system keeps on upgrading. There used to be a Silicon Vertex Tracker (SVT) and a Silicon Strip Detector (SSD) between TPC and the beam pipe. They are decommissioned for the Heavy Flavor Tracker (HFT) upgrade. The Muon Telescope Detector (MTD) is installed at the outmost cylindrical layer behind the magnet irons. The MTD and the HFT have been completed installed for Run 2014.

2.2.2 The Time Projection Chamber (TPC)

The TPC is used as the primary tracking device in the STAR detector system. The STAR TPC is 4.2 m long and 4 m in diameter, sitting in a large solenoidal magnet. It was the largest time projection chamber when it was built. The Inner Field Cage (IFC) has a radius of 50 cm, and the Outer Field Cage (OFC) is at radius 200 cm. The TPC has the capacity to cover $|\eta| \leq 1.8$ units of pseudo-rapidity and full azimuthal angle. There is a thin conductive Central Membrane (CM) at the center of the TPC, dividing the TPC into two halves, each half is 210 cm long. The central membrane along with the end-caps and field cages provides a uniform electric field of about 135 V/cm. The TPC is filled with P10 gas (10% methane, 90% argon) regulated at 2 mbar above atmospheric pressure [24]. An illustration of the STAR TPC is shown in Figure 2.5.

The uniform electric field in the TPC is established by the correct boundary conditions with the central membrane, the end-caps and the concentric field cage

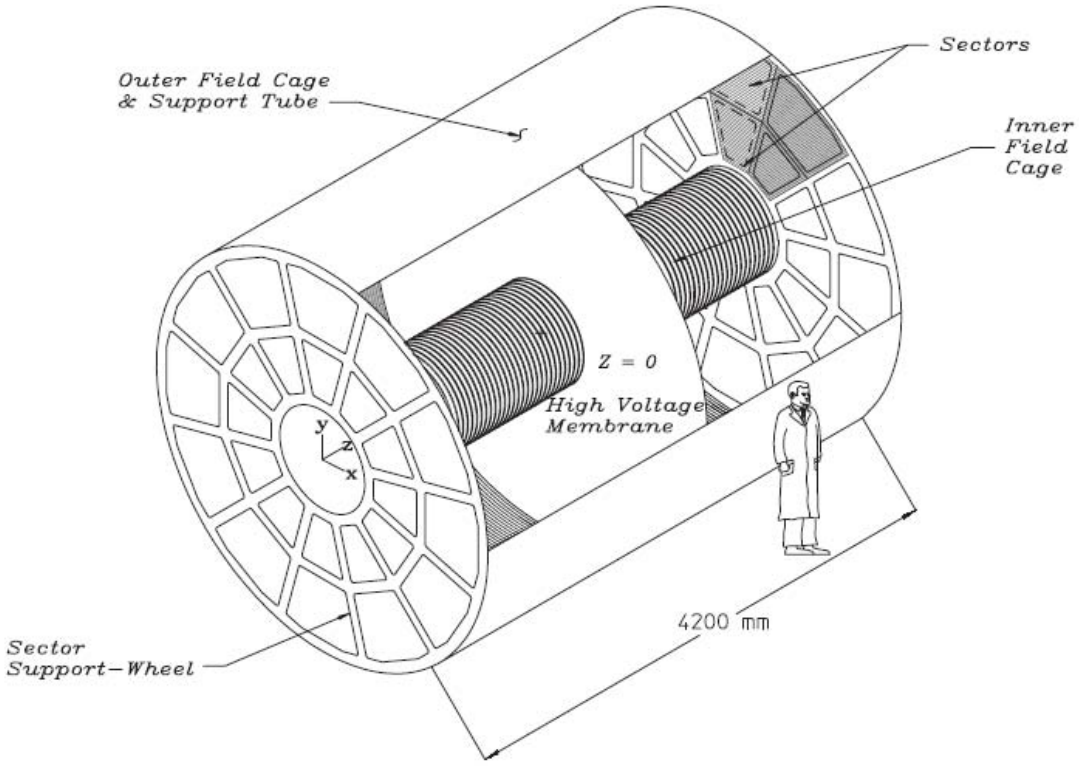

Figure 2.5: The STAR TPC is 4.2 m long and 4 m in diameter, surrounding a beam-beam interaction region at RHIC [24].

cylinders [24]. The central membrane is applied a negative voltage of 28 kV, and the end-caps are at ground (U = 0 V). The inner and outer field cage cylinders provide a series of equal potential rings, dividing the space between the CM cathode and the anode planes into 182 equally spaced segments [24]. The resistor chains of 183 of 2 MΩ resistors bias the rings, providing a uniform gradient between the central membrane and the grounded end-caps on both sides of the TPC. The STAR TPC is filled with P10 gas, which is widely used as working gas in TPCs. It has a fast drift velocity peaked at a low electric field. The gas system circulates the gas in the TPC, and maintains purity in order to reduce electro-negative impurities such as oxygen and water gas which will capture drifting electrons.

The readout system of the TPC is based on Multi-Wire Proportional Chambers (MWPC) with pad readout [24], to gather drifting electrons for charged particle's energy loss and position measurement. The readout pads are in concentrical rows in 12 super sectors along the ϕ distribution. Each readout super sector consists of inner and outer radius sub-sectors, which are designed to optimize different measurements [24]. Figure 2.6 shows the inner and outer sub-sectors of one readout pad. The outer sub-sectors are designed to optimize the dE/dx measurement with continuous pad coverage. The inner sub-sectors are in the region of highest track density, thus they are optimized for good two-hit resolution to improve the two track resolution.

The tracks of particles produced in heavy-ion collisions, passing through the TPC, are reconstructed by measuring the ionization clusters along the tracks. The clusters are found separately in x, y and z coordinates. (The x-y plane is vertical to the beam line, and the z axis is along the beam line.) The x and y coordinates of a cluster are determined by the charge measured on adjacent pads in a single pad row [24]. The z coordinate is determined by measuring the drift time of a cluster of secondary electrons from the original point to the anodes on the end-caps and the average drift velocity [24]. The tracking software associates

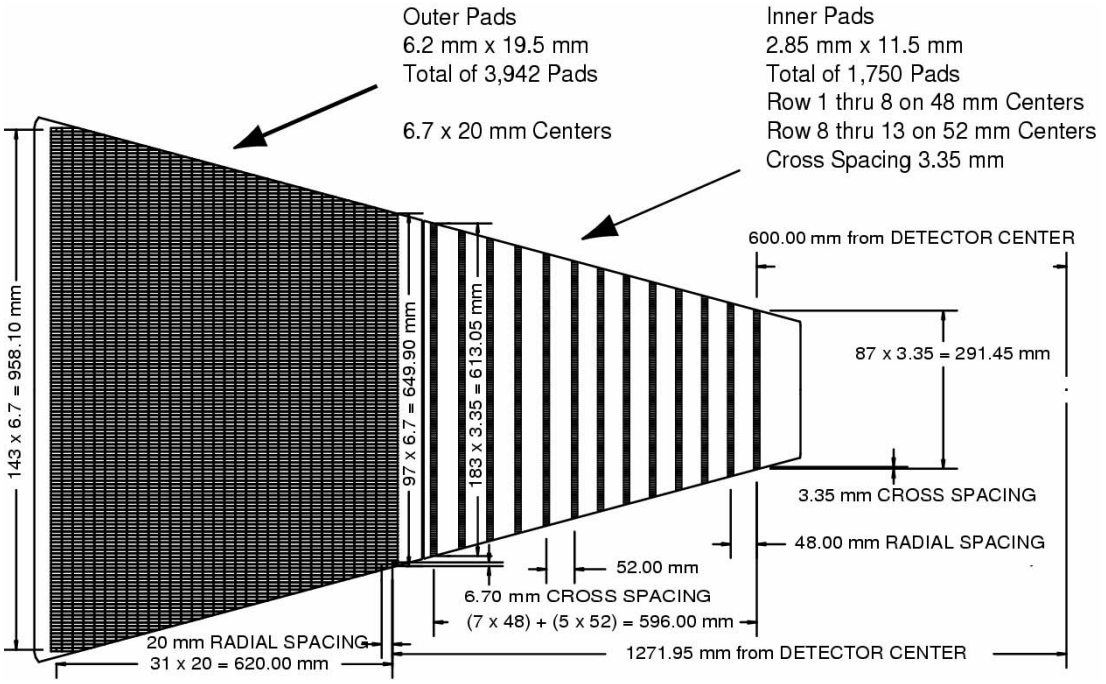

Figure 2.6: The inner sub-sector is on the right and it has small pads arranged in widely spaced rows, the outer sub-sector is on the left and it is densely packed with larger pads. [24].

space points to form tracks, and then fit the points with a track model to extract information such as momentum of the particle [24]. The energy loss (dE/dx) in the TPC gas is used for particle identification. The Figure 2.7 shows the dE/dx as a function of momentum for particles in the TPC. Pions and protons can be separated up to 1 GeV/c with the TPC [24].

2.2.3 The Time-of-Flight System (TOF)

The time-of-flight system in the STAR experiment is designed for direct identification of hadrons through the measurement of flight time of the hadron from the vertex of the collision till the hadron hits the detector. The system consists of two separate detector subsystems. One is the upgraded Vertex Position Detector (VPD), which provides the start time. The other one is the Time of Flight detector (TOF), which provides the stop time. Figure 2.8 shows the time-of-flight system.

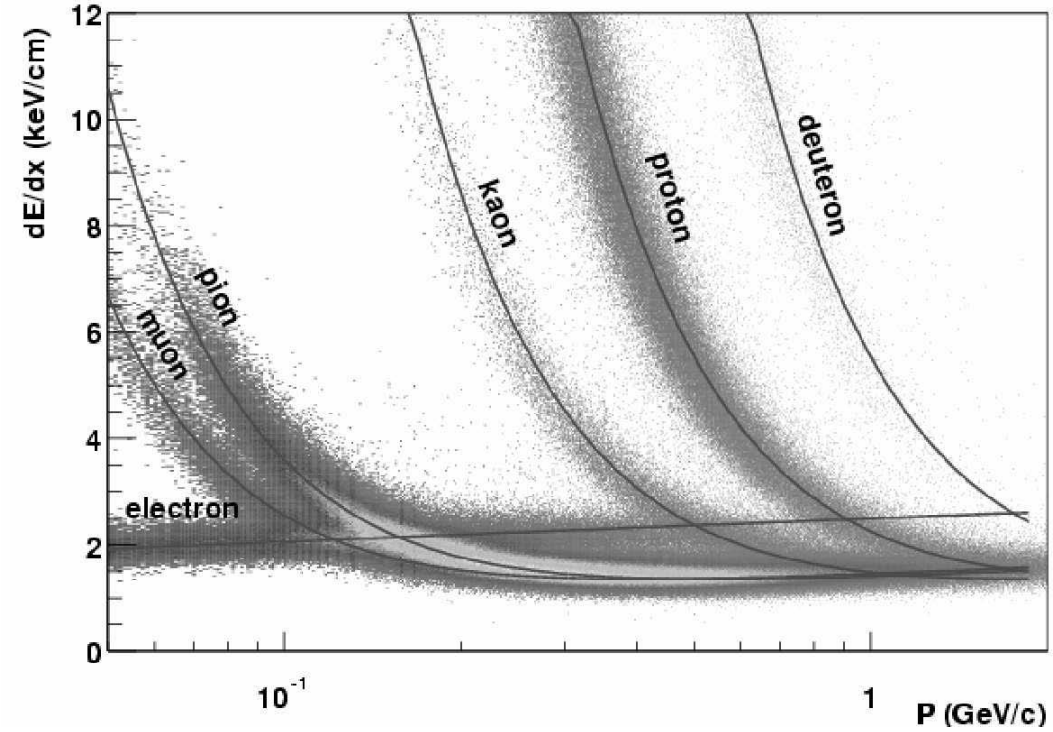

Figure 2.7: The energy loss as a function of momentum for charge particles in the STAR TPC. The magnetic field was 0.25 T. [24].

The TOF detector are based on the Multigap Resistive Plate Chamber (MRPC) technology. The time intervals of interest for particle flight time measurement are defined by the electronic signals from these detectors.

The VPD consists of two identical detector assemblies which are very close to the beam pipe, sitting on each side of the STAR detector system with equal space [25]. In RHIC full energy Au+Au collisions, a lot of high energy forward photons are produced, travelling away from the collision vertex effectively as a prompt pulse. Measuring the times of those forward particle pulses arrive at VPD on each side of the STAR provides the location of the collision vertex along the beam line. In the meanwhile, the average of the two arrival times is used as the collision time, or the start time of the event. The TOF trays are inside the STAR magnet and immediately outside the TPC, covering a pseudo-rapidity of ± 1.0 units. There are 120 trays, half of them are installed on the east side

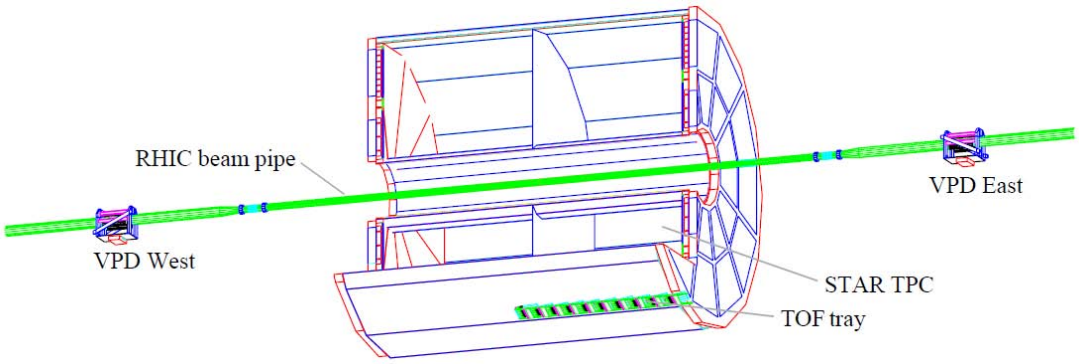

Figure 2.8: A scale drawing of the location of VPD and TOF detectors. The figure is originally from [25].

($z < 0$), and half of them are installed on the west side ($z > 0$). Each tray covers 6 degree in azimuthal direction (ϕ) around the TPC. When the charge hadrons hit the TOF, they will trigger the trays, and the TOF provides the stop time for each hadron. In RHIC full energy central Au+Au collisions, the start time resolution from the VPD is about 28 ps, the end time resolution from TOF is about 82 ps, and the total time resolution of the TOF system is about 87 ps.

The primary hadrons produced in the heavy-ion collisions can be identified directly through the flight time along with particle momentum measured by TPC. The inverse velocity as a function of momentum for hadrons is shown in Figure 2.9. Pions, kaons and protons can be distinguished with a momentum up to about 1.5 GeV/c, and protons can be identified from pions and kaons up to about 3 GeV/c [25][26]. The hadrons decayed from a secondary vertex, cannot be identified by TOF directly, because the flight time measured by the TOF system consists of the flight time of its parent. One way of using the TOF to identify weak decayed hadrons, is to reconstruct the parent and calculate the parent's flight time. With the parent's flight time subtracted from the TOF measured time, the new time can be considered as the real flight time for the decay daughter. Figure 2.10 shows the difference of the flight time measured by the TOF (parent's flight time has been subtracted) and the flight time calculated from flight length and

momentum measured by the TPC for kaon tracks decayed from Ω. The kaons from Ω decay are clearly identified. Through this way, the background of reconstructed strange particle, such as K^0_S, Λ, Ξ, and Ω, is largely reduced.

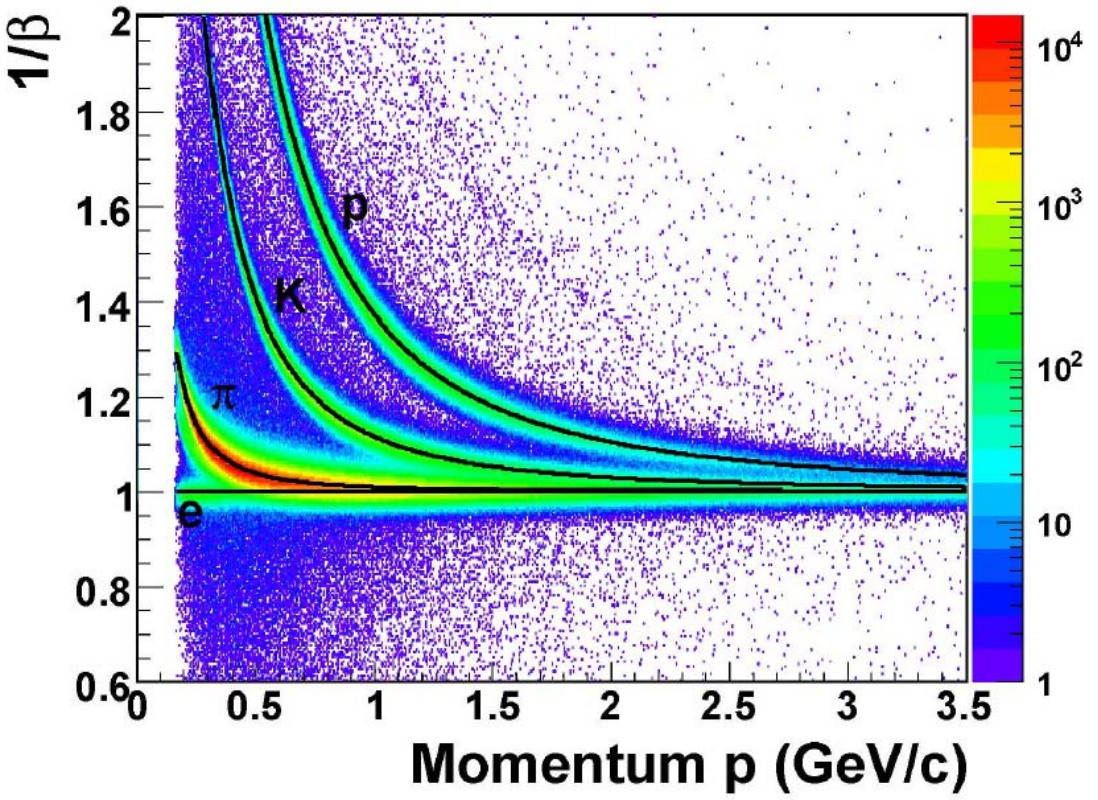

Figure 2.9: The inverse velocity as a function of momentum for hadrons.

2.2.4 The Heavy-Ion Physics with the STAR Detector

The major goal of the STAR heavy-ion physics program is to study soft physics, i.e. hadron production at transverse momenta below 2 GeV/c, as well as hard process, such as jets, hard photon and heavy flavor quarks production. With the TPC, π, K, p are identified. K^0_S, ϕ, Λ, Ξ and Ω can be reconstructed from decay daughters (π, K, p), through their decay topologies. The STAR detector system has done several major upgrades. In 2007, the BEMC is completed installed, and the STAR detector expanded its capability to study the high transverse momentum electrons.

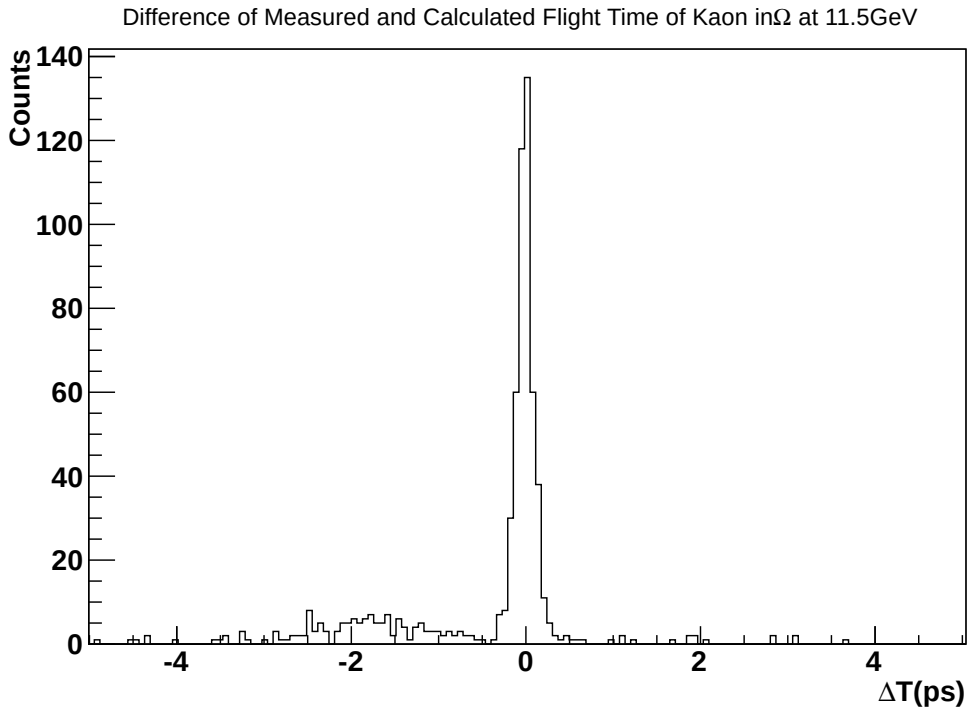

Figure 2.10: The difference between the measured flight time by the TOF system and the calculated flight time from flight length and momentum measured by the TPC for kaons decayed from Ω. The kaon peak is at $\Delta T = 0$.

J/ψ, even Υ, can be reconstructed through di-electron decay channel. In 2010, the TOF system is completed, and particle identification capability is extended from p_T less than 1 GeV/c to higher p_T range. With clean electron identified, di-electron analysis becomes possible. In 2013, the MTD is completely installed, improving the capability of muon identification in the STAR experiment, and making it possible to study di-muon and electron-muon correlation. J/ψ and Υ can also be reconstructed through di-muon channel. For Run 2014, the HFT was also completed, some weak decay charm hadrons such as D^0, Λ_c etc. can be reconstructed clearly, which will improve the ability of heavy flavor study in the STAR experiment.

The STAR detector now is an excellent mid-rapidity detector, with large coverage and excellent PID, which can detect nearly all particles produced at RHIC to study the spectra, flow and particle correlations.

CHAPTER 3

K^0_S, Λ, Ξ and Ω Reconstruction

The strange particles K^0_S, $\Lambda(\bar{\Lambda})$, $\Xi^-(\bar{\Xi}^+)$ and $\Omega^-(\bar{\Omega}^+)$ are weakly decaying particles with a decay length $c\tau$ about several centimeters. These particles fly some distance from the primary vertex where the heavy-ion collision occurs and they are created, but they decay before reaching the TPC. However, the decay daughters of these strange particles (pions, kaons and protons) can be detected by the TPC, and the strange particles can be reconstructed through their decay topologies from the decay daughters [31][32]. The decay daughters are identified through the energy loss (dE/dx) in the TPC.

3.1 Strange V0 (K^0_S, Λ and $\bar{\Lambda}$) Reconstruction

The decay daughters of K^0_S and $\Lambda(\bar{\Lambda})$ are charged pions and (anti-)protons, which can be detected by the TPC. The weak decay channels used for the K^0_S and $\Lambda(\bar{\Lambda})$ reconstruction are listed in Table 3.1. The decay topology of a strange V0 is shown in Figure 3.1. K^0_S, Λ and $\bar{\Lambda}$ all decay to a positive charged particle and a negative charged particle.

With identified positive and negative charged tracks, we can calculate the

Table 3.1: Weak Decay Channels of Strange V0

Particles	cτ(cm)	Decay Channel	Branching Ratio
K^0_S	2.6842	$\pi^+\pi^-$	69.20%
Λ	7.89	$p\pi^-$	63.9%
$\bar{\Lambda}$	7.89	$\bar{p}\pi^+$	63.9%

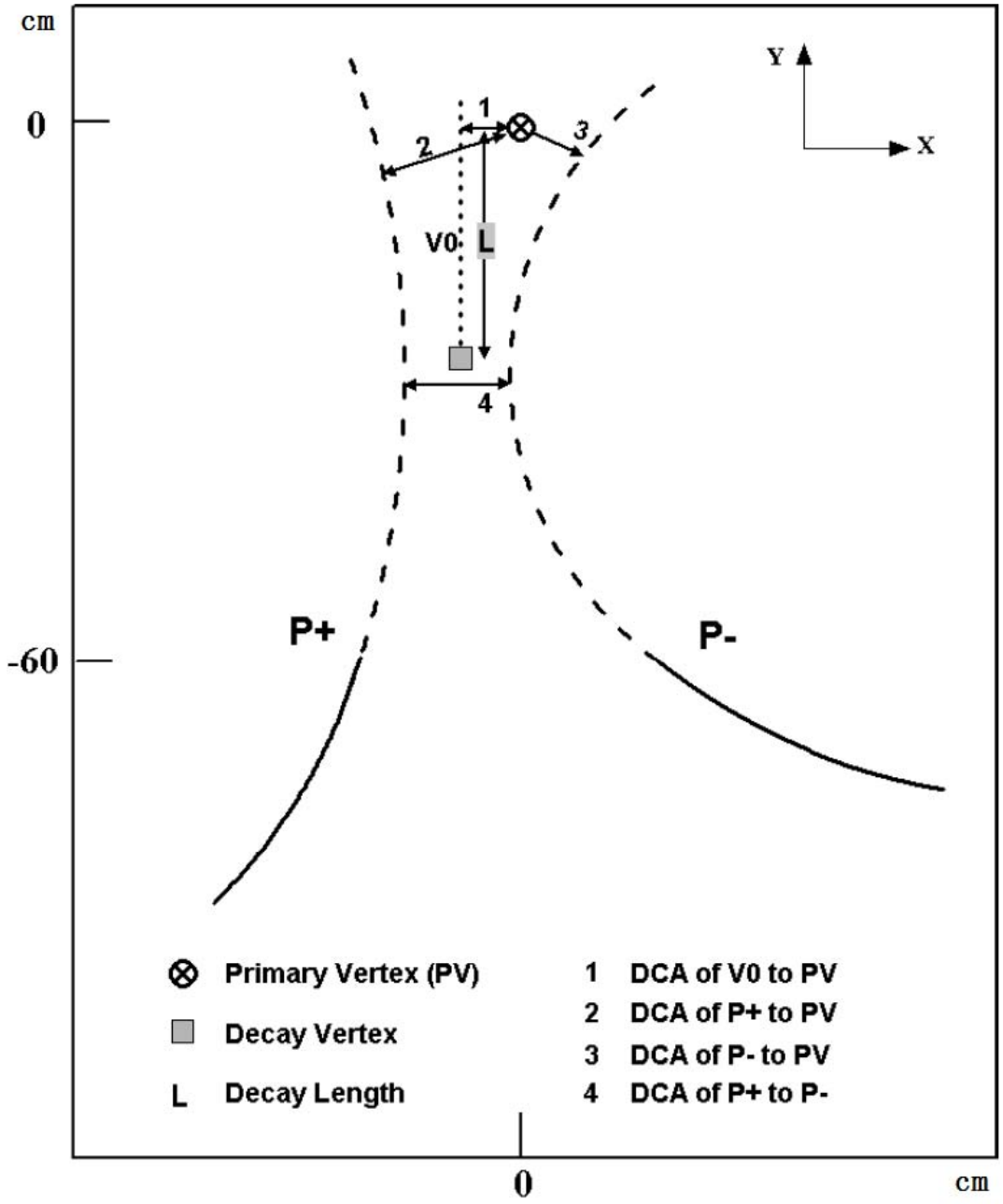

Figure 3.1: The strange V0 decay topology. P+ refers to a positively charged particle, and P- refers to a negatively charged particle. The solid line is detectable by the TPC anode sector 60 cm away from the beam line. The dashed line is extrapolated from the solid line or reconstructed V0. The topological cuts are shown in the plot. The plot is from Hai Jiang's thesis [34].

distance of closest approach (DCA) between the two tracks. The detailed math derivation for the DCA calculation is discussed in Hui Long's thesis [33]. Theoretically, if the two particles really come from a strange V0 decay, the DCA between the two tracks should be zero. Practically, due to the tracks' position resolution, a distance tolerance is allowed. We set a cut, for example DCA between the two tracks is less than 1 cm or 0.7 cm, to select strange V0 candidates. The momentum of the candidate is the sum of the two daughters' momenta, and the decay vertex is the average positions of the closest points of the two daughter tracks.

We can define a helix for the V0 candidate with the candidate's momentum and decay vertex, and we can calculate the DCA from the primary vertex to the helix. If we do not consider the weak decay contribution, the strange V0 is produced in the collision, it should come from the primary vertex, and the DCA should be zero. Setting a cut of DCA between the primary vertex and the helix of V0 candidate, will help to reject random combination of positive and negative tracks.

The decay length or flight length of the V0 candidate is calculated from the decay vertex and primary vertex. We set a decay length cut, by making it greater than several centimeters to reduce the combinatorial background from most primary tracks. Because the primary tracks can easily form V0 candidates with a small decay length, most of which can be effectively removed with a decay length cut.

As the two decay daughters of a strange V0 are from the decay vertex away from the primary vertex, we also set a cut of DCA of the decay daughter tracks to the primary vertex, to reduce the background.

The Table 3.2 summarizes the topological cuts used for strange V0 reconstruction. The cuts could be set to be different for different energies, centralities and even different purposes of our analysis. The Chapter 4 and 5 will discuss more detailed cuts.

Table 3.2: Topological Cuts for Strange V0

DCA of P+ to P-	less than
Decay Length of V0	greater than
DCA of V0 to primary vertex	less than
DCA of P+ to primary vertex	greater than
DCA of P- to primary vertex	greater than

The invariant mass of the V0 particle is calculated through the following equation with the energy and momentum conservations as well as Einstein's mass-energy equation.

$$m = \sqrt{E^2 - \overrightarrow{p}^2} = \sqrt{(E_+ + E_-)^2 - (\overrightarrow{p_+} + \overrightarrow{p_-})^2} \tag{3.1.1}$$

with $E_+ = \sqrt{m_+^2 + \overrightarrow{p_+}^2}$ and $E_- = \sqrt{m_-^2 + \overrightarrow{p_-}^2}$. With proper topological cuts, clean signals of strange V0 are observed. Figure 3.2 shows the invariant mass distributions of K_S^0 and $\Lambda(\bar{\Lambda})$, with topological cuts the background level is very low.

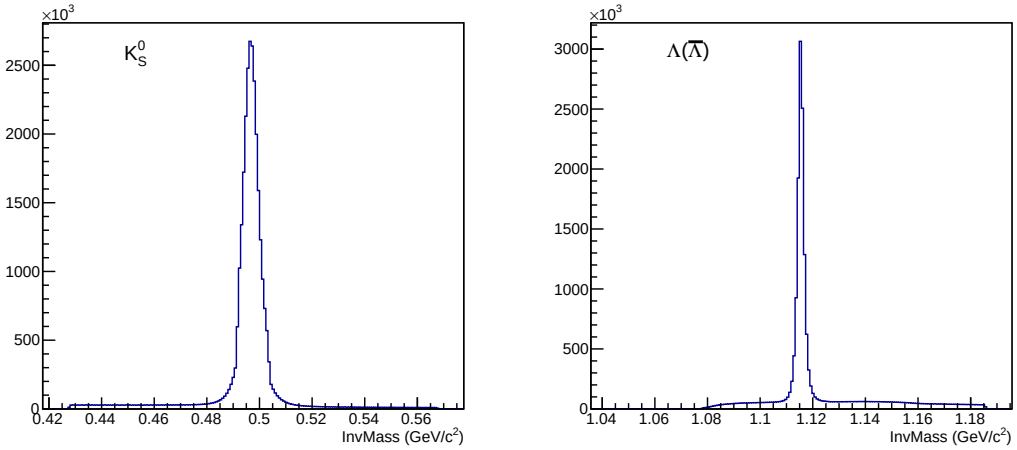

Figure 3.2: The left plot is the K_S^0 signal, and the right plot is the $\Lambda(\bar{\Lambda})$ signal. With topological cuts, the combinatorial background is largely reduced. Compared to signal, the background level is very low.

Table 3.3: Weak Decay Channels of Ξ and Ω

Particles	$c\tau$(cm)	Decay Channel	Branching Ratio
Ξ^-	4.91	$\Lambda\pi^-$	99.887%
$\bar{\Xi}^+$	4.91	$\bar{\Lambda}\pi^+$	99.887%
Ω^-	2.461	ΛK^-	67.8%
$\bar{\Omega}^+$	2.461	$\bar{\Lambda}K^+$	67.8%

3.2 Ξ^-, $\bar{\Xi}^+$, Ω^- and $\bar{\Omega}^+$ Reconstruction

The weak decay channels used for $\Xi^-(\bar{\Xi}^+)$ and $\Omega^-(\bar{\Omega}^+)$ reconstruction are listed in Table 3.3. The decay topology of Ξ^- is shown in Figure 3.3. The decay topologies of Ω^-, $\bar{\Omega}^+$ and $\bar{\Xi}^+$ are very similar.

The decay daughter $\pi^\pm$ and $K^\pm$ are identified with the TPC, Λ and $\bar{\Lambda}$ are reconstructed with the method discussed in Section 3.1. As $\Lambda(\bar{\Lambda})$ is decayed from its parent ($\Xi^-(\bar{\Xi}^+)$ or $\Omega^-(\bar{\Omega}^+)$), rather than produced in the primary vertex, we need to set a threshold for the DCA of $\Lambda(\bar{\Lambda})$ to primary vertex to exclude combinatorial background from primary $\Lambda(\bar{\Lambda})$ and charged mesons.

The $\Xi^-(\bar{\Xi}^+)$ and $\Omega^-(\bar{\Omega}^+)$ reconstruction process is analog with the strange V0 reconstruction, which just changes decay daughter from a charged particle to $\Lambda(\bar{\Lambda})$. Firstly, we calculate the DCA between $\Lambda(\bar{\Lambda})$ and $\pi^-(\pi^+)$ or $K^-(K^+)$, and set a cut to get the $\Xi^-(\bar{\Xi}^+)$ or $\Omega^-(\bar{\Omega}^+)$ candidates. And then by setting the cuts of $\Xi^-(\bar{\Xi}^+)$ or $\Omega^-(\bar{\Omega}^+)$ decay length, the DCA of $\Xi^-(\bar{\Xi}^+)$ or $\Omega^-(\bar{\Omega}^+)$ to the primary vertex, the DCA of $\Lambda(\bar{\Lambda})$ and $\pi^-(\pi^+)$ or $K^-(K^+)$ to the primary vertex, the background can be greatly suppressed. The Table 3.4 summarizes the topological cuts used for $\Xi^-(\bar{\Xi}^+)$ and $\Omega^-(\bar{\Omega}^+)$ reconstruction.

As the $\Omega^-(\bar{\Omega}^+)$ decay topology is very similar to $\Xi^-(\bar{\Xi}^+)$, and the TPC cannot distinguish pions and kaons with a $p_T > 0.6$ GeV/c, so the reconstructed $\Xi^-(\bar{\Xi}^+)$ mixes some mis-identified $\Omega^-(\bar{\Omega}^+)$ in the background. It is the same case for $\Omega^-(\bar{\Omega}^+)$ signals. The production cross section of $\Xi^-(\bar{\Xi}^+)$ is much larger than that of $\Omega^-(\bar{\Omega}^+)$, the mis-identified $\Omega^-(\bar{\Omega}^+)$ has little contribution of the $\Xi^-(\bar{\Xi}^+)$

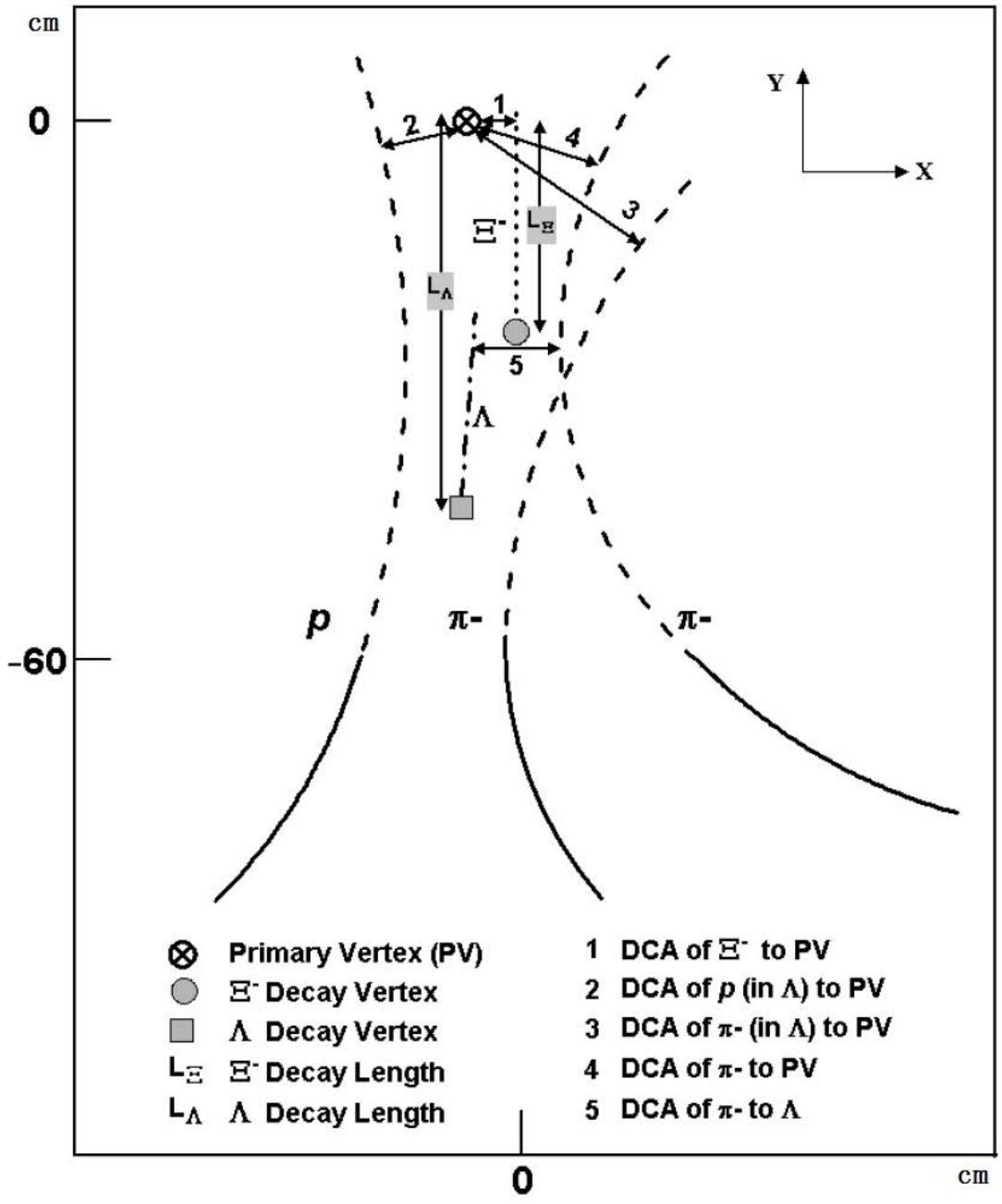

Figure 3.3: The Ξ^- decay topology. The solid line is detectable by the TPC anode sector 60 cm away from the beam line. The dashed line is extrapolated from the solid line or reconstructed Λ and Ξ^-. The topological cuts are shown in the plot. The Ω^- decay topology is similar, just changing the π^- from Ξ^- to k^-. The decay topology of $\bar{\Xi}^+$ and $\bar{\Omega}^+$ are the same, by changing the decay daughters to their anti-particles. The plot is from Hai Jiang's thesis [34].

Table 3.4: Topological Cuts for Ξ and Ω

DCA of proton to pion (in Λ)	less than
DCA of proton to primary vertex (in Λ)	greater than
DCA of pion to primary vertex (in Λ)	greater than
DCA of Λ to primary vertex	greater than
Decay Length of Λ	greater than
DCA of bachelor to Λ	less than
DCA of bachelor to primary vertex	greater than
DCA of Ξ or Ω to primary vertex	less than
Decay Length of Ξ or Ω	greater than

background, while the mis-identified $\Xi^-(\bar{\Xi}^+)$ has a significant contribution to the $\Omega^-(\bar{\Omega}^+)$ background. One method to identify $\Omega^-(\bar{\Omega}^+)$ from $\Xi^-(\bar{\Xi}^+)$ is using the TOF to identify kaons from pions, and the method is discussed in Section 2.2.3. Another method is to change the mass of the decay daughter from kaon mass to pion mass, to reconstruct the mis-identified $\Xi^-(\bar{\Xi}^+)$s, and set a mass window to exclude the mis-identified $\Xi^-(\bar{\Xi}^+)$ background from $\Omega^-(\bar{\Omega}^+)$ signal. We took the second method in the Ω^- and $\bar{\Omega}^+$ spectra analysis for the convenience of reconstruction efficiency estimation. Figure 3.4 shows the invariant mass distribution of $\Xi^-(\bar{\Xi}^+)$ and $\Omega^-(\bar{\Omega}^+)$.

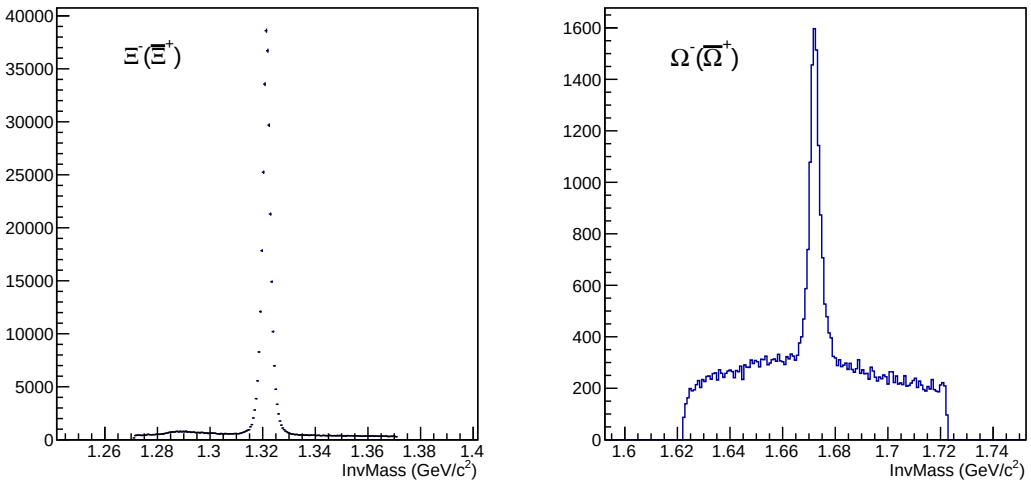

Figure 3.4: The left plot is the $\Xi^-(\bar{\Xi}^+)$ signal, and the right plot is the $\Omega^-(\bar{\Omega}^+)$ signal. We use topological cuts to get rid of the combinatorial background.

CHAPTER 4

Strangeness Production in the RHIC Beam Energy Scan Program

In the years 2010 and 2011, the STAR experiment took high-statistics data in the RHIC Beam Energy Scan Program (BES) to study the QCD phase diagram and search for a possible QCD critical point. Strangeness is a sensitive probe to study the medium created in the heavy-ion collision. The measurements of strange particle (K^0_S, Λ, Ξ, Ω) production in the BES program are discussed in this chapter.

4.1 Introduction to Strangeness Physics in Heavy-Ion Collisions

4.1.1 Strangeness Production in Heavy-Ion Collisions

Relativistic heavy-ion collisions aim at creating the QGP. The enhanced production of strange hadrons in A+A with respect to p+p collisions, has been proposed for the possible signature of the QGP state [35]. The strange quarks are not present in the nuclei of the incoming beams, and they are produced in the collisions. Therefore, the strange hadrons in the final state provide valuable insight into the properties of the created system, and the production rates and phase space distributions of the strange particles may reveal different characteristics of the created medium. Until now, strange particles have been extensively stud-

ied in many experiments at different accelerator facilities and different collision energies [31][32][36][37][38][39][40][41][42][43][44][45][46][47].

The mechanism of strangeness production varies with the collision energy. In RHIC Au+Au 200 GeV collisions, it is observed that the nuclear modification factors (R_{CP}) of baryons and mesons at intermediate p_T follow different trends, and the baryon-to-meson ratios are enhanced at intermediate p_T range in central collisions [45][7]. At high p_T, the R_{CP} is much less than unity. And there is no significant difference between the behaviors of strange hadrons and other light flavor hadrons. The R_{CP} and baryon-to-meson ratios in Au+Au 200 GeV collisions, are shown in Figure 4.1 and Figure 4.2. Those phenomena may be explained by the partonic energy loss in the medium and recombination/coalescence model, which is an indication of the formation of strongly coupled quark-gluon plasma. At low beam energies, such as AGS and SPS energies, where there is a significant net baryon density, the strange baryon production is enhanced, and the strangeness conservation can be achieved through associated production of strange baryons and kaons. Our measurement of strange particle yields, R_{CP}, anti-baryon to baryon ratios, and baryon-to-meson ratios in the RHIC Beam Energy Scan Program will examine how the strangeness production mechanism changes with the beam energy.

4.1.2 RHIC Beam Energy Scan Program

The results at RHIC top energies suggest that a strongly coupled Quark Gluon Plasma (sQGP) is created, which reaches equilibration very early in the collision. Hadrochemical species equilibrium is observed just after hadronization. No distinct discontinuity was observed experimentally, which is consistent with Lattice QCD prediction for a smooth crossover at high temperature and low chemical potentials, i.e. the transition from the QGP to hadrons is smooth and continuous [7][48]. Theoretical model calculations predict that at low temperatures and

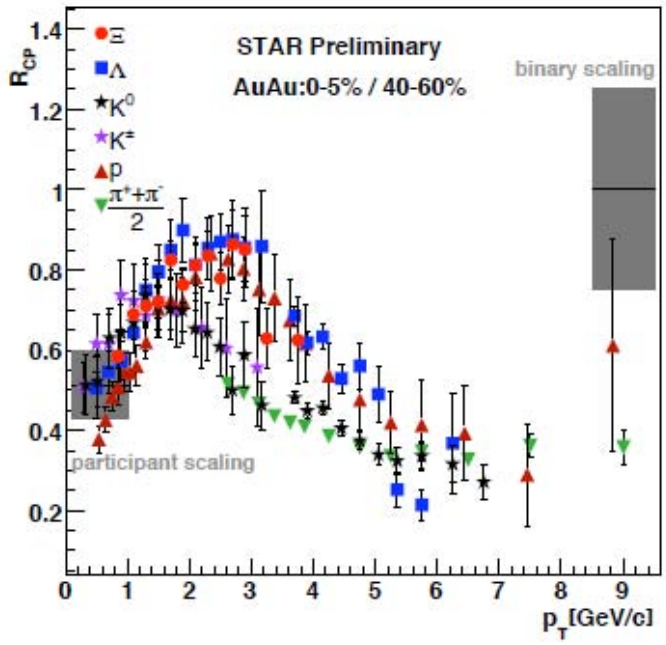

Figure 4.1: The plot shows the R_{CP} of $\pi^{\pm}$, $K^{\pm}$, K^0_S, p, Λ, and Ξ. The baryons and mesons at intermediate p_T follow different trends. The figure is from [7].

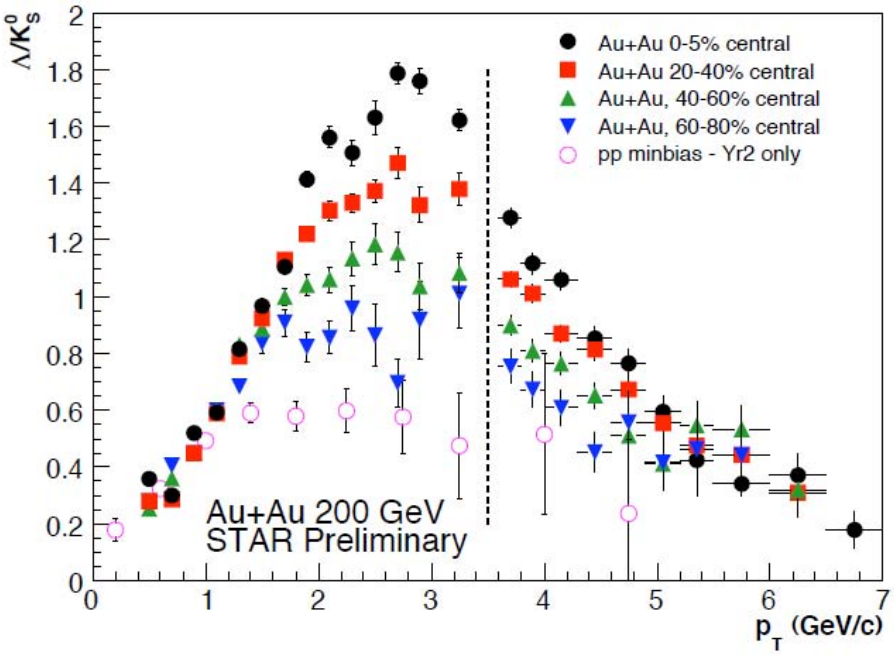

Figure 4.2: The plot shows the Λ/K^0_S ratios as a function of p_T at different centralities. The ratios are enhanced at intermediate p_T range. The figure is from [7].

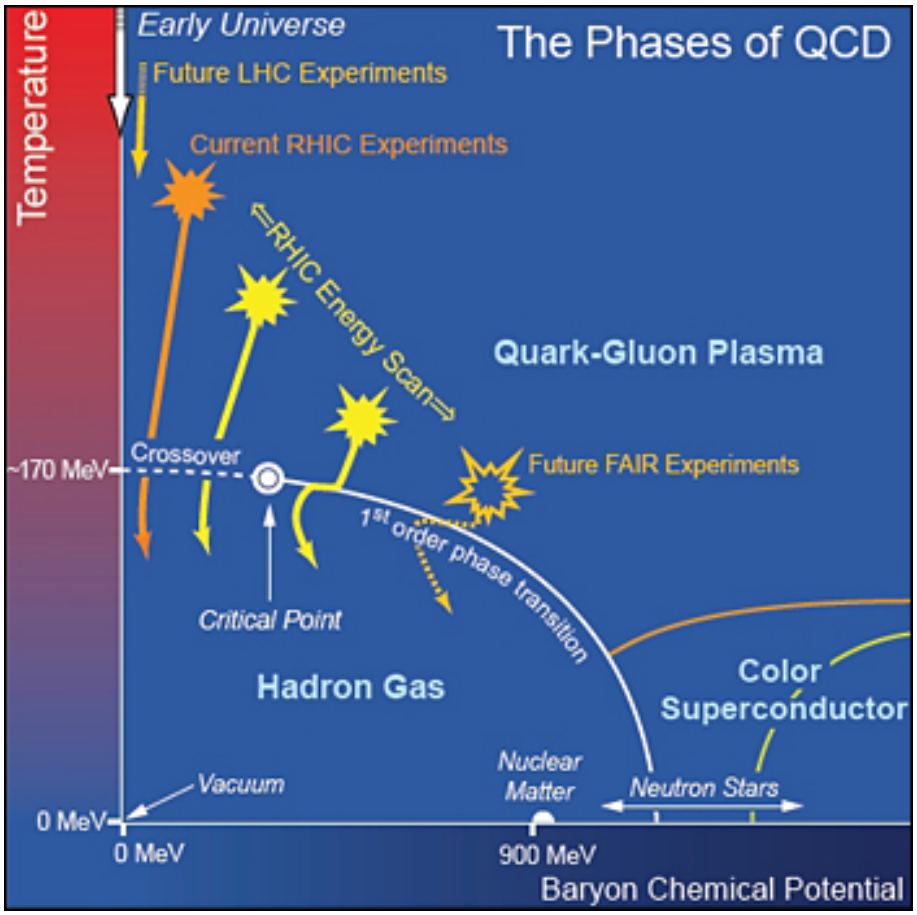

Figure 4.3: A schematic phase diagram of nuclear matter.

high baryon chemical potentials, it is a first order phase transition [7]. Therefore, a critical point exists at intermediate temperature and finite baryon chemical potential. Figure 4.3 shows a schematic QCD Phase Diagram, with smooth crossover, critical point and the first order transition regions.

The RHIC Beam Energy Scan (BES) Phase I, took place in 2010 and 2011, which consisted of Au+Au collisions at 7.7, 11,5, 19.6, 27, and 39 GeV. The RHIC BES tries to search for the evidence of a critical point and phase transition, and tries to find the collision energy at which, the presence of the sQGP turn off as $\sqrt{s_{NN}}$ decreases [7].

4.1.3 Statistical Thermal Model

The statistical thermal model can describe the particle yields by using only two chemical freeze-out parameters, the temperature (T) and baryon chemical potential (μ_B), with assumption that the particles are produced following the phase space distribution of thermalized equilibrium statistics [49]. The statistical thermal model is successful from the low energies at the GSI Schwerionen-Synchrotron (SIS) up to the high energies at RHIC and LHC.

The particle abundances can be described by [50]:

$$N_j = \gamma_S^{|n_S|} \lambda_j \frac{\partial}{\partial \lambda_j} \ln Z(T, V, \dots) \tag{4.1.1}$$

where λ_j is the fugacity for particle species j [51], given by $\lambda_j = \exp(-\mu_j/T)$, Z is the standard partition function, γ_S is the strangeness phase space suppression factor modifying the yield of strangeness which does not reach its full equilibration [5]. The average chemical potential μ_j is given by:

$$\mu_j = n_B \mu_B + n_S \mu_S \tag{4.1.2}$$

where μ_S is the strangeness chemical potential, which depends on T and μ_B.

In the Boltzmann approximation, the number of particles of species j, is

$$N_j = \gamma_S^{|n_S|} \frac{g_j m_j^2 T}{2\pi^2} K_2(\frac{m_j}{T}) \exp(\frac{\mu_j}{T}) \tag{4.1.3}$$

where g_j is the degeneracy factor, m_j is the invariant mass of particle j, K_2 is the modified Bessel function.

The particle and its anti-particle have the same γ_S and m_j. Therefore, the anti-

Table 4.1: The data set and event selection criteria, as well as the total number of good events used in the analysis.

$\sqrt{S_{NN}}$	Year	Vertex Cut	Number of Good Events
39 GeV	2010	$\|V_Z\| < 40$ cm, $\|V_r\| < 2$ cm	130 million
27 GeV	2011	$\|V_Z\| < 50$ cm, $\|V_r\| < 2$ cm	50 million
19.6 GeV	2011	$\|V_Z\| < 50$ cm, $\|V_r\| < 2$ cm	26 million
11.5 GeV	2010	$\|V_Z\| < 50$ cm, $\|V_r\| < 2$ cm	11 million
7.7 GeV	2010	$\|V_Z\| < 70$ cm, $\|V_r\| < 2$ cm	4 million

particle to particle ratio only depends on the chemical potential and temperature:

$$\frac{N_{\bar{j}}}{N_j} = \exp(-\frac{2\mu_j}{T}). \tag{4.1.4}$$

For Λ, $\mu_\Lambda = \mu_B - \mu_S$, and $\frac{N_{\bar{\Lambda}}}{N_\Lambda} = \exp(-\frac{2\mu_B}{T} + \frac{2\mu_S}{T})$.

For Ξ^-, $\mu_{\Xi^-} = \mu_B - 2\mu_S$, and $\frac{N_{\bar{\Xi}+}}{N_{\Xi^-}} = \exp(-\frac{2\mu_B}{T} + \frac{4\mu_S}{T})$.

For Ω^-, $\mu_{\Omega^-} = \mu_B - 3\mu_S$, and $\frac{N_{\bar{\Omega}+}}{N_{\Omega^-}} = \exp(-\frac{2\mu_B}{T} + \frac{6\mu_S}{T})$.

4.2 Data Set and Event Selection

STAR has collected high-statistics data in year 2010 and 2011 in the RHIC Beam Energy Scan Program at 7.7, 11.5, 19.6, 27, and 39 GeV Au+Au collisions. In this thesis, the strange particle spectra are studied at those five energies.

In order to investigate the centrality dependence, minimum bias data are selected. Some basic vertex cuts are set to select good events. Table 4.1 lists the data set and cuts used in the event selection, where V_Z is the collision vertex position along the beam direction from the detector center, and V_r is the distance between collision vertex and the beam pipe.

The whole data set of each energy is separated to nine intervals. A C++ class StRefMultCorr is used in STAR as a standard class to define the centrality and provide the weight for each event, according to the reference multiplicity of each

event and luminosity at the same time. Figure 4.4 shows the reference multiplicity distribution of the five data sets.

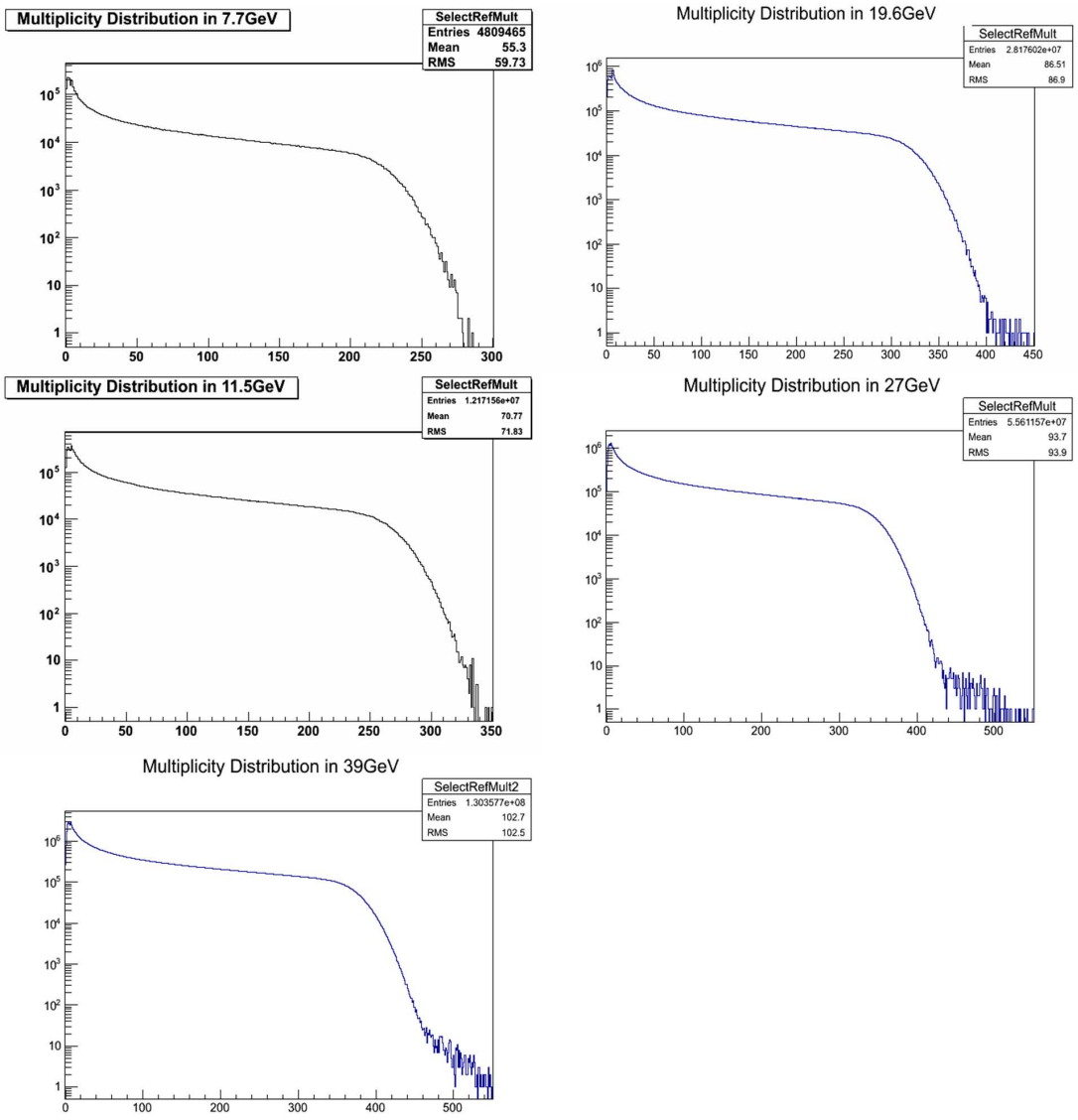

Figure 4.4: The figures show the reference multiplicity distribution of Au+Au collisions at 7.7, 11.5, 19.6, 27, and 39 GeV.

4.3 Analysis Methods

The strange particles K^0_S, $\Lambda(\bar{\Lambda})$, $\Xi^-(\bar{\Xi}^+)$, and $\Omega^-(\bar{\Omega}^+)$ are reconstructed from their decay daughters. The reconstruction method has been discussed in the Chapter 3. In this section, we will discuss the details of the strange particle p_T spectra analysis process in the RHIC Beam Energy Scan Program. I study the $\Omega^-(\bar{\Omega}^+)$ spectra at all the five beam energies, and K^0_S, $\Lambda(\bar{\Lambda})$, $\Xi^-(\bar{\Xi}^+)$ spectra at 19.6 GeV and 27 GeV. And the K^0_S, $\Lambda(\bar{\Lambda})$, $\Xi^-(\bar{\Xi}^+)$ spectra at 7.7 GeV, 11.5 GeV, and 39 GeV are done by Dr. Xianglei Zhu from Tsinghua University, who has a long collaboration with the UCLA group.

4.3.1 Decay Daughter Selection and Weak Decay Topological Cuts

The decay daughters of K^0_S, $\Lambda(\bar{\Lambda})$, $\Xi^-(\bar{\Xi}^+)$, and $\Omega^-(\bar{\Omega}^+)$ are protons, pions, and kaons, which are identified with the TPC. The cuts for the daughter identification are shown in Table 4.2.

Table 4.2: Decay Daughter Identification

p and $\bar{p}$	$n\sigma_p \leq 3.0$	Nhits$>$ 15	$p_T \geq 0.15$ GeV/c
π^- and π^+	$n\sigma_\pi \leq 4.0$	Nhits$>$ 15	$p_T \geq 0.15$ GeV/c
K^- and K^+	$n\sigma_K \leq 4.0$	Nhits$>$ 15	$p_T \geq 0.15$ GeV/c

The topological cuts for K^0_S signal reconstruction are shown in Table 4.3. The reconstructed K^0_S signals are shown in Figure 4.5.

Table 4.3: K^0_S Topological Cuts

Energy (GeV)	19.6	27
Particle	K^0_S	K^0_S
$\|y\|$ of K^0_S	< 0.5	< 0.5
DCA π to PV	> 1.2 cm	> 1.2 cm
DCA π^+ to π^-	< 0.8 cm	< 0.8 cm
DCA K^0_S to PV	< 0.7 cm	< 0.7 cm
K^0_S Decay Length ($L_{K^0_S}$)	> 3.0 cm	> 3.0 cm
$(\vec{r_{K^0_S}} - \vec{r_{PV}}) \cdot \vec{p_{K^0_S}}$	> 0	> 0

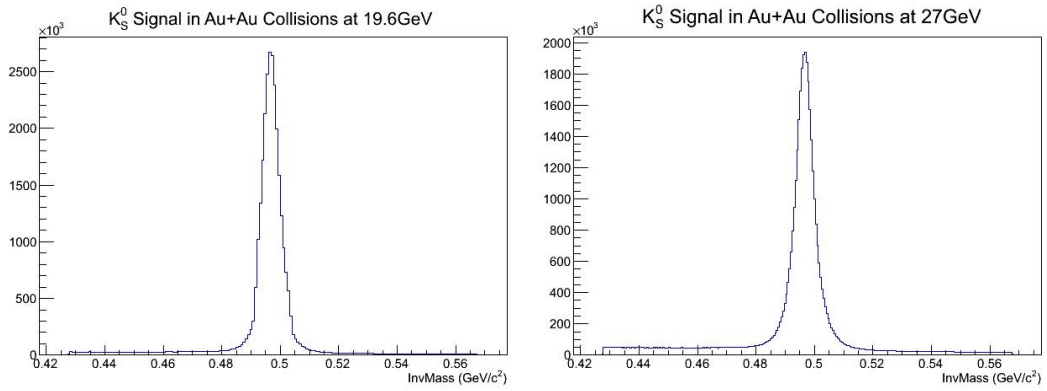

Figure 4.5: The figures show the reconstructed K^0_S signals at 19.6 and 27 GeV.

The topological cuts for $\Lambda(\bar{\Lambda})$ signal reconstruction are shown in Table 4.4. The reconstructed $\Lambda(\bar{\Lambda})$ signals are shown in Figure 4.6.

Table 4.4: Λ and $\bar{\Lambda}$ Topological Cuts

Energy (GeV)	19.6	27
Particle	$\Lambda(\bar{\Lambda})$	$\Lambda(\bar{\Lambda})$
$\lvert y\rvert$ of Λ	< 0.5	< 0.5
DCA proton to PV	> 0.5 cm	> 0.5 cm
	(0.7 cm for V0 $p_T < 0.6$ GeV/c)	(0.7 cm for V0 $p_T < 0.6$ GeV/c)
DCA π to PV	> 1.5 cm	> 1.5 cm
	(2.5 cm for V0 $p_T < 0.6$ GeV/c)	(2.5 cm for V0 $p_T < 0.6$ GeV/c)
DCA π to proton	< 0.8 cm	< 0.8 cm
DCA Λ to PV	< 0.7 cm	< 0.7 cm
Λ Decay Length (L_Λ)	> 4.0 cm	> 4.0 cm
$(\vec{r_\Lambda} - \vec{r_{PV}}) \cdot \vec{p_\Lambda}$	> 0	> 0

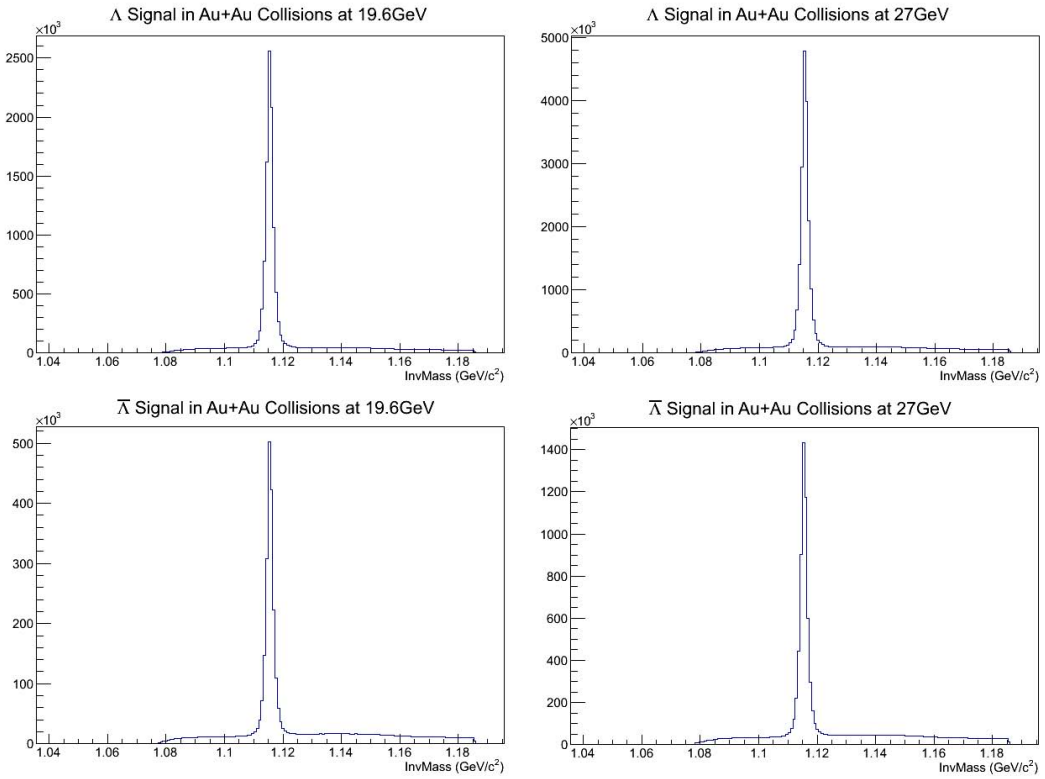

Figure 4.6: The figures show the reconstructed Λ and $\bar{\Lambda}$ signals at 19.6 and 27 GeV.

The topological cuts for $\Xi^-(\bar{\Xi}^+)$ signal reconstruction are shown in Table 4.5. The reconstructed $\Xi^-(\bar{\Xi}^+)$ signals are shown in Figure 4.7.

Table 4.5: Ξ^- and $\bar{\Xi}^+$ Topological Cuts

Energy (GeV)	19.6	27
Particle	$\Xi^-(\bar{\Xi}^+)$	$\Xi^-(\bar{\Xi}^+)$
$\|y\|$ of Ξ	< 0.5	< 0.5
DCA p to PV	> 0.6 cm	> 0.6 cm
DCA π to PV	> 2.0 cm	> 2.0 cm
DCA π(bachelor) to PV	> 1.5 cm	> 1.5 cm
DCA π to p	< 0.8 cm	< 0.8 cm
DCA π to Λ	< 0.8 cm	< 0.8 cm
DCA Λ to PV	> 0.5 cm	> 0.5 cm
DCA Ξ to PV	< 0.5 cm	< 0.5 cm
Λ Decay Length (L_Λ)	> 5.0 cm	> 5.0 cm
Ξ Decay Length (L_Ξ)	> 4.0 cm	> 4.0 cm
$L_\Lambda > L_\Xi$	yes	yes
$(\vec{r_\Lambda} - \vec{r_\Xi}) \cdot \vec{p_\Lambda}$	> 0	> 0
$(\vec{r_\Xi} - \vec{r_{PV}}) \cdot \vec{p_\Xi}$	> 0	> 0
$\|(\vec{r_\Xi} - \vec{r_{PV}}) \times \vec{p_\Xi}\|/\|(\vec{r_\Xi} - \vec{r_{PV}})\|/\|\vec{p_\Xi}\|$	< 0.20	< 0.20

The topological cuts for $\Omega^-(\bar{\Omega}^+)$ signal reconstruction are shown in Table 4.6. The reconstructed $\Omega^-(\bar{\Omega}^+)$ signals are shown in Figure 4.8.

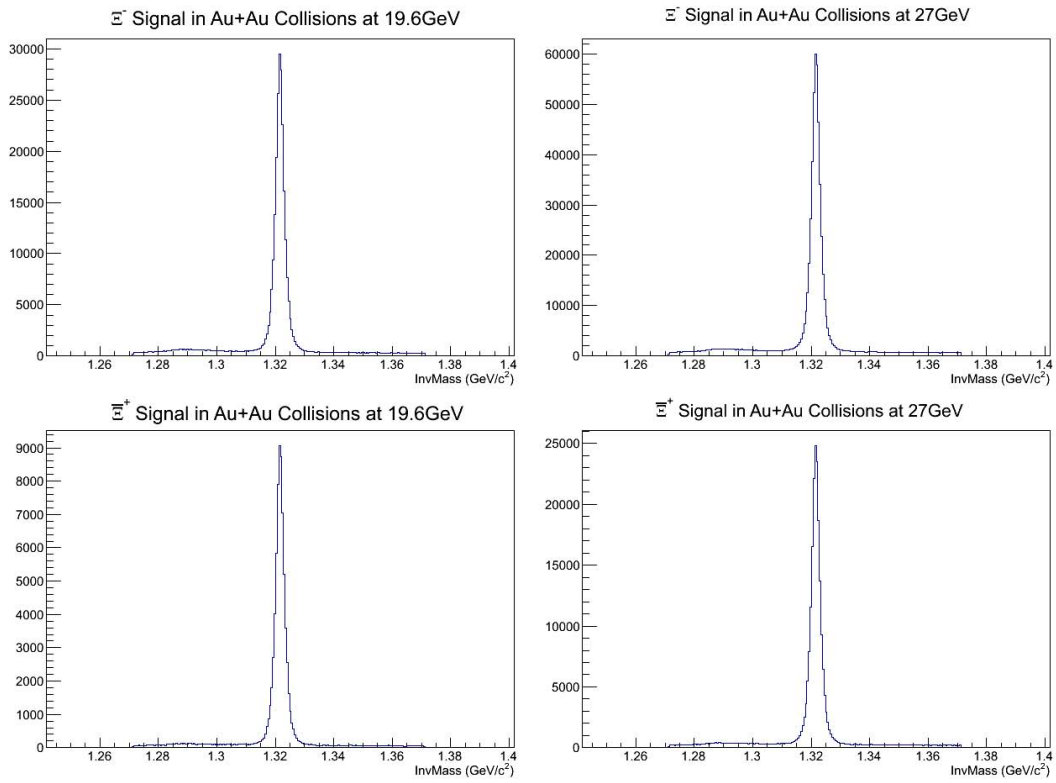

Figure 4.7: The figures show the reconstructed Ξ^- and $\bar{\Xi}^+$ signals at 19.6 and 27 GeV.

Table 4.6: Ω^- and $\bar{\Omega}^+$ Topological Cuts

Energy (GeV)	7.7	11.5	19.6	27	39
Particle	Ω^-	Ω^-	Ω^-	Ω^-	Ω^-
$\|y\|$ of Ω^-	< 0.5	< 0.5	< 0.5	< 0.5	< 0.5
DCA p to PV	> 0.6 cm	> 0.6 cm	> 0.6 cm	> 0.6 cm	> 0.6 cm
DCA π to PV	> 2.0 cm	> 2.0 cm	> 2.0 cm	> 2.0 cm	> 2.0 cm
DCA K to PV	> 1.0 cm	> 1.0 cm	> 1.0 cm	> 1.0 cm	> 1.0 cm
DCA π to p	< 0.7 cm	< 0.7 cm	< 0.7 cm	< 0.7 cm	< 0.7 cm
DCA k to Λ	< 0.7 cm	< 0.7 cm	< 0.7 cm	< 0.7 cm	< 0.7 cm
DCA Λ to PV	> 0.3 cm	> 0.4 cm	> 0.4 cm	> 0.4 cm	> 0.4 cm
DCA Ω to PV	< 0.4 cm	< 0.4 cm	< 0.5 cm	< 0.4 cm	< 0.4 cm
Λ Decay Length (L_Λ)	> 4.0 cm	> 5.0 cm	> 5.0 cm	> 5.0 cm	> 5.0 cm
Ω Decay Length (L_Ω)	> 2.0 cm	> 3.0 cm	> 3.0 cm	> 3.0 cm	> 3.0 cm
$L_\Lambda > L_\Omega$	yes	yes	yes	yes	yes
$(\vec{r_\Lambda} - \vec{r_\Omega}) \cdot \vec{p_\Lambda}$	> 0	> 0	> 0	> 0	> 0
$(\vec{r_\Omega} - \vec{r_{PV}}) \cdot \vec{p_\Omega}$	> 0	> 0	> 0	> 0	> 0
$\|(\vec{r_\Omega} - \vec{r_{PV}}) \times \vec{p_\Omega}\|/\|(\vec{r_\Omega} - \vec{r_{PV}})\|/\|\vec{p_\Omega}\|$	< 0.15	< 0.15	< 0.12	< 0.12	< 0.12
Particle	$\bar{\Omega}^+$	$\bar{\Omega}^+$	$\bar{\Omega}^+$	$\bar{\Omega}^+$	$\bar{\Omega}^+$
$\|y\|$ of $\bar{\Omega}^+$	< 0.5	< 0.5	< 0.5	< 0.5	< 0.5
DCA p to PV	> 0.6 cm	> 0.6 cm	> 0.6 cm	> 0.6 cm	> 0.6 cm
DCA π to PV	> 2.0 cm	> 2.0 cm	> 2.0 cm	> 2.0 cm	> 2.0 cm
DCA K to PV	> 1.0 cm	> 1.0 cm	> 1.0 cm	> 1.0 cm	> 1.0 cm
DCA π to p	< 1.0 cm	< 0.7 cm	< 0.7 cm	< 0.7 cm	< 0.7 cm
DCA k to Λ	< 1.0 cm	< 0.7 cm	< 0.7 cm	< 0.7 cm	< 0.7 cm
DCA Λ to PV	> 0.3 cm	> 0.4 cm	> 0.4 cm	> 0.4 cm	> 0.4 cm
DCA Ω to PV	< 0.6 cm	< 0.4 cm	< 0.5 cm	< 0.5 cm	< 0.4 cm
Λ Decay Length (L_Λ)	> 4.0 cm	> 4.0 cm	> 5.0 cm	> 5.0 cm	> 5.0 cm
Ω Decay Length (L_Ω)	> 2.0 cm	> 2.0 cm	> 3.0 cm	> 3.0 cm	> 3.0 cm
$L_\Lambda > L_\Omega$	yes	yes	yes	yes	yes
$(\vec{r_\Lambda} - \vec{r_\Omega}) \cdot \vec{p_\Lambda}$	> 0	> 0	> 0	> 0	> 0
$(\vec{r_\Omega} - \vec{r_{PV}}) \cdot \vec{p_\Omega}$	> 0	> 0	> 0	> 0	> 0
$\|(\vec{r_\Omega} - \vec{r_{PV}}) \times \vec{p_\Omega}\|/\|(\vec{r_\Omega} - \vec{r_{PV}})\|/\|\vec{p_\Omega}\|$	< 0.15	< 0.15	< 0.12	< 0.12	< 0.12

For the $\Xi^-(\bar{\Xi}^+)$ and $\Omega^-(\bar{\Omega}^+)$ reconstruction, we firstly reconstruct $\Lambda(\bar{\Lambda})$, and then select pure $\Lambda(\bar{\Lambda})$ with a mass window cut ($|M_\Lambda - M_{PDG}| < 6$ MeV) to reconstruct $\Xi^-(\bar{\Xi}^+)$ and $\Omega^-(\bar{\Omega}^+)$. The Ξ has a similar decay topology with Ω, and in the $p_T > 0.6$ GeV/c range, kaon dE/dx band merges with pion band, as shown in Figure 2.7. In addition, the Ξ^- and $\bar{\Xi}^+$ yields are much higher than the

Ω^- and $\bar{\Omega}^+$ yields respectively. In this case, the $\Xi^-(\bar{\Xi}^+)$ contributes a lot to the background in the reconstructed $\Omega^-(\bar{\Omega}^+)$ signal. So when we reconstruct the Ω signal, we change the mass of the bachelor particle (which is kaon in the Ω decay, and pion in the Ξ decay) to be the mass of pion instead of kaon, and calculated the invariant mass of parent. If the mass falls in the mass window around the Ξ mass ($|M_\Xi - M_{PDG}| < 10$ MeV), we exclude this Ω candidate to reduce the background from Ξ.

4.3.2 Signal Extraction

In order to study the p_T spectra, the raw yields of strange particles at each p_T bin for various centrality bins need to be extracted. If there is no background in the invariant mass distribution, all the counts will be the raw yields. However, there are significant combinatorial backgrounds, although strict topological cuts are applied. Therefore, we need to study the background in order to get the raw yield for each bin. After the background is subtracted from the invariant mass distribution, the raw yield can be counted. There are three methods to study the background: rotational background method, fitting method, and side band method. Different methods are used for different particles and p_T bins due to the background level in the invariant mass distribution.

Rotational background method is to simulate the combinatorial background by rotating one daughter's track by some angle with respect to the primary vertex [52]. A large part of the background in the invariant mass distribution is from random combinations of uncorrelated identified daughter particles. The rotational background method destroys all the secondary vertices and only combinational background is reconstructed in the invariant mass distribution. This method is used for $\Omega^-(\bar{\Omega}^+)$ spectra analysis, by rotating the kaon tracks with angles $\pi/3$, $2\pi/3$, π, $4\pi/3$, and $5\pi/3$ when reconstructing the $\Omega^-(\bar{\Omega}^+)$ candidates. The rotational background can describe the real background well. Figure 4.8 shows the

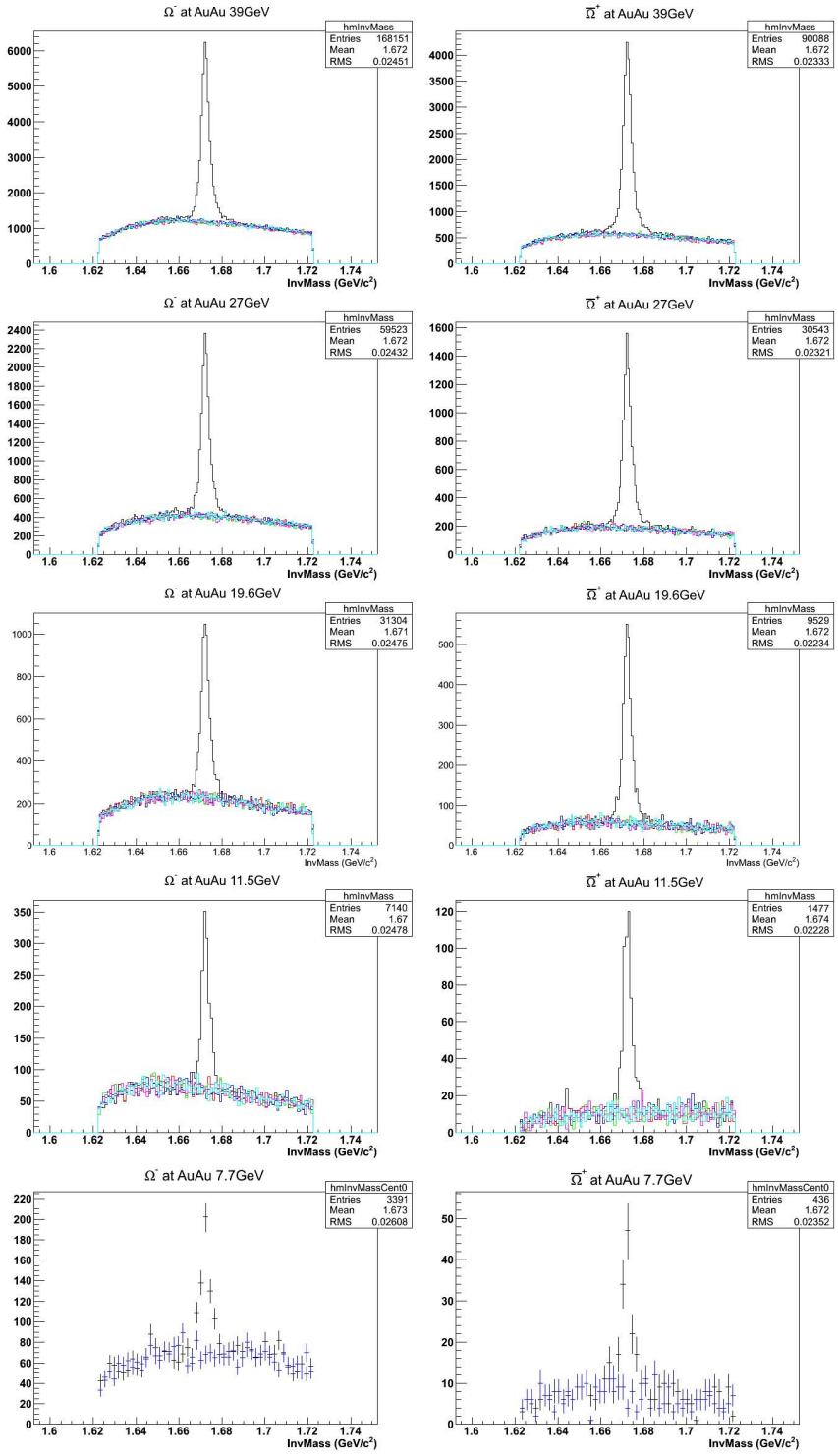

Figure 4.8: The figures show the reconstructed Ω^- and $\bar{\Omega}^+$ signals at 7.7, 11.5, 19.6, 27, and 39 GeV. The black curves or points are the real signals. The rotational background method is applied. The red, green, blue, magenta and cyan curves are the rotational backgrounds with rotation angles $\pi/3$, $2\pi/3$, π, $4\pi/3$ and $5\pi/3$ separately. We only rotate π angle for 7.7 GeV.

comparison between them. The rotational background is not used for K^0_S, $\Lambda(\bar{\Lambda})$ and $\Xi^-(\bar{\Xi}^+)$. There are other correlations between positive and negative tracks other than the combinatorial, which contributes to the background, in the K^0_S and $\Lambda(\bar{\Lambda})$ signals. For example, π^+ and π^- may come from other particle decay, and contribute to the background in the K^0_S signal; misidentified K^0_S can contribute to the background in the $\Lambda(\bar{\Lambda})$ signal. But with a track rotated, the background is also destroyed, and no longer exists in the rotational background. In addition, the background levels of K^0_S, $\Lambda(\bar{\Lambda})$ and $\Xi^-(\bar{\Xi}^+)$ are lower than $\Omega^-(\bar{\Omega}^+)$ signals, so it is easier to use polynomial function to fit the background.

Fitting method is used for extracting K^0_S, $\Lambda(\bar{\Lambda})$ and $\Xi^-(\bar{\Xi}^+)$ signals, when the statistics of the signal is high, usually the number of entries in the invariant mass distribution is above 400. We use a combination of two Gaussian functions and a third order polynomial function to fit the invariant mass distribution, and use the polynomial function to describe the background. Figure 4.9 shows an example of fitting background method.

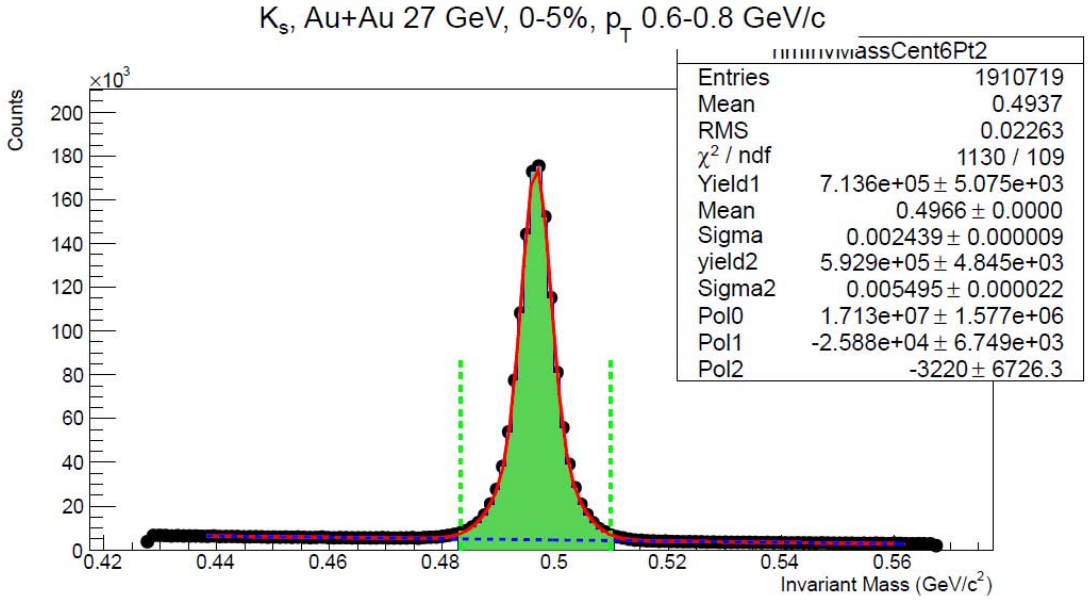

Figure 4.9: A combination of two Gaussian functions and a third order polynomial function is used to fit the invariant mass distribution.

A side band method is used for K^0_S, $\Lambda(\bar{\Lambda})$ and $\Xi^-(\bar{\Xi}^+)$ signals when the statistics of the signal is low, and the number of entries is less than 400. In this case, the function cannot fit the invariant mass distribution well, and we use the background on both side of the peak to estimate the background under the peak. Figure 4.10 shows an example of side band method.

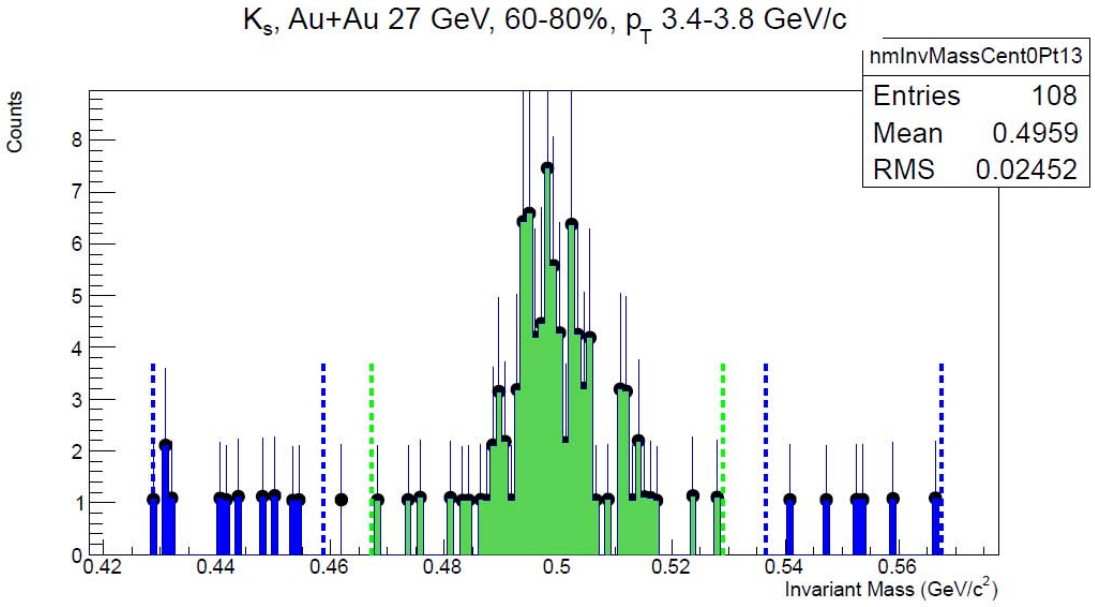

Figure 4.10: The side band method is used to estimate the background under the peak.

4.3.3 Raw p_T Spectra

After extracting the raw yields for each particle at p_T bins for each centrality, the raw spectra are calculated with the formula:

$$\frac{1}{N_{event}} \frac{d^2N}{2\pi p_T dp_T dy} = \frac{N}{2\pi N_{event} p_T \Delta p_T \Delta y} \tag{4.3.5}$$

where N_{event} is the number of collision events from the centrality bin, N is the raw yield of the particle at the p_T bin, p_T and Δp_T are the center and the width of the p_T bin, Δy is the rapidity width which is 1.0 for our spectra analysis with

$|y| < 0.5$. Figure 4.11 to Figure 4.15 show the K^0_S, Λ, $\bar{\Lambda}$, Ξ^-, and $\bar{\Xi}^+$ raw spectra in Au+Au collisions at 19.6 GeV and 27 GeV. Figure 4.16 to Figure 4.20 show the Ω^- and $\bar{\Omega}^+$ raw spectra in Au+Au collisions at 7.7, 11.5, 19.6, 27, and 39 GeV.

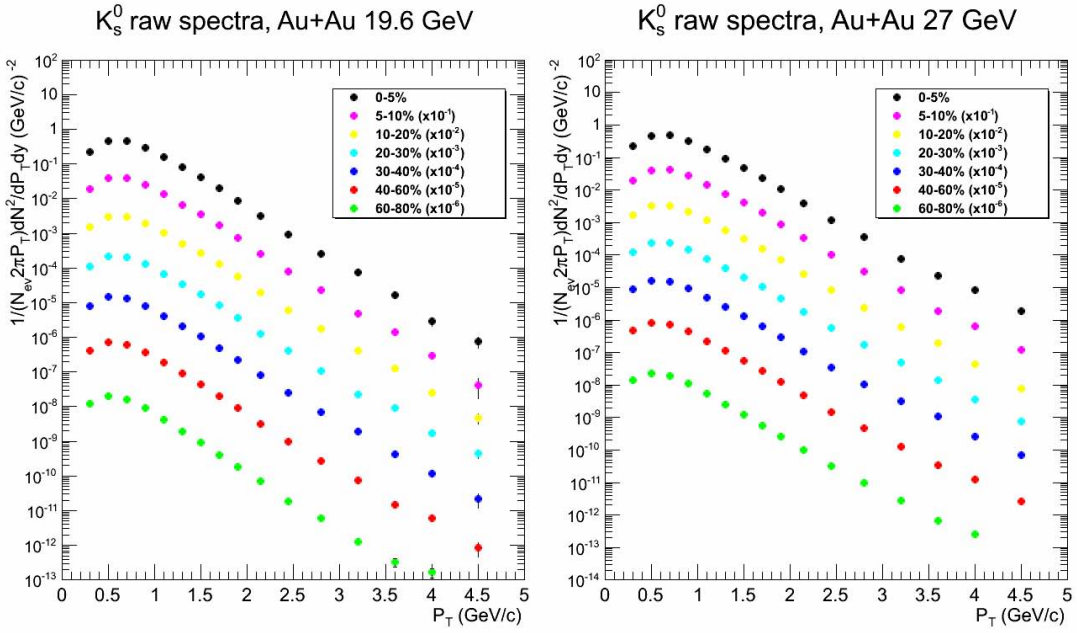

Figure 4.11: K^0_S raw spectra at Au+Au 19.6 and 27 GeV.

4.3.4 Efficiency Corrections

The raw spectra are not the real p_T distribution of the particles. The raw yield we measured only takes a fraction of the total yield of each particle created in the collision, due to the detector acceptance, response, tracking efficiency, reconstruction efficiency, and vertex finding efficiency. Therefore, in order to measure the real yields and spectra of particles, we need to correct the detection efficiency for each particle.

In the STAR experiment, embedding data are used to study the efficiency, with simulated particles embedded into real data and are forced to decay by GEANT 100% according to the desired decay channels. In each real event, five Monte-

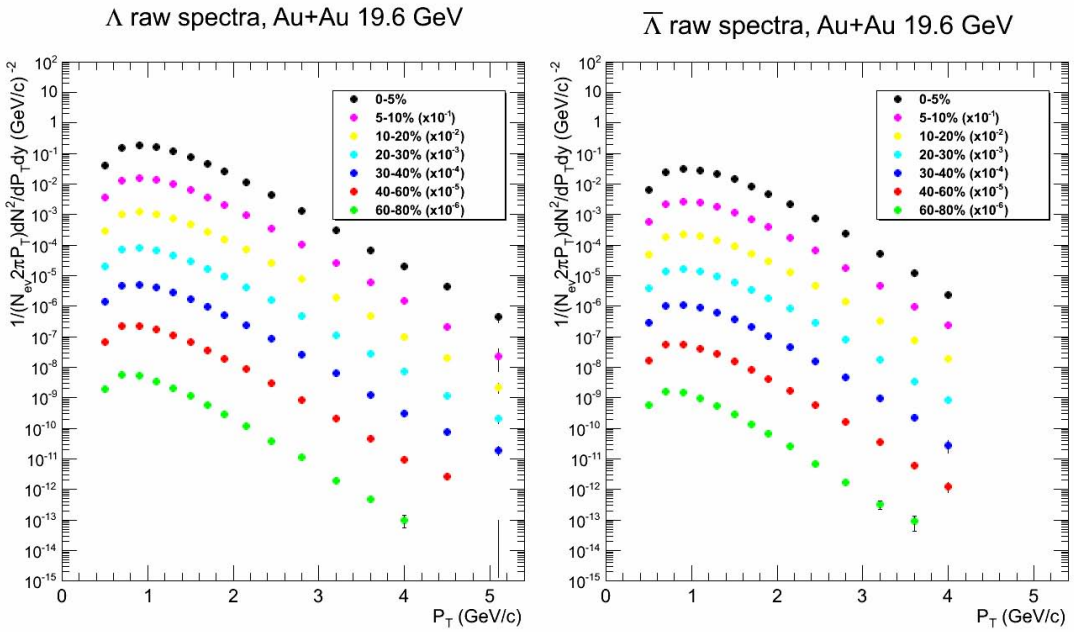

Figure 4.12: Λ and $\bar{\Lambda}$ raw spectra at Au+Au 19.6 GeV.

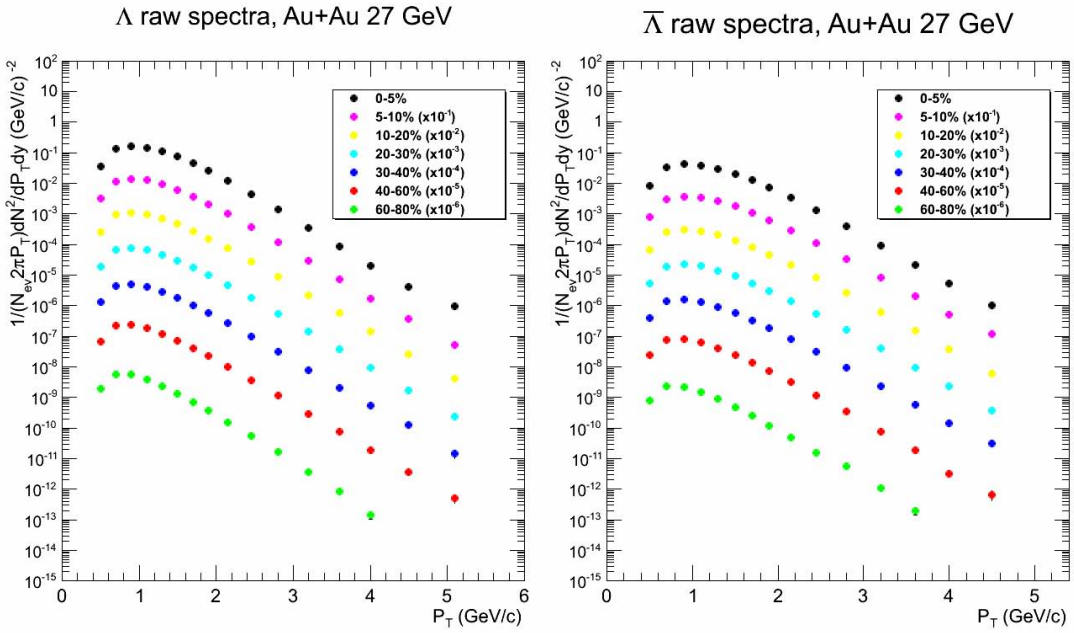

Figure 4.13: Λ and $\bar{\Lambda}$ raw spectra at Au+Au 27 GeV.

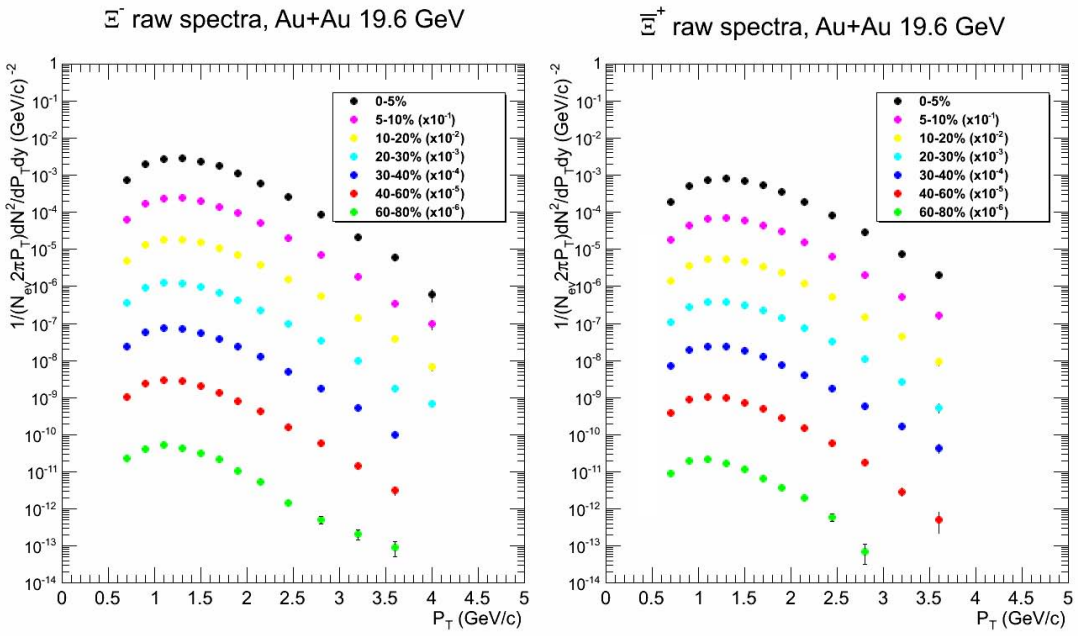

Figure 4.14: Ξ^- and $\bar{\Xi}^+$ raw spectra at Au+Au 19.6 GeV.

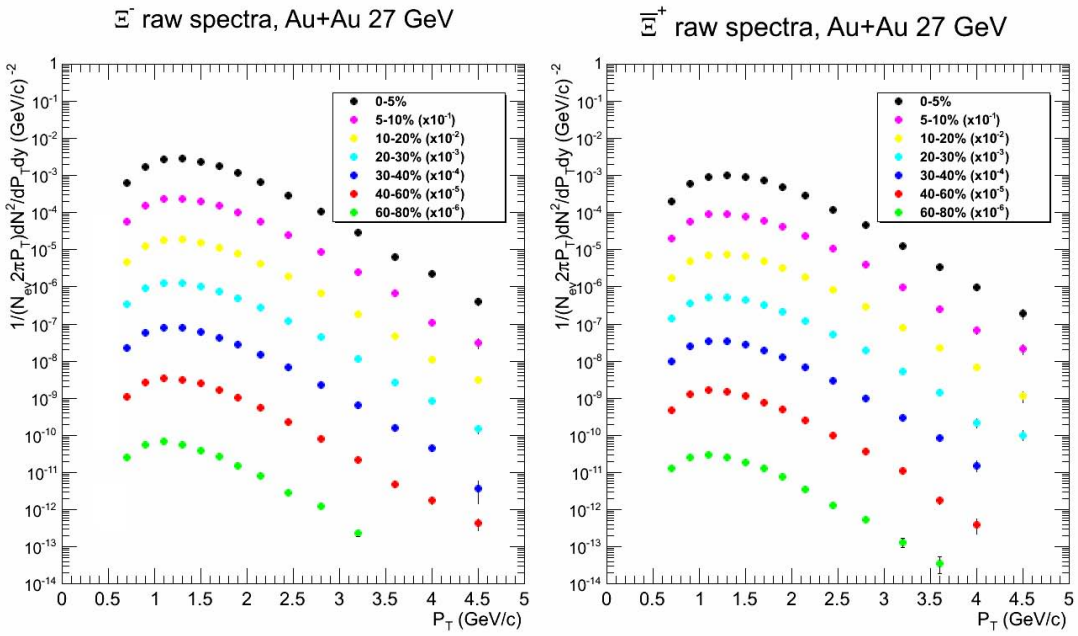

Figure 4.15: Ξ^- and $\bar{\Xi}^+$ raw spectra at Au+Au 27 GeV.

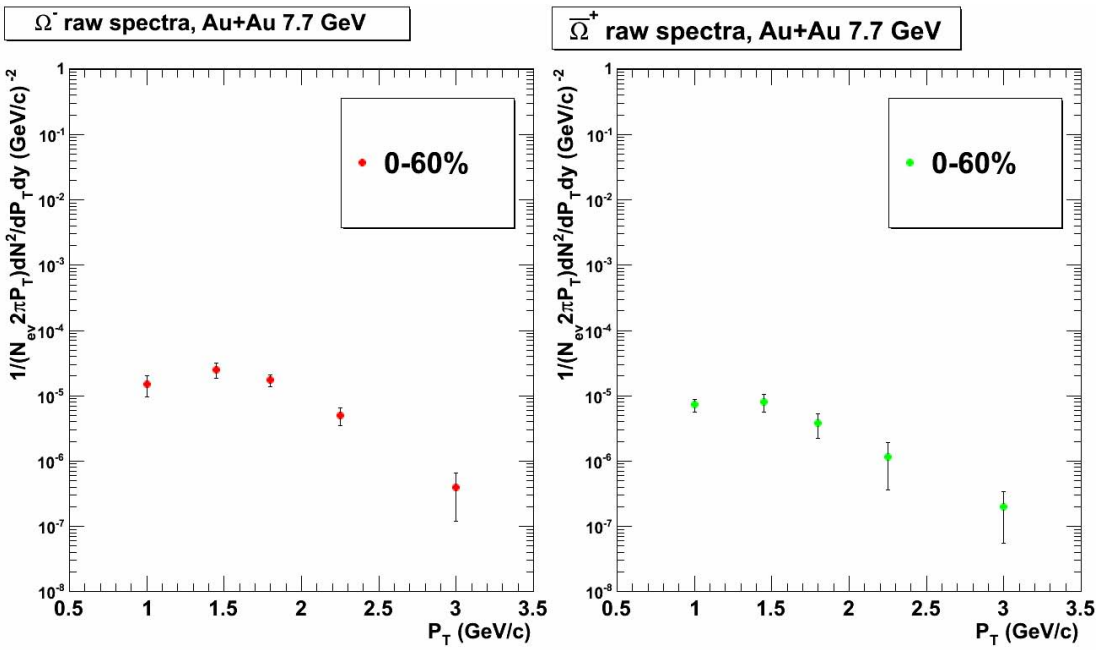

Figure 4.16: Ω^- and $\bar{\Omega}^+$ raw spectra at Au+Au 7.7 GeV.

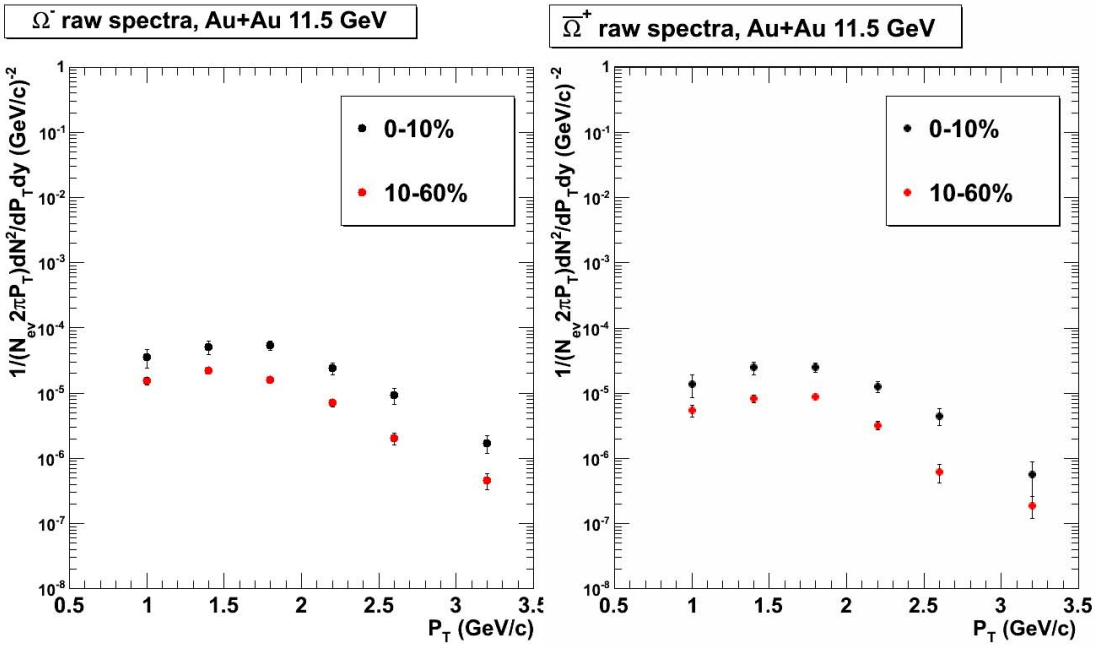

Figure 4.17: Ω^- and $\bar{\Omega}^+$ raw spectra at Au+Au 11.5 GeV.

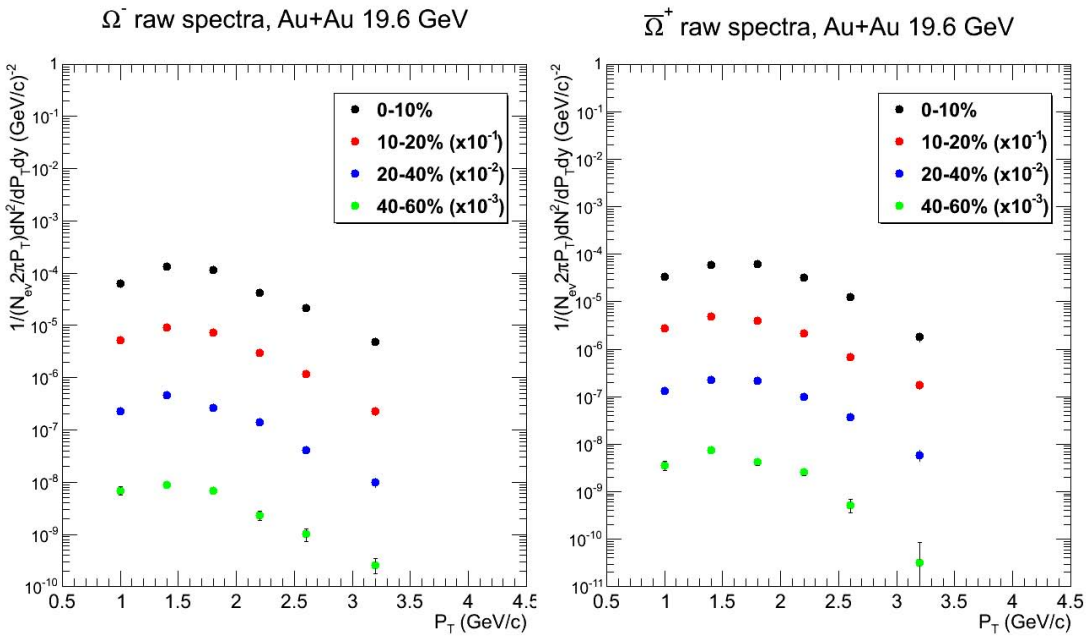

Figure 4.18: Ω^- and $\bar{\Omega}^+$ raw spectra at Au+Au 19.6 GeV.

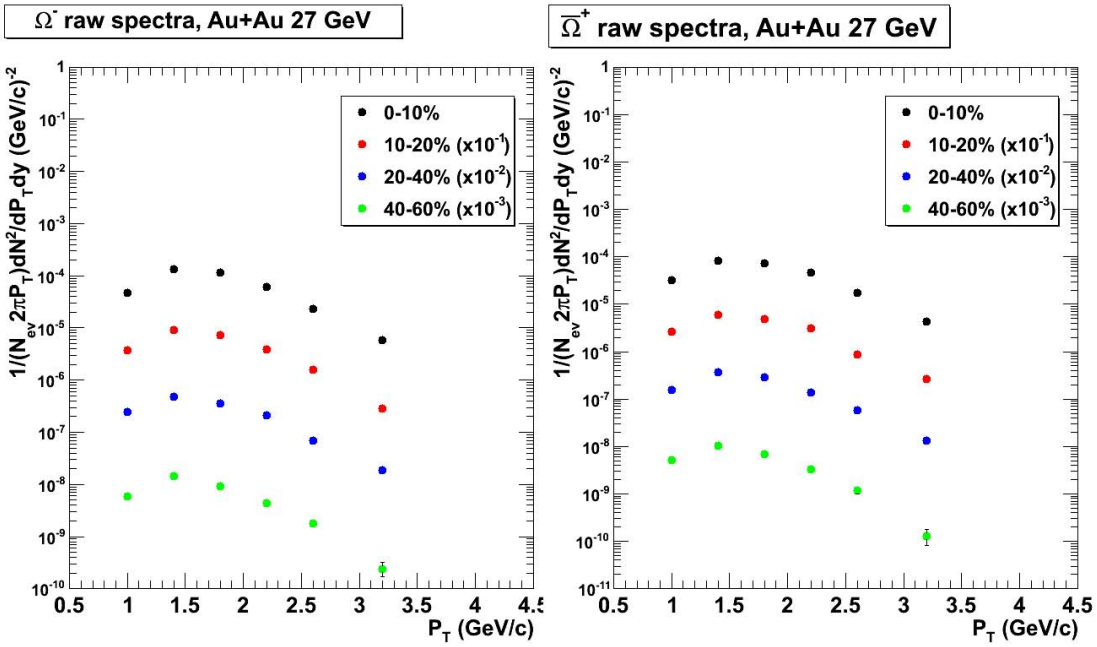

Figure 4.19: Ω^- and $\bar{\Omega}^+$ raw spectra at Au+Au 27 GeV.

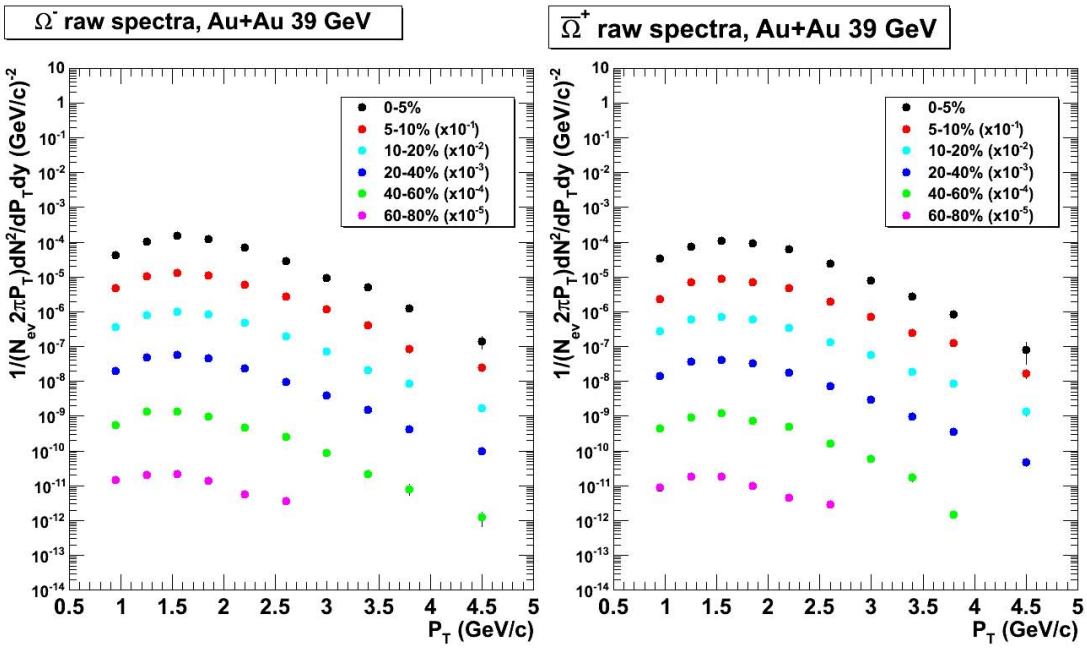

Figure 4.20: Ω^- and $\bar{\Omega}^+$ raw spectra at Au+Au 39 GeV.

Carlo (MC) particles are embedded into each event. The p_T distribution of the particles are either flat or exponential with an inverse slope of 350 MeV depending on our requirement. The efficiency depends on p_T of the particle and centrality of the collision event. For each bin, we get the efficiency from samples with flat p_T and exponential p_T distributions, and choose the efficiency with smaller statistical error. So the efficiencies of low p_T bins are calculated from the data samples with exponential p_T distribution, and the efficiencies of high p_T bins are calculated from the data samples with flat p_T distribution.

The samples with both flat p_T and exponential p_T distributions need to be corrected with real p_T distribution of the particle. We use Levy function to describe the real p_T spectra. We analyze the embedding data using the Levy function with initialized parameters, and calculate the efficiencies. Then we correct the efficiencies to get the corrected p_T spectra, and use Levy function to fit the p_T spectra. Then we run the embedding data with the updated parameters of the Levy function to update efficiencies. We repeat the above steps until the spectra

converge. With this method, we get the efficiency for each bin, and correct the efficiency for the p_T spectra. Figure 4.21 to Figure 4.30 show the efficiencies for K^0_S, Λ, $\bar{\Lambda}$, Ξ^-, $\bar{\Xi}^+$, Ω^-, and $\bar{\Omega}^+$.

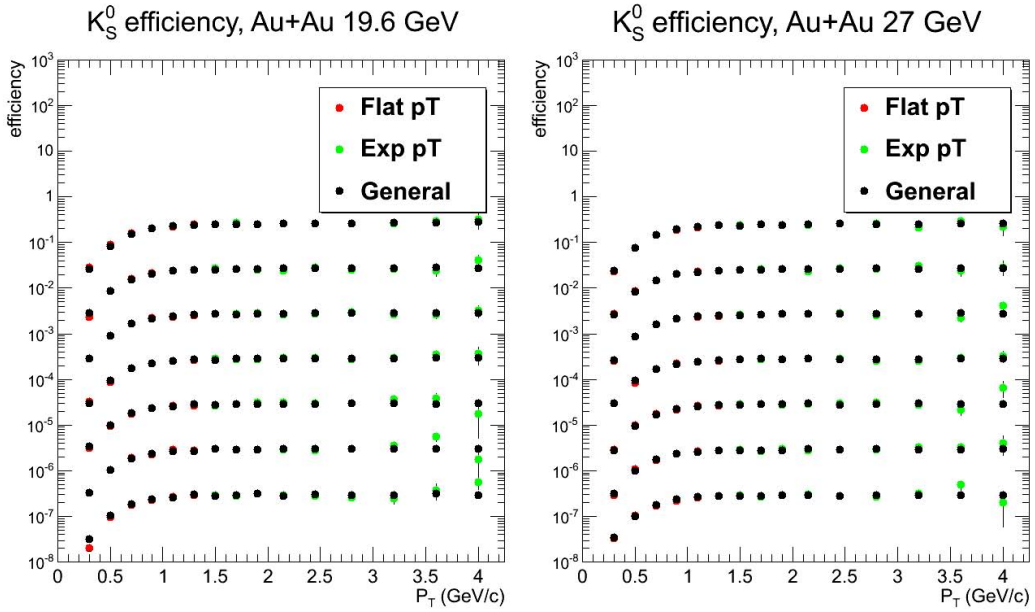

Figure 4.21: K^0_S efficiency as a function of p_T at Au+Au 19.6 and 27 GeV. From up to down, the data points are the efficiencies at 0-5%, 5-10%$\times 10^{-1}$, 10-20%$\times 10^{-2}$, 20-30%$\times 10^{-3}$, 30-40%$\times 10^{-4}$, 40-60%$\times 10^{-5}$, and 60-80%$\times 10^{-6}$.

4.3.5 Weak Decay Feed-down Contributions to $\Lambda(\bar{\Lambda})$

Not all the $\Lambda(\bar{\Lambda})$ particles are produced at the primary vertex, they may come from $\Xi^-(\bar{\Xi}^+)$, $\Xi^0(\bar{\Xi}^0)$, and $\Omega^-(\bar{\Omega}^+)$ weak decays. However, the yields of $\Omega^-(\bar{\Omega}^+)$ are much smaller then the yields of $\Xi^-(\bar{\Xi}^+)$ and $\Xi^0(\bar{\Xi}^0)$, therefore the feed-down contributions from $\Omega^-(\bar{\Omega}^+)$ are ignored.

The feed-down contribution from Ξ are estimated with the Ξ embedding data. We reconstruct Λs from the Ξ embedded events with the same cuts used in Λ reconstruction and the real Ξ p_T spectra as weight. Then we calculate the fraction of feed-down Λ to each p_T bin. As the integrated yields (dN/dy) of Ξ are measured,

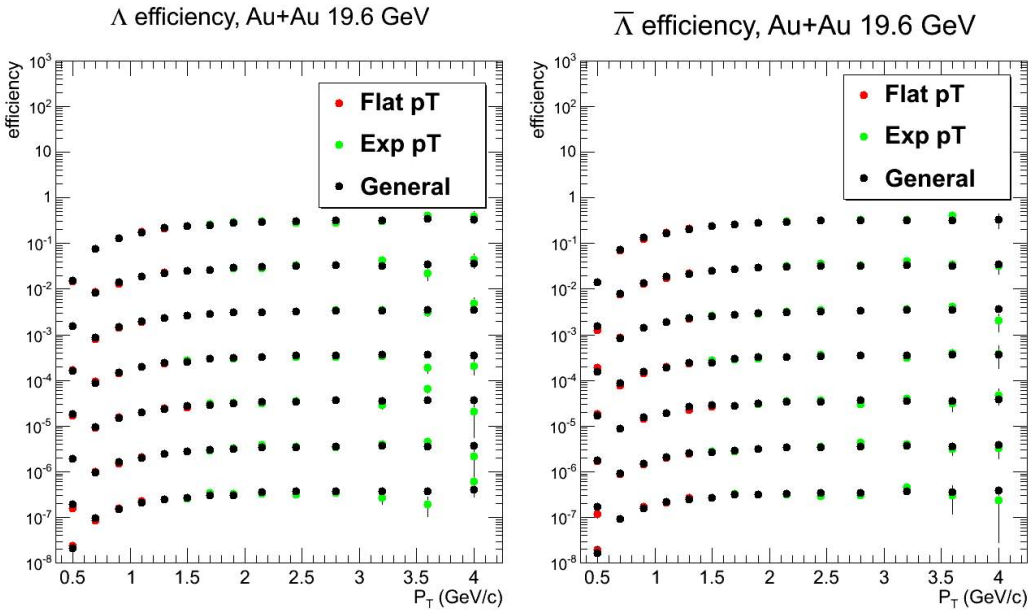

Figure 4.22: Λ and $\bar{\Lambda}$ efficiencies as a function of p_T at Au+Au 19.6 GeV. From up to down, the data points are the efficiencies at 0-5%, 5-10%$\times 10^{-1}$, 10-20%$\times 10^{-2}$, 20-30%$\times 10^{-3}$, 30-40%$\times 10^{-4}$, 40-60%$\times 10^{-5}$, and 60-80%$\times 10^{-6}$.

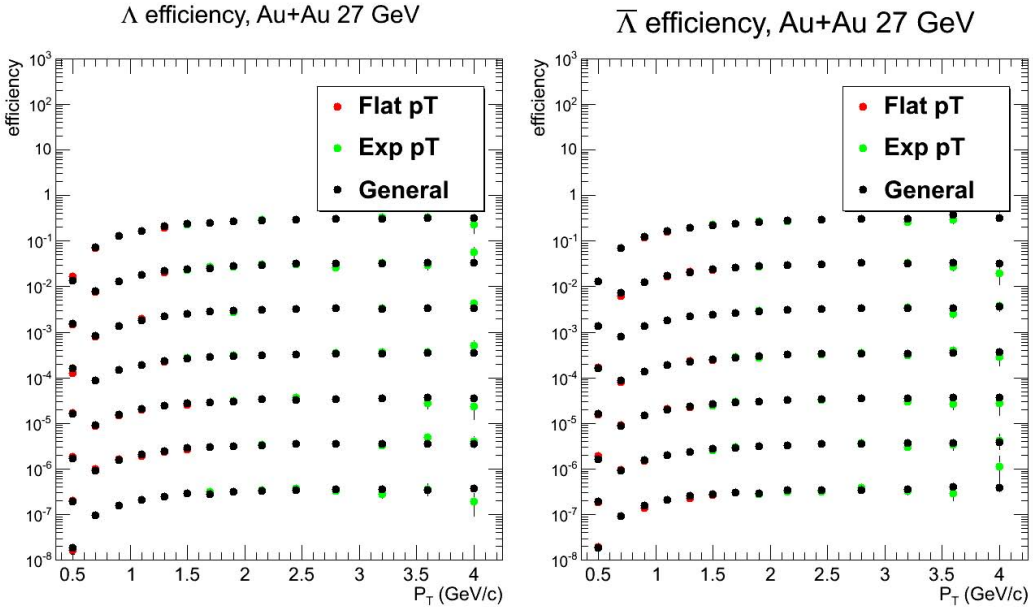

Figure 4.23: Λ and $\bar{\Lambda}$ efficiencies as a function of p_T at Au+Au 27 GeV. From up to down, the data points are the efficiencies at 0-5%, 5-10%$\times 10^{-1}$, 10-20%$\times 10^{-2}$, 20-30%$\times 10^{-3}$, 30-40%$\times 10^{-4}$, 40-60%$\times 10^{-5}$, and 60-80%$\times 10^{-6}$.

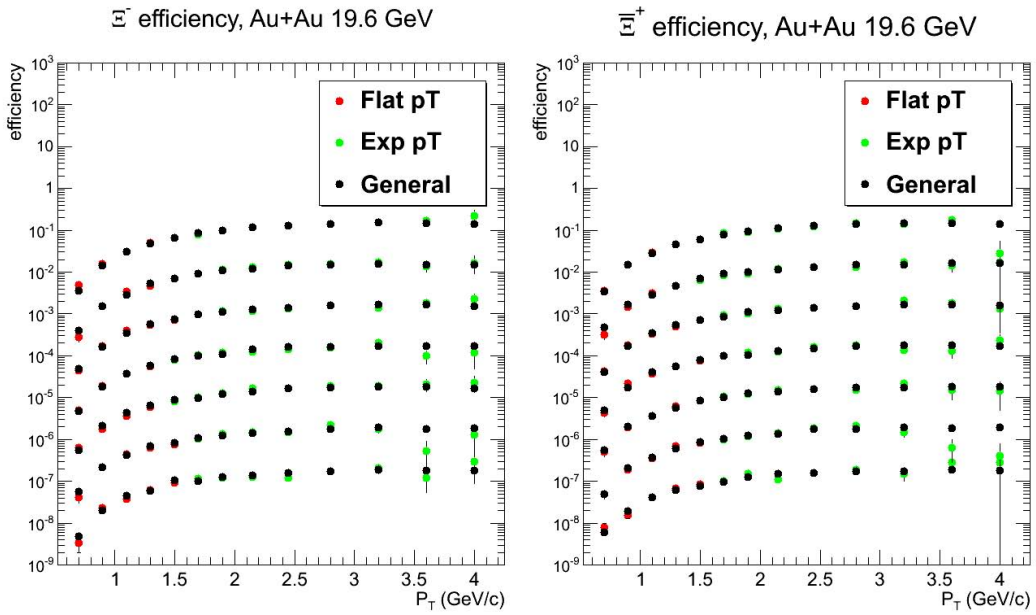

Figure 4.24: Ξ^- and $\bar{\Xi}^+$ efficiencies as a function of p_T at Au+Au 19.6 GeV. From up to down, the data points are the efficiencies at 0-5%, 5-10%$\times 10^{-1}$, 10-20%$\times 10^{-2}$, 20-30%$\times 10^{-3}$, 30-40%$\times 10^{-4}$, 40-60%$\times 10^{-5}$, and 60-80%$\times 10^{-6}$.

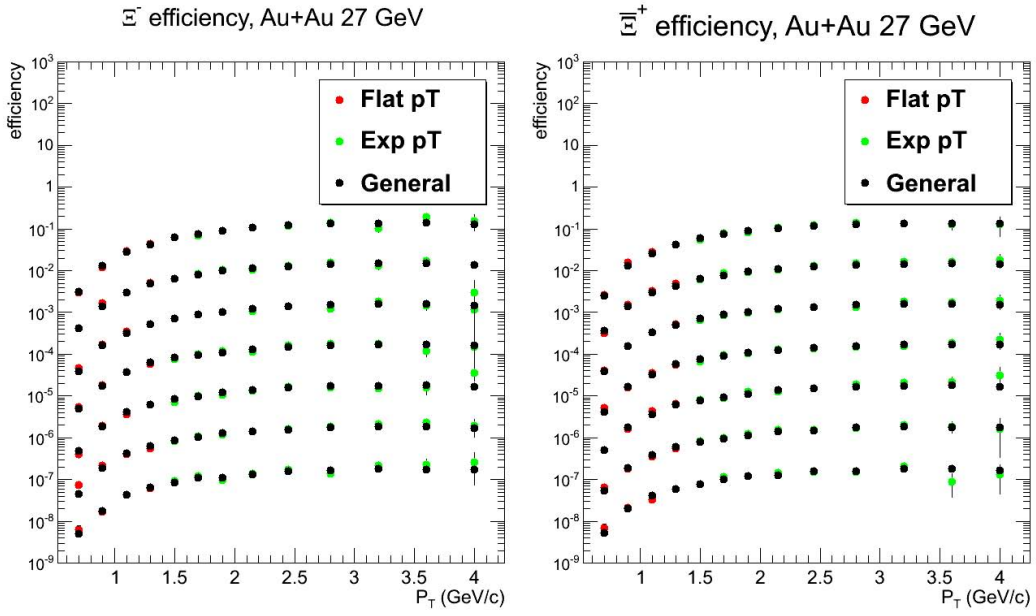

Figure 4.25: Ξ^- and $\bar{\Xi}^+$ efficiencies as a function of p_T at Au+Au 27 GeV. From up to down, the data points are the efficiencies at 0-5%, 5-10%$\times 10^{-1}$, 10-20%$\times 10^{-2}$, 20-30%$\times 10^{-3}$, 30-40%$\times 10^{-4}$, 40-60%$\times 10^{-5}$, and 60-80%$\times 10^{-6}$.

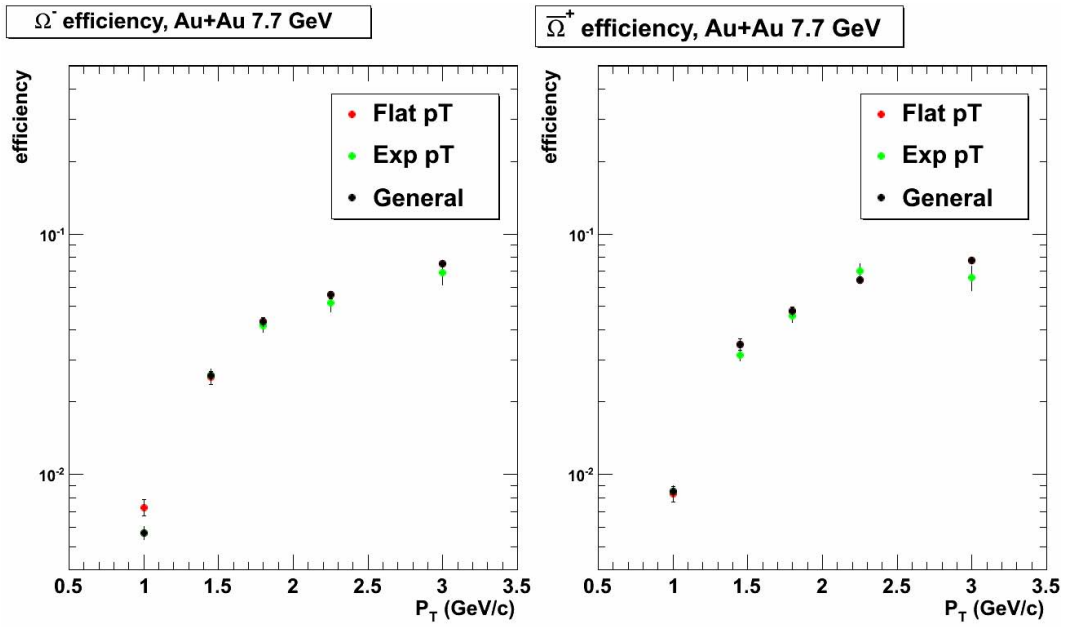

Figure 4.26: Ω^- and $\bar{\Omega}^+$ efficiencies as a function of p_T at Au+Au 7.7 GeV 0-60% centrality.

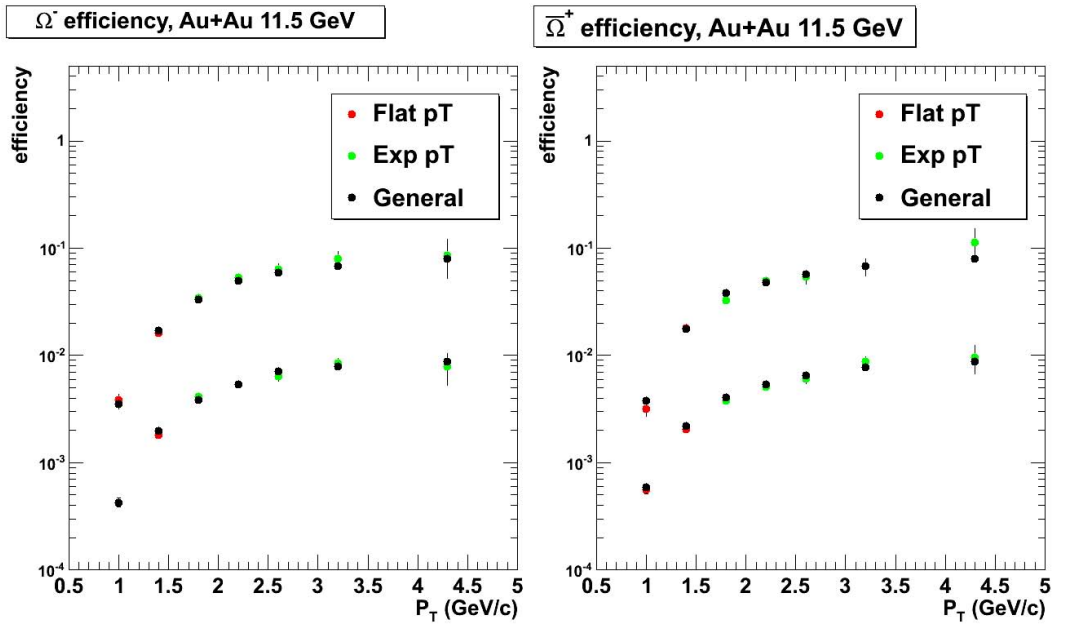

Figure 4.27: Ω^- and $\bar{\Omega}^+$ efficiencies as a function of p_T at Au+Au 11.5 GeV. From up to down, the data points are the efficiencies at 0-10% and 10-60%$\times 10^{-1}$.

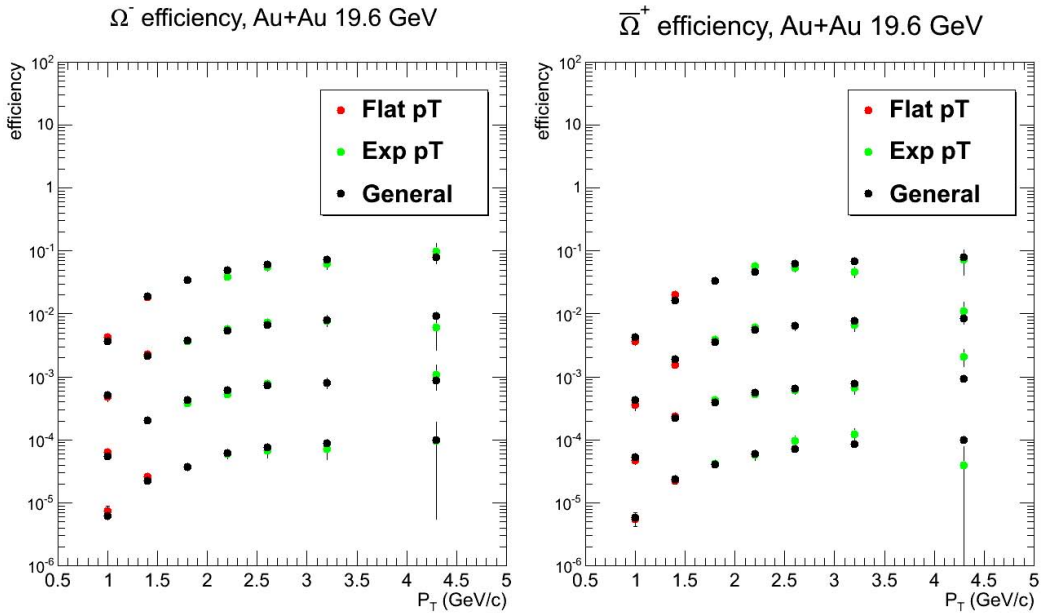

Figure 4.28: Ω^- and $\bar{\Omega}^+$ efficiencies as a function of p_T at Au+Au 19.6 GeV. From up to down, the data points are the efficiencies at 0-10%, 10-20%$\times 10^{-1}$, 20-40%$\times 10^{-2}$, and 40-60%$\times 10^{-3}$.

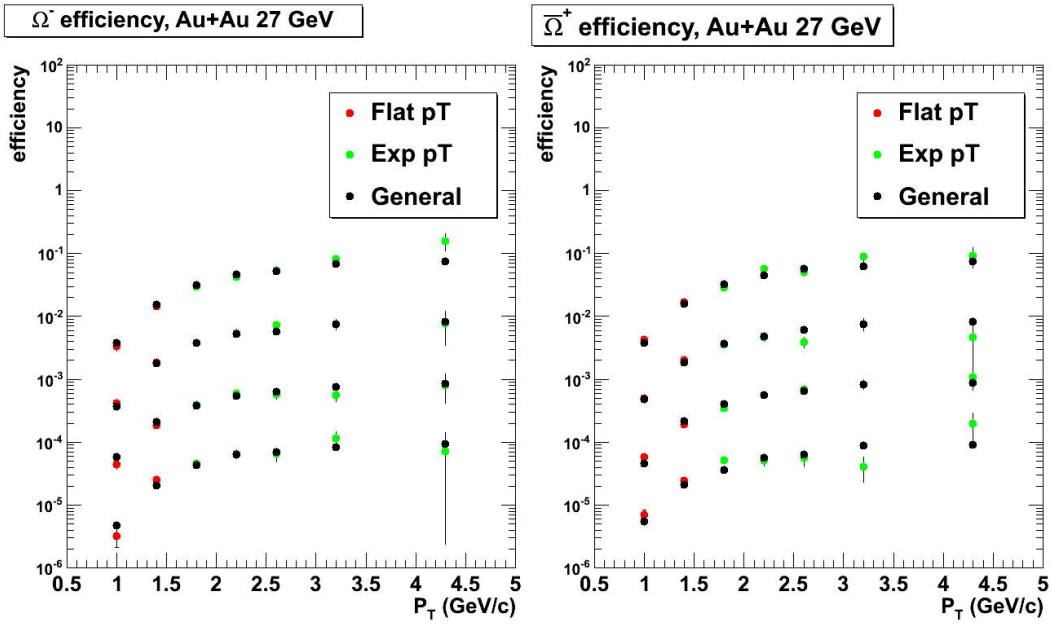

Figure 4.29: Ω^- and $\bar{\Omega}^+$ efficiencies as a function of p_T at Au+Au 27 GeV. From up to down, the data points are the efficiencies at 0-10%, 10-20%$\times 10^{-1}$, 20-40%$\times 10^{-2}$, and 40-60%$\times 10^{-3}$.

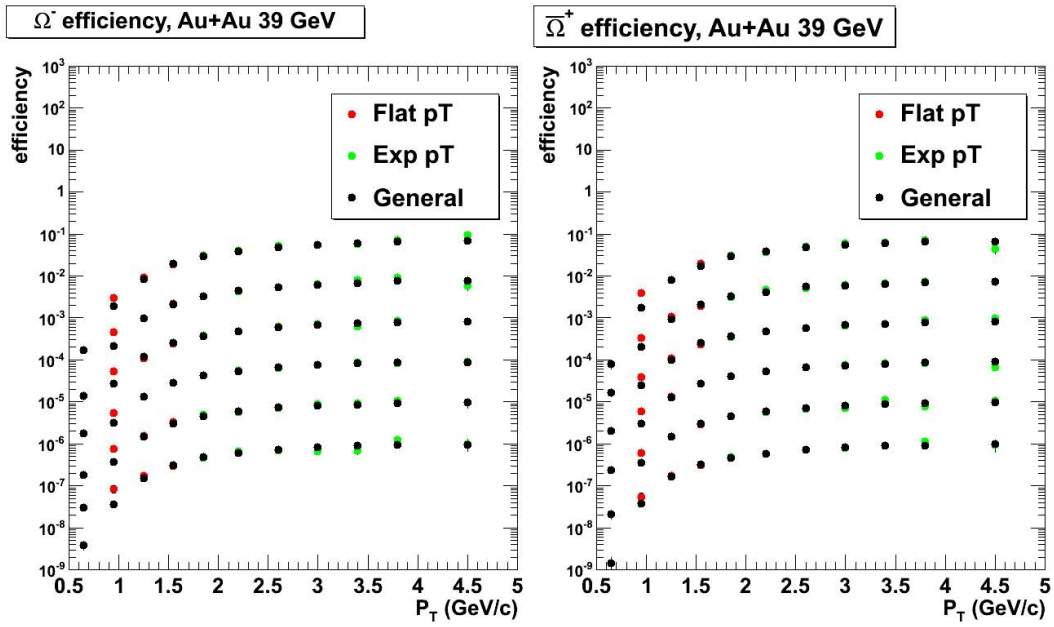

Figure 4.30: Ω^- and $\bar{\Omega}^+$ efficiencies as a function of p_T at Au+Au 39 GeV. From up to down, the data points are the efficiencies at 0-5%, 5-10%$\times 10^{-1}$, 10-20%$\times 10^{-2}$, 20-40%$\times 10^{-3}$, 40-60%$\times 10^{-4}$, and 60-80%$\times 10^{-5}$.

we can get the raw Λ counts from the Ξ feed-down in i-th p_T bin in a specific centrality with the formula:

$$\Lambda^i_\Xi = (\frac{dN}{dy})_\Xi \cdot \frac{N^i_\Lambda}{N_\Xi} \tag{4.3.6}$$

where $(\frac{dN}{dy})_\Xi$ is the Ξ integrated yield, N^i_Λ is the counts of Λ in i-th p_T bin and N_Ξ is the total counts of input Ξs with the weight of real Ξ p_T spectra, over the whole p_T range in the same rapidity, centrality as for the reconstructed Λs. The dN/dy of $\Xi^0(\bar{\Xi}^0)$ cannot be measured, but it is assumed to be the same as the dN/dy of $\Xi^-(\bar{\Xi}^+)$. The corrected Λ counts in i-th p_T bin is

$$\Lambda^i = \frac{\Lambda^i_{inclusive} - \Lambda^i_{\Xi^-} - \Lambda^i_{\Xi^0}}{\eta_\Lambda} \tag{4.3.7}$$

where $\Lambda^i_{inclusive}$ is the inclusive Λ raw counts, $\Lambda^i_{\Xi^-}$ and $\Lambda^i_{\Xi^0}$ are the feed-down

Λ from Ξ^- and Ξ^0 respectively, and η_Λ is the efficiency for Λ in that p_T bin. The formula for $\bar{\Lambda}$ is the same by changing the particles in the formula to their anti-particles.

It is impossible to estimate the feed-down contribution from Σ^0 and other resonance particles that decay at the primary vertex. So the feed-down correction here only excludes the $\Lambda(\bar{\Lambda})$ particles from weak decays of (anti-)multi-strange hyperons.

4.4 Systematic Uncertainty

The systematic uncertainties come from various sources: time-varying experimental running status, detector response, analysis methods and cuts used, etc. In this analysis, we focus on the systematic uncertainties due to the analysis method and cuts. We analyze three parts of the systematic uncertainties, which are: the signal extraction uncertainty, efficiency correction uncertainty, and unmeasured p_T range in dN/dy measurement.

The signal extraction uncertainty is related to the background level. If there is no background, there will be no uncertainty. We study the dependence of yield on the invariant mass range used to fit the background. The uncertainty of the yield is evaluated by comparing the raw yields with default mass range and other mass ranges. We change the mass range wider and narrower, and choose the larger relative difference as the systematic uncertainty for that bin.

The uncertainty of efficiency correction is due to the mismatch between the experiment data and the embedding simulation data. When we apply topological cuts to reconstruct the strange particle signal, there is a reconstruction efficiency. And the embedding simulation data are used to study the efficiency. If the embedding data completely describe the detector response, each cut parameter distribution from real particles should have the same shape as that from MC

particles in the embedding data, and there will be not systematic uncertainty. We separate all the cuts to several groups: the number of track hits, the DCA of decay daughter to the primary vertex, the DCA of reconstructed strange particle to the primary vertex, the DCA between the two decay daughters, the decay lengths of strange particles, and the $\Lambda(\bar{\Lambda})$ invariant mass window in $\Xi^-(\bar{\Xi}^+)$ and $\Omega^-(\bar{\Omega}^+)$ reconstruction. For each group, we vary the cuts in the real data and embedding data simultaneously, and get the corrected spectra with the new cuts. We compare the results with new cuts and the default cuts, and choose the larger relative difference as the uncertainty. We sum the uncertainties from different groups of cuts and from signal extraction quadratically, and take it as the overall uncertainty of that bin.

The integrated dN/dy sums the yield from each p_T bin. In the low p_T region, the strange particles cannot be measured well due to the low reconstruction efficiency. However, there is a sizable contribution to the dN/dy from the low p_T region. Some functions are used to estimate the yield of low p_T region, by fitting the p_T spectra and integrating the function over the unmeasured p_T region. We use Levy function as the default fitting function, and Boltzmann function and exponential function for comparison, to fit the p_T spectra and get dN/dy of unmeasured p_T region. We use the value from Levy function as the default value, and the larger difference between default value and values from Boltzmann function and exponential function as the systematic error.

The Levy function is:

$$(\frac{dN}{dy}) \cdot \frac{(a-1)(a-2)}{2\pi a \cdot T(a \cdot T + m(a-2))} \cdot (1 + \frac{\sqrt{p_T^2 + m^2} - m}{a \cdot T})^a \tag{4.4.8}$$

The Boltzmann function is:

$$(\frac{dN}{dy}) \cdot \frac{\sqrt{p_T^2 + m^2}}{2\pi T(m^2 + 2m \cdot T + 2T^2)} \cdot e^{-\frac{\sqrt{p_T^2+m^2}-m}{T}} \tag{4.4.9}$$

The exponential function is:

$$(\frac{dN}{dy}) \cdot \frac{m+T}{2\pi T} \cdot e^{-\frac{\sqrt{p_T^2+m^2}-m}{T}} \tag{4.4.10}$$

where dN/dy, T, and a are fitting parameters, m is the invariant mass of the particle.

4.5 Results

In the section, we present the main results for the production of the strange hadrons, K^0_S, $\Lambda(\bar{\Lambda})$, $\Xi^-(\bar{\Xi}^+)$, and $\Omega^-(\bar{\Omega}^+)$ in Au+Au collisions at 7.7, 11.5, 19.6, 27, and 39 GeV.

4.5.1 Transverse Momentum Spectra

The corrected p_T spectra are obtained by the raw spectra divided by the efficiency at each p_T and centrality bin. Figure 4.31 to Figure 4.35 show the K^0_S, Λ, $\bar{\Lambda}$, Ξ^-, and $\bar{\Xi}^+$ spectra in Au+Au collisions at 19.6 and 27 GeV. Figure 4.36 to Figure 4.40 show the Ω^- and $\bar{\Omega}^+$ spectra in Au+Au collisions at 7.7, 11.5, 19.6, 27, and 39 GeV. The blue curves are the Levy functions which fit the p_T spectra. The p_T spectra have been used for other analysis, such as the dN/dy, nuclear modification factor R_{CP}, particle ratios, etc.

4.5.2 Integrated Yield dN/dy

The integrated dN/dy sums up yields from measured p_T bins, and uses fitting functions to estimate the contribution from the unmeasured p_T range. Levy function is used as the default fitting function. Boltzmann function and exponential function are used to estimate the systematic uncertainty. Figure 4.41 shows the dN/dy at mid-rapidity for Λ, $\bar{\Lambda}$, Ξ^- and $\bar{\Xi}^+$ from the most central (0-5%) Au+Au

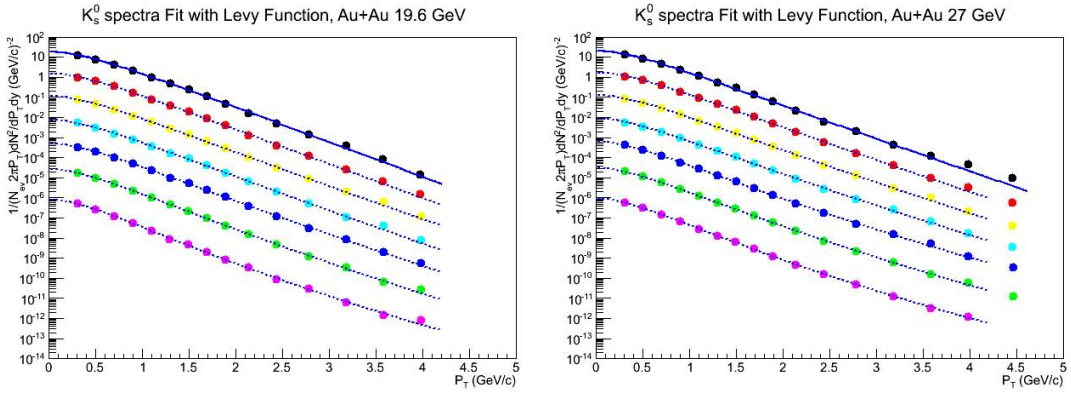

Figure 4.31: K^0_S p_T spectra at Au+Au 19.6 and 27 GeV. From up to down, the data points are the p_T spectra at 0-5%, 5-10%$\times 10^{-1}$, 10-20%$\times 10^{-2}$, 20-30%$\times 10^{-3}$, 30-40%$\times 10^{-4}$, 40-60%$\times 10^{-5}$, and 60-80%$\times 10^{-6}$.

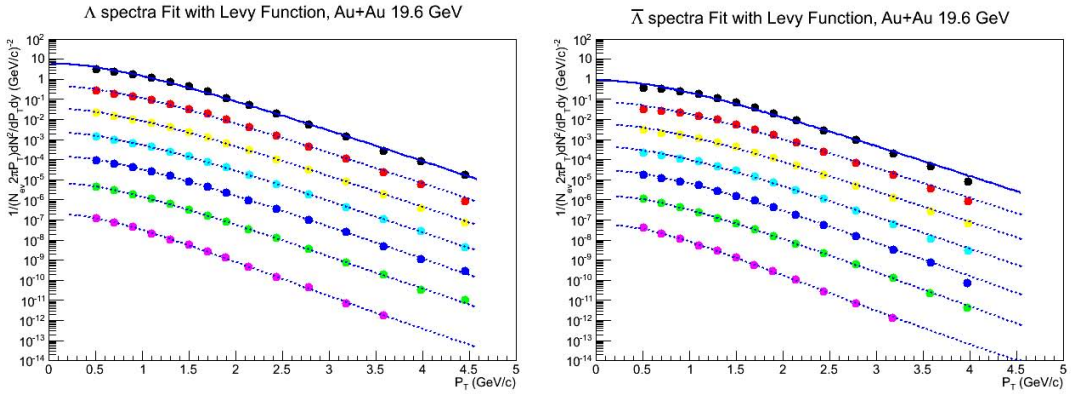

Figure 4.32: Λ and $\bar{\Lambda}$ p_T spectra at Au+Au 19.6 GeV. From up to down, the data points are the p_T spectra at 0-5%, 5-10%$\times 10^{-1}$, 10-20%$\times 10^{-2}$, 20-30%$\times 10^{-3}$, 30-40%$\times 10^{-4}$, 40-60%$\times 10^{-5}$, and 60-80%$\times 10^{-6}$.

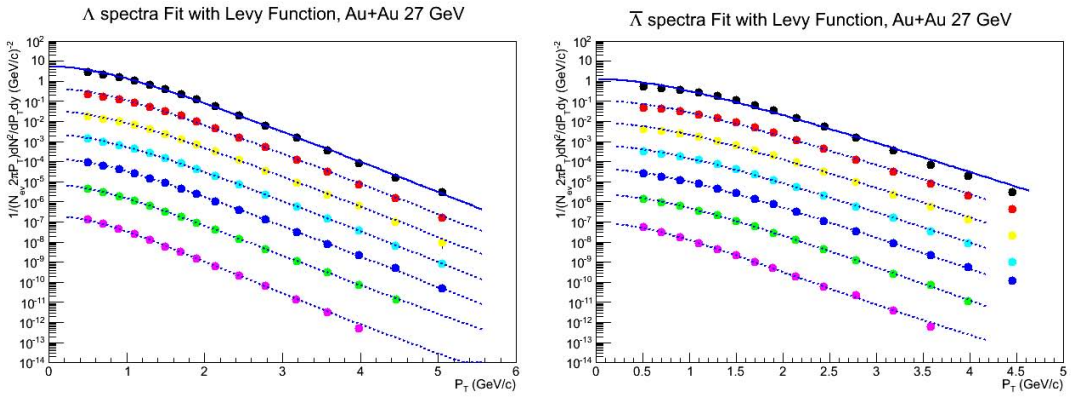

Figure 4.33: Λ and $\bar{\Lambda}$ p_T spectra at Au+Au 27 GeV. From up to down, the data points are the p_T spectra at 0-5%, 5-10%$\times 10^{-1}$, 10-20%$\times 10^{-2}$, 20-30%$\times 10^{-3}$, 30-40%$\times 10^{-4}$, 40-60%$\times 10^{-5}$, and 60-80%$\times 10^{-6}$.

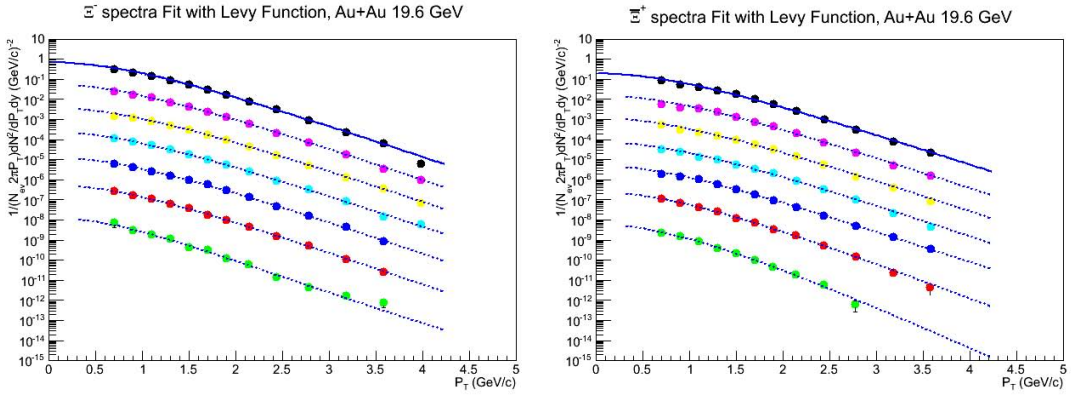

Figure 4.34: Ξ^- and $\bar{\Xi}^+$ p_T spectra at Au+Au 19.6 GeV. From up to down, the data points are the p_T spectra at 0-5%, 5-10%$\times 10^{-1}$, 10-20%$\times 10^{-2}$, 20-30%$\times 10^{-3}$, 30-40%$\times 10^{-4}$, 40-60%$\times 10^{-5}$, and 60-80%$\times 10^{-6}$.

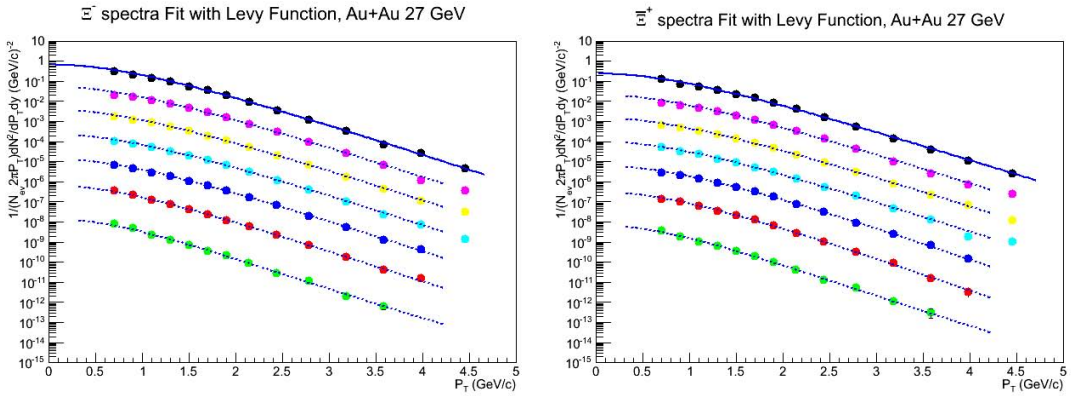

Figure 4.35: Ξ^- and $\bar{\Xi}^+$ p_T spectra at Au+Au 27 GeV. From up to down, the data points are the p_T spectra at 0-5%, 5-10%$\times 10^{-1}$, 10-20%$\times 10^{-2}$, 20-30%$\times 10^{-3}$, 30-40%$\times 10^{-4}$, 40-60%$\times 10^{-5}$, and 60-80%$\times 10^{-6}$.

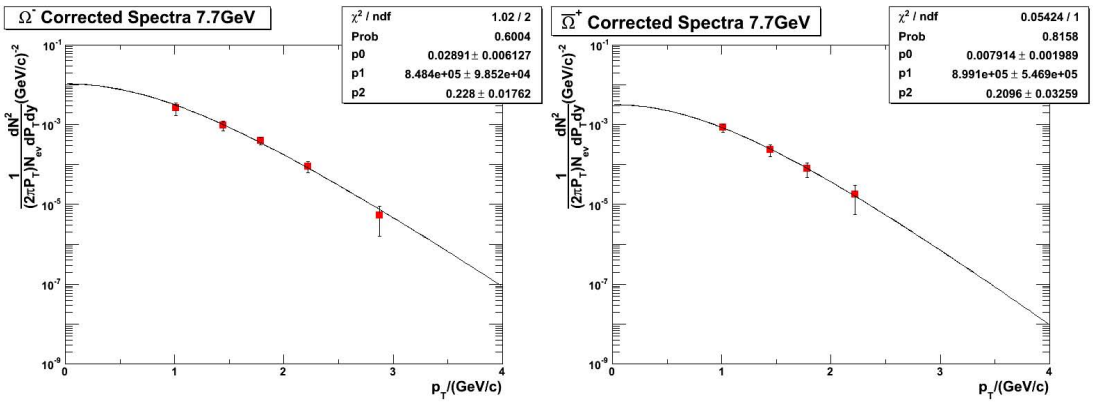

Figure 4.36: Ω^- and $\bar{\Omega}^+$ p_T spectra at Au+Au 7.7 GeV 0-60% centrality.

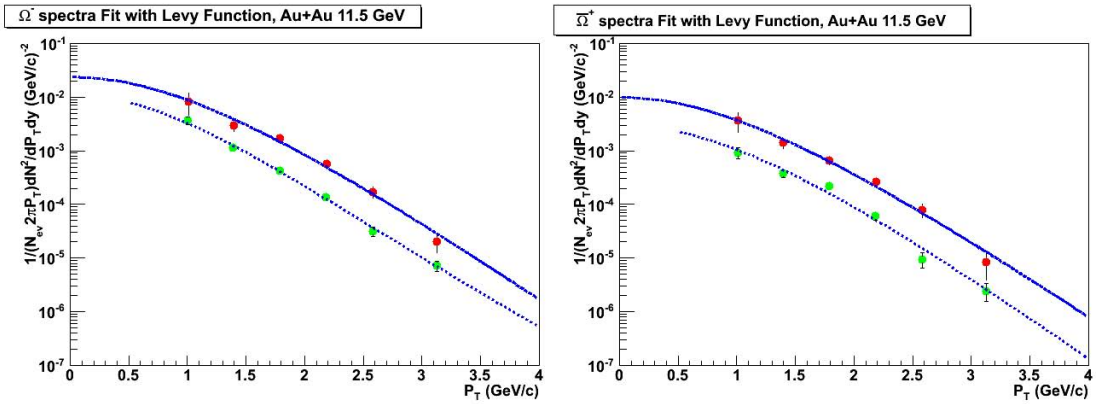

Figure 4.37: Ω^- and $\bar{\Omega}^+$ p_T spectra at Au+Au 11.5 GeV. From up to down, the data points are the p_T spectra at 0-10% and 10-60%$\times 10^{-1}$.

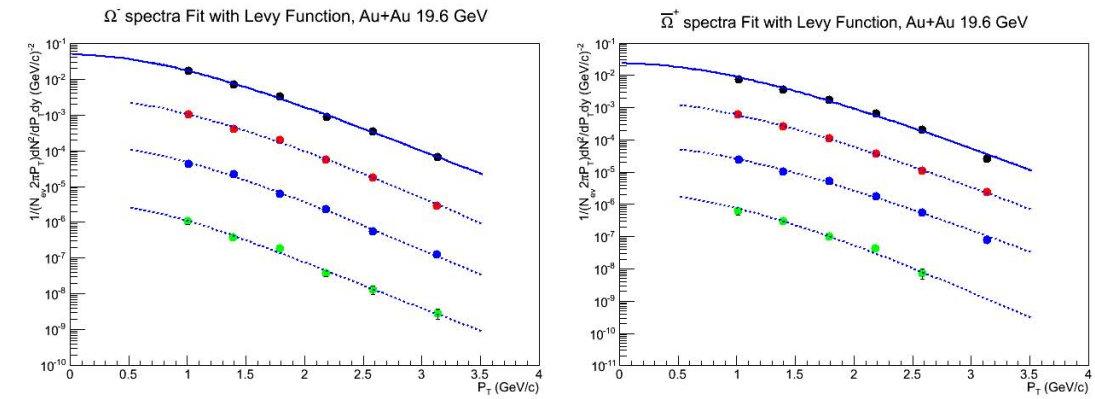

Figure 4.38: Ω^- and $\bar{\Omega}^+$ p_T spectra at Au+Au 19.6 GeV. From up to down, the data points are the p_T spectra at 0-10%, 10-20%$\times 10^{-1}$, 20-40%$\times 10^{-2}$, and 40-60%$\times 10^{-3}$.

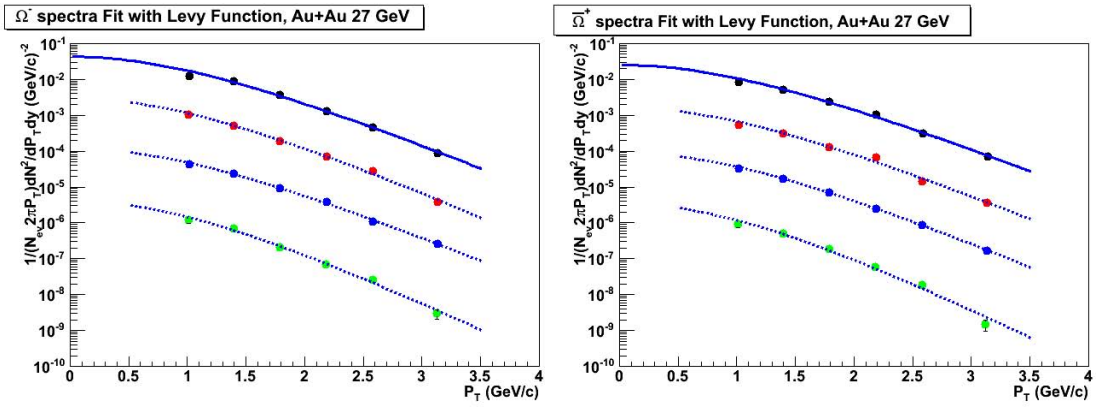

Figure 4.39: Ω^- and $\bar{\Omega}^+$ p_T spectra at Au+Au 27 GeV. From up to down, the data points are the p_T spectra at 0-10%, 10-20%$\times 10^{-1}$, 20-40%$\times 10^{-2}$, and 40-60%$\times 10^{-3}$.

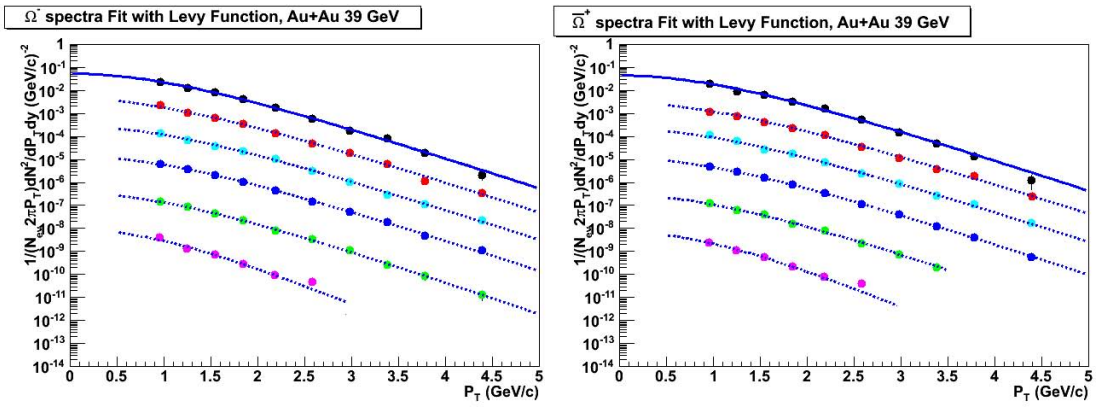

Figure 4.40: Ω^- and $\bar{\Omega}^+$ p_T spectra at Au+Au 39 GeV. From up to down, the data points are the p_T spectra at 0-5%, 5-10%$\times 10^{-1}$, 10-20%$\times 10^{-2}$, 20-40%$\times 10^{-3}$, 40-60%$\times 10^{-4}$, and 60-80%$\times 10^{-5}$.

collisions from the STAR BES program, compared with NA49 [42], NA57 [41], and STAR high energy data [31][32][45][46]. The dN/dy data are scaled by the number of participants (N_{part}, named number of wounded nucleons N_w in NA49 and NA57). The yields of anti-baryons ($\bar{\Lambda}$, $\bar{\Xi}^+$) increase monotonically with increasing beam energy; Λ yields decrease with increasing beam energy at low energies and increase again from 39 GeV to higher energies; while the Ξ^- yields almost remain the same from 11.5 to 62.4 GeV. At low energy, the Λ production in enhanced due to the large baryon stopping at mid-rapidity. This effect decreases with increasing beam energy. On the other hand, the QGP dominates the particle production at high energies, and decrease with decreasing beam energy. At intermediate energies, the interplay of both effects may result in a dip in the Λ yield as a function of beam energy.

4.5.3 Nuclear Modification Factor R_{CP}

The R_{CP} is calculated as the ratio of particle yields from central collisions to yields from peripheral collisions scaled by the number of inelastic binary collisions (N_{bin}). Previous measurements showed that the nuclear modification factors (R_{CP}) of baryons and mesons at intermediate p_T follow different trends, in RHIC Au+Au 200 GeV collisions. At high p_T, the R_{CP} is much less than unity. Figure 4.42 shows the R_{CP} for K^0_S, $\Lambda(\bar{\Lambda})$, $\Xi^-(\bar{\Xi}^+)$, $\Omega^-(\bar{\Omega}^+)$ as a function of p_T from Au+Au collisions at beam energies from 7.7 to 39 GeV. The strange baryon R_{CP} has a similar behavior at 19.6, 27, and 39 GeV. Although the baryon/meson separation is not as significant as that at 200 GeV, there seems to be a difference between K^0_S R_{CP} and strange baryon R_{CP}. At lower energies (7.7 and 11.5 GeV), the R_{CP} for K^0_S, Λ, Ξ^- all increase with p_T. We also compare the R_{CP} for K^0_S at different energies in Figure 4.43. The K^0_S R_{CP} increases with decreasing beam energy from 62.4 to 7.7 GeV, and the R_{CP} with a p_T above 2 GeV/c is below or consistent with unity at 19.6, 27, and 39 GeV, however it is greater than unity at 7.7 and

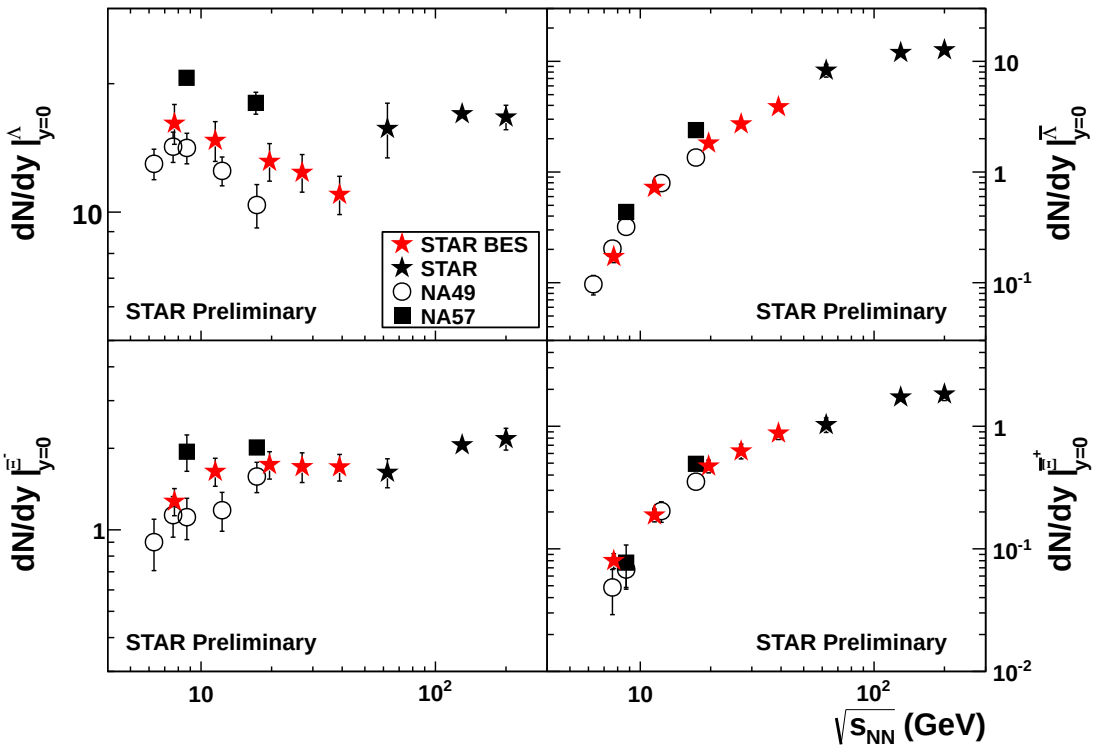

Figure 4.41: The strange baryon dN/dy at mid-rapidity in most central collisions. The upper left plot is Λ, the upper right plot is $\bar{\Lambda}$, the lower left plot is Ξ^-, and the lower right plot is $\bar{\Xi}^+$. The rapidity ranges are $|y| < 0.5$ for STAR and NA57, $|y| < 0.4$ for NA49 $\Lambda(\bar{\Lambda})$ and $|y| < 0.5$ for NA49 $\Xi^-(\bar{\Xi}^+)$. The centrality bins are 0-5% for STAR, 0-7% for NA49 6.3 to 12.3 GeV and 0-10% for NA49 17.3 GeV, and 0-10% for NA57.

11.5 GeV. The change of R_{CP} behavior indicates that the partonic energy loss effect does not play a prominent role at low energies, while the cold nuclear effect (Cronin effect) [53] begins to take over.

4.5.4 Λ/K^0_S Ratios

In the low energy, the Λ production is enhanced due to the large net-baryon density at mid-rapidity. Therefore, it is suggested to study the $\bar{\Lambda}/K^0_S$ ratios instead of Λ/K^0_S to make a comparison with baryon enhancement observed at higher energies. Figure 4.44 shows the $\bar{\Lambda}/K^0_S$ ratios for different centralities from 7.7 to 39 GeV. There is an enhancement of $\bar{\Lambda}/K^0_S$ ratios at p_T around 3 GeV/c at 19.6, 27, and 39 GeV. And there is a strong centrality dependence of $\bar{\Lambda}/K^0_S$ ratios at these three energies, the ratios can reach a maximum value of unity in the most central collisions, while in the peripheral collisions, the maximum value is less than 0.5. It shows that there is baryon enhancement at intermediate p_T at 19.6, 27, and 39 GeV, which is similar to that observed at higher energies. At 7.7 and 11.5 GeV, $\bar{\Lambda}/K^0_S$ ratios increase monotonically with increasing p_T, and the $\bar{\Lambda}/K^0_S$ ratios have a weaker centrality dependency than these at higher collision energies.

4.5.5 Anti-Baryon to Baryon Ratios

The anti-baryon to baryon ratios from STAR [31][32][44][45][46] and NA49 [42][43][54] data are shown in Figure 4.45. The STAR BES data and the NA49 data are consistent with each other.

In the statistical thermal model, particle yields can be described by invariant mass, degeneracy factor and chemical potential (μ) of each particle type, strangeness-suppression factor (γ_S), and chemical freeze-out temperature (T), which has been discussed in Section 4.1.3. When we take the anti-baryon to baryon ratios, the parameters are cancelled except μ_B/T and μ_S/T:

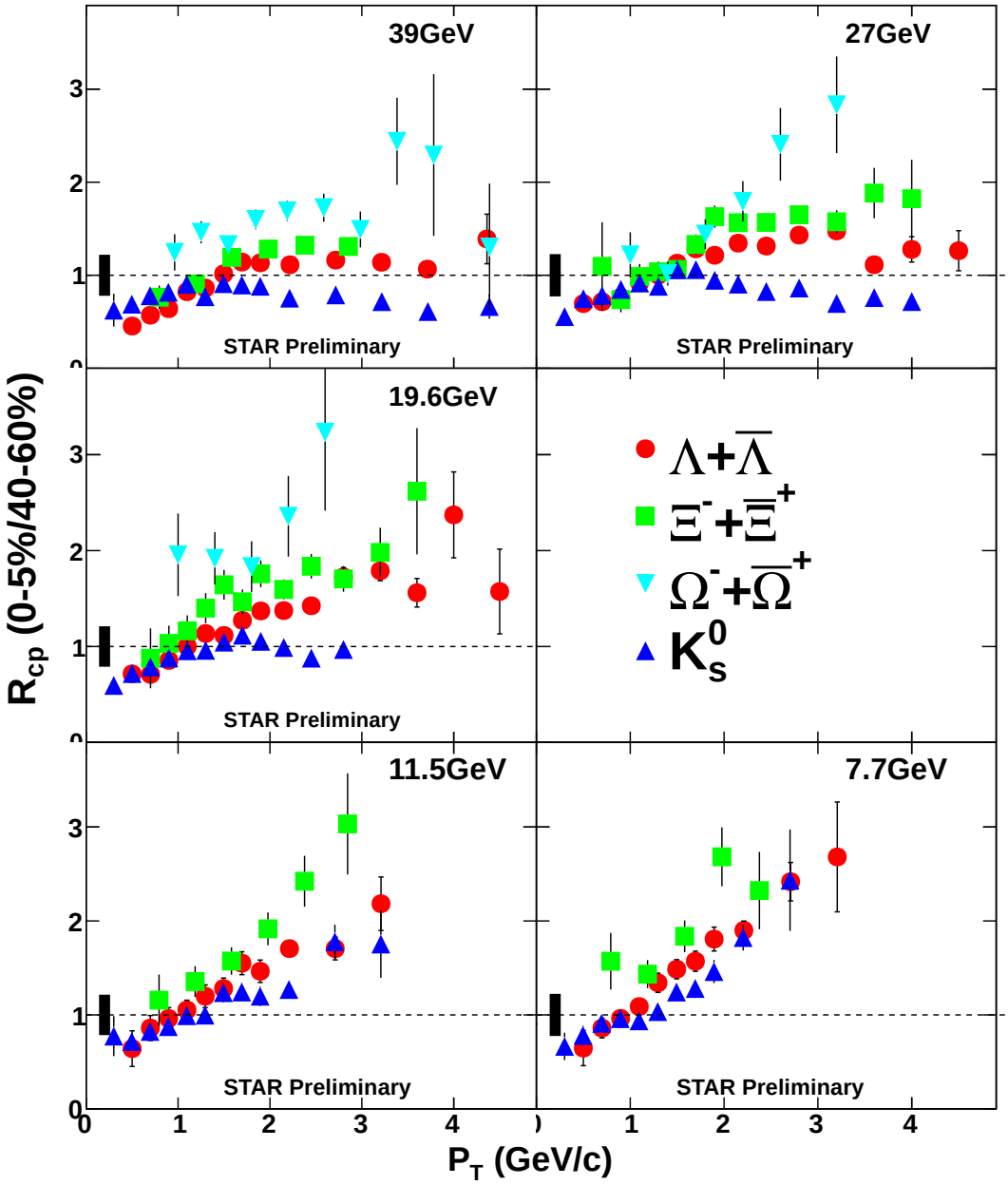

Figure 4.42: The nuclear modification factor (R_{CP}), as a function of p_T for K^0_S, $\Lambda(\bar{\Lambda})$, $\Xi^-(\bar{\Xi}^+)$, and $\Omega^-(\bar{\Omega}^+)$ at $|y| <$ 0.5 from Au+Au collisions at $\sqrt{s_{NN}}$ from 39 to 7.7 GeV.

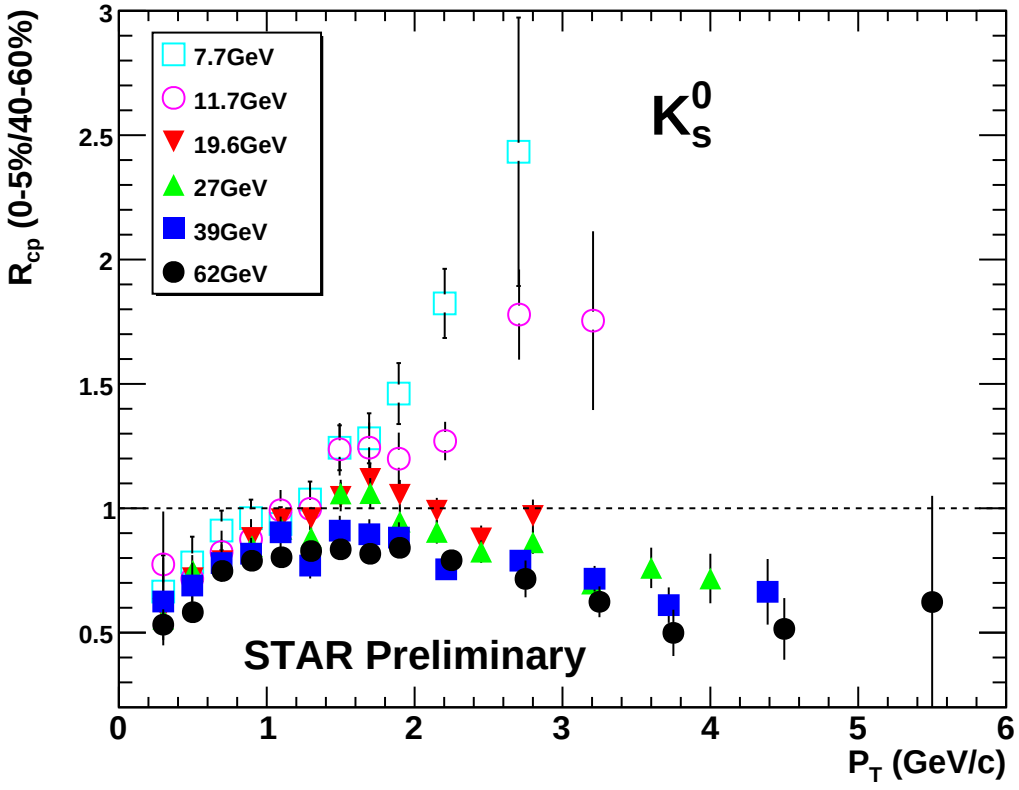

Figure 4.43: The R_{CP} of K^0_S as a function of p_T from Au+Au collisions at $\sqrt{s_{NN}}$ from 7.7 to 62.4 GeV.

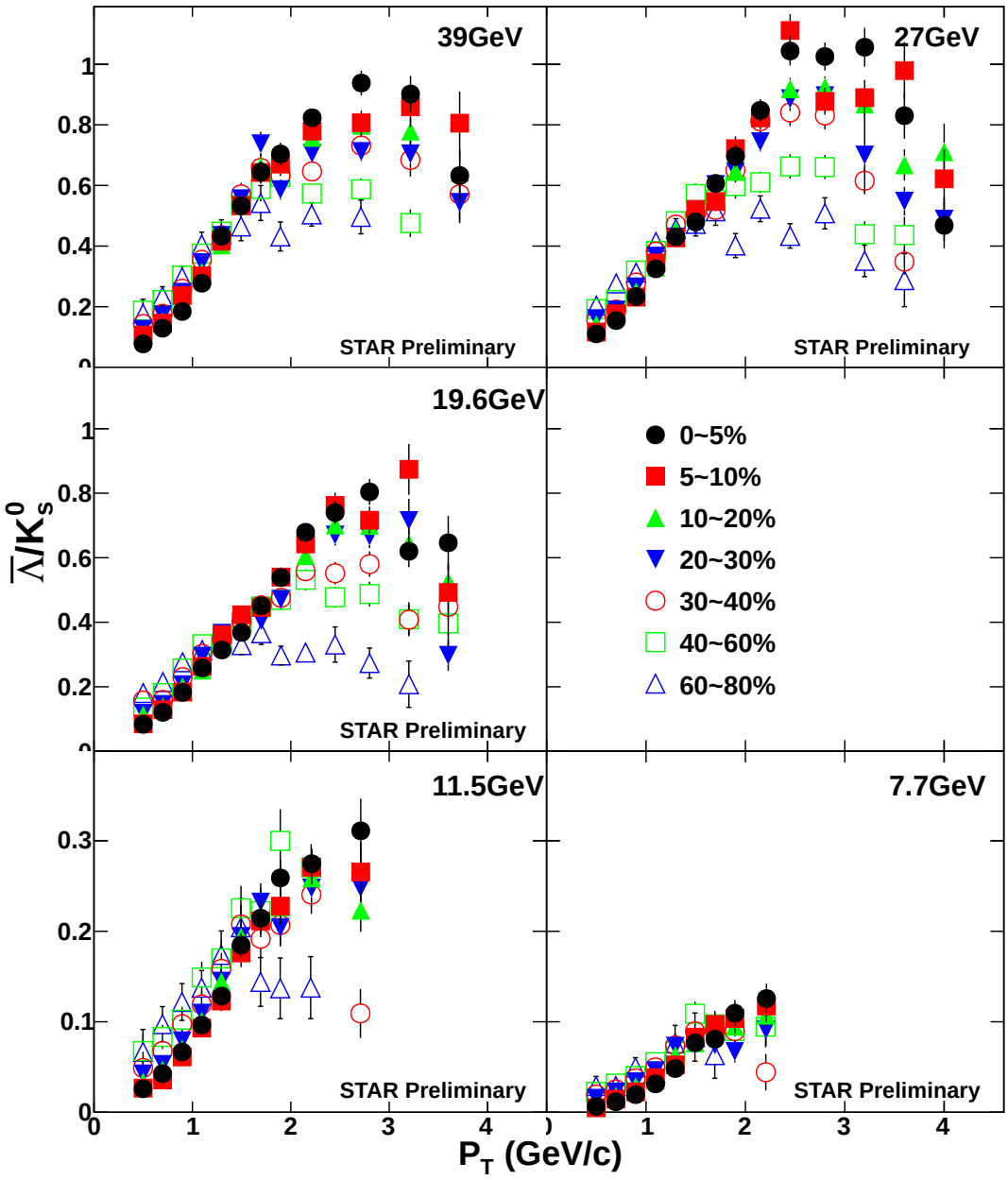

Figure 4.44: The $\bar{\Lambda}/K^0_S$ ratios as a function of p_T within $|y| < 0.5$ from Au+Au collisions at $\sqrt{s_{NN}}$ from 39 to 7.7 GeV.

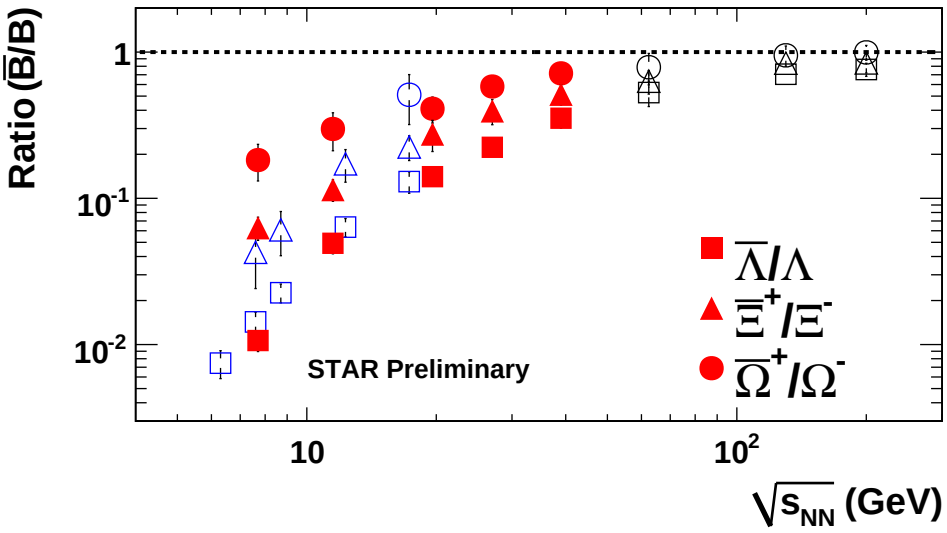

Figure 4.45: The anti-baryon to baryon ratios as a function of $\sqrt{S_{NN}}$ for most central Au+Au collisions from STAR and for Pb+Pb collisions from NA49. Solid symbols are STAR BES data, open symbols are STAR higher energies (greater than 62.4 GeV) data and NA49 data.

$$\ln(ratio) = -2\frac{\mu_B}{T} + \frac{\mu_S}{T}\Delta S \tag{4.5.11}$$

where μ_B is the baryon chemical potential, and μ_S is the strangeness chemical potential. The ΔS in the formula is the strangeness-number difference between baryon and anti-baryon. The above formula describes, for each particle type, a straight line described by the parameters $\frac{\mu_B}{T}$ and $\frac{\mu_S}{T}$. The $\frac{\mu_B}{T}$ and $\frac{\mu_S}{T}$ are the properties of the collision system, independent of the particle type. When we draw the $\ln(ratio)$ of $\frac{\bar{\Lambda}}{\Lambda}$, $\frac{\bar{\Xi}^+}{\Xi^-}$, and $\frac{\bar{\Omega}^+}{\Omega^-}$ in one plot, with $\frac{\mu_B}{T}$ on the x-axis and $\frac{\mu_S}{T}$ on the y-axis, the three lines should cross at one point, if the statistical thermal model assumptions are valid. With this method, we can test the statistical thermal model. The 7.7, 11.5, 19.6, 27, and 39 GeV results are shown in Figure 4.46, and the statistical thermal model seems to describe the data well.

When we draw the $\ln(ratio)$ of $\frac{\bar{\Lambda}}{\Lambda}$, $\frac{\bar{\Xi}^+}{\Xi^-}$, and $\frac{\bar{\Omega}^+}{\Omega^-}$ in one plot for each energy, with

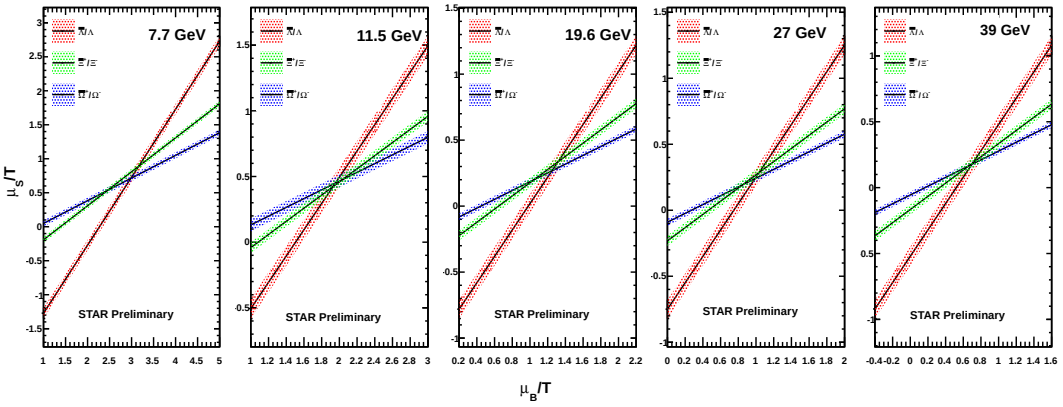

Figure 4.46: Testing of statistical thermal model in $\frac{\mu_B}{T}$ and $\frac{\mu_S}{T}$ parameter space with strange anti-baryon to baryon ratios in 7.7, 11.5, 19.6, 27, and 39 GeV Au+Au central collisions. The shadow of each line is the statistical error.

ΔS on the x-axis and ln($ratio$) on the y-axis, the three ratios should fall in one line. For each collision energy, we can use linear function to fit the three points with $\frac{\mu_B}{T}$ and $\frac{\mu_S}{T}$ as the fitting parameters. Figure 4.47 shows the fitting results. The $\frac{\mu_B}{T}$ and $\frac{\mu_S}{T}$ from 7.7 to 39 GeV are shown in Figure 4.48, and the $\frac{\mu_B}{T}$ values fall on the curve of parameterization with μ_B and T fitting of AGS, SPS, and RHIC 130 GeV central collision data [55].

The strangeness chemical potential μ_S is a function on μ_B and T. In a relatively small μ_B and T range, μ_S has a good linear relationship with μ_B. Figure 4.49 shows the $\frac{\mu_S}{T}$ vs. $\frac{\mu_B}{T}$. We use a linear function to fit the points of $\frac{\mu_S}{T}$ and $\frac{\mu_B}{T}$ at 39 GeV to 7.7 GeV, and get $\frac{\mu_S}{T} = 0.2412 \times \frac{\mu_S}{T}$. After we get the function and parameters to describe μ_S, we can check whether the fitting functions and parameters can describe the anti-baryon to baryon ratios well. In Figure 4.50 left panel, both $\frac{\mu_B}{T}$ and $\frac{\mu_S}{T}$ values fall on the curve of parameterization; and in the right panel, the curves of parameterization can to describe the anti-baryon to baryon ratios well.

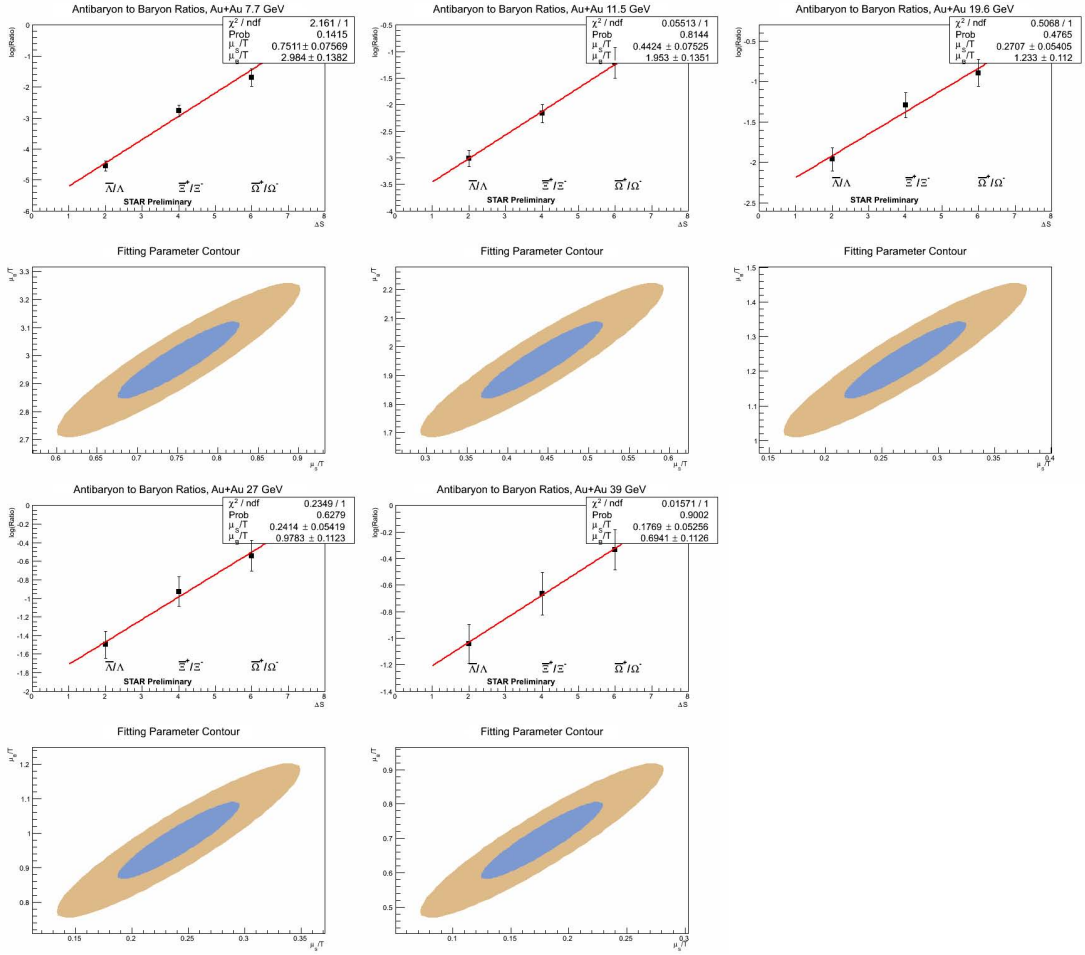

Figure 4.47: The anti-baryon to baryon ratios are fitted with a linear function $\ln(ratio) = -2\frac{\mu_B}{T} + \frac{\mu_S}{T}\Delta S$, to get the parameters $\frac{\mu_B}{T}$ and $\frac{\mu_S}{T}$ for each collision energy.

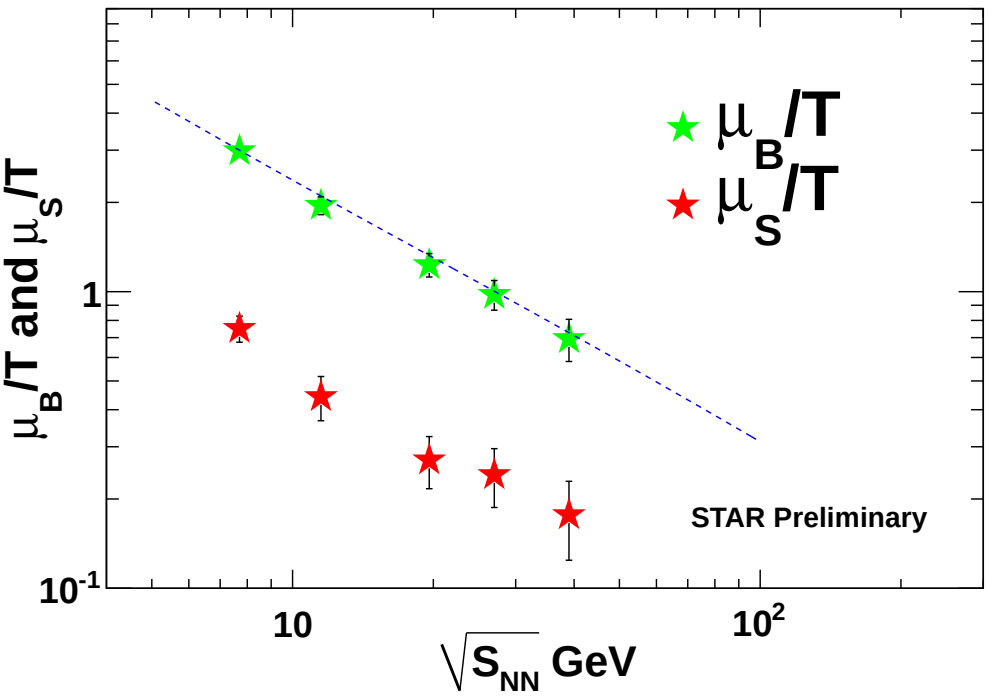

Figure 4.48: The $\frac{\mu_B}{T}$ and $\frac{\mu_S}{T}$ parameters as a function of beam energy. The curve is the parameterization with μ_B and T fitting of AGS, SPS, and RHIC 130 GeV data, $T = T_0 - b\mu_B^2$, $\mu_B = \alpha \frac{\log \sqrt{\sigma_{NN}}}{(\sqrt{s_{NN}})^\beta}$, where $T_0 = 167.5$ MeV, $b = 0.1583$ GeV^{-2}, $\alpha = 2.06$, $\beta = 1.13$ [55].

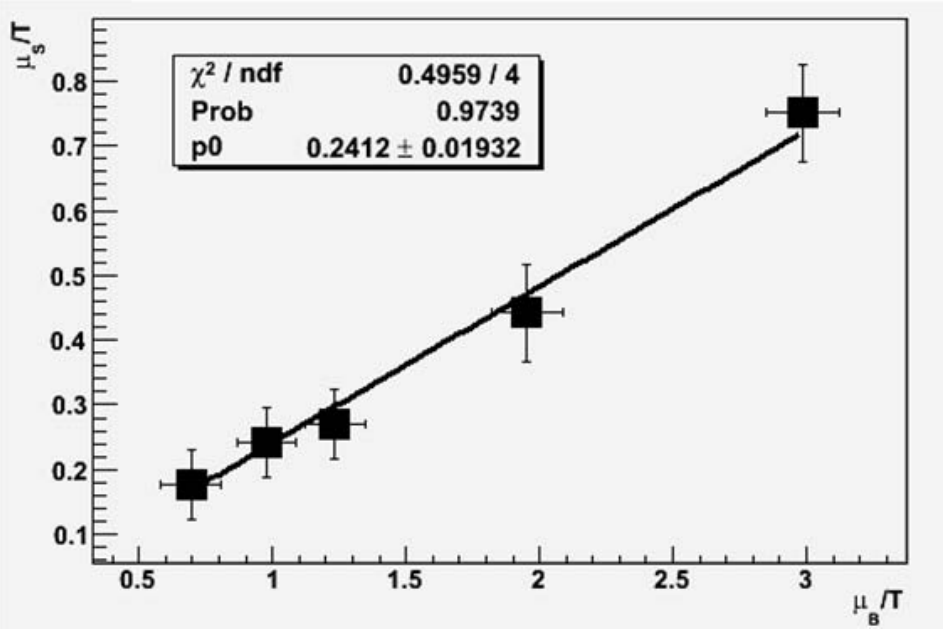

Figure 4.49: The relationship between $\frac{\mu_S}{T}$ and $\frac{\mu_B}{T}$. A linear function is used to fit the points of $\frac{\mu_S}{T}$ and $\frac{\mu_B}{T}$.

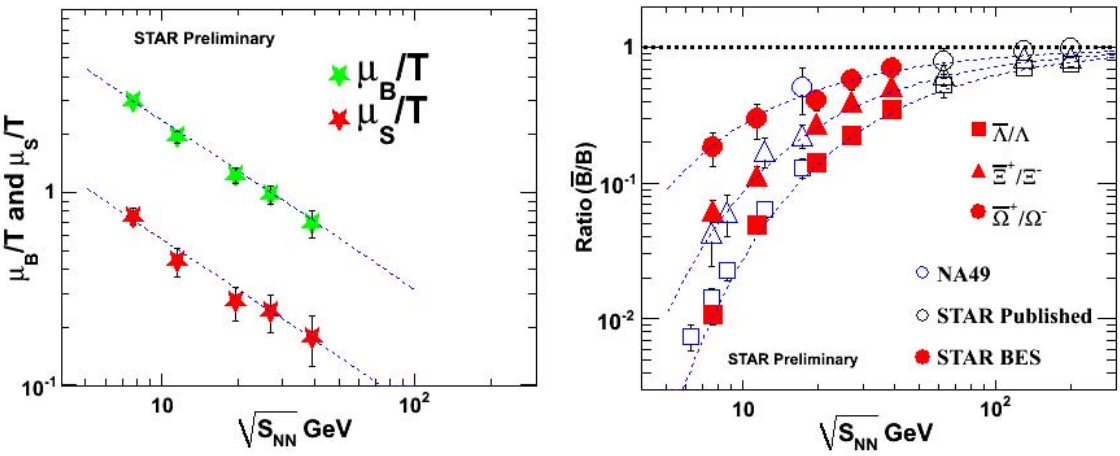

Figure 4.50: The $\frac{\mu_S}{T}$, $\frac{\mu_B}{T}$ and anti-baryon to baryon ratios are compared with the curves of parameterization.

CHAPTER 5

Reaction Plane Dependent V0 and Charged Hadron Azimuthal Correlation

Quantum Chromodynamics (QCD) allows for the formation of parity-odd domains inside the Quark-Gluon Plasma (QGP). The Chiral Magnetic Effect (CME) will lead to charge separation with respect to the reaction plane. Previous measurements from RHIC and LHC using charge-dependent two-particle azimuthal correlations with respect to the reaction plane are consistent with the expectation of charge separation from CME. The correlation between strange V0 and charged hadrons is expected to provide an estimate of the intrinsic background from particle correlation, which extends our understanding of the two-particle azimuthal correlations. In addition, the theoretical calculations of the Chiral Vortical Effect (CVE) predict a difference in baryon versus anti-baryon azimuthal correlations with respect to the reaction plane. In this chapter, we will discuss the study of $\Lambda(\bar{\Lambda})-h^{\pm}$, $K^0_S-h^{\pm}$, $\Lambda(\bar{\Lambda})-p(\bar{p})$ and $K^0_S-p(\bar{p})$ azimuthal correlations with respect to the event plane, and investigate the CME and CVE in heavy-ion collisions.

5.1 Introduction to CME & CVE

5.1.1 The Local Parity Violation in the Strong Interaction

Quantum Chromodynamics is the theory to describe the strong interaction. One of the most remarkable concepts in QCD is the concept of vacuum. The QCD vacuum is not considered as the void of everything, but it is fully filled with

fluctuating quark and gluon fields. A state of such quantum field with global or local minimum energy is called a vacuum. The true vacuum, which is at the global minimum energy state is unique, but there are an infinity of QCD vacuums at local minimum energy states. The spatial part of different states at time t are represented by the Chern-Simons topological charge, i.e. Chern-Simons number $N_{CS}(t)$ [56][57].

$$N_{CS}(t) = \frac{g^2}{16\pi^2} \int d^3x \epsilon^{ijk} (A_i^a \partial_j A_k^a + \frac{1}{3} \epsilon^{abc} A_i^a A_j^b A_k^c) \tag{5.1.1}$$

The variable A_i^a is the gluon gauge fields of the vacuum, which is a function of time and space. Indices (i, j, k) and (a, b, c) represent the spatial and color components, corresponding to each QCD vacuum. All gauge field configurations can be characterized by a topological invariant, the winding number Q_w. The winding number is an integer and given by integration of gluonic field tensor $(F_{\mu\nu}^a)$ and its dual $(\tilde{F}_a^{\mu\nu})$ [58].

$$Q_w = \frac{g^2}{32\pi^2} \int d^4x F_{\mu\nu}^a \tilde{F}_a^{\mu\nu} \tag{5.1.2}$$

The more historical topological invariant, Q_w, represents the difference of Chern-Simons number at temporal infinity and negative infinity:

$$Q_w = N_{CS}(+\infty) - N_{CS}(-\infty). \tag{5.1.3}$$

The Chern-Simons number N_{CS} can vary by integers, thus $\frac{dN_{CS}(t)}{dt} \neq 0$, which corresponds to the QCD vacuum transition. The vacuum transition is localized in space and time, so it is a local phenomenon [59]. The many QCD vacua are shown schematically in Figure 5.1. A transition from a QCD vacuum to another by tunneling through the potential energy barrier is called an *instanton*. Another type of transition is *sphaleron*, which goes over the potential energy barrier. It

is predicted that instanton rates are heavily suppressed at a very large energy density [59], such as those achieved at RHIC. However, at a large energy density, sphaleron rates are not suppressed, and the total vacuum transition rates are predicted to dramatically increase [58].

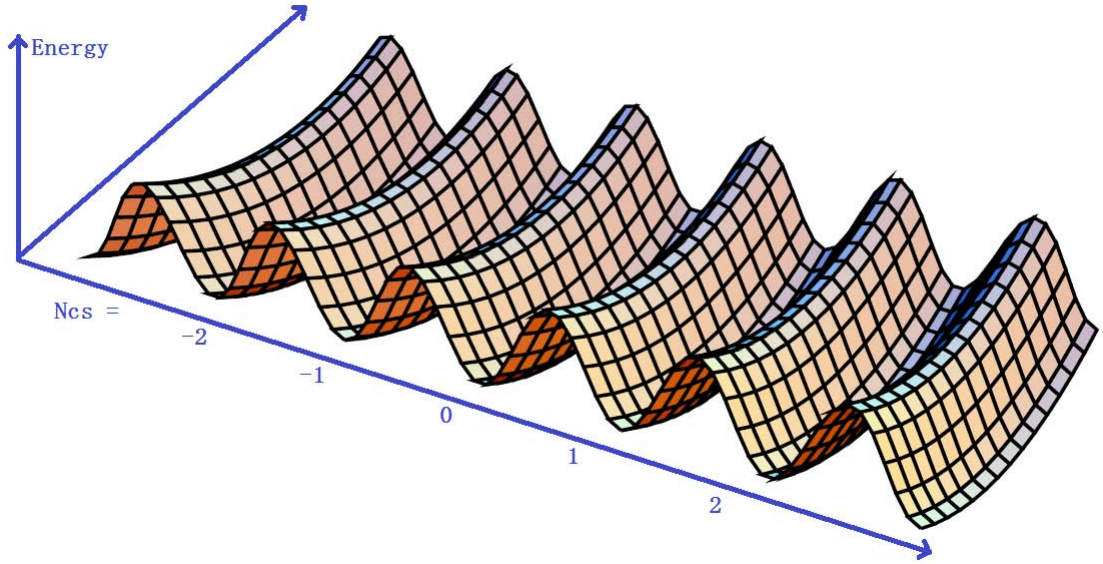

Figure 5.1: The potential energy of the gluon field vs. N_{CS}. Each local energy minimum state is a QCD vacuum. The plot is from [57].

The axial vector current in QCD represents the flow of net handedness (left-handed - right-handed particles).

$$j^5_\mu = \sum_f \langle \bar{\psi}_f \gamma_\mu \gamma_5 \psi_f \rangle_A \tag{5.1.4}$$

The divergence of j^5_μ is given by:

$$\partial^\mu j^5_\mu = 2 \sum_f m_f \langle \bar{\psi}_f i\gamma_5 \psi_f \rangle_A - \frac{N_f g^2}{16\pi^2} F^a_{\mu\nu} \tilde{F}^{\mu\nu}_a. \tag{5.1.5}$$

Here N_f is the number of quark flavors, ψ_f is a quark field, and m_f is the mass

of a quark. In the chiral limit, i.e. $m_f = 0$,

$$\partial^\mu j^5_\mu = -\frac{N_f g^2}{16\pi^2} F^a_{\mu\nu} \tilde{F}^{\mu\nu}_a. \tag{5.1.6}$$

The net number of left/right handed quarks (N_L/N_R) as a function of time is given by:

$$N_L(t) - N_R(t) = -\int_{-\infty}^{t} dt \int d^3x \frac{N_f g^2}{16\pi^2} F^a_{\mu\nu} \tilde{F}^{\mu\nu}_a. \tag{5.1.7}$$

Assuming initially at $t = -\infty$, we have an equal number of fermions (quarks and anti-quarks), i.e. $N_R(t = -\infty) = N_L(t = -\infty)$. Inserting Equation 5.1.2 into 5.1.7, and at $t = \infty$, we obtain

$$N_L(t = \infty) - N_R(t = \infty) = 2N_f Q_w \tag{5.1.8}$$

which means that configurations with positive Q_w convert right-handed fermions into left-handed ones. It is the phenomenon of parity violation in the strong interaction. However, it should be stressed that the phenomenon is not a global but rather a local one, i.e. the vacuum transitions are localized in space and time. Thus the phenomenon is called **Local Parity Violation** (LPV) in literature.

5.1.2 The Chiral Magnetic Effect and Chiral Vortical Effect

The chiral asymmetry cannot be directly observed in the heavy-ion collision. The Chiral Magnetic Effect (CME), proposed by Dimitri Kharzeev et. al., can convert the chiralty asymmetry to an other type of asymmetry with the help of the magnetic field created in the non-central heavy-ion collisions [58].

Figure 5.2 illustrates the existence of the background magnetic field. In a non-central heavy-ion collision, two nuclei collide to form a fire ball with significant amount of energy deposited in the almond-shaped area. The charged spectators keep moving along the original directions at a speed close to the speed of light,

generating two electric currents with opposite directions. An extremely strong magnetic field is induced by the spectators in the central collision area. The participant region also has contribution to the magnetic field, as it is charged and carries orbital angular momentum. Theoretical calculations indicates that the magnetic field generated in the heavy-ion collisions is as strong as the QCD energy scale, and in the early stage of Au+Au collisions, the magnitude can reach up to 10^{15} T.

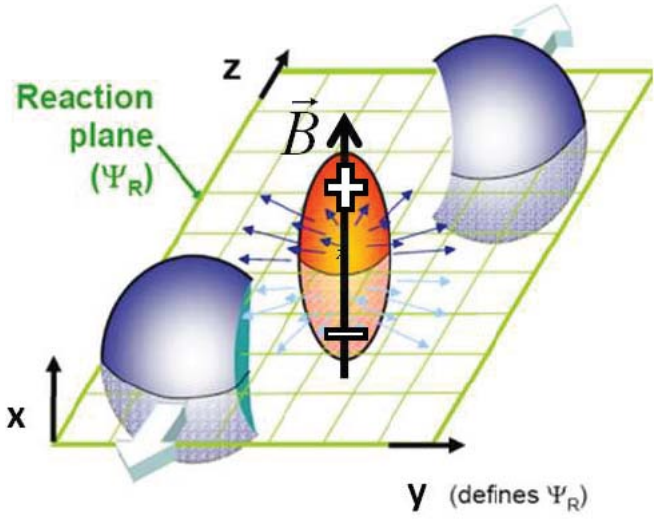

Figure 5.2: A strong magnetic field is created in the non-central heavy-ion collision.

The strong magnetic field has interaction with quarks in the QGP. Since gluons are not electrically charged, they do not interact with the magnetic field. The quarks in such a strong magnetic field will stay in the lowest Landau level, moving either along or opposite to the magnetic field. Furthermore, positive quarks have their spin parallel with the magnetic field, and negative quarks have their spin anti-parallel with the magnetic field. A cartoon with a few up and down quarks is shown in the stage 1 of Figure 5.3. After a vacuum transition has occurred as shown in the stage 2 of Figure 5.3, here assuming Q_w = -1, we have more right-handed quarks than left-handed quarks, i.e. some left-handed quarks are

converted to right-handed quarks. At chiral limit ($m_f = 0$), a quark's chirality is equal to its helicity. The chirality can be changed through either flipping the spin or reversing the momentum. However, due to the strong magnetic field, the flipping of the spin is suppressed. Thus, left-handed quarks will reverse their momenta as shown in the stage 3 of Figure 5.3. In the end, the quarks with different charges move in opposite directions along the magnetic field, which leads to a charge separation and creates an electric current. As the reaction plane is perpendicular to the magnetic field, if there is a surplus of positive charges on one side of the reaction plane, there will be a surplus of negative charges on the other side. This is the **Chiral Magnetic Effect**. The situation of $Q_w = +1$ is just reversed. Positive and negative transitions are equally probable, since the vacuum transition fluctuates from event to event.

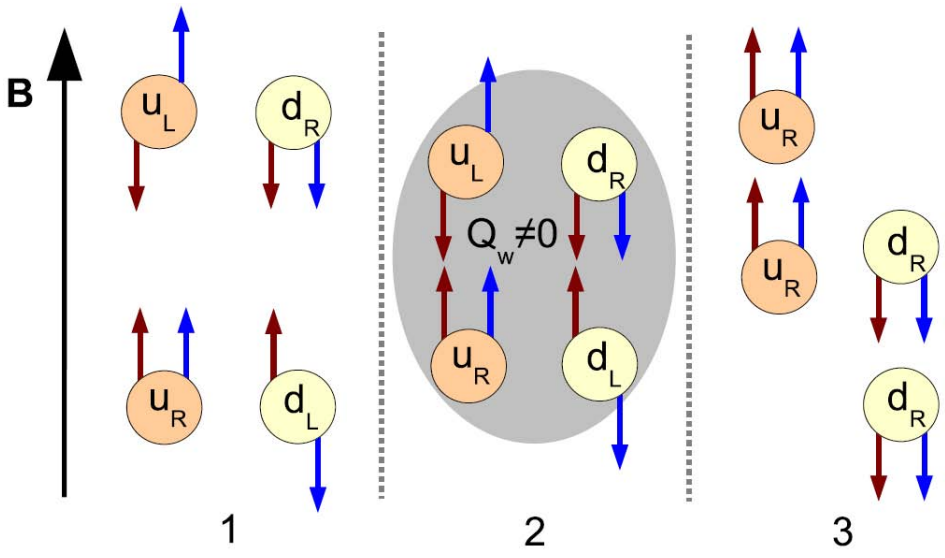

Figure 5.3: The u and d in the figure stand for up and down quarks. L and R are the handedness of the quarks. The blue arrows (on the right side of quarks) are the spin directions, and the red arrows (on the left side of quarks) are the momentum directions. The figure is from [58].

In addition to the CME, theoretical calculation also predicts the existence of the Chiral Vortical Effect (CVE), which is analog to the CME. The vorticity $\vec{\omega}$ of

the participant nucleons, combined with a baryon chemical potential μ_B, creates an effective magnetic field $\mu_B \overrightarrow{\omega}$ [60]. In the SU(3) symmetry, the CME and CVE lead to completely different currents: the CME contributes only to the electric charge current, and the CVE contributes only to the baryon current. If the CVE exists, there should be a baryon number separation of the same sign as the electric charge separation due to the CME [60].

5.1.3 The Three-Point Correlator and Experimental Observable

The Chiral Magnetic Effect leads to an electric charge separation along the direction of the magnetic field created in the heavy-ion collisions, and the particles with the same electric charge emission along the same direction, and the particles with opposite charges emission along the opposite directions. The Fourier series of the charged particle azimuthal distribution can be used to describe the effect:

$$\begin{aligned} \frac{dN_\alpha}{d\phi} \propto 1 + 2v_{1,\alpha}\cos(\Delta\phi) + 2v_{2,\alpha}\cos(2\Delta\phi) + \cdots \\ + 2a_{1,\alpha}\sin(\Delta\phi) + 2a_{2,\alpha}\sin(2\Delta\phi) + \cdots \end{aligned} \tag{5.1.9}$$

where the coefficients a reflects the charge separation effect, the coefficients v are the flow harmonics, and α denotes the sign of electric charge of particles, and $\Delta\phi = (\phi - \Psi_{RP})$ is the azimuthal angle with respect to the reaction plane. However, as discussed in section 5.1.2, even in the same event, there are more than one local vacua with different transitions or different Q_w, and the positive and negative transitions are equally probable. Therefore, the electric charge separation direction is random, which is determined by the sign of the topological charge (Q_w). A direct measurement of the coefficients a should be zero, after averaging over a large number of events.

To extract the charge separation signal, a three-point correlator is proposed [61].

$$\begin{aligned}
&\langle\cos(\phi_\alpha + \phi_\beta - 2\Psi_{RP})\rangle \\
=&\langle\cos\Delta\phi_\alpha \cos\Delta\phi_\beta\rangle\langle\sin\Delta\phi_\alpha \sin\Delta\phi_\beta\rangle \\
=&[\langle v_{1,\alpha}v_{1,\beta}\rangle + B_{in}] - [\langle a_{1,\alpha}a_{1,\beta}\rangle + B_{out}]
\end{aligned} \tag{5.1.10}$$

The $\langle a_{1,\alpha}a_{1,\beta}\rangle$ is the signal term. The $a_{1,\alpha}a_{1,\beta}$ is a parity-even quantity, and it no longer depends on the sign of Q_w. Therefore, the signal cumulates, after the averaging over a large number of events. The $\langle v_{1,\alpha}v_{1,\beta}\rangle$ term provides a directed flow reference, which is expected to be the same for same-charge and opposite-charge particle correlations. The B_{in} and B_{out} are the background terms of the in-plane and out-of-plane directions, which are largely cancelled out. The three-point correlator is expected to be negative for the same-charge correlation ($\alpha = \beta$), and positive for the opposite charge correlation ($\alpha \neq \beta$), because $-\langle a_{1,\alpha}a_{1,\beta}\rangle$ is measured.

The STAR experiment has published the measurement of the centrality dependence of three-point correlator in Au+Au and Cu+Cu collisions at $\sqrt{s_{NN}} = 200$ GeV [62]. The results for same-charge and opposite-charge particle correlations are consistent with expectations based on the out-of-plane electric charge separation, while the models without LPV mechanism built-in cannot reproduce STAR data.

5.1.4 The Motivation of Strange V0 and Charged Hadron Azimuthal Correlation Study

The previous results of two-particle azimuthal correlations have already revealed that there is an electric charge separation effect across the reaction plane. The study of correlation with a charged particle replaced by a neutral particle will extend our understanding of background in the charged particle azimuthal correlations. This study can test whether the different behaviors of same-charge

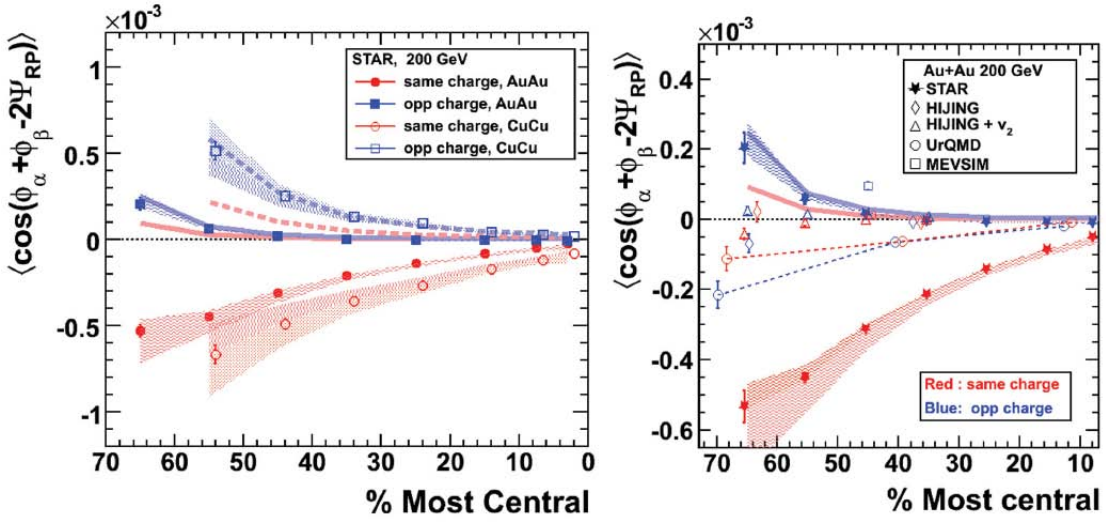

Figure 5.4: The left figure shows the there points correlator in Au+Au and Cu+Cu collisions measured by the STAR experiment. The right figure compares the measured Au+Au results with the model calculations. The figure is from [62].

and opposite-charge particle correlation are really due to the electric charge. The theory expects that the neutral-positive-charge correlation and neutral-negative-charge correlation are identical. But we need to study the neutral and charge particle correlation to confirm it. If the results show a difference between neutral-positive-charge and neutral-negative-charge correlations, there must be some other effects or background we have not understood yet. It is difficult to identify neutral hadrons, such as π^0s and neutrons with the STAR detector. Fortunately, we can reconstruct strange V0 from their decay daughters. K^0_S is a mixed state of K^0 and $\bar{K}^0$. In high energy heavy-ion collisions, such as RHIC top energies, the strangeness chemical potential is close to zero, which makes the $\bar{K}^0/K^0$ ratio close to one [63][64][65]. So half of the K^0_S particles are K^0 and the other half are $\bar{K}^0$. No matter whether strange quarks participate in the chiral dynamics, the K^0_S is completely charge neutral. (If only up and down quarks participate in the chiral dynamics, K^0 and $\bar{K}^0$ behave like they carry a charge in CME, but K^0_S still looks neutral because there are equal amounts of K^0 and $\bar{K}^0$.) Therefore, the

$K^0_S - h^{\pm}$ correlation will help to test whether different behaviors of same-charge and opposite-charge particle correlation are really due to the electric charge or not.

$\Lambda(\bar{\Lambda})$ is also electric charge neutral. It may help to study whether s quarks participate in the chiral dynamics. If $\Lambda(\bar{\Lambda}) - h^{\pm}$ has similar behaviors as $K^0_S - h^{\pm}$, $\Lambda(\bar{\Lambda})$ looks like charge neutral in the CME, which means there is no difference between s and u, d quarks. Then under SU(3) symmetry, and s quarks fully participate in the chiral dynamics as u and d quarks. If $\Lambda(\bar{\Lambda}) - h^{+}$ and $\Lambda(\bar{\Lambda}) - h^{-}$ show different behaviors, while $K^0_S - h^{+}$ and $K^0_S - h^{-}$ are consistent with each other, then $\Lambda(\bar{\Lambda})$ looks like a charged particle in the CME, which means it is SU(2) symmetry and s quarks do not fully participate in the chiral dynamics as u and d quarks.

Both Λs and protons are baryons. $\Lambda(\bar{\Lambda}) - p(\bar{p})$ may help to test the CVE. Protons are baryons themselves, but the p-p correlation also involves the CME, because protons also carry electric charges. $\Lambda(\bar{\Lambda}) - h^{\pm}$ and $K^0_S - p(\bar{p})$ correlations provide background study for the $\Lambda(\bar{\Lambda}) - p(\bar{p})$ correlation, since not both particles in the $\Lambda(\bar{\Lambda}) - h^{\pm}$ and $K^0_S - p^{\pm}$ correlations are baryons.

5.2 Data Set and Event Selection

As the relatively low production of strange V0 in the heavy-ion collisions and low reconstruction efficiency, only several $\Lambda(\bar{\Lambda})$ and K^0_S can be reconstructed in each event. Therefore, the analysis of strange V0 and charged particle correlation is most often statistics limited. In years 2010 and 2011, STAR experiment took high statistics data of Au+Au collisions at 39 GeV and 200 GeV, which makes it possible to study the correlations. In this thesis, those two data sets have been used for the correlation analysis.

In order to investigate the centrality dependency, minimum bias data are se-

Table 5.1: The data set and event selection criteria, as well as the total number of good events used in the analysis.

Year	$\sqrt{S_{NN}}$	Vertex Cut	Number of Good Events
2010	39 GeV	$\|V_Z\| < 40$ cm, $\|V_r\| < 2$ cm	130 million
2011	200 GeV	$\|V_Z\| < 40$ cm, $\|V_r\| < 2$ cm	480 million

lected. Some basic vertex cuts are set to select good events. Table 5.1 lists the data set and cuts used in the event selection, where V_Z is the collision vertex position along the beam direction from the detector center, and V_r is the distance between collision vertex and the beam pipe.

The whole minimum bias data set for each energy is separated to nine centrality bins. The same C++ class StRefMultCorr is used as the centrality definition in the analysis of strange particle production which is discussed in the Chapter 4. Figure 5.5 shows the reference multiplicity distribution for Run10 Au+Au 39 GeV and Run11 Au+Au 200 GeV data.

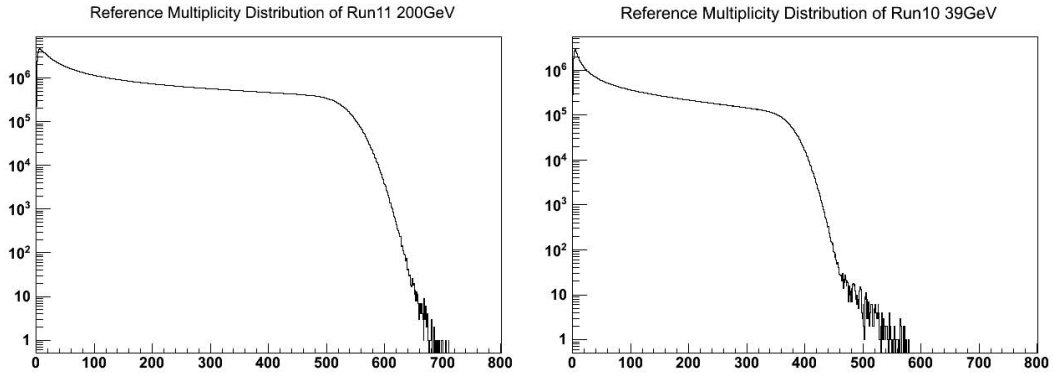

Figure 5.5: The figures show the reference multiplicity distribution of Au+Au collisions at 200 GeV and 39 GeV.

5.3 Event Plane Reconstruction

In order to calculate the three-point correlator, the event plane is reconstructed, which is an estimation of the reaction plane. There are several steps to measure

the azimuthal angle of the event plane Ψ_{EP}, which are summarized below.

The event plane is reconstructed from the primary tracks. All the primary tracks with 0.15 GeV/c $< p_T <$ 2 GeV/c and $|\eta| < 1$ are used to reconstruct the event plane. Since strange V0 and (anti-)proton correlation will be studied, a cut with $n\sigma_p <$ -3 is set to avoid the self-correlation due to the (anti-)proton. Since the detector response is not perfectly uniform along the azimuthal angle ϕ, the tracks' ϕ angle distribution is not uniform. We apply a weight to each angle, to make the ϕ angle distribution flat. The weight for each angle is the inverse of track multiplicity in that angle over all the tracks.

The primary tracks used for event plane reconstruction are randomly separated to two equal sub-groups, and a sub-event plane is reconstructed for each sub-group through the flow vector Q_n [66].

$$\begin{aligned} Q_{n,x} &= \sum_i w_i \cos(n\phi_i) = Q_n \cos(n\Psi_{EP,n}) \\ Q_{n,y} &= \sum_i w_i \sin(n\phi_i) = Q_n \sin(n\Psi_{EP,n}) \end{aligned} \tag{5.3.11}$$

where $\Psi_{EP,n}$ is the n-th order event plane azimuthal angle, ϕ_i is the azimuthal angle of particle i, w_i is a particle weight to optimize the event plane resolution, usually p_T is chosen to be the weight w_i. Then the n-th order event plane angle is:

$$\Psi_{EP,n} = \frac{1}{n} \tan^{-1}\left(\frac{Q_{n,y}}{Q_{n,x}}\right). \tag{5.3.12}$$

For the three-point correlator analysis, we use the 2nd order event plane, i.e. $n = 2$.

From physics point of view, the reaction plane azimuthal angle distribution should be flat, as the truly random collision impact parameter. To remove the effects of detector acceptance and efficiency, a shifting method [67] is used to force the calculated event plane azimuthal angle distribution to be uniform. Figure 5.6

shows an example of event plane azimuthal angle distribution.

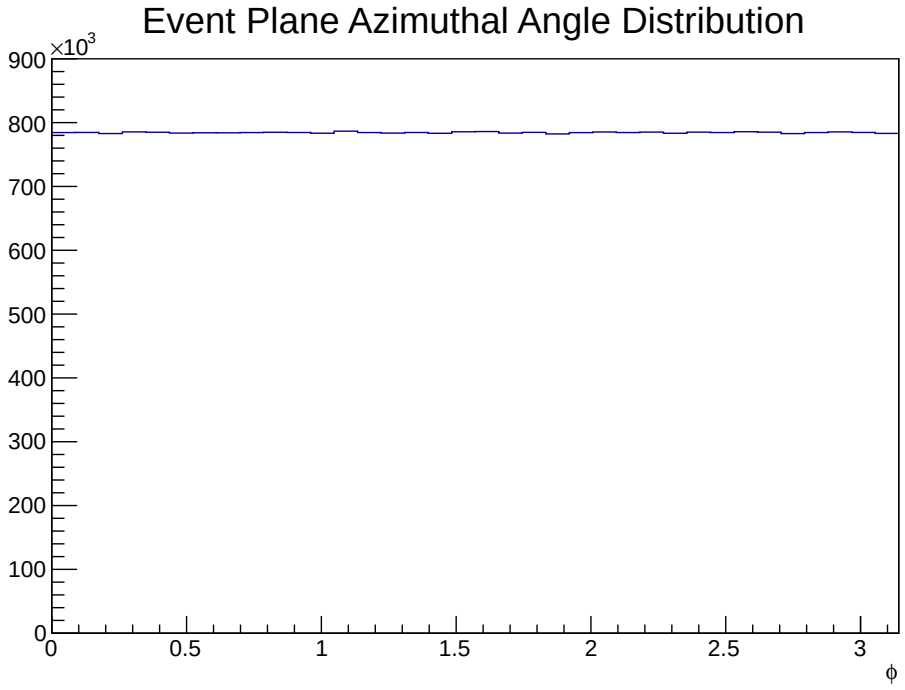

Figure 5.6: The event plane azimuthal angle distribution is uniform after all the corrections.

The measured three-point correlator should be corrected for the event plane resolution:

$$Corr_{real} = \frac{Corr_{obs}}{\mathcal{R}}. \tag{5.3.13}$$

The sub-event plane resolution can be estimated from the two sub-event planes, which is

$$\mathcal{R}_{n,sub} = \sqrt{\langle \cos[n(\Psi^{A}_{EP,n} - \Psi^{B}_{EP,n})] \rangle}. \tag{5.3.14}$$

The event plane resolution has a relationship with χ_m, where $\chi_m = v_m\sqrt{2N}$. The Figure 5.7 shows the event plane resolution as a function of χ. For the full event plane, N is twice of that of sub-event plane, therefore, $\chi_{full} = \sqrt{2}\chi_{sub}$. When we get the sub-event plane resolution, we can project the resolution to χ space, and multiple the factor $\sqrt{2}$ to get the χ_{full}, and project back to the resolution

space. For the three-point correlator analysis, the full event plane resolution can be calculated as

$$\mathcal{R}_{full}(\chi) = \frac{\sqrt{\pi}}{2\sqrt{2}}\chi \exp(-\chi^2/4)[I_{(k-1)/2}(\chi^2/4) + I_{(k+1)/2}(\chi^2/4)]. \tag{5.3.15}$$

where I is the modified Bessel function [66].

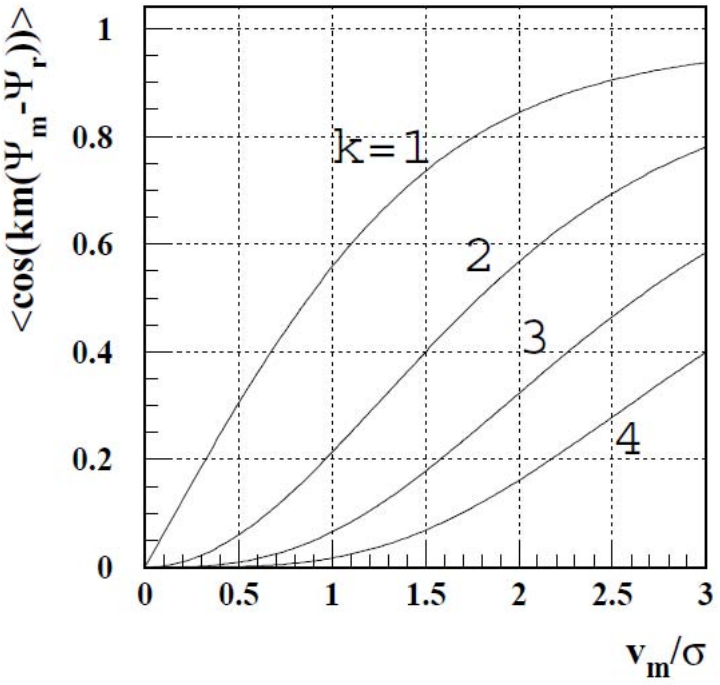

Figure 5.7: The event plane resolution for the n-th ($n = k \times m$) harmonic of the particle distribution with respect to the m-th harmonic plane as a function of χ. For three-point correlator analysis, we use $k = 1$, $m = n = 2$. The figure is from [66].

Figure 5.8 shows the event plane resolution as a function of centrality. In the peripheral collisions, there are fewer primary tracks used for event plane reconstruction, and in the central collisions, the v_2 is small. Therefore, the event plane resolutions at both peripheral and most central collisions are worse than that at mid-central collisions.

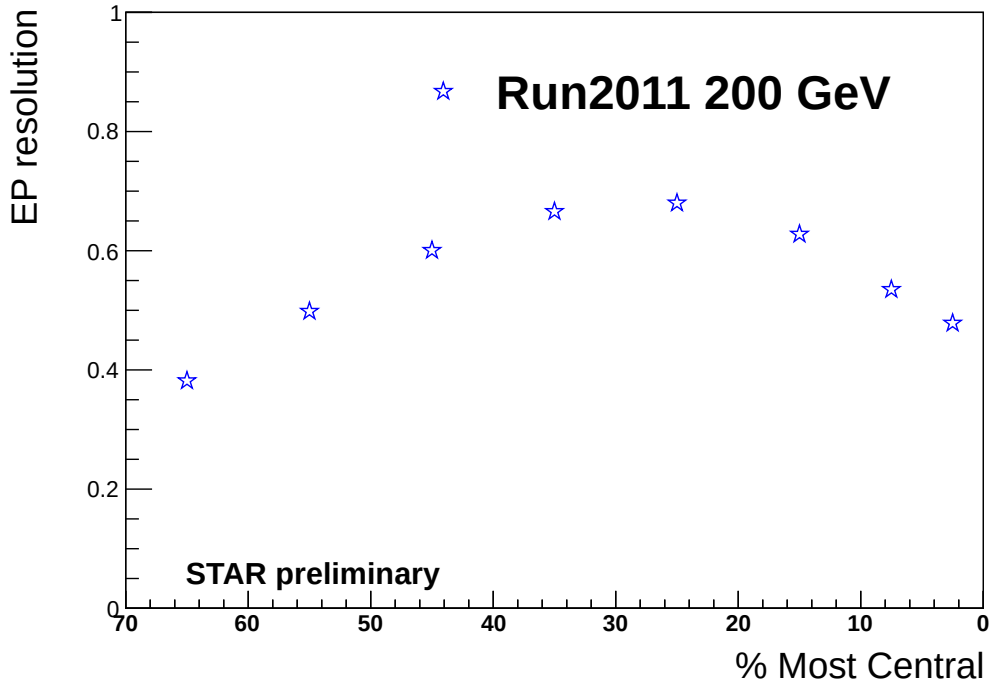

Figure 5.8: The event plane resolution as a function of centrality.

5.4 Particle Selection

For the strange V0 and charged hadron azimuthal correlation study, charged hadrons, (anti-)protons and strange V0(Λ, $\bar{\Lambda}$, K^0_S) need to be identified. Charged hadrons mainly consist of pions and kaons, but (anti-)protons are excluded with a cut of $n\sigma_p$ from the TPC. Protons are identified with the TPC and TOF. Table 5.2 shows the cuts for the charged hadrons and (anti-)protons selection.

Table 5.2: The basic cuts to select charged hadrons and protons with the TPC and TOF.

	charged hadrons	(anti-)protons
p_T	0.15 GeV/c - 2 GeV/c	0.4 GeV/c - 2 GeV/c
Global DCA to PV	$<$ 2 cm	$<$ 2 cm
TPC Number of Hits	$>$ 15	$>$ 15
TPC dE/dx	$n\sigma_p <$ -3	$\lvert n\sigma_p \rvert < 2$
TOF m^2		0.8 $(GeV/c^2)^2$ - 1.0 $(GeV/c^2)^2$

K^0_S and $\Lambda(\bar{\Lambda})$ are reconstructed from their decay daughters, using the algorithm described in Chapter 3. Table 5.3 lists the topological cuts and invariant mass window to select the K^0_S and $\Lambda(\bar{\Lambda})$ candidates. The DCA of strange V0 to the primary vertex varies from most peripheral to most central collisions to control the background level. Figure 5.9 shows the reconstructed signals of K^0_S and $\Lambda(\bar{\Lambda})$. The background in the most central collisions is higher than that in the peripheral collisions, although more strict cuts are set to the central collisions. The worst case is the K^0_S from most central collisions, however the purity of K^0_S is higher than 90%. The purity of $\Lambda(\bar{\Lambda})$ is higher than K^0_S.

Table 5.3: The topological cuts for K^0_S and $\Lambda(\bar{\Lambda})$ at Au+Au 200 GeV and 39 GeV.

	Au+Au 200 GeV	Au+Au 39 GeV
	K^0_S	
TPC Number of Hits	> 15	> 15
Pion selection $\lvert n\sigma_\pi \rvert$	< 4	< 4
DCA of pion to PV	> 1.2 cm	> 1.5 cm
DCA of P+ to P-	< 0.8 cm	< 0.8 cm
Decay Length of V0	> 5 cm (0-40%)	> 4 cm
	> 4 cm (40-80%)	
DCA of V0 to PV	< 0.5 cm for 0-5%	< 0.6 cm for 0-5%
	< 0.525 cm for 5-10%	< 0.625 cm for 5-10%
	< 0.55 cm for 10-20%	< 0.65 cm for 10-20%
	< 0.575 cm for 20-30%	< 0.675 cm for 20-30%
	< 0.6 cm for 30-40%	< 0.7 cm for 30-40%
	< 0.625 cm for 40-50%	< 0.725 cm for 40-50%
	< 0.65 cm for 50-60%	< 0.75 cm for 50-60%
	< 0.675 cm for 60-70%	< 0.775 cm for 60-70%
	< 0.7 cm for 70-80%	< 0.8 cm for 70-80%
p_T range	0.2 GeV/c - 2 GeV/c	0.2 GeV/c - 2 GeV/c
Mass window	0.4876 GeV/c^2 - 0.5076 GeV/c^2	0.4926 GeV/c^2 - 0.5026 GeV/c^2
	$\Lambda(\bar{\Lambda})$	
TPC Number of Hits	> 15	> 15
Proton selection $\lvert n\sigma_p \rvert$	< 4	< 4
Pion selection $\lvert n\sigma_\pi \rvert$	< 4	< 4
DCA of proton to PV	> 0.6 cm	> 0.5 cm
	(0.7 cm for V0 $p_T < 0.6$ GeV/c)	(0.7 cm for V0 $p_T < 0.6$ GeV/c)
DCA of pion to PV	> 1.8 cm	> 1.5 cm
	(0.7 cm for V0 $p_T < 2.5$ GeV/c)	(2.5 cm for V0 $p_T < 0.6$ GeV/c)
DCA of P+ to P-	< 0.7 cm	< 0.8 cm
Decay Length of V0	> 6 cm	> 4 cm
DCA of V0 to PV	< 0.4 cm for 0-5%	< 0.5 cm for 0-5%
	< 0.425 cm for 5-10%	< 0.525 cm for 5-10%
	< 0.45 cm for 10-20%	< 0.55 cm for 10-20%
	< 0.475 cm for 20-30%	< 0.575 cm for 20-30%
	< 0.5 cm for 30-40%	< 0.6 cm for 30-40%
	< 0.525 cm for 40-50%	< 0.625 cm for 40-50%
	< 0.55 cm for 50-60%	< 0.65 cm for 50-60%
	< 0.575 cm for 60-70%	< 0.675 cm for 60-70%
	< 0.6 cm for 70-80%	< 0.7 cm for 70-80%
Decay Length of V0	> 6 cm	> 4 cm
Decay Length of V0	> 6 cm	> 4 cm
p_T range	0.5 GeV/c - 2 GeV/c	0.5 GeV/c - 2 GeV/c
Mass window	1.1117 GeV/c^2 - 1.1197 GeV/c^2	1.1107 GeV/c^2 - 1.1207 GeV/c^2

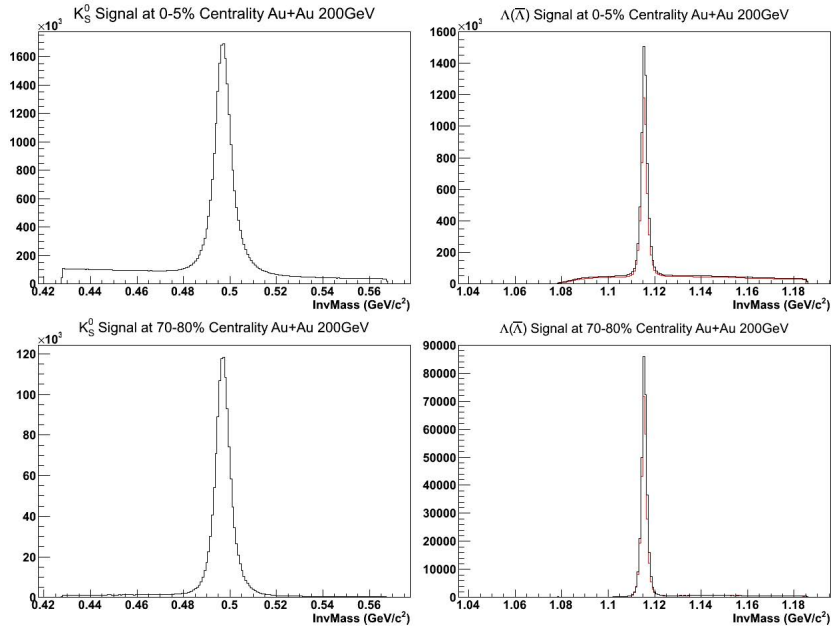

Figure 5.9: The reconstructed K^0_S and $\Lambda(\bar{\Lambda})$ at Au+Au 200 GeV. In the plots of $\Lambda(\bar{\Lambda})$ signals, the black curves are the Λ signals, and the red curves are the $\bar{\Lambda}$ signals.

5.5 Results

5.5.1 $K^0_S - h^{\pm}$ Azimuthal Correlation

Figure 5.10 shows the measurements of $K^0_S - h^{\pm}$ azimuthal correlations in Au+Au collisions at 200 GeV and 39 GeV. The $K^0_S - h^+$ and $K^0_S - h^-$ are consistent with each other at different centralities and collision energies, and the difference between $K^0_S - h^+$ and $K^0_S - h^-$ is consistent with zero. There is no significant charge-separation effect in the $K^0_S - h^{\pm}$ correlation, which indicates that the charge separation observed in charged hadron correlation results from correlated emission of charged particle pairs with respect to the event plane.

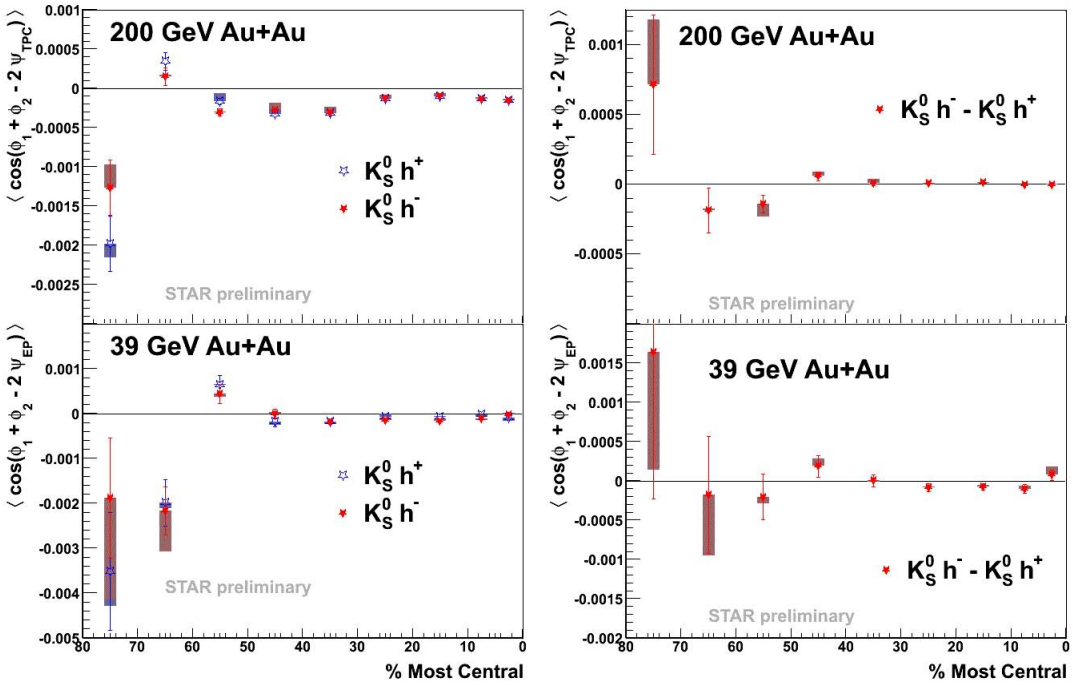

Figure 5.10: The left two panels show the $K^0_S - h^+$ and $K^0_S - h^-$ as a function of centrality in Au+Au collisions at 200 GeV and 39 GeV respectively. The right two panels show the difference between $K^0_S - h^-$ and $K^0_S - h^+$ as a function of centrality at those two collision energies. The error bars are statistical errors. The shadows are systematic uncertainties.

5.5.2 $\Lambda(\bar{\Lambda}) - h^{\pm}$ Azimuthal Correlation

$\Lambda(\bar{\Lambda})$ particles are made of up, down and strange quarks, and carry no electric charge. However, if for some reason the strange quark does not participate the chiral dynamics as much as the up and down quarks, the Λ particle could respond similarly to an effectively positive charged particle, and $\bar{\Lambda}$ would be a negative charged particle. Therefore, $\Lambda - h^{+}$ should have same performance as $\bar{\Lambda} - h^{-}$, and we can combine them. It is the same case for $\Lambda - h^{-}$ and $\bar{\Lambda} - h^{+}$. Figure 5.11 shows the combined $\Lambda(\bar{\Lambda}) - h^{\pm}$ azimuthal correlations at Au+Au 200 GeV and 39 GeV. The (anti-)protons have been excluded from the charged hadrons to avoid the correlation between baryons. The $\Lambda(\bar{\Lambda})$ behaves the same as K^0_S, which suggests that strange quarks fully participate in the chiral dynamics, so that the $\Lambda(\bar{\Lambda})$ behave like charge neutral particles not influenced by the CME.

5.5.3 $K^0_S - p(\bar{p})$ Azimuthal Correlation

From the result of $K^0_S - h^{\pm}$ azimuthal correlation, there is no charge-separation effect in the $K^0_S - h^{\pm}$ correlation. K^0_S is a meson, which does not participate in the CVE. Although protons are baryons, there should be no separation in the $K^0_S - p(\bar{p})$ azimuthal correlation, expected from the CME and the CVE. The measurement of $K^0_S - p(\bar{p})$ azimuthal correlation provides a background study for the $\Lambda(\bar{\Lambda}) - p(\bar{p})$ azimuthal correlation. Figure 5.12 shows the $K^0_S - p(\bar{p})$ correlation results, which indicates there is no separation effect in the $K^0_S - p(\bar{p})$ correlation.

5.5.4 $\Lambda(\bar{\Lambda}) - p(\bar{p})$ Azimuthal Correlation

Both $\Lambda(\bar{\Lambda})$ and (anti-)protons are baryons. If the CVE exists, there would be a baryon number separation in the $\Lambda(\bar{\Lambda}) - p(\bar{p})$ correlation. The $\Lambda(\bar{\Lambda}) - h^{\pm}$ correlation results show no charge-separation-like effect, which provides an important background study for the $\Lambda(\bar{\Lambda}) - p(\bar{p})$ correlation. If there is a separation in the

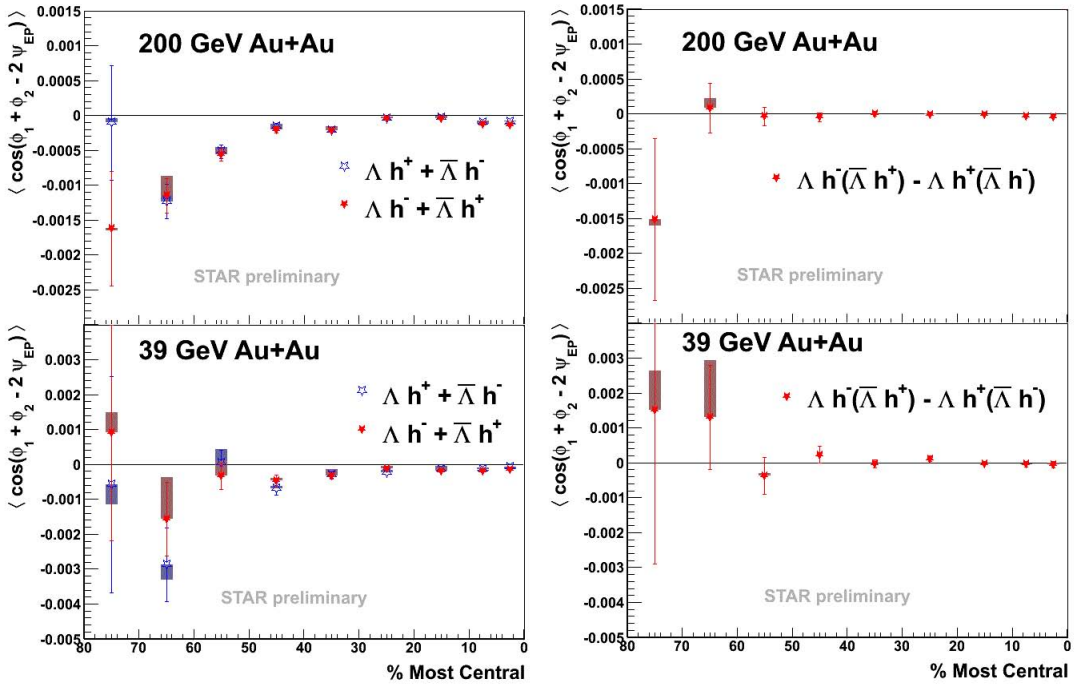

Figure 5.11: The left two panels show the $\Lambda - h^+(\bar{\Lambda} - h^-)$ and $\Lambda - h^-(\bar{\Lambda} - h^+)$ as a function of centrality in Au+Au collisions at 200 GeV and 39 GeV respectively. The right two panels show the difference between $\Lambda - h^-(\bar{\Lambda} - h^+)$ and $\Lambda - h^+(\bar{\Lambda} - h^-)$ as a function of centrality at those two collision energies. The error bars are statistical errors. The shadows are systematic uncertainties.

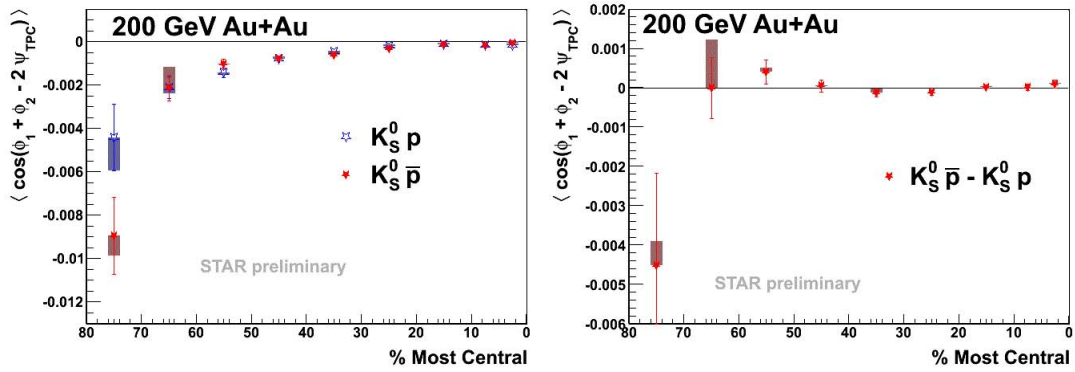

Figure 5.12: The left plot shows the $K^0_S - p$ and $K^0_S - \bar{p}$ as a function of centrality in Au+Au collisions at 200 GeV. The right plot shows the difference between $K^0_S - \bar{p}$ and $K^0_S - p$ as a function of centrality at those two collision energies. The error bars are statistical errors. The shadows are systematic uncertainties.

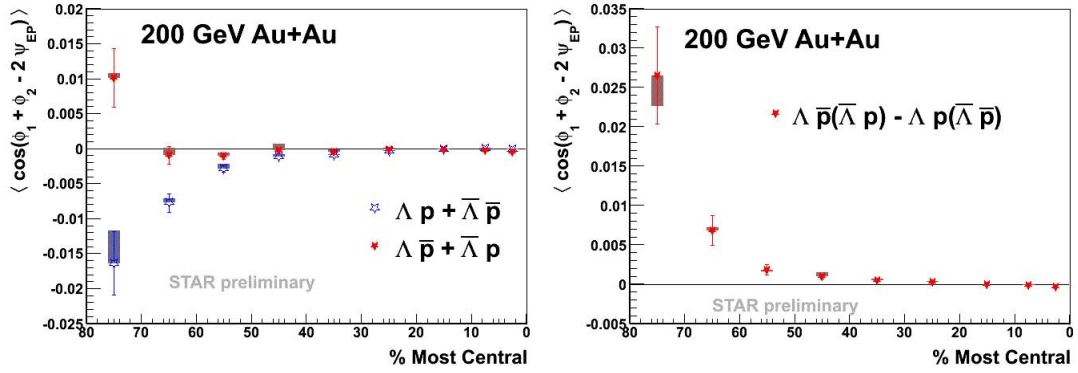

Figure 5.13: The left plot shows the same-baryon-number correlation and the opposite-baryon-number correlation as a function of centrality. The right plot shows the difference between them. The same-baryon-number correlation has different behavior with the opposite-baryon-number correlation at mid-central and peripheral centralities. The error bars are statistical errors. The shadows are systematic uncertainties.

$\Lambda(\bar{\Lambda}) - p(\bar{p})$, we know it is not due to the electric charge effect. Figure 5.13 shows the $\Lambda(\bar{\Lambda}) - p(\bar{p})$ correlation results. It seems that the same-baryon-number correlation has a different behavior from the opposite-baryon-number correlation from mid-central to peripheral collisions. There appears a baryon number separation effect in the $\Lambda(\bar{\Lambda}) - p(\bar{p})$ azimuthal correlation, its origin remains to be studied.

5.6 Systematic Uncertainty

The systematic uncertainty mainly comes from three sources. One is the systematic uncertainty due to other physics mechanism, such as the Hanbury Brown and Twiss (HBT) effect and Coulomb effect. The HBT effect has significant contribution to the correlation between particles with a relative transverse momentum within 0.1 GeV/c ($|\Delta p_T| < 0.1$ GeV/c), including $\Lambda(\bar{\Lambda})$ and K^0_S [68][69]. We set $\Delta p_T > 0.15$ GeV/c and $\Delta\eta > 0.15$ cuts to exclude the HBT effect contribution to the particle correlation, and use the difference between the correlation with and without the HBT effect as the systematic uncertainty due to this ef-

fect. The second source of systematic uncertainty is the feed-down contribution to the correlated particles in the analysis. The feed-down daughters cannot be fully excluded, however, by tightening the DCA of the track to the primary vertex, we can reduce the feed-down contribution and estimate the uncertainty from the feed-down contribution. The third source is the purity of the identified particles, such as $\Lambda(\bar{\Lambda})$, K^0_S and (anti-)protons. The (anti-)protons can be well identified with the TPC and the TOF. The $\Lambda(\bar{\Lambda})$ and K^0_S signals also have very high purity ($> 90\%$). So the systematic uncertainty of this part is small, and it can also be studied by tightening the topological cuts, when the $\Lambda(\bar{\Lambda})$ and K^0_S candidates are reconstructed. The most sensitive cut is the DCA of the track to the primary vertex. Therefore, the systematic uncertainty due to the feed-down contribution and the signal purity can be studied together.

Compared with the systematic uncertainty due to the HBT effect, the uncertainty due to the feed-down contribution and the signal purity is less significant. In the $\Lambda(\bar{\Lambda}) - p(\bar{p})$ correlation study, it is important to study how significant the separation is. Therefore, we studied all the three sources of the systematic uncertainty. In the $K^0_S - h^{\pm}$, $K^0_S - p(\bar{p})$, and $\Lambda(\bar{\Lambda}) - h^{\pm}$ correlation study, there is no significant separation effect. More study of systematic uncertainty can only further support there is no separation effect. Therefore, the systematic uncertainty is not as important as the systematic uncertainty of $\Lambda(\bar{\Lambda}) - p(\bar{p})$ correlation. And we only study the most significant source of the systematic uncertainty, which is the uncertainty due to the HBT effect.

In the Figure 5.10 to Figure 5.13, the shadows are systematic uncertainties for the $K^0_S - h^{\pm}$, $\Lambda(\bar{\Lambda}) - h^{\pm}$, $K^0_S - p(\bar{p})$, and $\Lambda(\bar{\Lambda}) - p(\bar{p})$ correlations respectively.

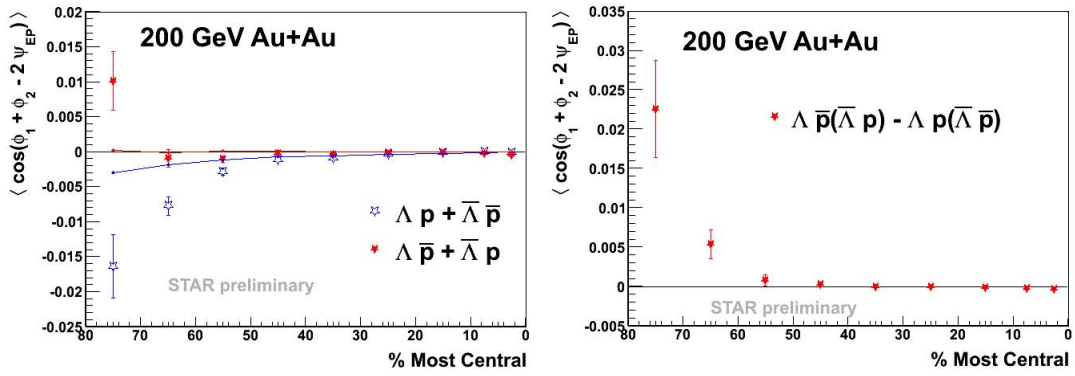

Figure 5.14: The left plot shows the same-baryon-number correlation and the opposite-baryon-number correlation as a function of centrality. The lines are the background due to the baryon number conservation coupled with collective flow. The right plot shows the difference between same-baryon-number correlation and the opposite-baryon-number correlation with background subtracted. The error bars are statistical only.

5.7 Discussion

Alternative theory has been proposed to explain the charge separation effect [70][71]. It is speculated that the local charge conservation combined with collective elliptic flow has a significant contribution to the charge separation effect. Similarly, the local baryon number conservation combined with collective elliptic flow may also have a contribution to the baryon number separation effect we observed in the $\Lambda(\bar{\Lambda})$ azimuthal correlation. We used the formula $v_2\langle\cos(\phi_1-\phi_2)\rangle$ as proposed by model calculations to estimate the background due to the local charge (or baryon number) conservation coupled with collective flow [72].

The $v_2\langle\cos(\phi_1-\phi_2)\rangle$ is calculated for $\Lambda(\bar{\Lambda})-h^{\pm}$, $K^0_S-h^{\pm}$, $K^0_S-p(\bar{p})$, and $\Lambda(\bar{\Lambda})-p(\bar{p})$. The effect is the same for "same sign" and "opposite sign" correlations in the $\Lambda(\bar{\Lambda})-h^{\pm}$, $K^0_S-h^{\pm}$, $K^0_S-p(\bar{p})$ correlations, therefore the effect is cancelled in the difference between the "same sign" and "opposite sign" correlations and will not change our conclusions. The baryon number conservation effect seems to have some contribution to the separation in $\Lambda(\bar{\Lambda})-p(\bar{p})$ correlations. In

central Au+Au collisions at 200 GeV where there is small net baryon density at mid-rapidity, there is little baryon number separation, consistent with no Chiral Vortical Effect. For the most peripheral collision bins, there is a significant baryon number separation. It is expected that in peripheral collisions the effect of baryon number and momentum conservations is also large. More detailed theoretical calculations are needed to address the background from these conservations. The theory does not point the elliptic flow of which particle should be used in the formula for background. Right now, we use the v_2 of pions, that is an estimate of the elliptic flow of the medium. Some other people argue that we should use v_2 of Λs and protons. However, the v_2 of which particle should be used is still an open question. The v_2 of pions is higher than that of protons and Λ baryons at low p_T, but lower at high p_T. The integrated v_2 of pions is closed to that of protons and Λ baryons. No matter the v_2 of which particle we use, our conclusion remains unchanged.

CHAPTER 6

Summary and Discussion

In this thesis, we have carried out two research projects: strangeness production in the RHIC Beam Energy Scan Program, and strange V0 and charged hadron azimuthal correlation.

From the strangeness production in BES program, we have observed many interesting results. The behavior of baryon yield (dN/dy) as a function of $\sqrt{s_{NN}}$ indicates strange baryon production is significantly enhanced due to high net baryon densities in lower energies, while in higher energies the baryon-antibaryon pair production dominates. The R_{CP} and Λ/K^0_S ratio suggest that the medium created in collisions at 19.6, 27, and 39 GeV are similar as that at higher collision energies, such as 62.4, 130, and 200 GeV, but quantitatively different as the medium created at 11.5 and 7.7 GeV. Combined with the elliptic flow analysis from STAR experiment at BES energies [73][74], it may indicate a change of collision dynamics from 19.6 GeV to 11.5 GeV. The statistical thermal model can describe the anti-baryon to baryon ratios well in all the beam energies. However, the statistics for Au+Au collisions at 7.7 and 11.5 GeV are very low, the p_T range of strange particle spectra at those two energies does not exceed 3 GeV/c, and the spectra have considerable statistical errors. The Ω^- and $\bar{\Omega}^+$ signals at those two energies have very low statistics, and we can only obtain the spectra for one or two centrality bins. STAR has proposed a BES Phase II program, which will enhance data statistics by an order of magnitude at those energies. In addition, to study the change of collision dynamics from 19.6 GeV to 11.5 GeV, it is necessary

to take data at an energy between 19.6 and 11.5 GeV. In 2014, STAR took about twenty million events of Au+Au collisions at 14.5 GeV, to fill the gap between 19.6 and 11.5 GeV.

From the strange V0 and charged hadron correlation analysis, we have observed that correlations between neutral strange hadrons and charged hadrons show no charge separation effect, unlike the correlations between two charged hadrons. It indicates that the charge separation effect observed for two charged hadrons has its origin related to electric charges. Results for correlations with K^0_S and $\Lambda(\bar{\Lambda})$ particles reveal no sign of the CME and suggest that strange quarks participate in the chiral dynamics in the same way as up and down quarks do. The $\Lambda(\bar{\Lambda}) - p(\bar{p})$ correlations show a baryon-number separation with respect to the event plane, which is consistent with the expectation for the Chiral Vortical Effect. However, alternative theory has been proposed to explain the separation effect [70][71]. The theory indicates that the local charge (or baryon number) conservation combined with collective elliptic flow has a significant contribution to the charge (or baryon number) separation effect. We used the formula $v_2\langle\cos(\phi_1 - \phi_2)\rangle$ as proposed by model calculations to estimate the background due to the local charge (or baryon number) conservation coupled with collective flow [72]. The effect is the same for "same sign" and "opposite sign" correlations in the $\Lambda(\bar{\Lambda}) - h^{\pm}$, $K^0_S - h^{\pm}$, $K^0_S - p(\bar{p})$ correlations, therefore the effect is cancelled in the difference between the "same sign" and "opposite sign" correlations and will not change our conclusions. However, the baryon number conservation effect seems to have some contribution to the measured $\Lambda(\bar{\Lambda}) - p(\bar{p})$ correlations. More background studies are needed in order to draw a firm conclusion.

APPENDIX A

Data Table of Strange Particle p_T Spectra

Table A.1: The K^0_S Spectra at 19.6 GeV, 0-5% Centrality Bin

p_T	$\frac{1}{2\pi}\frac{dN^2}{Np_T dp_T dy}$	Statistical Error	Systematic Error
0.311505	12.1203	0.399397	0.323974
0.503522	7.8554	0.143836	0.218154
0.700031	4.34517	0.0630936	0.0983203
0.898187	2.11805	0.0303155	0.0550871
1.0971	1.00395	0.0160781	0.0218361
1.29639	0.487202	0.00934715	0.0170163
1.4959	0.245933	0.00508358	0.0167215
1.69555	0.116258	0.00240722	0.0108003
1.89527	0.0503515	0.00109211	0.00561132
2.13886	0.0171447	0.00033811	0.00161482
2.43835	0.00501897	0.000126123	0.000382064
2.77869	0.0014227	4.66034e-05	0.000114167
3.17806	0.00039696	2.10795e-05	8.932e-05
3.57759	8.653e-05	7.47126e-06	2.40363e-05
3.97725	1.49463e-05	3.82365e-06	1.6652e-05

Table A.2: The K^0_S Spectra at 19.6 GeV, 5-10% Centrality Bin

p_T	$\frac{1}{2\pi}\frac{dN^2}{Np_T dp_T dy}$	Statistical Error	Systematic Error
0.311444	9.78609	0.36865	0.490692
0.503448	6.48492	0.137365	0.140766
0.699957	3.59562	0.0617942	0.0750499
0.898126	1.72316	0.0290441	0.0257425
1.09704	0.802226	0.0150125	0.0156091
1.29634	0.386315	0.0085164	0.010336
1.49587	0.197096	0.0047821	0.0134607
1.69551	0.0933237	0.00224852	0.00804014
1.89526	0.0405638	0.00102567	0.00378353
2.13888	0.0133478	0.000298976	0.00136417
2.4384	0.00413568	0.000117283	0.000222696
2.77888	0.00127351	4.63993e-05	0.000111324
3.17834	0.000254878	1.65735e-05	2.72454e-05
3.57798	6.9214e-05	7.15509e-06	1.90481e-05
3.97773	1.52491e-05	3.33087e-06	3.74343e-06

Table A.3: The K^0_S Spectra at 19.6 GeV, 10-20% Centrality Bin

p_T	$\frac{1}{2\pi}\frac{dN^2}{Np_T dp_T dy}$	Statistical Error	Systematic Error
0.311371	7.77176	0.228645	0.182781
0.503351	4.93715	0.080424	0.0665414
0.69986	2.5478	0.0327293	0.0483797
0.898041	1.26608	0.0162582	0.015164
1.09698	0.594387	0.00859169	0.0100875
1.29631	0.27877	0.00472238	0.00803351
1.49584	0.13992	0.00256556	0.00778091
1.69553	0.0687087	0.00131051	0.00531192
1.89528	0.0293012	0.00056197	0.00261451
2.13899	0.0103077	0.000183209	0.000754881
2.43858	0.00308425	6.67438e-05	0.00013544
2.77934	0.000913031	2.57042e-05	9.36167e-05
3.17897	0.000210028	1.06002e-05	3.73797e-05
3.57877	6.3748e-05	4.5666e-06	8.17925e-06
3.97867	1.23822e-05	2.13355e-06	6.63565e-06

Table A.4: The K^0_S Spectra at 19.6 GeV, 20-30% Centrality Bin

p_T	$\frac{1}{2\pi}\frac{dN^2}{Np_T dp_T dy}$	Statistical Error	Systematic Error
0.311334	5.3899	0.186169	0.161943
0.50329	3.2539	0.0617349	0.063875
0.699786	1.65297	0.024697	0.0248405
0.897968	0.825184	0.0126315	0.016496
1.09691	0.377287	0.00644658	0.00686806
1.29623	0.173743	0.00347389	0.00432756
1.49578	0.0936493	0.00209869	0.00515336
1.69547	0.0418575	0.000928509	0.00295503
1.89523	0.0182004	0.000413885	0.00147997
2.13888	0.0064435	0.00013432	0.000603326
2.43851	0.00202664	5.28994e-05	0.000102456
2.77922	0.00053782	1.77624e-05	2.00504e-05
3.17889	0.000111818	6.83295e-06	4.17426e-05
3.5787	4.29593e-05	3.3723e-06	6.18592e-06
3.97864	8.15054e-06	1.62878e-06	3.74574e-06

Table A.5: The K^0_S Spectra at 19.6 GeV, 30-40% Centrality Bin

p_T	$\frac{1}{2\pi}\frac{dN^2}{Np_T dp_T dy}$	Statistical Error	Systematic Error
0.311188	3.37688	0.141568	0.118461
0.503107	2.10743	0.0504825	0.0571779
0.699603	1.05485	0.0200187	0.0191527
0.897809	0.499112	0.00944521	0.00726927
1.09677	0.231053	0.00495171	0.00427813
1.29614	0.103031	0.00256164	0.00213574
1.49571	0.0535619	0.00148904	0.00254822
1.69543	0.0246728	0.000682732	0.00154641
1.89523	0.0113112	0.00033116	0.000887734
2.13897	0.00402519	0.000106896	0.000337913
2.43871	0.00126627	4.10679e-05	9.72718e-05
2.77977	0.000321003	1.33162e-05	1.59648e-05
3.17966	9.1073e-05	5.91259e-06	1.62964e-05
3.57969	2.07491e-05	2.6821e-06	2.58077e-06
3.97982	5.46818e-06	1.10332e-06	9.06006e-07

Table A.6: The K^0_S Spectra at 19.6 GeV, 40-60% Centrality Bin

p_T	$\frac{1}{2\pi}\frac{dN^2}{Np_T dp_T dy}$	Statistical Error	Systematic Error
0.310931	1.75659	0.0782127	0.0830899
0.502765	1.00772	0.0253201	0.0186435
0.699249	0.489498	0.00972622	0.00872564
0.897467	0.228269	0.00464199	0.0035224
1.09645	0.100155	0.00229489	0.00180052
1.29586	0.0474613	0.00131959	0.00106658
1.49547	0.0212358	0.000598924	0.000972256
1.69522	0.010045	0.000293626	0.000531072
1.89506	0.00438129	0.000135645	0.000276865
2.13866	0.00151529	4.1921e-05	9.5398e-05
2.43851	0.000486854	1.69379e-05	3.35296e-05
2.77962	0.000127375	5.62771e-06	6.29769e-06
3.17972	3.58794e-05	2.43466e-06	3.42326e-06
3.57994	6.98148e-06	1.06484e-06	1.00548e-06
3.98023	2.83412e-06	5.29462e-07	3.12289e-07

Table A.7: The K^0_S Spectra at 19.6 GeV, 60-80% Centrality Bin

p_T	$\frac{1}{2\pi}\frac{dN^2}{Np_T dp_T dy}$	Statistical Error	Systematic Error
0.310394	0.535126	0.0328198	0.0432926
0.502094	0.272949	0.00918305	0.00726923
0.698566	0.124785	0.0033674	0.00287044
0.896844	0.0552712	0.001522	0.00143184
1.09593	0.0231417	0.00070581	0.000868654
1.29542	0.00908846	0.000314842	0.000190732
1.49512	0.00472827	0.000190239	0.000255533
1.69496	0.00197122	8.04646e-05	0.000126965
1.89489	0.000840589	3.64556e-05	5.33874e-05
2.13853	0.000363744	1.56347e-05	2.76956e-05
2.4386	8.94648e-05	5.37457e-06	9.09141e-06
2.78023	2.96424e-05	2.35717e-06	2.24316e-06
3.18076	6.25564e-06	9.4653e-07	1.70716e-06
3.58134	1.46387e-06	3.73882e-07	2.75064e-07
3.98195	8.05526e-07	2.46619e-07	1.97182e-07

Table A.8: The K^0_S Spectra at 27 GeV, 0-5% Centrality Bin

p_T	$\frac{1}{2\pi}\frac{dN^2}{Np_T dp_T dy}$	Statistical Error	Systematic Error
0.311493	13.5148	0.396707	0.597942
0.50351	8.65607	0.138448	0.1776
0.700043	4.79034	0.060605	0.0826329
0.898224	2.38172	0.029962	0.0441235
1.09716	1.15121	0.016115	0.0232769
1.29648	0.54561	0.00899203	0.0208585
1.49601	0.297256	0.00593424	0.0194553
1.69568	0.135994	0.00262134	0.012551
1.89544	0.0624033	0.00124256	0.00629081
2.13932	0.0222058	0.000382889	0.00169602
2.43889	0.00650774	0.000129436	0.00033043
2.7798	0.00203916	4.68128e-05	0.000183055
3.17936	0.000451609	1.74793e-05	4.36989e-05
3.5791	0.0001289	8.25139e-06	2.88723e-05
3.97894	4.78647e-05	3.91028e-06	9.28987e-06
4.45326	9.92758e-06	1.41941e-06	2.43855e-06

Table A.9: The K^0_S Spectra at 27 GeV, 5-10% Centrality Bin

p_T	$\frac{1}{2\pi}\frac{dN^2}{Np_T dp_T dy}$	Statistical Error	Systematic Error
0.311481	11.0076	0.347464	0.282399
0.503497	7.13148	0.124946	0.166228
0.700031	3.95334	0.0548882	0.0702327
0.898224	1.92886	0.0263657	0.0279042
1.09716	0.967844	0.0151913	0.0202647
1.29649	0.458527	0.00842901	0.0149867
1.49604	0.234427	0.00501889	0.0144511
1.69571	0.114689	0.00248942	0.0101083
1.89548	0.0490531	0.00105166	0.00468544
2.13941	0.0184902	0.000348544	0.00134349
2.43902	0.00575859	0.000124536	0.000366188
2.7801	0.00169986	4.17421e-05	0.000148107
3.17973	0.000448818	1.78522e-05	4.92937e-05
3.57952	9.90268e-05	6.54672e-06	8.97853e-06
3.97941	3.37406e-05	3.44922e-06	1.48551e-05
4.45443	6.04747e-06	1.28894e-06	2.93292e-06

Table A.10: The K^0_S Spectra at 27 GeV, 10-20% Centrality Bin

p_T	$\frac{1}{2\pi}\frac{dN^2}{Np_T dp_T dy}$	Statistical Error	Systematic Error
0.311383	8.85438	0.218829	0.247659
0.503375	5.47894	0.0739863	0.0772662
0.699908	2.89907	0.030775	0.0281214
0.898114	1.44247	0.0152642	0.0190545
1.09708	0.686992	0.00811519	0.0129128
1.29642	0.332197	0.00464819	0.0080486
1.49599	0.180002	0.00304431	0.010566
1.6957	0.0832117	0.00138001	0.00653665
1.89548	0.0367046	0.000611312	0.00308822
2.13948	0.0134589	0.000195643	0.00103396
2.43917	0.00439495	7.32729e-05	0.000275003
2.78047	0.00127125	2.42031e-05	6.68534e-05
3.18027	0.000316096	9.18591e-06	1.40711e-05
3.58021	0.000100798	4.57379e-06	1.58807e-05
3.98024	2.31166e-05	1.86671e-06	2.26825e-06
4.45652	4.04084e-06	6.53499e-07	1.32887e-06

Table A.11: The K^0_S Spectra at 27 GeV, 20-30% Centrality Bin

p_T	$\frac{1}{2\pi}\frac{dN^2}{Np_T dp_T dy}$	Statistical Error	Systematic Error
0.311285	5.76694	0.160523	0.152544
0.503253	3.57289	0.0551939	0.0433116
0.699786	1.93762	0.0240126	0.0280606
0.898004	0.967821	0.0120893	0.0120019
1.09699	0.452189	0.00636228	0.00630966
1.29637	0.214715	0.00350263	0.00646185
1.49597	0.11018	0.00213966	0.00540941
1.6957	0.0525681	0.00100095	0.00367188
1.89551	0.0241242	0.000477528	0.00187511
2.13961	0.0090084	0.000154534	0.000681777
2.43939	0.0028936	5.65853e-05	0.000141485
2.78101	0.000876288	1.97207e-05	5.61193e-05
3.18096	0.000257297	8.23772e-06	3.76981e-05
3.58105	6.84073e-05	3.6129e-06	1.83938e-05
3.98122	1.7785e-05	1.5745e-06	5.04578e-06
4.45894	3.80905e-06	5.97231e-07	1.79947e-06

Table A.12: The K^0_S Spectra at 27 GeV, 30-40% Centrality Bin

p_T	$\frac{1}{2\pi}\frac{dN^2}{Np_T dp_T dy}$	Statistical Error	Systematic Error
0.311017	4.39122	0.156799	0.143757
0.502899	2.39608	0.045746	0.0453748
0.699432	1.2818	0.0200177	0.0144804
0.897687	0.597874	0.00915677	0.00609491
1.09672	0.281679	0.00482514	0.00448447
1.29615	0.130155	0.00260475	0.00270642
1.49579	0.0656179	0.00157181	0.00432266
1.69557	0.0314593	0.000732333	0.0019045
1.89544	0.0147243	0.000358037	0.00107701
2.13959	0.00534762	0.000111206	0.000405486
2.4395	0.00175919	4.21996e-05	6.71544e-05
2.78148	0.000523187	1.38387e-05	2.41722e-05
3.1817	0.000153075	5.77819e-06	1.60064e-05
3.58203	5.40609e-05	2.79438e-06	1.55494e-05
3.9824	1.27492e-05	1.24422e-06	3.61337e-06
4.46196	3.56201e-06	5.12412e-07	1.69245e-06

Table A.13: The K^0_S Spectra at 27 GeV, 40-60% Centrality Bin

p_T	$\frac{1}{2\pi}\frac{dN^2}{Np_T dp_T dy}$	Statistical Error	Systematic Error
0.310907	2.13525	0.0778577	0.0555707
0.502765	1.19391	0.0240351	0.0161109
0.699286	0.587115	0.00950083	0.0101913
0.89754	0.269559	0.00431877	0.00312618
1.09659	0.124635	0.00226172	0.00131242
1.29603	0.0564968	0.00117853	0.00085526
1.49568	0.0290938	0.00073538	0.00109577
1.69548	0.0139247	0.000354458	0.000921278
1.89536	0.00645799	0.000168647	0.000452337
2.13943	0.00233044	5.11682e-05	0.00016028
2.43937	0.000738642	1.85183e-05	2.74997e-05
2.78132	0.000231017	6.33556e-06	1.43275e-05
3.18161	6.35737e-05	2.58495e-06	7.11828e-06
3.58199	1.65697e-05	1.1416e-06	1.64372e-06
3.98242	5.86938e-06	5.6376e-07	4.70763e-07
4.46211	1.24058e-06	1.99548e-07	1.16823e-07

Table A.14: The K^0_S Spectra at 27 GeV, 60-80% Centrality Bin

p_T	$\frac{1}{2\pi}\frac{dN^2}{Np_T dp_T dy}$	Statistical Error	Systematic Error
0.310541	0.592439	0.0281184	0.024368
0.502289	0.329069	0.0088728	0.0110548
0.69881	0.154255	0.00338661	0.00252164
0.897101	0.0671772	0.00145127	0.00114133
1.0962	0.0290112	0.000706149	0.000882077
1.2957	0.0131812	0.000382578	0.000296481
1.49542	0.00635311	0.000212921	0.000238175
1.69526	0.00297831	0.000104066	0.000178486
1.89518	0.00127945	4.54411e-05	7.71297e-05
2.13919	0.000491911	1.61535e-05	2.67672e-05
2.43926	0.000168504	6.59097e-06	7.30763e-06
2.78137	4.92986e-05	2.32989e-06	6.29021e-06
3.18189	1.33351e-05	1.01945e-06	1.20165e-06
3.58246	3.2087e-06	4.46961e-07	5.549e-07
3.98306	1.25003e-06	2.51616e-07	2.92148e-07

Table A.15: The Λ Spectra at 19.6 GeV, 0-5% Centrality Bin

p_T	$\frac{1}{2\pi}\frac{dN^2}{Np_T dp_T dy}$	Statistical Error	Systematic Error
0.506903	3.04543	0.150607	0.182409
0.703217	2.45842	0.0582922	0.0699425
0.900995	1.75481	0.0353148	0.0358348
1.09951	1.1845	0.0238759	0.027498
1.29847	0.713785	0.0153108	0.0107966
1.49771	0.434547	0.0099784	0.0164789
1.69715	0.244662	0.00552442	0.0061878
1.89671	0.119867	0.0025502	0.00250212
2.1417	0.0537312	0.000944258	0.00153364
2.44085	0.019418	0.000354782	0.000452074
2.78259	0.00570048	0.000173929	0.000184429
3.18152	0.00138018	3.31497e-05	6.98853e-05
3.58074	0.000281531	1.75064e-05	7.09165e-05
3.98016	8.61997e-05	5.57443e-06	2.18037e-05
4.45489	1.77134e-05	1.82756e-06	4.95809e-06

Table A.16: The Λ Spectra at 19.6 GeV, 5-10% Centrality Bin

p_T	$\frac{1}{2\pi}\frac{dN^2}{Np_T dp_T dy}$	Statistical Error	Systematic Error
0.506903	2.67891	0.151177	0.191248
0.703217	1.84938	0.0482116	0.0507414
0.900983	1.38422	0.0309566	0.0284346
1.09951	0.937015	0.0211903	0.0137772
1.29847	0.585769	0.0145018	0.00951201
1.49771	0.340112	0.00919081	0.0115022
1.69714	0.196668	0.00517221	0.00452073
1.89671	0.0965539	0.00241511	0.00163141
2.14168	0.0426722	0.000865059	0.000728414
2.44084	0.01514	0.000318012	0.000377207
2.78256	0.00447458	9.12886e-05	0.000119297
3.1815	0.00114094	3.10539e-05	8.35071e-05
3.58073	0.000246615	1.42188e-05	2.81398e-05
3.98013	6.30455e-05	4.75243e-06	6.28302e-06
4.45484	8.23933e-06	1.48694e-06	2.09869e-06

Table A.17: The Λ Spectra at 19.6 GeV, 10-20% Centrality Bin

p_T	$\frac{1}{2\pi}\frac{dN^2}{Np_T dp_T dy}$	Statistical Error	Systematic Error
0.506879	2.10778	0.0886561	0.17678
0.703192	1.48341	0.0297038	0.0400301
0.900958	1.04843	0.0179065	0.0201238
1.09947	0.682338	0.0117071	0.0149747
1.29843	0.423548	0.0079632	0.00868714
1.49766	0.239472	0.00486028	0.0052351
1.6971	0.12894	0.00254389	0.00229315
1.89666	0.0668698	0.0012817	0.00148153
2.14159	0.0306187	0.000481449	0.000627365
2.44074	0.0107563	0.00017812	0.000225502
2.78237	0.00326101	5.18701e-05	7.46386e-05
3.1813	0.000777124	1.6655e-05	2.62233e-05
3.58052	0.000194643	9.61347e-06	2.24612e-05
3.97993	4.01299e-05	2.75683e-06	4.39442e-06
4.4544	7.75951e-06	8.56451e-07	1.26606e-06

Table A.18: The Λ Spectra at 19.6 GeV, 20-30% Centrality Bin

p_T	$\frac{1}{2\pi}\frac{dN^2}{Np_T dp_T dy}$	Statistical Error	Systematic Error
0.50683	1.37922	0.0675577	0.0766315
0.703131	1.00664	0.0243479	0.0315445
0.900885	0.689646	0.0145046	0.0149738
1.0994	0.431909	0.00903254	0.00632716
1.29835	0.247467	0.00553152	0.00276087
1.49759	0.150388	0.00375469	0.00369851
1.69702	0.0776524	0.00183465	0.00198924
1.89656	0.0409432	0.000963239	0.000750587
2.14137	0.0178289	0.000340723	0.000217003
2.44052	0.00621579	0.000121792	0.000128264
2.78199	0.00190444	3.71259e-05	3.69254e-05
3.18093	0.000441897	1.1361e-05	1.44304e-05
3.58015	0.000109712	4.7428e-06	2.90795e-05
3.97955	2.98079e-05	2.1292e-06	2.51188e-06
4.45357	4.33469e-06	6.0142e-07	5.80996e-07

Table A.19: The Λ Spectra at 19.6 GeV, 30-40% Centrality Bin

p_T	$\frac{1}{2\pi}\frac{dN^2}{Np_T dp_T dy}$	Statistical Error	Systematic Error
0.506769	0.918752	0.0543414	0.0469027
0.703046	0.637276	0.0182896	0.0113391
0.900787	0.444075	0.0113331	0.010872
1.09929	0.270239	0.00707779	0.00631735
1.29824	0.156311	0.00438163	0.00193443
1.49745	0.0801806	0.00256075	0.00130173
1.69688	0.0465958	0.00143956	0.000652509
1.89644	0.0228069	0.000664768	0.000377441
2.14107	0.00967327	0.00023052	0.00016318
2.44021	0.00359009	9.24855e-05	4.90101e-05
2.78144	0.00100986	2.48445e-05	1.64048e-05
3.18036	0.000264253	8.90207e-06	1.68313e-05
3.57957	4.84853e-05	3.05708e-06	5.22206e-06
3.97897	1.18159e-05	1.33274e-06	3.12586e-06
4.45235	2.91448e-06	5.10008e-07	5.18037e-07

Table A.20: The Λ Spectra at 19.6 GeV, 40-60% Centrality Bin

p_T	$\frac{1}{2\pi}\frac{dN^2}{Np_T dp_T dy}$	Statistical Error	Systematic Error
0.506561	0.451482	0.0281096	0.017483
0.702777	0.311467	0.0096842	0.00791095
0.900494	0.189716	0.00509514	0.00446901
1.09897	0.114327	0.00314701	0.00127294
1.29791	0.0614233	0.00185425	0.00128873
1.49714	0.031437	0.00103084	0.000506114
1.69658	0.016339	0.000513877	0.00024124
1.89615	0.00828243	0.000255175	0.000186544
2.14049	0.00353054	9.03102e-05	6.26155e-05
2.43972	0.00124784	3.41961e-05	3.55281e-05
2.78078	0.000352345	9.76355e-06	1.22704e-05
3.17995	7.76656e-05	3.1036e-06	3.3225e-06
3.5794	1.89365e-05	1.32124e-06	1.64817e-06
3.97903	3.50542e-06	5.13971e-07	8.72376e-07
4.45312	1.02767e-06	2.12521e-07	2.89265e-07

Table A.21: The Λ Spectra at 19.6 GeV, 60-80% Centrality Bin

p_T	$\frac{1}{2\pi}\frac{dN^2}{Np_T dp_T dy}$	Statistical Error	Systematic Error
0.506	0.119652	0.00976175	0.0128927
0.702081	0.0771028	0.00324604	0.00322992
0.899701	0.045747	0.00172794	0.00167941
1.09814	0.0222399	0.000835712	0.00088614
1.29708	0.0111211	0.000456217	0.000334942
1.49633	0.00584112	0.000265428	0.000175933
1.69579	0.00265001	0.000117008	4.11491e-05
1.89543	0.00132067	5.89667e-05	2.25862e-05
2.13904	0.000462401	1.71536e-05	3.00162e-05
2.43847	0.00014782	6.57798e-06	9.40078e-06
2.77903	4.36185e-05	2.41874e-06	2.99695e-06
3.17872	7.29622e-06	8.09034e-07	7.91093e-07
3.57867	1.78213e-06	3.90285e-07	8.93268e-07

Table A.22: The $\bar{\Lambda}$ Spectra at 19.6 GeV, 0-5% Centrality Bin

p_T	$\frac{1}{2\pi}\frac{dN^2}{Np_T dp_T dy}$	Statistical Error	Systematic Error
0.506952	0.382902	0.0231583	0.0294962
0.703278	0.328817	0.00948414	0.0161201
0.901068	0.245388	0.00576911	0.00980325
1.09959	0.186102	0.00430716	0.00712045
1.29857	0.118581	0.00285875	0.00463088
1.49781	0.0722651	0.00178749	0.00292055
1.69725	0.0397791	0.000938512	0.00148089
1.89682	0.0206244	0.000488738	0.000687217
2.14193	0.00915124	0.000185028	0.000276913
2.44109	0.00297192	6.90679e-05	0.000115638
2.78301	0.00092804	2.53847e-05	7.45493e-05
3.18196	0.000201866	9.54691e-06	4.26293e-05
3.5812	4.68246e-05	4.01083e-06	6.04918e-06
3.9806	8.15064e-06	1.47748e-06	2.37858e-06

Table A.23: The $\bar{\Lambda}$ Spectra at 19.6 GeV, 5-10% Centrality Bin

p_T	$\frac{1}{2\pi}\frac{dN^2}{Np_T dp_T dy}$	Statistical Error	Systematic Error
0.50694	0.322331	0.0215696	0.0287971
0.703278	0.276341	0.00892322	0.0165312
0.901056	0.215119	0.00577291	0.010574
1.09958	0.146788	0.00369636	0.00576395
1.29855	0.101984	0.0027324	0.00382459
1.4978	0.0586693	0.0016323	0.0021675
1.69724	0.0321215	0.000880941	0.00143359
1.8968	0.0167582	0.000453442	0.000538962
2.1419	0.00722804	0.00017101	0.00031642
2.44106	0.00258055	6.7394e-05	9.46517e-05
2.78294	0.000701764	2.18224e-05	3.30614e-05
3.1819	0.0001804	9.05586e-06	3.20537e-05
3.58112	3.72813e-05	3.72146e-06	4.09468e-06
3.98052	8.94492e-06	1.67385e-06	2.75043e-06

Table A.24: The $\bar{\Lambda}$ Spectra at 19.6 GeV, 10-20% Centrality Bin

p_T	$\frac{1}{2\pi}\frac{dN^2}{Np_T dp_T dy}$	Statistical Error	Systematic Error
0.506903	0.304138	0.015058	0.0172024
0.703217	0.221936	0.00525791	0.00907565
0.900983	0.169849	0.00338322	0.00504217
1.09951	0.117116	0.00230113	0.00414403
1.29847	0.0725787	0.00147646	0.00204323
1.49771	0.0447074	0.00097827	0.00123723
1.69714	0.0235454	0.000506674	0.000801431
1.89671	0.0120225	0.000255257	0.000386557
2.14168	0.00525091	9.67961e-05	0.000154896
2.44084	0.00183741	3.81012e-05	9.12834e-05
2.78256	0.000508925	1.2464e-05	2.74387e-05
3.1815	0.000122877	5.21803e-06	1.10113e-05
3.58073	2.72313e-05	2.15662e-06	5.3934e-06
3.98013	6.79208e-06	9.56727e-07	1.26386e-06

Table A.25: The $\bar{\Lambda}$ Spectra at 19.6 GeV, 20-30% Centrality Bin

p_T	$\frac{1}{2\pi}\frac{dN^2}{Np_T dp_T dy}$	Statistical Error	Systematic Error
0.506793	0.229338	0.0124348	0.00868095
0.703082	0.174421	0.00466258	0.00524854
0.900824	0.118242	0.00268527	0.00229382
1.09932	0.0819933	0.00188456	0.00183257
1.29827	0.0467688	0.00112015	0.00128361
1.4975	0.0300538	0.000800205	0.00121853
1.69692	0.0141651	0.000357935	0.000673269
1.89648	0.00730812	0.000182189	0.000245356
2.14117	0.00317803	6.82426e-05	6.90376e-05
2.44032	0.00110714	2.75871e-05	4.3529e-05
2.78161	0.000289029	8.71462e-06	1.65788e-05
3.18055	6.45657e-05	3.40465e-06	4.37921e-06
3.57975	1.17151e-05	1.30865e-06	1.37705e-06
3.97916	2.93253e-06	6.31515e-07	4.35264e-07

Table A.26: The $\bar{\Lambda}$ Spectra at 19.6 GeV, 30-40% Centrality Bin

p_T	$\frac{1}{2\pi}\frac{dN^2}{Np_T dp_T dy}$	Statistical Error	Systematic Error
0.506683	0.174703	0.0121276	0.0144781
0.702936	0.125661	0.00442733	0.00484368
0.900653	0.0810703	0.00242753	0.00209249
1.09913	0.0552675	0.00166963	0.00154736
1.29807	0.0279235	0.000852711	0.000671211
1.49728	0.0160539	0.000545667	0.000400424
1.6967	0.00922346	0.000305523	0.00019564
1.89625	0.00426295	0.000141281	0.000144074
2.14063	0.00173892	4.93874e-05	4.77447e-05
2.43976	0.00056975	1.92906e-05	9.7756e-06
2.78063	0.000161644	6.44264e-06	5.63835e-06
3.17955	3.36495e-05	2.5792e-06	5.90145e-06
3.57875	8.03203e-06	1.08154e-06	1.91645e-06
3.97814	7.40451e-07	2.76573e-07	4.19314e-07

Table A.27: The $\bar{\Lambda}$ Spectra at 19.6 GeV, 40-60% Centrality Bin

p_T	$\frac{1}{2\pi}\frac{dN^2}{Np_T dp_T dy}$	Statistical Error	Systematic Error
0.506464	0.112664	0.00787363	0.00787161
0.702655	0.0686992	0.00227017	0.00218402
0.900336	0.044203	0.00131147	0.000938912
1.09879	0.0235759	0.000674365	0.000631224
1.29771	0.0127357	0.000398814	0.000302412
1.49693	0.00707935	0.000248299	0.000280061
1.69634	0.0035241	0.000117983	7.62034e-05
1.8959	0.00162525	5.49924e-05	3.71296e-05
2.1399	0.000643354	1.92031e-05	1.79361e-05
2.4391	0.000219409	7.99192e-06	1.13703e-05
2.77961	6.05266e-05	2.81268e-06	4.13691e-06
3.1787	1.31685e-05	1.17361e-06	1.61265e-06
3.57808	2.35163e-06	4.79198e-07	3.12863e-07
3.97764	4.50704e-07	1.5847e-07	1.85639e-07

Table A.28: The $\bar{\Lambda}$ Spectra at 19.6 GeV, 60-80% Centrality Bin

p_T	$\frac{1}{2\pi}\frac{dN^2}{Np_T dp_T dy}$	Statistical Error	Systematic Error
0.505731	0.0424263	0.0039827	0.00522111
0.70174	0.0222469	0.000996274	0.000591641
0.899323	0.011552	0.000456678	0.000382278
1.09774	0.00560298	0.000220899	0.000152436
1.29667	0.00289358	0.000124653	6.53995e-05
1.49594	0.00140398	6.87638e-05	4.57792e-05
1.69543	0.000574013	2.76196e-05	4.10763e-05
1.89507	0.000287377	1.5713e-05	1.16047e-05
2.13833	0.000107489	5.76398e-06	2.3267e-06
2.43785	2.84929e-05	2.36776e-06	3.5305e-06
2.77812	6.80263e-06	9.25078e-07	5.74429e-07
3.178	1.28947e-06	3.87324e-07	5.01395e-07

Table A.29: The Λ Spectra at 27 GeV, 0-5% Centrality Bin

p_T	$\frac{1}{2\pi}\frac{dN^2}{Np_T dp_T dy}$	Statistical Error	Systematic Error
0.506964	2.91077	0.133411	0.270985
0.703302	2.14565	0.0449534	0.0935926
0.90108	1.56177	0.0277902	0.0445585
1.09962	1.10625	0.0195461	0.0248028
1.29858	0.685575	0.0128229	0.0173452
1.49783	0.415031	0.00861428	0.00930844
1.69727	0.239869	0.00482066	0.00530374
1.89683	0.12622	0.00244864	0.00289344
2.14199	0.0568962	0.000883321	0.00131972
2.44115	0.02072	0.000331507	0.000543457
2.7831	0.00624643	9.51996e-05	0.000326695
3.18205	0.00153182	2.93013e-05	7.60025e-05
3.58128	0.000373394	1.05716e-05	3.6085e-05
3.98068	8.79586e-05	4.49184e-06	1.12911e-05
4.45605	1.65191e-05	1.42925e-06	6.66032e-06
5.05491	3.15125e-06	5.24213e-07	6.85854e-07

Table A.30: The Λ Spectra at 27 GeV, 5-10% Centrality Bin

p_T	$\frac{1}{2\pi}\frac{dN^2}{Np_T dp_T dy}$	Statistical Error	Systematic Error
0.506964	2.22049	0.106727	0.296598
0.703302	1.74994	0.0387733	0.0772975
0.90108	1.31748	0.025087	0.0415065
1.09962	0.903549	0.0169088	0.0256679
1.29858	0.55438	0.0110159	0.0189377
1.49783	0.340343	0.00775466	0.00947808
1.69727	0.200828	0.00455393	0.0065778
1.89683	0.100574	0.00212763	0.00253432
2.14199	0.045419	0.000789885	0.00107228
2.44115	0.0163311	0.000284069	0.000405658
2.7831	0.00517875	8.61533e-05	0.00019659
3.18206	0.00123	2.56272e-05	5.62303e-05
3.58128	0.000305164	9.59698e-06	2.89087e-05
3.98069	7.33606e-05	4.17886e-06	8.47374e-06
4.45605	1.52281e-05	1.39905e-06	4.22924e-06
5.05493	1.64964e-06	3.70574e-07	4.1496e-07

Table A.31: The Λ Spectra at 27 GeV, 10-20% Centrality Bin

p_T	$\frac{1}{2\pi}\frac{dN^2}{Np_T dp_T dy}$	Statistical Error	Systematic Error
0.506952	1.84577	0.0668798	0.121704
0.70329	1.347	0.0228575	0.0310586
0.90108	0.993115	0.0145201	0.0199444
1.0996	0.669203	0.00977327	0.0117199
1.29858	0.411675	0.00641392	0.00797065
1.49782	0.241795	0.00425345	0.00672524
1.69726	0.128955	0.00213467	0.00214612
1.89683	0.0698843	0.00113117	0.00145191
2.14197	0.0320438	0.000421545	0.000624681
2.44113	0.0120916	0.000165445	0.000279698
2.78307	0.00364087	4.75475e-05	8.7422e-05
3.18203	0.000925104	1.50462e-05	3.19456e-05
3.58124	0.000240609	5.62756e-06	1.74144e-05
3.98066	6.14705e-05	2.48237e-06	6.74989e-06
4.45597	1.00448e-05	7.84424e-07	3.49536e-06

Table A.32: The Λ Spectra at 27 GeV, 20-30% Centrality Bin

p_T	$\frac{1}{2\pi}\frac{dN^2}{Np_T dp_T dy}$	Statistical Error	Systematic Error
0.506927	1.41417	0.0601916	0.0686867
0.703253	0.950441	0.0183346	0.0311708
0.901031	0.663512	0.0111276	0.012643
1.09955	0.437285	0.0073339	0.0108383
1.29852	0.260703	0.00474431	0.00362635
1.49777	0.15062	0.00310057	0.00278365
1.6972	0.0835296	0.0016514	0.00144452
1.89676	0.0443475	0.000861959	0.000622852
2.14182	0.019937	0.000313234	0.000378482
2.44098	0.00726405	0.000116769	0.000115615
2.78281	0.00227343	3.48689e-05	6.82534e-05
3.18176	0.000573633	1.10488e-05	1.60107e-05
3.58099	0.000150965	4.31995e-06	1.20357e-05
3.98039	3.78576e-05	1.8209e-06	2.59942e-06
4.45539	6.82292e-06	5.71995e-07	7.43187e-07
5.05427	8.78699e-07	1.99417e-07	2.82261e-07

Table A.33: The Λ Spectra at 27 GeV, 30-40% Centrality Bin

p_T	$\frac{1}{2\pi}\frac{dN^2}{Np_T dp_T dy}$	Statistical Error	Systematic Error
0.506866	0.914463	0.0461105	0.0488241
0.703168	0.624633	0.0146989	0.015063
0.900946	0.413689	0.00832226	0.00842395
1.09946	0.255933	0.00514017	0.00435061
1.29842	0.148995	0.003247	0.00219528
1.49767	0.0858376	0.00216563	0.00126369
1.69711	0.047581	0.00116519	0.000660177
1.89667	0.0254699	0.00060554	0.000362607
2.14164	0.0108157	0.000209128	0.000153234
2.44084	0.0041253	8.32034e-05	7.09296e-05
2.78261	0.00131656	2.51998e-05	4.37921e-05
3.18163	0.000319089	7.87195e-06	1.01775e-05
3.58094	8.35437e-05	2.99658e-06	3.73978e-06
3.98043	2.19849e-05	1.41864e-06	2.86501e-06
4.45568	4.99071e-06	4.81811e-07	1.37652e-06
5.05482	5.07583e-07	1.5564e-07	2.89767e-07

Table A.34: The Λ Spectra at 27 GeV, 40-60% Centrality Bin

p_T	$\frac{1}{2\pi}\frac{dN^2}{Np_T dp_T dy}$	Statistical Error	Systematic Error
0.506573	0.44558	0.0227728	0.0327217
0.702802	0.311527	0.00804372	0.0124731
0.900531	0.190184	0.00415958	0.00567363
1.09904	0.113062	0.00249267	0.00255646
1.298	0.0649417	0.00157917	0.00149858
1.49727	0.0335442	0.000893465	0.000789114
1.69675	0.018245	0.000473956	0.00047439
1.89634	0.00930793	0.000236861	0.000160166
2.14104	0.00409336	8.60636e-05	7.69801e-05
2.44038	0.00142436	3.02349e-05	2.38163e-05
2.78214	0.000458527	9.71474e-06	9.86979e-06
3.18155	0.000116212	3.11945e-06	4.49976e-06
3.58123	3.13228e-05	1.27356e-06	1.45189e-06
3.9811	7.68234e-06	5.59909e-07	4.46344e-07
4.45808	1.4118e-06	1.95333e-07	1.55854e-07
5.05833	1.97548e-07	6.51943e-08	8.31659e-08

Table A.35: The Λ Spectra at 27 GeV, 60-80% Centrality Bin

p_T	$\frac{1}{2\pi}\frac{dN^2}{Np_T dp_T dy}$	Statistical Error	Systematic Error
0.506171	0.13354	0.00939271	0.00849798
0.702313	0.0796228	0.00268914	0.00369036
0.899969	0.0458414	0.00135093	0.00142028
1.09844	0.0248159	0.000749574	0.000652817
1.29741	0.012725	0.000422735	0.000435817
1.49667	0.00606759	0.000219018	0.000130655
1.69616	0.0034145	0.000129717	0.000121099
1.89579	0.00158172	5.54098e-05	5.21242e-05
2.13988	0.000635531	1.93774e-05	9.31727e-06
2.43935	0.000222981	7.44093e-06	6.21283e-06
2.78057	6.72571e-05	2.42208e-06	2.97562e-06
3.18027	1.4226e-05	8.62961e-07	1.28457e-06
3.58022	3.31917e-06	3.7337e-07	2.82299e-07
3.98033	5.15742e-07	1.44369e-07	1.98528e-07

Table A.36: The $\bar{\Lambda}$ Spectra at 27 GeV, 0-5% Centrality Bin

p_T	$\frac{1}{2\pi}\frac{dN^2}{Np_T dp_T dy}$	Statistical Error	Systematic Error
0.507025	0.525637	0.0319096	0.0484824
0.703375	0.468099	0.0118168	0.0202459
0.901178	0.365031	0.0074058	0.0120194
1.09973	0.266265	0.00509428	0.0102759
1.2987	0.179952	0.00367391	0.0042521
1.49796	0.111866	0.00246122	0.00360306
1.69741	0.0656503	0.0013916	0.00218298
1.89697	0.0345786	0.000707481	0.00129831
2.1423	0.0149772	0.000254868	0.000432885
2.44148	0.00558511	0.000101182	0.000231208
2.78367	0.00165219	3.1761e-05	7.95591e-05
3.18264	0.000371845	1.14282e-05	3.45889e-05
3.58187	7.11952e-05	9.5122e-06	1.42043e-05
3.98128	1.94129e-05	1.87438e-06	9.92708e-06
4.45733	2.97219e-06	6.72803e-07	1.17728e-06

Table A.37: The $\bar{\Lambda}$ Spectra at 27 GeV, 5-10% Centrality Bin

p_T	$\frac{1}{2\pi}\frac{dN^2}{Np_T dp_T dy}$	Statistical Error	Systematic Error
0.507001	0.493737	0.0302959	0.0343701
0.703363	0.415937	0.0110643	0.0226276
0.901154	0.318249	0.00685517	0.0143969
1.09969	0.227765	0.0046933	0.0109601
1.29868	0.151825	0.00332223	0.00708869
1.49792	0.0891936	0.00213945	0.00397605
1.69737	0.0506859	0.00112751	0.00186266
1.89693	0.0271495	0.000606574	0.000974325
2.14221	0.0123692	0.000229505	0.000533421
2.44138	0.00465751	9.15243e-05	0.000216506
2.78351	0.00129335	3.21072e-05	6.98637e-05
3.18248	0.000321057	9.95992e-06	3.78224e-05
3.58171	8.33375e-05	4.30923e-06	2.05072e-05
3.98112	2.06471e-05	1.93257e-06	6.17297e-06
4.45698	4.37354e-06	6.79068e-07	1.99695e-06

Table A.38: The $\bar{\Lambda}$ Spectra at 27 GeV, 10-20% Centrality Bin

p_T	$\frac{1}{2\pi}\frac{dN^2}{Np_T dp_T dy}$	Statistical Error	Systematic Error
0.506976	0.411332	0.0167228	0.0371211
0.703314	0.330979	0.00652851	0.0134225
0.901105	0.256058	0.0041331	0.00713493
1.09964	0.172624	0.00269916	0.00511882
1.29861	0.109989	0.00182778	0.00324791
1.49787	0.0684699	0.00127587	0.0018609
1.69731	0.0383202	0.00068174	0.00149162
1.89687	0.0201275	0.00034995	0.000540019
2.14206	0.00895384	0.0001289	0.000246517
2.44124	0.00323511	5.01393e-05	8.96129e-05
2.78326	0.00099227	1.60235e-05	5.42652e-05
3.18221	0.000232707	5.90375e-06	2.50444e-05
3.58144	5.70365e-05	2.38857e-06	4.97365e-06
3.98085	1.3499e-05	1.01239e-06	1.55469e-06
4.45639	2.20018e-06	3.13762e-07	5.03975e-07

Table A.39: The $\bar{\Lambda}$ Spectra at 27 GeV, 20-30% Centrality Bin

p_T	$\frac{1}{2\pi}\frac{dN^2}{Np_T dp_T dy}$	Statistical Error	Systematic Error
0.506927	0.337764	0.0158738	0.0194188
0.703253	0.241661	0.00521382	0.00779835
0.901031	0.18476	0.00347087	0.00536355
1.09955	0.119749	0.00219562	0.00162581
1.29852	0.0737258	0.00143109	0.00155999
1.49776	0.0436679	0.000956725	0.00118554
1.6972	0.0241968	0.000511236	0.000566246
1.89676	0.0125632	0.000258716	0.000249578
2.14182	0.00557942	9.4473e-05	0.000139181
2.44098	0.00198572	3.66321e-05	5.83019e-05
2.78279	0.000611525	1.17724e-05	2.7759e-05
3.18174	0.000156901	4.56713e-06	1.38412e-05
3.58098	3.40406e-05	1.72463e-06	5.99043e-06
3.98038	8.44137e-06	7.88814e-07	2.1119e-06
4.45537	1.05184e-06	2.21902e-07	9.91271e-07

Table A.40: The $\bar{\Lambda}$ Spectra at 27 GeV, 30-40% Centrality Bin

p_T	$\frac{1}{2\pi}\frac{dN^2}{Np_T dp_T dy}$	Statistical Error	Systematic Error
0.506854	0.2704	0.0153295	0.0176053
0.703156	0.180101	0.00497218	0.00566702
0.900909	0.123292	0.00288145	0.00233907
1.09942	0.0781383	0.00182119	0.00150869
1.29837	0.045343	0.00111611	0.00127471
1.49761	0.0267929	0.000725506	0.000589666
1.69704	0.0146692	0.000387726	0.000387549
1.8966	0.00769133	0.000206143	0.00020023
2.14144	0.00312277	6.67278e-05	0.000100057
2.4406	0.00114695	2.65967e-05	3.66986e-05
2.78211	0.000338047	8.345e-06	1.70054e-05
3.18106	8.81689e-05	3.22952e-06	5.86313e-06
3.58027	2.22132e-05	1.42361e-06	1.37646e-06
3.97967	5.75879e-06	6.51395e-07	5.05542e-07
4.45385	1.19293e-06	2.29912e-07	1.93392e-07

Table A.41: The $\bar{\Lambda}$ Spectra at 27 GeV, 40-60% Centrality Bin

p_T	$\frac{1}{2\pi}\frac{dN^2}{Np_T dp_T dy}$	Statistical Error	Systematic Error
0.506683	0.142294	0.00764821	0.00857243
0.702936	0.0998529	0.00276433	0.00286522
0.900653	0.0637063	0.00152198	0.00158754
1.09913	0.037674	0.000904393	0.000632173
1.29807	0.0214926	0.000557484	0.000611179
1.49728	0.0113392	0.000318304	0.000319532
1.69671	0.00593155	0.000165223	0.000116117
1.89626	0.00292735	7.96319e-05	5.40122e-05
2.14067	0.00125668	2.89463e-05	1.96325e-05
2.43981	0.000429235	1.06897e-05	1.01169e-05
2.78076	0.000129115	3.6454e-06	5.28297e-06
3.17971	2.71815e-05	1.1942e-06	2.28341e-06
3.57894	7.31421e-06	5.88194e-07	2.51803e-06
3.97836	1.13237e-06	2.26779e-07	7.1155e-07

Table A.42: The $\bar{\Lambda}$ Spectra at 27 GeV, 60-80% Centrality Bin

p_T	$\frac{1}{2\pi}\frac{dN^2}{Np_T dp_T dy}$	Statistical Error	Systematic Error
0.505829	0.0556569	0.0039838	0.00368768
0.701886	0.032025	0.00113059	0.00143005
0.899506	0.017058	0.000537869	0.000528261
1.09797	0.00907184	0.000291679	0.000221009
1.29694	0.00435913	0.000149219	9.96698e-05
1.49626	0.00223045	8.72616e-05	5.58137e-05
1.69578	0.00105549	4.13184e-05	2.62944e-05
1.89547	0.00051138	2.13523e-05	2.06558e-05
2.13926	0.000188738	6.90754e-06	9.96316e-06
2.43889	5.86246e-05	2.74485e-06	4.12733e-06
2.7801	2.23922e-05	1.20931e-06	1.466e-06
3.18012	4.11016e-06	4.21528e-07	3.55002e-07
3.58038	5.90902e-07	1.42917e-07	2.58441e-07

Table A.43: The Ξ^- Spectra at 19.6 GeV, 0-5% Centrality Bin

p_T	$\frac{1}{2\pi}\frac{dN^2}{Np_T dp_T dy}$	Statistical Error	Systematic Error
0.703705	0.325617	0.0523691	0.0330905
0.901471	0.211576	0.01881	0.00954593
1.09995	0.144091	0.0092578	0.00443508
1.29885	0.092744	0.00461881	0.00418959
1.49804	0.056034	0.00248299	0.00168931
1.69742	0.0321983	0.00126938	0.00114226
1.89693	0.0175479	0.000664599	0.000810343
2.14208	0.00808841	0.000248772	0.000197354
2.44113	0.00322031	0.000110325	0.000184639
2.78287	0.00094906	3.73639e-05	5.27514e-05
3.18167	0.000224377	1.48876e-05	1.83746e-05
3.58078	6.49933e-05	7.10238e-06	7.18332e-06
3.9801	6.57323e-06	2.46446e-06	2.52609e-06

Table A.44: The Ξ^- Spectra at 19.6 GeV, 5-10% Centrality Bin

p_T	$\frac{1}{2\pi}\frac{dN^2}{Np_T dp_T dy}$	Statistical Error	Systematic Error
0.703668	0.249913	0.0633227	0.0320261
0.901434	0.173787	0.0188597	0.00943092
1.09991	0.131955	0.0095861	0.00480855
1.29881	0.0724131	0.00451718	0.00244113
1.49799	0.0438371	0.00223962	0.00142856
1.69737	0.0235304	0.00106213	0.000883061
1.89688	0.0132219	0.000565716	0.000446929
2.14195	0.00648673	0.000227847	0.000226459
2.441	0.00213052	8.35462e-05	9.04732e-05
2.78265	0.000747428	3.30275e-05	3.04441e-05
3.18144	0.000187916	1.36568e-05	1.99978e-05
3.58055	3.67598e-05	5.54586e-06	9.34063e-06
3.97986	9.78235e-06	2.70331e-06	2.13206e-06

Table A.45: The Ξ^- Spectra at 19.6 GeV, 10-20% Centrality Bin

p_T	$\frac{1}{2\pi}\frac{dN^2}{Np_T dp_T dy}$	Statistical Error	Systematic Error
0.703717	0.155001	0.0246093	0.0102292
0.901483	0.128118	0.0102904	0.00614883
1.09997	0.0818642	0.00435307	0.00136785
1.29887	0.0496754	0.00222994	0.00121382
1.49807	0.0322744	0.00127576	0.00110438
1.69744	0.0173244	0.000606468	0.000622966
1.89695	0.0100598	0.000338711	0.000278984
2.14214	0.00464524	0.000128412	0.000105755
2.44118	0.00176099	5.42547e-05	4.91005e-05
2.78299	0.00052417	1.82625e-05	1.25041e-05
3.18178	0.000129628	7.55346e-06	1.08602e-05
3.5809	3.56853e-05	3.56274e-06	4.16783e-06
3.98022	6.81374e-06	1.58615e-06	1.43306e-06

Table A.46: The Ξ^- Spectra at 19.6 GeV, 20-30% Centrality Bin

p_T	$\frac{1}{2\pi}\frac{dN^2}{Np_T dp_T dy}$	Statistical Error	Systematic Error
0.703656	0.116923	0.0213244	0.0112337
0.901422	0.080663	0.00757715	0.00419811
1.0999	0.0516722	0.00341786	0.00175903
1.2988	0.0318896	0.00171961	0.00117189
1.49799	0.0177715	0.000792741	0.000670552
1.69737	0.0105126	0.000438152	0.000315506
1.89689	0.00596312	0.000244082	0.00019185
2.14201	0.00252885	8.21243e-05	3.92354e-05
2.44107	0.000926079	3.3825e-05	3.00276e-05
2.78286	0.000326635	1.38355e-05	8.589e-06
3.18172	8.73064e-05	5.88157e-06	7.36272e-06
3.5809	1.55951e-05	2.35039e-06	8.75537e-07
3.98029	6.40147e-06	1.34411e-06	1.02747e-06

Table A.47: The Ξ^- Spectra at 19.6 GeV, 30-40% Centrality Bin

p_T	$\frac{1}{2\pi}\frac{dN^2}{Np_T dp_T dy}$	Statistical Error	Systematic Error
0.703656	0.0648729	0.0134742	0.00409349
0.90141	0.0410465	0.00510202	0.00221094
1.09988	0.0266579	0.00230498	0.00117635
1.29879	0.0168239	0.00113792	0.000923307
1.49796	0.00953818	0.000539707	0.000362058
1.69733	0.00605024	0.000328779	0.000185251
1.89684	0.00300689	0.000152136	8.76178e-05
2.14188	0.00139478	5.89425e-05	3.04705e-05
2.44093	0.000459797	2.25416e-05	1.33193e-05
2.78251	0.00015744	9.37158e-06	6.20953e-06
3.1813	4.66532e-05	4.36261e-06	4.39411e-06
3.58041	8.59668e-06	1.72142e-06	1.58481e-06

Table A.48: The Ξ^- Spectra at 19.6 GeV, 40-60% Centrality Bin

p_T	$\frac{1}{2\pi}\frac{dN^2}{Np_T dp_T dy}$	Statistical Error	Systematic Error
0.703461	0.0285968	0.00772637	0.00295571
0.901178	0.0178794	0.00215036	0.00121747
1.09963	0.0111237	0.000934225	0.000557597
1.29852	0.0061416	0.000424901	0.000330602
1.4977	0.00387609	0.000251001	9.90058e-05
1.69708	0.0018824	0.000102993	6.50418e-05
1.8966	0.00102383	5.739e-05	3.30187e-05
2.14135	0.0004547	2.14905e-05	1.12979e-05
2.44045	0.000161906	9.5299e-06	7.73705e-06
2.78181	5.33911e-05	3.67419e-06	4.4261e-06
3.18076	1.1371e-05	1.39381e-06	8.47064e-07
3.58004	2.69931e-06	6.73424e-07	4.16714e-07

Table A.49: The Ξ^- Spectra at 19.6 GeV, 60-80% Centrality Bin

p_T	$\frac{1}{2\pi}\frac{dN^2}{Np_T dp_T dy}$	Statistical Error	Systematic Error
0.702789	0.00732551	0.00306138	0.000961371
0.900421	0.00320116	0.000525955	0.000323685
1.09883	0.00187799	0.000235991	0.000113728
1.29772	0.00113287	0.000116106	4.9327e-05
1.49693	0.000463788	4.10714e-05	5.18645e-05
1.69637	0.000344186	3.18568e-05	4.40045e-05
1.89595	0.00013134	1.36089e-05	1.39323e-05
2.14014	6.14844e-05	6.07708e-06	4.6085e-06
2.43952	1.48824e-05	2.53673e-06	2.16e-06
2.78079	4.62551e-06	1.0942e-06	1.35175e-06
3.18045	1.74692e-06	5.33889e-07	9.60589e-07
3.5804	7.75469e-07	3.39178e-07	1.79357e-07

Table A.50: The $\bar{\Xi}^{+}$ Spectra at 19.6 GeV, 0-5% Centrality Bin

p_T	$\frac{1}{2\pi}\frac{dN^2}{Np_T dp_T dy}$	Statistical Error	Systematic Error
0.703815	0.0859108	0.0169288	0.0192415
0.901593	0.0528052	0.00508936	0.00196072
1.10009	0.0411364	0.00282351	0.00169922
1.29902	0.02772	0.0015335	0.00123077
1.49821	0.0184955	0.000916532	0.00095783
1.6976	0.0105367	0.000474707	0.000254834
1.89713	0.00588859	0.000264031	0.000335567
2.14252	0.00262372	0.000104171	0.000194779
2.44159	0.00100921	4.89566e-05	6.11626e-05
2.7837	0.000311287	1.96597e-05	2.33111e-05
3.18251	7.7993e-05	8.38822e-06	5.92796e-06
3.58163	2.15208e-05	4.08645e-06	2.59793e-06

Table A.51: The $\bar{\Xi}^{+}$ Spectra at 19.6 GeV, 5-10% Centrality Bin

p_T	$\frac{1}{2\pi}\frac{dN^2}{Np_T dp_T dy}$	Statistical Error	Systematic Error
0.703766	0.0573267	0.0140606	0.00587788
0.901544	0.0399419	0.00462503	0.00340085
1.10003	0.0356136	0.00284511	0.00179662
1.29894	0.0237024	0.00153699	0.00135211
1.49814	0.0130082	0.000719401	0.000537285
1.69752	0.00759722	0.000381099	0.000344905
1.89704	0.00471507	0.000243182	0.000214489
2.14234	0.00208625	9.48541e-05	0.000126642
2.44138	0.000740523	4.23268e-05	3.08879e-05
2.78334	0.000219505	1.60432e-05	1.22203e-05
3.18215	5.43882e-05	7.40268e-06	5.35452e-06
3.58127	1.58198e-05	3.32321e-06	2.78319e-06

Table A.52: The $\bar{\Xi}^{+}$ Spectra at 19.6 GeV, 10-20% Centrality Bin

p_T	$\frac{1}{2\pi}\frac{dN^2}{Np_T dp_T dy}$	Statistical Error	Systematic Error
0.703741	0.0550831	0.00926777	0.00667018
0.90152	0.0327063	0.00276727	0.00157875
1.10001	0.0239597	0.0014422	0.00107688
1.29892	0.0158704	0.000796231	0.000636979
1.49811	0.0101225	0.000430524	0.000256173
1.69749	0.00608621	0.00024917	0.000160407
1.89702	0.00320952	0.000125802	9.0876e-05
2.14226	0.00153933	5.36326e-05	4.63332e-05
2.44131	0.000585653	2.49191e-05	9.82158e-06
2.78322	0.000150563	9.039e-06	6.06956e-06
3.18203	4.20962e-05	4.14493e-06	6.22876e-06
3.58115	8.66104e-06	1.73601e-06	1.02499e-06

Table A.53: The $\bar{\Xi}^{+}$ Spectra at 19.6 GeV, 20-30% Centrality Bin

p_T	$\frac{1}{2\pi}\frac{dN^2}{Np_T dp_T dy}$	Statistical Error	Systematic Error
0.703717	0.0337022	0.00677072	0.00413597
0.901483	0.0246317	0.00227363	0.00168879
1.09997	0.0144208	0.000996027	0.000686731
1.29887	0.0104837	0.000598846	0.000217998
1.49807	0.00597746	0.000301024	0.000271903
1.69744	0.00351883	0.000164821	6.96102e-05
1.89695	0.00214052	0.000104361	9.37454e-05
2.14214	0.000877314	3.72567e-05	5.50783e-05
2.44118	0.000339899	1.79812e-05	1.12439e-05
2.78298	0.000101726	6.87048e-06	3.15731e-06
3.18178	2.28811e-05	2.81965e-06	1.47861e-06
3.58089	4.75157e-06	1.33283e-06	1.09808e-06

Table A.54: The $\bar{\Xi}^{+}$ Spectra at 19.6 GeV, 30-40% Centrality Bin

p_T	$\frac{1}{2\pi}\frac{dN^2}{Np_T dp_T dy}$	Statistical Error	Systematic Error
0.703485	0.01947	0.00467893	0.00172853
0.901227	0.0150019	0.0018362	0.000804061
1.09969	0.0105814	0.000947854	0.000464726
1.29859	0.006354	0.000439958	0.00030768
1.49778	0.0033915	0.000206399	0.000124739
1.69719	0.0019063	0.000114331	9.89629e-05
1.89672	0.000961722	5.81196e-05	6.7503e-05
2.14168	0.00045815	2.58453e-05	1.68408e-05
2.44084	0.000167759	1.20911e-05	1.10692e-05
2.78259	5.13981e-05	4.85786e-06	4.66604e-06
3.18166	1.46101e-05	2.26595e-06	2.43099e-06
3.58106	3.81508e-06	1.06382e-06	9.41905e-07

Table A.55: The $\bar{\Xi}^{+}$ Spectra at 19.6 GeV, 40-60% Centrality Bin

p_T	$\frac{1}{2\pi}\frac{dN^2}{Np_T dp_T dy}$	Statistical Error	Systematic Error
0.703351	0.0117602	0.00296067	0.00213436
0.901044	0.00687914	0.000890386	0.000501518
1.09947	0.00441358	0.000419749	0.000231952
1.29832	0.00260888	0.000186659	0.000146467
1.49748	0.00125551	8.61861e-05	5.74344e-05
1.69682	0.000741028	4.75837e-05	2.69215e-05
1.89632	0.000349437	2.41387e-05	1.31945e-05
2.14065	0.000178225	1.15079e-05	4.61369e-06
2.43966	5.22682e-05	4.35915e-06	6.40986e-06
2.78024	1.52391e-05	1.84308e-06	9.59755e-07
3.179	2.36489e-06	6.13003e-07	3.82509e-07
3.57807	4.36425e-07	2.51418e-07	1.56249e-07

Table A.56: The $\bar{\Xi}^{+}$ Spectra at 19.6 GeV, 60-80% Centrality Bin

p_T	$\frac{1}{2\pi}\frac{dN^2}{Np_T dp_T dy}$	Statistical Error	Systematic Error
0.702814	0.00236111	0.000712073	0.000361292
0.900397	0.00157364	0.000314977	0.000121
1.09874	0.000844937	0.000114628	7.52759e-05
1.29753	0.000417909	4.84236e-05	3.44955e-05
1.49661	0.000227413	2.65202e-05	2.44974e-05
1.69592	0.000103283	1.34421e-05	1.42526e-05
1.89538	4.58468e-05	7.08591e-06	8.98625e-06
2.13849	2.00427e-05	3.02018e-06	2.55959e-06
2.43743	5.85346e-06	1.40377e-06	4.46366e-07
2.7763	6.25369e-07	3.48183e-07	5.49998e-07

Table A.57: The Ξ^- Spectra at 27 GeV, 0-5% Centrality Bin

p_T	$\frac{1}{2\pi}\frac{dN^2}{Np_T dp_T dy}$	Statistical Error	Systematic Error
0.703827	0.321599	0.0561827	0.0357682
0.90163	0.21124	0.0180886	0.0136243
1.10013	0.146118	0.00803941	0.0045698
1.29905	0.102324	0.00459093	0.00545914
1.49825	0.0578573	0.00214588	0.00206263
1.69764	0.037151	0.00129288	0.000925795
1.89716	0.0202406	0.000656681	0.000518866
2.14261	0.00994685	0.00025641	0.000275068
2.44168	0.00376746	0.000102493	0.000120459
2.78387	0.00124759	3.56903e-05	4.47986e-05
3.18268	0.000331453	1.44081e-05	1.18326e-05
3.58181	7.37428e-05	6.14747e-06	8.9116e-06
3.98113	2.62085e-05	3.31635e-06	2.7628e-06
4.45685	4.88926e-06	1.12103e-06	8.30793e-07

Table A.58: The Ξ^- Spectra at 27 GeV, 5-10% Centrality Bin

p_T	$\frac{1}{2\pi}\frac{dN^2}{Np_T dp_T dy}$	Statistical Error	Systematic Error
0.703827	0.21162	0.0353715	0.0195915
0.90163	0.171672	0.0143259	0.00811354
1.10013	0.11685	0.00730493	0.00495559
1.29905	0.0762126	0.00357639	0.00199707
1.49825	0.0490611	0.00208252	0.00234127
1.69764	0.0290358	0.00111213	0.000917894
1.89716	0.0163089	0.000577365	0.000603811
2.14261	0.0076928	0.000216248	0.000201613
2.44168	0.00311182	9.22667e-05	9.20837e-05
2.78387	0.000953519	3.04796e-05	2.40164e-05
3.18268	0.00026545	1.22783e-05	8.5043e-06
3.58181	7.04314e-05	5.63626e-06	3.49764e-06
3.98113	1.23972e-05	2.38032e-06	3.01236e-06
4.45685	3.60664e-06	1.06023e-06	1.39049e-06

Table A.59: The Ξ^- Spectra at 27 GeV, 10-20% Centrality Bin

p_T	$\frac{1}{2\pi}\frac{dN^2}{Np_T dp_T dy}$	Statistical Error	Systematic Error
0.703827	0.187381	0.0239611	0.0164207
0.901617	0.119119	0.00787796	0.0049388
1.10012	0.0881611	0.00404635	0.00233918
1.29904	0.055296	0.00203111	0.00175623
1.49824	0.0340344	0.00108355	0.000455016
1.69763	0.0198167	0.000570254	0.000301719
1.89715	0.011613	0.000319461	0.000210156
2.14258	0.0054344	0.000117794	0.000100538
2.44164	0.00212835	4.89854e-05	3.7782e-05
2.78381	0.000693962	1.68694e-05	1.96159e-05
3.18262	0.000178754	6.74576e-06	1.42533e-05
3.58174	4.73379e-05	3.08784e-06	3.93719e-06
3.98107	1.16364e-05	1.48254e-06	2.34304e-06
4.45672	3.29361e-06	5.93022e-07	5.24353e-07

Table A.60: The Ξ^- Spectra at 27 GeV, 20-30% Centrality Bin

p_T	$\frac{1}{2\pi}\frac{dN^2}{Np_T dp_T dy}$	Statistical Error	Systematic Error
0.703815	0.107139	0.0153597	0.011159
0.901605	0.0795601	0.00607877	0.00311588
1.1001	0.0543462	0.00284811	0.00169738
1.29902	0.0319374	0.0013734	0.00084706
1.49821	0.0198222	0.000719188	0.000398953
1.6976	0.0119902	0.000404432	0.00026101
1.89713	0.00702361	0.000225149	0.000146318
2.14254	0.00332564	8.5026e-05	6.77898e-05
2.44159	0.00123936	3.38144e-05	2.94802e-05
2.78372	0.000425131	1.23654e-05	1.62764e-05
3.18254	0.000102087	4.72602e-06	4.08357e-06
3.58166	2.51994e-05	2.17608e-06	3.04356e-06
3.98099	7.868e-06	1.17024e-06	9.91746e-07
4.45652	1.41834e-06	3.55619e-07	1.75097e-07

Table A.61: The Ξ^- Spectra at 27 GeV, 30-40% Centrality Bin

p_T	$\frac{1}{2\pi}\frac{dN^2}{Np_T dp_T dy}$	Statistical Error	Systematic Error
0.703766	0.0726938	0.0149728	0.00630822
0.901544	0.0490768	0.00449704	0.00311481
1.10004	0.029024	0.00190972	0.00109838
1.29896	0.0196142	0.00100643	0.000655873
1.49815	0.0112088	0.000489261	0.000138308
1.69753	0.00680446	0.000284192	0.000165348
1.89705	0.00364429	0.000142512	0.000119404
2.14236	0.00172316	5.50891e-05	3.45966e-05
2.4414	0.000685341	2.336e-05	1.55895e-05
2.78339	0.000207969	7.99928e-06	8.91072e-06
3.1822	5.85353e-05	3.52475e-06	2.97991e-06
3.58132	1.36529e-05	1.58291e-06	1.10416e-06
3.98065	4.27122e-06	7.86761e-07	6.24871e-07

Table A.62: The Ξ^- Spectra at 27 GeV, 40-60% Centrality Bin

p_T	$\frac{1}{2\pi}\frac{dN^2}{Np_T dp_T dy}$	Statistical Error	Systematic Error
0.703497	0.0382045	0.00620491	0.00511321
0.901239	0.0220012	0.00208555	0.00119749
1.0997	0.0127067	0.000873804	0.000578465
1.29861	0.00791596	0.000455434	0.000320038
1.49781	0.00447238	0.000210288	8.18857e-05
1.6972	0.00241515	0.000104615	4.00642e-05
1.89673	0.00125364	5.14568e-05	3.94117e-05
2.14171	0.000617598	2.14073e-05	1.55044e-05
2.44087	0.000229769	9.01057e-06	2.88505e-06
2.78267	7.09057e-05	3.18295e-06	3.84104e-06
3.18176	1.82217e-05	1.31563e-06	1.38661e-06
3.58116	4.09708e-06	5.70912e-07	5.14753e-07
3.98078	1.58775e-06	3.52612e-07	1.27262e-07

Table A.63: The Ξ^- Spectra at 27 GeV, 60-80% Centrality Bin

p_T	$\frac{1}{2\pi}\frac{dN^2}{Np_T dp_T dy}$	Statistical Error	Systematic Error
0.703058	0.00792855	0.00187615	0.00165778
0.900739	0.00491807	0.000700553	0.000517278
1.09919	0.00244092	0.000225702	8.3466e-05
1.29809	0.0013412	0.000105185	6.23859e-05
1.49731	0.000720183	5.08521e-05	2.81886e-05
1.69675	0.000378088	2.42676e-05	1.82997e-05
1.89632	0.000216098	1.52708e-05	9.03071e-06
2.14095	9.7136e-05	6.17499e-06	5.22747e-06
2.4403	2.79353e-05	2.44101e-06	3.00123e-06
2.78207	1.19324e-05	1.20584e-06	1.77051e-06
3.18162	2.08128e-06	4.70372e-07	7.51165e-07
3.58149	6.45573e-07	2.21051e-07	2.74789e-07

Table A.64: The $\bar{\Xi}^{+}$ Spectra at 27 GeV, 0-5% Centrality Bin

p_T	$\frac{1}{2\pi}\frac{dN^2}{Np_T dp_T dy}$	Statistical Error	Systematic Error
0.703949	0.128248	0.0243246	0.0150766
0.901764	0.0736639	0.00579713	0.00409954
1.10029	0.0546684	0.00314402	0.00107573
1.29922	0.0363766	0.00174824	0.00139616
1.49843	0.0234234	0.000947203	0.000845053
1.69783	0.0151309	0.000560913	0.000359702
1.89737	0.00856183	0.000304995	0.000257382
2.14307	0.00440561	0.000130663	0.000165643
2.44215	0.00161995	5.44599e-05	8.48449e-05
2.78474	0.000577606	2.18178e-05	1.48383e-05
3.18358	0.000142664	8.94327e-06	4.42044e-06
3.58271	3.9286e-05	4.23259e-06	3.58337e-06
3.98205	1.13232e-05	2.14807e-06	9.67442e-07
4.45883	2.50259e-06	7.92963e-07	4.3716e-07

Table A.65: The $\bar{\Xi}^{+}$ Spectra at 27 GeV, 5-10% Centrality Bin

p_T	$\frac{1}{2\pi}\frac{dN^2}{Np_T dp_T dy}$	Statistical Error	Systematic Error
0.703888	0.08362	0.0163342	0.00751674
0.901691	0.0624466	0.00566408	0.00138641
1.1002	0.0464871	0.00284602	0.00137223
1.29914	0.0325642	0.00163568	0.00109416
1.49835	0.019099	0.000834276	0.000610977
1.69774	0.0124884	0.000519652	0.000644059
1.89726	0.00680927	0.000262997	0.000162958
2.14285	0.00336953	0.000109203	0.000106581
2.44192	0.00137032	4.92302e-05	5.03784e-05
2.7843	0.000435351	1.80601e-05	1.01422e-05
3.18312	0.000106033	7.25221e-06	5.49332e-06
3.58226	2.67724e-05	3.31266e-06	1.79835e-06
3.98159	7.49904e-06	1.86387e-06	1.31456e-06
4.45784	2.4464e-06	7.39486e-07	5.54643e-07

Table A.66: The $\bar{\Xi}^{+}$ Spectra at 27 GeV, 10-20% Centrality Bin

p_T	$\frac{1}{2\pi}\frac{dN^2}{Np_T dp_T dy}$	Statistical Error	Systematic Error
0.703888	0.0699416	0.00966637	0.00764713
0.901691	0.0498201	0.00348138	0.00139706
1.1002	0.033362	0.00160058	0.00072509
1.29913	0.0231016	0.000887898	0.000567747
1.49833	0.014169	0.000468876	0.000400101
1.69774	0.00846513	0.000258406	0.000162354
1.89726	0.00504757	0.00015058	0.000133724
2.14283	0.00233455	5.74822e-05	7.49468e-05
2.4419	0.000937256	2.62204e-05	2.36171e-05
2.78428	0.000306199	9.89816e-06	8.6955e-06
3.1831	7.91905e-05	4.31542e-06	3.65548e-06
3.58223	2.20544e-05	2.01238e-06	7.13458e-07
3.98157	6.77885e-06	1.10099e-06	9.22866e-07
4.45779	1.20001e-06	3.7472e-07	2.96306e-07

Table A.67: The $\bar{\Xi}^{+}$ Spectra at 27 GeV, 20-30% Centrality Bin

p_T	$\frac{1}{2\pi}\frac{dN^2}{Np_T dp_T dy}$	Statistical Error	Systematic Error
0.703839	0.052822	0.00771282	0.00410642
0.901642	0.0337514	0.00284089	0.00219144
1.10014	0.0242262	0.00135516	0.00112623
1.29907	0.0140927	0.000637721	0.000458568
1.49826	0.00895591	0.000341391	0.000229025
1.69765	0.00544639	0.000198532	8.17933e-05
1.89717	0.00306532	0.000107011	7.6183e-05
2.14265	0.00147151	4.36606e-05	2.64115e-05
2.44171	0.000568564	1.90138e-05	2.18755e-05
2.78394	0.00019881	7.83775e-06	1.21857e-05
3.18276	4.88856e-05	3.15049e-06	1.68794e-06
3.58189	1.33969e-05	1.5096e-06	5.21005e-07
3.98122	2.00406e-06	5.74043e-07	4.81912e-07
4.45703	1.02948e-06	3.1104e-07	3.9817e-07

Table A.68: The $\bar{\Xi}^{+}$ Spectra at 27 GeV, 30-40% Centrality Bin

p_T	$\frac{1}{2\pi}\frac{dN^2}{Np_T dp_T dy}$	Statistical Error	Systematic Error
0.703839	0.0290524	0.00528682	0.00350238
0.90163	0.0221315	0.00225073	0.00106792
1.10012	0.0149989	0.000963888	0.000549758
1.29903	0.00868457	0.000454922	0.000245696
1.4982	0.00563447	0.000271356	0.000176146
1.69758	0.00330288	0.000149654	9.24456e-05
1.89708	0.00179812	7.80027e-05	4.41814e-05
2.14234	0.000787155	2.86967e-05	1.35272e-05
2.44131	0.000310946	1.35157e-05	1.20295e-05
2.78303	9.48371e-05	5.08849e-06	2.84083e-06
3.18161	2.60585e-05	2.28602e-06	1.73963e-06
3.58047	7.33419e-06	1.0712e-06	9.22604e-07
3.97955	1.4523e-06	4.60754e-07	4.43256e-07

Table A.69: The $\bar{\Xi}^{+}$ Spectra at 27 GeV, 40-60% Centrality Bin

p_T	$\frac{1}{2\pi}\frac{dN^2}{Np_T dp_T dy}$	Statistical Error	Systematic Error
0.703558	0.0143142	0.00249559	0.00172376
0.901288	0.0104077	0.00106328	0.000520533
1.09975	0.00669659	0.000497484	0.000213096
1.29864	0.00376764	0.000220383	0.00011097
1.49781	0.00227121	0.000116359	8.15099e-05
1.69717	0.00131117	6.37957e-05	6.34879e-05
1.89669	0.000675371	3.14757e-05	2.21468e-05
2.14151	0.000271776	1.0975e-05	9.30713e-06
2.44056	0.000104935	5.34289e-06	2.94561e-06
2.78189	3.17728e-05	1.91408e-06	1.38339e-06
3.18069	9.45e-06	9.4617e-07	1.00205e-06
3.57983	1.53648e-06	3.74642e-07	4.30493e-07
3.97917	3.50523e-07	1.55318e-07	8.79764e-08

Table A.70: The $\bar{\Xi}^+$ Spectra at 27 GeV, 60-80% Centrality Bin

p_T	$\frac{1}{2\pi}\frac{dN^2}{Np_T dp_T dy}$	Statistical Error	Systematic Error
0.703119	0.00377615	0.000879413	0.000774175
0.9008	0.00199005	0.000273616	0.000204289
1.09924	0.00108969	0.000118268	7.00412e-05
1.29814	0.000679376	5.84126e-05	2.504e-05
1.49734	0.000368293	2.91685e-05	2.17799e-05
1.69676	0.00020328	1.55824e-05	1.85262e-05
1.89632	0.000100657	8.29363e-06	4.82894e-06
2.14087	4.22049e-05	3.58814e-06	3.51144e-06
2.44016	1.30946e-05	1.57772e-06	1.36206e-06
2.7817	5.30913e-06	7.72782e-07	7.99258e-07
3.18111	1.15607e-06	3.12304e-07	2.29629e-07
3.58084	3.12567e-07	1.51385e-07	7.28612e-08

Table A.71: The Ω^- and $\bar{\Omega}^+$ p_T Spectra at 7.7 GeV

Centrality	p_T	$\frac{1}{2\pi}\frac{dN^2}{Np_T dp_T dy}$	Statistical Error	Systematic Error
Ω^-	1.01427	0.00261527	0.000944016	0.000312062
0-60%	1.44464	0.000978677	0.000270339	0.000167983
	1.78541	0.000404759	8.62406e-05	4.58896e-05
	2.22129	9.08301e-05	2.88634e-05	1.43706e-05
$\bar{\Omega}^+$	1.0088	0.000855682	0.000204696	4.29255e-05
0-60%	1.4436	0.000234903	7.45194e-05	2.53923e-05
	1.78349	7.95117e-05	3.20239e-05	9.04318e-06
	2.21821	1.81605e-05	1.24703e-05	8.54971e-06

Table A.72: The $\Omega^{-} p_T$ Spectra at 11.5 GeV

Centrality	p_T	$\frac{1}{2\pi}\frac{dN^2}{Np_T dp_T dy}$	Statistical Error	Systematic Error
0-10%	1.01313	0.00814011	0.00350706	0.00123738
	1.39583	0.00297549	0.000723081	0.000406702
	1.78956	0.00172435	0.000273602	0.000120962
	2.1861	0.000565869	0.000103202	3.70281e-05
	2.58393	0.000172394	4.3147e-05	1.51498e-05
	3.13005	2.05214e-05	7.97135e-06	1.73688e-06
10-60%	1.00563	0.00364036	0.00060951	0.00022089
	1.39186	0.00113642	0.000122437	6.81066e-05
	1.78653	0.000428949	4.17648e-05	2.7983e-05
	2.18393	0.00013559	1.6255e-05	9.75575e-06
	2.58266	3.18495e-05	6.14252e-06	3.73544e-06
	3.13015	7.31537e-06	1.5676e-06	5.51835e-07

Table A.73: The $\bar{\Omega}^{+} p_T$ Spectra at 11.5 GeV

Centrality	p_T	$\frac{1}{2\pi}\frac{dN^2}{Np_T dp_T dy}$	Statistical Error	Systematic Error
0-10%	1.01367	0.00367224	0.00148974	0.00369203
	1.3961	0.00140577	0.00031946	0.000231605
	1.7898	0.000653242	0.0001118	7.37817e-05
	2.18636	0.000262759	5.20221e-05	1.4515e-05
	2.58419	7.855e-05	2.23603e-05	6.10852e-06
	3.13102	8.46299e-06	4.5805e-06	8.90806e-07
10-60%	1.0113	0.000970335	0.000211822	9.95379e-05
	1.39489	0.000395753	5.50952e-05	1.51357e-05
	1.78865	0.000234294	2.50402e-05	9.76809e-06
	2.18517	6.37403e-05	9.66436e-06	4.78446e-06
	2.58297	1.01077e-05	3.27398e-06	1.92162e-06
	3.12641	2.61219e-06	9.57011e-07	2.27913e-07

Table A.74: The $\Omega^- p_T$ Spectra at 19.6 GeV

Centrality	p_T	$\frac{1}{2\pi}\frac{dN^2}{Np_T dp_T dy}$	Statistical Error	Systematic Error
0-10%	1.01203	0.0170832	0.00296004	0.00251965
	1.39542	0.00707997	0.000674653	0.000563584
	1.78947	0.00331902	0.000280701	0.000244399
	2.18638	0.000854749	9.7949e-05	0.000162385
	2.58461	0.000347719	4.33678e-05	5.57209e-05
	3.13475	6.67558e-05	9.39822e-06	1.22649e-05
10-20%	1.0126	0.0102127	0.0015584	0.00148067
	1.39557	0.00417735	0.000424869	0.00044988
	1.78931	0.00197503	0.000179893	0.00014164
	2.18585	0.000554177	6.24609e-05	8.775e-05
	2.58366	0.000178461	2.58696e-05	2.78197e-05
	3.12905	2.92421e-05	5.69909e-06	4.18861e-06
20-40%	1.00867	0.00419571	0.000591435	0.000641952
	1.39357	0.00225078	0.000205111	0.000181032
	1.78775	0.000620339	5.69479e-05	5.23943e-05
	2.1847	0.000230813	2.30432e-05	3.59344e-05
	2.58295	5.64163e-05	8.88816e-06	8.64608e-06
	3.1289	1.24654e-05	2.394e-06	1.78018e-06
40-60%	1.00552	0.00110674	0.000245822	0.000205001
	1.39191	0.000389916	6.47817e-05	3.35968e-05
	1.78674	0.000183049	2.89577e-05	1.428e-05
	2.18432	3.82172e-05	8.25889e-06	6.09312e-06
	2.58322	1.32465e-05	3.65834e-06	2.27302e-06
	3.13297	2.9554e-06	9.48778e-07	5.42546e-07

Table A.75: The $\bar{\Omega}^{+} p_T$ Spectra at 19.6 GeV

Centrality	p_T	$\frac{1}{2\pi}\frac{dN^2}{Np_T dp_T dy}$	Statistical Error	Systematic Error
0-10%	1.01483	0.00780381	0.00125578	0.00054454
	1.39664	0.00367763	0.000399356	0.000270005
	1.79031	0.00180344	0.000158798	0.00015186
	2.18687	0.000679038	6.88774e-05	2.72305e-05
	2.58471	0.0002032	2.70923e-05	2.7714e-05
	3.13304	2.66992e-05	5.65005e-06	6.58442e-06
10-20%	1.01418	0.0063183	0.00105186	0.000800465
	1.39634	0.00257344	0.000281131	0.000167403
	1.79003	0.00110879	0.00011062	8.99004e-05
	2.18659	0.00038033	4.20205e-05	2.52479e-05
	2.58443	0.000108106	1.82675e-05	1.55106e-05
	3.13194	2.35251e-05	4.41111e-06	2.19719e-06
20-40%	1.01491	0.0024452	0.000367367	0.000207725
	1.39667	0.00102401	0.000104086	5.99532e-05
	1.79035	0.000548453	4.76946e-05	4.20097e-05
	2.18691	0.000178079	1.81421e-05	8.81391e-06
	2.58475	5.56916e-05	8.16267e-06	7.62273e-06
	3.13318	7.77912e-06	1.96016e-06	7.05653e-07
40-60%	1.00869	0.000617707	0.000164295	4.7414e-05
	1.39337	0.000310459	5.04858e-05	2.44599e-05
	1.78715	0.000103307	1.86916e-05	8.49428e-06
	2.18362	4.2699e-05	7.78225e-06	1.76535e-06
	2.58135	7.4499e-06	2.51914e-06	1.23896e-06

Table A.76: The $\Omega^- p_T$ Spectra at 27 GeV

Centrality	p_T	$\frac{1}{2\pi}\frac{dN^2}{Np_T dp_T dy}$	Statistical Error	Systematic Error
0-10%	1.01754	0.0124927	0.00204919	0.00139717
	1.39777	0.00865718	0.000767841	0.000667535
	1.79135	0.00368167	0.000269663	0.000375214
	2.18793	0.00130169	9.47594e-05	0.000169243
	2.5858	0.000442722	4.14181e-05	4.26519e-05
	3.1372	8.83589e-05	8.30889e-06	1.10068e-05
10-20%	1.01456	0.0100671	0.00162976	0.00130854
	1.39651	0.00518716	0.000480465	0.0003642
	1.79019	0.00193869	0.000154097	0.000121925
	2.18676	0.000716157	5.77449e-05	8.87863e-05
	2.5846	0.000277121	2.62264e-05	2.37117e-05
	3.13259	3.80716e-05	4.84698e-06	4.79573e-06
20-40%	1.01729	0.00418737	0.000483233	0.00048164
	1.39767	0.00234685	0.000183764	0.000157054
	1.79127	0.000924254	6.64142e-05	5.86529e-05
	2.18784	0.000384396	2.6126e-05	4.14167e-05
	2.58571	0.000106905	9.88205e-06	9.1321e-06
	3.13685	2.55497e-05	2.36213e-06	3.32363e-06
40-60%	1.01142	0.00124037	0.000256704	0.000144039
	1.39495	0.000715879	9.43549e-05	4.83292e-05
	1.78871	0.000213957	2.53438e-05	1.35878e-05
	2.18524	7.06493e-05	8.67516e-06	7.58653e-06
	2.58303	2.59733e-05	4.0219e-06	2.22405e-06
	3.12667	2.98132e-06	9.19676e-07	3.99199e-07

Table A.77: The $\bar{\Omega}^{+} p_T$ Spectra at 27 GeV

Centrality	p_T	$\frac{1}{2\pi}\frac{dN^2}{Np_T dp_T dy}$	Statistical Error	Systematic Error
0-10%	1.02033	0.00848074	0.00134475	0.00125046
	1.39879	0.00517073	0.000470267	0.000413838
	1.79225	0.0023014	0.000178634	0.000119314
	2.18884	0.00103122	7.52202e-05	7.31802e-05
	2.58672	0.000302677	2.95642e-05	2.73506e-05
	3.14075	6.99047e-05	7.09398e-06	8.44036e-06
10-20%	1.01778	0.00546324	0.000818779	0.00075296
	1.39787	0.00313816	0.000297686	0.000247821
	1.79144	0.00131549	0.000110281	7.56148e-05
	2.18802	0.000652817	5.33592e-05	4.92434e-05
	2.58589	0.00014271	1.73693e-05	1.17796e-05
	3.13753	3.55171e-05	4.39631e-06	3.39167e-06
20-40%	1.01628	0.00332534	0.000433737	0.000484053
	1.39726	0.00167727	0.000131418	0.000133861
	1.79089	0.000713622	5.03964e-05	3.69368e-05
	2.18746	0.000246654	1.84123e-05	1.79938e-05
	2.58532	8.94659e-05	8.27051e-06	6.62418e-06
	3.13536	1.64359e-05	1.79187e-06	1.58493e-06
40-60%	1.00999	0.00092586	0.000187503	0.000121921
	1.39415	0.000493195	6.73542e-05	3.88722e-05
	1.78793	0.000189466	2.54691e-05	1.0149e-05
	2.18443	5.93032e-05	8.29557e-06	4.38956e-06
	2.5822	1.8805e-05	3.56701e-06	1.37112e-06
	3.12355	1.4826e-06	5.38501e-07	1.95485e-07

Table A.78: The $\Omega^- p_T$ Spectra at 39 GeV, 0-5% Centrality Bin

p_T	$\frac{1}{2\pi}\frac{dN^2}{Np_T dp_T dy}$	Statistical Error	Systematic Error
0.964511	0.0219906	0.00418377	0.00243898
1.25135	0.0123583	0.00113967	0.000655964
1.54719	0.00791966	0.000486096	0.000535862
1.84496	0.00403859	0.00024748	0.000207353
2.18823	0.00178677	0.000104579	0.000121663
2.5861	0.000583055	4.46881e-05	3.62699e-05
2.98469	0.000175305	1.95473e-05	1.23396e-05
3.38367	8.2603e-05	9.707e-06	9.53049e-06
3.78294	1.98664e-05	4.23158e-06	2.1258e-06

Table A.79: The $\Omega^- p_T$ Spectra at 39 GeV, 5-10% Centrality Bin

p_T	$\frac{1}{2\pi}\frac{dN^2}{Np_T dp_T dy}$	Statistical Error	Systematic Error
0.964987	0.0233191	0.00321152	0.00175369
1.25149	0.0108186	0.000829887	0.000564417
1.5473	0.00645427	0.000384831	0.000426884
1.84507	0.0033582	0.000191006	0.000201884
2.18841	0.00137512	7.61259e-05	8.94509e-05
2.5863	0.000508042	3.41342e-05	4.10817e-05
2.98488	0.000190317	1.52775e-05	1.29386e-05
3.38388	6.11445e-05	7.22466e-06	6.68444e-06
3.78314	1.15512e-05	3.10767e-06	1.2274e-06

Table A.80: The $\Omega^- p_T$ Spectra at 39 GeV, 10-20% Centrality Bin

p_T	$\frac{1}{2\pi}\frac{dN^2}{Np_T dp_T dy}$	Statistical Error	Systematic Error
0.964951	0.0139117	0.00130655	0.000972202
1.25147	0.00685703	0.000373611	0.000351166
1.5473	0.00383364	0.000166526	0.00019191
1.84507	0.00224125	9.30772e-05	0.000137383
2.1884	0.00101058	3.94607e-05	6.54338e-05
2.58629	0.000326136	1.62243e-05	2.05695e-05
2.98487	0.000108617	7.69933e-06	7.47314e-06
3.38387	2.80399e-05	3.51073e-06	3.02206e-06
3.78312	1.11986e-05	1.72558e-06	1.51884e-06

Table A.81: The $\Omega^- p_T$ Spectra at 39 GeV, 20-40% Centrality Bin

p_T	$\frac{1}{2\pi}\frac{dN^2}{Np_T dp_T dy}$	Statistical Error	Systematic Error
0.964529	0.00613366	0.000464408	0.000482266
1.25135	0.0036376	0.000152306	0.00018011
1.54721	0.00203621	6.96722e-05	0.000102693
1.84497	0.0010535	3.59518e-05	5.34074e-05
2.18824	0.000451825	1.51067e-05	2.83077e-05
2.58611	0.000149032	6.52618e-06	9.04302e-06
2.9847	5.18299e-05	3.19059e-06	3.46051e-06
3.38369	1.83105e-05	1.59193e-06	1.92681e-06
3.78295	4.86789e-06	7.8599e-07	5.78471e-07

Table A.82: The $\Omega^- p_T$ Spectra at 39 GeV, 40-60% Centrality Bin

p_T	$\frac{1}{2\pi}\frac{dN^2}{Np_T dp_T dy}$	Statistical Error	Systematic Error
0.962424	0.00150255	0.000168779	0.00011467
1.25067	0.000873941	5.65913e-05	4.42422e-05
1.54666	0.000446857	2.55647e-05	2.26753e-05
1.84444	0.000217455	1.30817e-05	1.13446e-05
2.18729	7.99036e-05	5.02446e-06	5.01505e-06
2.58514	3.44753e-05	2.53849e-06	2.41237e-06
2.9837	1.084e-05	1.25925e-06	8.48381e-07
3.38267	2.55218e-06	5.25301e-07	2.74997e-07

Table A.83: The $\Omega^- p_T$ Spectra at 39 GeV, 60-80% Centrality Bin

p_T	$\frac{1}{2\pi}\frac{dN^2}{Np_T dp_T dy}$	Statistical Error	Systematic Error
0.955978	0.000395057	7.6762e-05	2.85425e-05
1.24767	0.000137647	1.8828e-05	6.79811e-06
1.54398	7.23025e-05	8.64694e-06	4.17389e-06
1.84177	2.90401e-05	3.93771e-06	1.65186e-06
2.18244	9.48253e-06	1.63222e-06	6.05358e-07
2.58013	4.88535e-06	8.93084e-07	3.80133e-07

Table A.84: The $\bar{\Omega}^{+} p_T$ Spectra at 39 GeV, 0-5% Centrality Bin

p_T	$\frac{1}{2\pi}\frac{dN^2}{Np_T dp_T dy}$	Statistical Error	Systematic Error
0.964328	0.0187996	0.00298593	0.00157598
1.25129	0.00922456	0.000818335	0.000401911
1.54715	0.00635392	0.000404823	0.000399175
1.84492	0.00329351	0.000194724	0.000226219
2.18815	0.00159298	8.45269e-05	0.00011271
2.58603	0.000525121	3.62808e-05	4.66908e-05
2.98461	0.000144081	1.54141e-05	1.91855e-05
3.3836	4.7635e-05	7.55315e-06	5.48612e-06
3.78286	1.32325e-05	3.32735e-06	2.89071e-06

Table A.85: The $\bar{\Omega}^{+} p_T$ Spectra at 39 GeV, 5-10% Centrality Bin

p_T	$\frac{1}{2\pi}\frac{dN^2}{Np_T dp_T dy}$	Statistical Error	Systematic Error
0.966324	0.0113505	0.00203278	0.000806675
1.25186	0.00767646	0.00062246	0.000348094
1.54759	0.00425723	0.000276944	0.000181824
1.84534	0.00222152	0.000144529	0.000129361
2.1889	0.00117129	6.43318e-05	7.7389e-05
2.58679	0.000354153	2.63332e-05	3.17318e-05
2.98538	0.00011909	1.27636e-05	7.74561e-06
3.38439	3.90352e-05	6.00599e-06	4.37323e-06
3.78366	1.82734e-05	3.41554e-06	2.40392e-06

Table A.86: The $\bar{\Omega}^{+} p_T$ Spectra at 39 GeV, 10-20% Centrality Bin

p_T	$\frac{1}{2\pi}\frac{dN^2}{Np_T dp_T dy}$	Statistical Error	Systematic Error
0.965262	0.011051	0.00102827	0.000870082
1.25157	0.00610198	0.000338657	0.000222224
1.54737	0.00279582	0.00012737	0.000143071
1.84512	0.00169046	7.37022e-05	8.73265e-05
2.18852	0.000749598	3.14249e-05	4.52517e-05
2.58641	0.000239253	1.36043e-05	2.08925e-05
2.98499	8.48907e-05	6.28114e-06	6.08529e-06
3.38399	2.67788e-05	3.25632e-06	3.05086e-06
3.78326	1.15415e-05	1.72943e-06	1.65885e-06

Table A.87: The $\bar{\Omega}^{+} p_T$ Spectra at 39 GeV, 20-40% Centrality Bin

p_T	$\frac{1}{2\pi}\frac{dN^2}{Np_T dp_T dy}$	Statistical Error	Systematic Error
0.96387	0.00471022	0.000369886	0.000326242
1.25114	0.0028673	0.000124328	0.000100199
1.54704	0.00154131	5.69661e-05	6.27121e-05
1.84481	0.000832524	3.06329e-05	4.32569e-05
2.18796	0.000335101	1.22217e-05	2.10045e-05
2.58583	0.000111427	5.33866e-06	9.78318e-06
2.98441	4.0074e-05	2.62248e-06	2.64615e-06
3.38339	1.18529e-05	1.28043e-06	1.2367e-06
3.78265	4.22458e-06	6.95414e-07	5.51819e-07

Table A.88: The $\bar{\Omega}^{+} p_T$ Spectra at 39 GeV, 40-60% Centrality Bin

p_T	$\frac{1}{2\pi}\frac{dN^2}{Np_T dp_T dy}$	Statistical Error	Systematic Error
0.962204	0.00119804	0.000144036	8.18628e-05
1.2506	0.000615025	4.45353e-05	2.48371e-05
1.54659	0.000395916	2.33153e-05	1.60627e-05
1.84437	0.000160727	1.03952e-05	8.24992e-06
2.18716	8.10099e-05	4.85982e-06	5.00156e-06
2.58502	2.24916e-05	2.08384e-06	1.96354e-06
2.98358	7.14426e-06	9.85557e-07	5.68896e-07
3.38255	1.98146e-06	4.71987e-07	2.04934e-07

Table A.89: The $\bar{\Omega}^{+} p_T$ Spectra at 39 GeV, 60-80% Centrality Bin

p_T	$\frac{1}{2\pi}\frac{dN^2}{Np_T dp_T dy}$	Statistical Error	Systematic Error
0.95607	0.000235876	5.39199e-05	1.78122e-05
1.24772	0.000110506	1.52906e-05	5.97741e-06
1.54404	5.57292e-05	6.99255e-06	3.42604e-06
1.84181	2.15681e-05	3.28713e-06	1.11545e-06
2.18253	7.85769e-06	1.50318e-06	5.3586e-07
2.58023	3.99415e-06	7.9905e-07	3.7056e-07

APPENDIX B

Data Table of Strange Particle dN/dy

Table B.1: The K^0_S dN/dy

		K^0_S		
Energy	Centrality	dN/dy	Stat_Err	Sys_Err
27 GeV	0-5%	23.4608	0.184125	0.803043
	5-10%	19.2747	0.164732	0.664027
	10-20%	14.6685	0.0979301	0.556008
	20-30%	9.66451	0.0752485	0.397568
	30-40%	6.56729	0.0658161	0.334484
	40-60%	3.11378	0.0335869	0.168607
	60-80%	0.832945	0.0129548	0.0523479
19.6 GeV	0-5%	21.0136	0.190014	0.633776
	5-10%	17.1702	0.182699	0.564741
	10-20%	12.8878	0.106224	0.439176
	20-30%	8.52321	0.0828938	0.302806
	30-40%	5.37491	0.0668607	0.223596
	40-60%	2.5854	0.0351001	0.123448
	60-80%	0.701406	0.0140789	0.0448103

Table B.2: The Λ and $\bar{\Lambda}$ dN/dy

		Λ			$\bar{\Lambda}$		
Energy	Centrality	dN/dy	Stat_Err	Sys_Err	dN/dy	Stat_Err	Sys_Err
27 GeV	0-5%	12.523	0.0986795	0.356634	2.90898	0.0264658	0.0716985
	5-10%	10.1533	0.0877966	0.31395	2.50348	0.0245017	0.0655394
	10-20%	7.63072	0.0502942	0.198574	1.95162	0.0143452	0.0497626
	20-30%	5.18224	0.0380865	0.132891	1.38844	0.0119441	0.0329385
	30-40%	3.19287	0.0350673	0.0923374	0.95616	0.0108381	0.0238407
	40-60%	1.49362	0.0190592	0.0734593	0.485461	0.00675674	0.0128007
	60-80%	0.372609	0.00716617	0.0220901	0.147908	0.00326446	0.0100471
19.6 GeV	0-5%	13.5214	0.124265	0.338916	1.97557	0.0210184	0.0487331
	5-10%	10.8106	0.110803	0.274835	1.64934	0.0200398	0.0428585
	10-20%	8.12758	0.0668637	0.220166	1.31555	0.0120638	0.0302655
	20-30%	5.23155	0.0513071	0.136154	0.938293	0.0101812	0.020953
	30-40%	3.30028	0.0377854	0.0840888	0.640749	0.00931681	0.0173609
	40-60%	1.48071	0.0237305	0.0528799	0.336451	0.00605149	0.0103521
	60-80%	0.354257	0.00899181	0.0206641	0.103221	0.00313628	0.00626957

Table B.3: The Ξ^- and $\bar{\Xi}^+$ dN/dy

		Ξ^-			$\bar{\Xi}^+$		
Energy	Centrality	dN/dy	Stat_Err	Sys_Err	dN/dy	Stat_Err	Sys_Err
27 GeV	0-5%	1.80806	0.0394294	0.0823548	0.676678	0.0153543	0.0280729
	5-10%	1.39817	0.0338772	0.0613239	0.55396	0.0143418	0.0220828
	10-20%	1.03013	0.0184683	0.0442439	0.411474	0.0081972	0.0165308
	20-30%	0.624685	0.0130844	0.0270563	0.278551	0.00633414	0.0114425
	30-40%	0.369642	0.00953039	0.0157103	0.169088	0.00705268	0.00700716
	40-60%	0.165986	0.00745476	0.0114568	0.0782753	0.00364916	0.00338947
	60-80%	0.0337505	0.00269309	0.00350648	0.0157098	0.00128874	0.00131534
19.6 GeV	0-5%	1.77205	0.0458699	0.0783067	0.49934	0.014971	0.0238159
	5-10%	1.42113	0.0443178	0.0660478	0.388539	0.0140746	0.0150714
	10-20%	0.971514	0.0233193	0.0400111	0.299309	0.00795358	0.0118822
	20-30%	0.615316	0.0253766	0.0293617	0.191038	0.00592319	0.00768778
	30-40%	0.32878	0.0120774	0.012783	0.118258	0.00752661	0.00655993
	40-60%	0.13542	0.00828794	0.00742067	0.0546374	0.00249077	0.00277317
	60-80%	0.0274921	0.00310966	0.00259198	0.0115101	0.00099926	0.000503011

Table B.4: The Ω^- and $\bar{\Omega}^+$ dN/dy

		Ω^-			$\bar{\Omega}^+$		
Energy	Centrality	dN/dy	Stat_Err	Sys_Err	dN/dy	Stat_Err	Sys_Err
39 GeV	0-5%	0.20264	0.00900492	0.00825241	0.166105	0.00691071	0.00614294
	5-10%	0.177013	0.00684442	0.00657822	0.112017	0.00491252	0.00380827
	10-20%	0.111571	0.00312123	0.00380873	0.0871698	0.00260734	0.00296746
	20-40%	0.0545675	0.00131194	0.00179019	0.04253	0.00109382	0.00133382
	40-60%	0.0127127	0.000524924	0.000413617	0.010129	0.000448424	0.000289939
	60-80%	0.00271887	0.000258469	8.52111e-05	0.00196502	0.000166152	7.73212e-05
27 GeV	0-10%	0.154464	0.00991486	0.00606177	0.097128	0.00644993	0.00423082
	10-20%	0.102613	0.00705708	0.00457674	0.0604311	0.00407852	0.00253276
	20-40%	0.0440682	0.00247146	0.00171593	0.0334974	0.00197105	0.00155707
	40-60%	0.0131746	0.00140327	0.000517131	0.0103893	0.00107676	0.000419111
19.6 GeV	0-10%	0.160162	0.0196019	0.0113662	0.0812905	0.00611435	0.00265233
	10-20%	0.0959867	0.00752222	0.0047012	0.0569186	0.00482428	0.00251965
	20-40%	0.043665	0.00502187	0.00302201	0.0236951	0.0017385	0.000800428
	40-60%	0.0104316	0.00223982	0.00119814	0.00671811	0.000940283	0.00021567
11.5 GeV	0-10%	0.0824223	0.0130436	0.00386625	0.0356727	0.00591868	0.00197067
	10-60%	0.0329979	0.00547655	0.00352239	0.00987569	0.00105947	0.000336112
7.7 GeV	0-60%	0.0272618	0.00612652	0.00138937	0.00799258	0.00198897	0.0002044

References

[1] T. D. Lee, G. C. Wick, "Vacuum stability and vacuum excitation in a spin-0 field theory." *Phys. Rev. D.* **9** 2291 (1974).

[2] R. Stock, "Relativistic Nucleus-Nucleus Collisions and the QCD Matter Phase Diagram." arXiv:0807.1610.

[3] J. Adams et al. (STAR Collaboration), "Experimental and Theoretical Challenges in the Search for the Quark Gluon Plasma: The STAR Collaboration's Critical Assessment of the Evidence from RHIC Collisions." *Nucl. Phys. A* **757** 102 (2005).

[4] F. Karsch, "Lattice QCD at high temperature and density." *Lect. Notes Phys.* **583** 209 (2002).

[5] J. Rafelski, "Strange anti-baryons from quark-gluon plasma." *Phys. Lett. B* **262**, 333 (1991).

[6] E. Schnedermann, J. Sollfrank, U. Heinz, "Thermal phenomenology of hadrons from 200A GeV S+S collisions." *Phys. Rev. C* **48**, 2462 (1993).

[7] M. M. Aggarwal et al. (STAR Collaboration), "An Experimental Exploration of the QCD Phase Diagram: The Search for the Critical Point and the Onset of De-confinement." arXiv:1007.2613 [nucl-ex].

[8] A. M.Poskanzer, S. A. Voloshin, "Methods for analyzing anisotropic flow in relativistic nuclear collisions." *Phys. Rev. C* **58**, 1671 (1998).

[9] J. Adams et al. (STAR Collaboration), "Azimuthal anisotropy in Au+Au collisions at $\sqrt{s_{NN}}$ =200 GeV." *Phys. Rev. C* **72**, 014904 (2005).

[10] J. Adams et al. (STAR Collaboration), "Azimuthal anisotropy and correlations at large transverse momenta in p+p and Au+Au collisions at $\sqrt{s_{NN}}$ =200 GeV." *Phys. Rev. Lett.* **93**, 252301 (2004).

[11] S. S. Adler et al. (PHENIX Collaboration), "Elliptic Flow of Identified Hadrons in Au+Au Collisions at $\sqrt{s_{NN}}$ =200 GeV." *Phys. Rev. Lett.* **91**, 182301 (2003).

[12] R. Fries, V. Greco, P. Sorensen, "Coalescence Models for Hadron Formation from Quark-Gluon Plasma." *Ann. Rev. Nucl. Part. Sci.* **58**, 177 (2008).

[13] D. Molnar, S. A. Volshin, "Elliptic Flow at Large Transverse Momenta from Quark Coalescence." *Phys. Rev. Lett.* **91**, 092301 (2003).

[14] R. J. Fries, B. Müller, C. Nonaka, S. A. Bass, "Hadronization in Heavy-Ion Collisions: Recombination and Fragmentation of Partons." *Phys. Rev. Lett.* **90**, 202303 (2003).

[15] R. J. Fries, C. Nonaka, "Evaluating results from the Relativistic Heavy Ion Collider with perturbative QCD and hydrodynamics." *Prog. Part. Nucl. Phys.* **66**, 607 (2011).

[16] B. Alver et al. (PHOBOS collaboration), "Event-by-event fluctuations of azimuthal particle anisotropy in Au+Au collisions at $\sqrt{s_{NN}} = 200$ GeV." *Phys. Rev. Lett.* **104**, 142301 (2010).

[17] J. Adams et al. (STAR Collaboration), "Azimuthal anisotropy at RHIC: the first and fourth harmonics." *Phys. Rev. Lett.* **92**, 062301 (2004).

[18] P. Romatschke, U. Romatschke, "Viscosity Information from Relativistic Nuclear Collisions:How Perfect is the Fluid Observed at RHIC?" *Phys. Rev. Lett.* **99**, 172301 (2007).

[19] Y. L. Dokshitzer, D. E. Kharzeev, "Heavy-quark colorimetry of QCD matter." *Phys. Lett. B* **519**, 199 (2001).

[20] L. Adamczyk et al. (STAR Collaboration), "Observation of D^0 meson nuclear modifications in Au+Au collisions at $\sqrt{s_{NN}}$ =200 GeV." arXiv:1404.6185 [nucl-ex].

[21] A. Adare et al. (PHENIX Collaboration), "Energy Loss and Flow of Heavy Quarks in Au+Au Collisions at $\sqrt{s_{NN}}$ =200 GeV." *Phys. Rev. Lett.* **98**, 172301 (2007).

[22] M. Harrison, S. Peggs, T. Roser, "The RHIC Accelerator." *Ann. Rev. Nucl. Part. Sci.* **52**, 425 (2002).

[23] K. H. Ackermann et al. (STAR Collaboration), "STAR dectector overview." *Nucl. Instrum. Meth.* **A499**, 624 (2003).

[24] M. Anderson et al., "The STAR time projection chamber: a unique tool for studying high multiplicity events at RHIC." *Nucl. Instrum. Meth.* **A499**, 659 (2003).

[25] W. J. Llope et al., "The TOFp/pVPD time-of-flight system for STAR." *Nucl. Instrum. Meth.* **A522**, 252 (2004).

[26] M. Shao et al., "Extensive particle identificaiton with TPC and TOF at the STAR experiment." *Nucl. Instrum. Meth.* **A558**, 419 (2006).

[27] M. Beddo et al., "The STAR Barrel Electromagnetic Calorimeter." *Nucl. Instrum. Meth.* **A499**, 725 (2003).

[28] C. E. Allgower et al., "The STAR endcap deletromagnetic calorimeter." *Nucl. Instrum. Meth.* **A499**, 740 (2003).

[29] F. Bergsma et al., "The STAR detector magnet subsystem." *Nucl. Instrum. Meth.* **A499**, 633 (2003).

[30] F. S. Bieser et al., "The STAR trigger." *Nucl. Instrum. Meth.* **A499**, 766 (2003).

[31] C. Adler et al. (STAR Collaboration), "Mid-rapidity Λ and $\bar{\Lambda}$ Production in Au+Au Collisions at $\sqrt{s_{NN}}$ = 130 GeV." *Phys. Rev. Lett.* **89**, 092301 (2002).

[32] J. Adam et al. (STAR Collaboration), "Multi-Strange Baryon Production in Au-Au collisions at $\sqrt{s_{NN}}$ =130 GeV." *Phys. Rev. Lett.* **92**, 182301 (2004).

[33] H. Long, "Mid-rapidity Λ and $\bar{\Lambda}$ Production in Au+Au Collisions at the Relativistic Heavy Ion Collider." Ph. D. Thesis, University of California at Los Angeles (2002).

[34] H. Jiang, "Strange Hadron(K^0_S, Λ and Ξ) Production in d+Au Collisions at $\sqrt{s_{NN}}$ =200 GeV at RHIC." Ph. D. Thesis, University of California at Los Angeles (2005).

[35] J. Rafelski, B. Müller, "Strange Production in the Quark-Gluon Plasma." *Phys. Rev. Lett.* **48** 1066 (1982).

[36] S. Albergo et al. (E896 Collaboration), "Λ Spectra in 11.6A GeV/c Au-Au Collisions." *Phys. Rev. Lett.* **88**, 062301 (2002).

[37] L. Ahle et al. (E802 Collaboration), "Particle production at high baryon density in central Au+Au reactions at 11.6A GeV/c." *Phys. Rev. C* **57**, 466 (1998).

[38] P. Chung et al. (E895 Collaboration), "Near-Threshold Production of the Multistrange Ξ^- Hyperon." *Phys. Rev. Lett.* **91**, 202301 (2003).

[39] B. B. Back et al. (E917 Collaboration), "Antilambda Production in Au+Au Collisions at 11.7A GeV/c." *Phys. Rev. Lett.* **87**, 242301 (2001).

[40] S. Ahmad et al. (E891 Collaboration), "Λ production by 11.6 A GeV/c Au beam on Au target." *Phys. Lett. B* **382**, 35 (1996).

[41] F. Antinori et al. (NA57 Collaboration), "Energy dependence of hyperon production in nucleus-nucleus collisions at SPS." *Phys. Lett. B* **595**, 68 (2004).

[42] C. Alt et al. (NA49 Collaboration), "Energy dependence of Λ and Ξ production in central Pb+Pb collisions at 20A, 30A, 40A, 80A, and 158A GeV measured at the CERN Super Proton Synchrotron." *Phys. Rev. C* **78**, 034918 (2008).

[43] T. Anticic et al. (NA49 Collaboration), "System-size dependence of Λ and Ξ production in nucleus-nucleus at 40A and 158A GeV measured at the CERN Super Proton Synchrotron." *Phys. Rev. C* **80**, 034906 (2009).

[44] B. I. Abelev et al. (STAR Collaboration), "Enhanced strange baryon production in Au+Au collisions compared to p+p at $\sqrt{s_{NN}}$ =200 GeV." *Phys. Rev. C* **77**, 044908 (2008).

[45] J. Adams et al. (STAR Collaboration), "Scaling Properties of Hyperon Production in Au+Au Collisions at $\sqrt{s_{NN}}$ =200 GeV." *Phys. Rev. Lett.* **98**, 062301 (2007).

[46] M. M. Aggarwal et al. (STAR Collaboration), "Strange and multistrange particle production in Au+Au collisions at $\sqrt{s_{NN}}$ =62.4 GeV." *Phys. Rev. C* **83**, 024901 (2011).

[47] K. Adcox et al. (PHENIX Collaboration), "Measurement of Λ and $\bar{\Lambda}$ Particles in Au+Au Collisions at $\sqrt{s_{NN}}$ =130 GeV." *Phys. Rev. Lett.* **89**, 092302 (2002).

[48] F. R. Brown et al., "On the Existence of a Phase Transition for QCD with Three Light Quarks." *Phys. Rev. Lett.* **65**, 2491 (1990).

[49] J. Cleymans, H. Oeschler, K. Redlich, S. Wheaton, "Comparision of chemical freeze-out criteria in heavy-ion collisions." *Phys. Rev. C* **73**, 034905 (2006).

[50] S. Margetis, K. Safarik, O. V. Baillie, "STRANGENESS PRODUCTION IN HEAVY-ION COLLISIONS." *Annu. Rev. Nucl. Part. Sci.* **50**, 299 (2000).

[51] P. Koch, B. Müller, J. Rafelski, "STRANGENESS IN RELATIVISTIC HEAVY ION COLLISIONS." *Phys. Rep.* **142**, 167 (1986).

[52] G. I. Kopylov, "Like particle correlations as a tool to study the multiple production mechanism." *Phys. Lett.* **50B**, 472 (1974).

[53] J. W. Cronin, H. J. Frisch, M. J. Shochet, J. P. Boymond, P. A. Piroue, R. L. Sumner, "Production of hadrons at large transverse momentum at 200, 300, and 400 GeV." *Phys. Lett. D* **11**, 3105 (1975).

[54] C. Alt et al. (NA49 Collaboration), "Ω^- and $\bar{\Omega}^+$ Production in Central Pb+Pb collisions at 40A and 158A GeV." *Phys. Rev. Lett.* **94**, 192301 (2005).

[55] F. Becattini, J. Manninen, M. Gazdzicki, "Energy and system size dependence of chemical freeze-out in relativistic nuclear collisions." *Phys. Rev. C* **73**, 044905 (2006).

[56] S. S. Chern, J. Simons, "Characteristic forms and geometric invariants." *Annals Math.* **99**, 48 (1974).

[57] D. Diakonov, "Instantons at Work." *Prog. Part. Nucl. Phys.* **51**, 173 (2003).

[58] D. E. Kharzeev, L. D. McLerran, K. J. Warringa, "The effects of topological charge change in heavy ion collisions:"Event by event P and CP violation"." *Nucl. Phys. A* **803** 227 (2008).

[59] G. 't Hooft, "Symmetry Breaking through Bell-Jackiw Anomalies." *Phys. Rev. Lett.* **37** 8 (1976).

[60] D. E. Kharzeev, D. T. Son, "Testing the Chiral Magnetic and Chiral Vortical Effects in Heavy Ion Collisions." *Phys. Rev. Lett.* **106**, 062301 (2011).

[61] S. A. Voloshin, "Parity violation in hot QCD: how to detect it." *Phys. Rev. C* **70**, 057901 (2004).

[62] B. I. Abelev et al. (STAR Collaboration), "Azimuthal Charged-Particle Correlations and Possible Local Strong Parity Violation." *Phys. Rev. Lett.* **103**, 251601 (2009).

[63] J. Adams et al. (STAR Collaboration), "Strange anti-particle to particle ratios at mid-rapidity in $\sqrt{s_{NN}} = 130$ GeV Au+Au Collisions." *Phys. Lett. B* **595**, 167 (2004).

[64] J. Adams et al. (STAR Collaboration), "Identified particle distributions in pp and Au+Au collisions at $\sqrt{s_{NN}} = 200$ GeV." *Phys. Rev. Lett.* **92**, 112301 (2004).

[65] M. Kaneta, N. Xu, "Centrality Dependence of Chemical Freeze-out in Au+Au Collisions at RHIC." arXiv:nucl-th/0405068v1.

[66] A. M. Poskanzer, S. A. Voloshin, "Methods for analyzing anisotropic flow in relativistic nuclear collisions." *Phys. Rev. C* **58**, 1671 (1998).

[67] J. Barrette et al. (E877 Collaboration), "Proton and pion production relative to the reaction plane in Au+Au collisions at 11A GeV/c." *Phys. Rev. C* **56**, 3254 (1997).

[68] B. I. Abelev et al. (STAR Collaboration), "Neutral Kaon Interferometry in Au+Au collisions at $\sqrt{s_{NN}}$ =200 GeV." *Phys. Rev. C* **74**, 54902 (2006).

[69] J. Adams et al. (STAR Collaboration), "Proton - Λ correlations in central Au+Au collisions at $\sqrt{s_{NN}}$ =200 GeV." *Phys. Rev. C* **74**, 64906 (2006).

[70] S. Schlichting, S. Pratt, "Charge conservation at energies available at the BNL Relativistic Heavy Ion Collider and contributions to local parity violation observables." *Phys. Rev. C* **83**, 014913 (2011).

[71] S. Pratt, S. Schlichting, S. Gavin, "Effects of momentum conservation and flow on angular correlations observed in experiments at the BNL Relativistic Heavy Ion Collider." *Phys. Rev. C* **84**, 024909 (2011).

[72] A. Bzdak, V. Koch, J. Liao, "Charge-Dependent Correlations in Relativistic Heavy Ion Collisions and the Chiral Magnetic Effect." *Lect. Notes Phys.* **871**, 503 (2013).

[73] L. Adamczyk et al. (STAR Collaboration), "Elliptic flow of identified hadrons in Au+Au collisions at $\sqrt{s_{NN}}$ =7.7-62.4 GeV." *Phys. Rev. C* **88**, 14902 (2013).

[74] L. Adamczyk et al. (STAR Collaboration), "Observation of an energy-dependent difference in elliptic flow between particles and anti-particles in relativistic heavy ion collisions." *Phys. Rev. Lett.* **110**, 142301 (2013).